Ollscoil na hÉireann, Corcaigh

National University of Ireland, Cork

Processing Techniques, Structural Configurations, and Electric Field Influence in Pyramidal Quantum Dots: An Experimental and Simulative Investigation

Thesis presented by

Luca Colavecchi

[https://orcid.org/0000-0002-2441-4887]

for the degree of

Doctor of Philosophy

University College Cork

Tyndall National Institute

UCC Head of School/Department: Fatima Gunning

Supervisor: Dr Emanuele Pelucchi Cosupervisor: Dr. Gediminas Juska

June 2025

Table of Contents

Declaration

This is to certify that the work I am submitting is my own and has not been submitted for another degree, either at University College Cork or elsewhere. All external references and sources are clearly acknowledged and identified within the contents. I have read and understood the regulations of University College Cork concerning plagiarism and intellectual property.

Luca Colavecchi,

Tyndall National Institute,

University College Cork,

June 2025

List of Publications:

Luca Colavecchi, Gediminas Juska and Emanuele Pelucchi: *Optimizing light extraction from non-planar site-controlled pyramidal quantum dot system: comparative modeling of three fabricable geometries*, *Mater. Quantum. Technol.* 2025, DOI: 10.1088/2633-4356/adb6ec.

Gediminas Juska, Simone Varo, Nicola Maraviglia, John O'Hara, Salvador Medina, **Luca Colavecchi**, Francesco Mattana, Armando Trapala, Michael Schmidt, and Emanuele Pelucchi: *Self-aligned pillar arrays embedding site-controlled single quantum dots for enhanced non-classical light emission. 2025,* https://doi.org/10.1002/adpr.202500116.

Ayse Ozcan-Atar, Pawel P. Michalowski, Agnieszka Gocalinska, John O'Hara, **Luca Colavecchi**, Gediminas Juska and Emanuele Pelucchi: *Suppressing Oxygen incorporation by Sb in III-V Aluminium Containing Alloys by MOVPE (and the Oxygen Paradox),* submitted

Luca Colavecchi, Salvador medina, Gediminas Juska, and Emanuele Pelucchi: *Minimization of polarized emission from self-aligned nanopillars,* on-going.

Presentations:

Luca Colavecchi, Gediminas Juska and Emanuele Pelucchi: *Pyramidal Quantum Dot Engineering: Towards electrical tuning of spectral properties*, poster presentation, Training School – "Modern directions in Epitaxy", Technical University of Denmark – Lyngby, 21st – 24th of June 2022

Luca Colavecchi, Gediminas Juska and Emanuele Pelucchi: *Coupling novel GaAs site-controlled QDs,* poster presentation, 15th Italian Quantum Information Science Conference,18-22 September 2023

List of acronyms

2DEG: 2-Dimensional Electron Gas

BE: Back Etching/Etched

CBR: Circular Bragg Reflector

CW: Continuous wave

DBR: Distributed Bragg Reflector

DE: Droplet Epitaxy

FDTD: Finite Difference Time Domain

FSS: Fine Structure Splitting

gdQD: gate-defined Quantum Dots

IC RIE: Inductively Coupled Reactive Ion Etching

JJ: Josephson Junction

JJ SQUID: Josephson Junction Superconducting Quantum Interference Device

LDE: Local Droplet Etching

LQW: Lateral Quantum Well

MBE: Molecular Beam Epitaxy

MOCVD: Metal-Organic Chemical Vapor Deposition

MOVPE: Metal-Organic Vapor Phase Epitaxy

PECVD: Plasma Enhanced Chemical Vapor Deposition

PIC: Photonic Integrated Circuit

PQD: Pyramidal Quantum Dots

PQC: Photonic Quantum Computing

QCSE: Quantum Confined Stark Effect

RSA: Rivest–Shamir–Adleman

SK: Stranski Kranstanov

SNSPDs: Superconducting Nanowire Single-Photon Detectors

SPADs: Single-Photon Avalanche Diodes

TPE: Two photon excitations

VQWr: Vertical Quantum Wire

What's the catch?

Abstract

Quantum computing promises to revolutionize information processing by leveraging quantum superposition and entanglement to perform calculations unattainable by classical computers. Among the various solid-state platforms employed in the quest for its practical realization, Quantum Dots (QDs) stand out as scalable and optically addressable artificial atoms, ideal for single-/entangled- photon sources and spin-based qubits. However, several challenges arising from the intrinsic properties of QDs still need to be addressed: the earlier development of optoelectronic technologies established key standards in terms of wavelength. As a result, QDs must be engineered to integrate seamlessly with existing platforms, one approach being precise emission wavelength tuning; external tuning is also a strategy to address the Fine Structure Splitting (FSS) of the exciton level, whose reduction is crucial to increase the degree of entanglement; efficient light-matter interaction is pivotal to harness their full potential, requiring engineered photonic environments that enhance emission properties and enable weak and strong coupling regimes.

In my thesis I have studied site-controlled Pyramidal Quantum Dots (PQDs) grown via MOVPE inside tetrahedral recesses defined on <111>B oriented GaAs substrates. This work puts emphasis on the post-growth processing that we generally perform to increase brightness, highlighting the huge impact that simple techniques like bonding, grinding and etching can have on the outcome in terms of specimen yield and photoluminescence.

Chapter 1

1 Introduction

1.1 The quantum information era

Advancements in science seldomly are the result of an intuition flashed into a single individual's mind; more often are the outcome of continuous efforts carried on by a community of researchers who work in similar fields and exchange ideas and solutions to obstacles that are on the road to grander objectives. In the summer of 1981, the MIT Laboratory for Computer Science and IBM sponsored the "Physics of Computation" conference, where a crowd of about 60 scientists, mostly physicists and computer scientists, gathered for three days at the MIT Endicott House venue and lit the spark that would ignite the quest for quantum computation[1]. The idea that classical computation could have been extended with the introduction of quantum mechanics was already in the air: Yuri Manin introduced the concept of quantum automaton making use of entanglement and superposition[2], Paul Benioff constructed a quantum mechanical model of a computation process based on the Turing machine[3]. However, the birth of quantum computation is conventionally attributed to Richard Feynman's "Simulating Physics with computers", transcription of the talk he gave at the Endicott House and that was credited for its pivotal role by later works[4]. Feynman discussed about the impossibility of simulating nature in an exact way with classical computers and envisioned a universal quantum simulator which Hamiltonian can be tailored to any discrete quantum mechanical system with a finite number of degrees of freedom[5]. The rally to quantum computation acquired more speed when in 1994 Peter Shor published his quantum factorization algorithm, which allows to decompose big integer numbers at an exponentially faster speed than classical alternatives by computing outputs of the periodic function simultaneously, exploiting quantum superposition[6]. The algorithm, although not implementable yet for big numbers because of the lack of quantum computational power available nowadays, threatens the security of digital systems as potentially able to crack RSA encoding. However, its publication cleared doubts over the

potentialities that quantum computation enclosed, paving the way to huge investments in the field and attracting interest into the new quantum cryptography field.

Thirty years later the landscape of quantum technologies is variegated, characterized by the presence of few big firms that laid the foundations and a plenitude of ventures, that followed in the wake of bigger companies, commercializing highly uncertain technologies[7]. The reason for this market flooding hides behind the youth of the sector, where the absence of standardized practices and, mainly, of a dominant technology, stand out if compared to a well-established sector as the one of microelectronics.

Di Vincenzo's criteria

In classical computation the output voltage of a transistor represents the information unit to process or deliver, called "bit". High and low voltage values encode respectively for 1 and 0, whereas a string of bits, each of which is 0 or 1, encodes for a decimal number in binary representation. Generally, a conventional computer processes data performing additions, multiplication, complement operations and more, on strings of binary digits. Quantum information technologies develop around the concept of quantum bit, or ***qubit***, which, similarly to its classical counterpart, is a system whose two levels can be addressed as $|0\rangle$ and $|1\rangle$. The stark difference, however, is that the latter abides by the laws of quantum mechanics, and hence is defined in a two-dimensional vector space which basis are $|0\rangle$ and $|1\rangle$, and which state can be any point in that space, written as linear combination of the basis:

$$|\psi\rangle = a|0\rangle + b|1\rangle, \tag{1.1}$$

where a and b are complex numbers which squared norms $|a|^2$ and $|b|^2$ are the probabilities of finding the qubit in state $|0\rangle$ and $|1\rangle$, respectively. This means that, regardless of the infinite number of states the qubit can be in, a measurement operation would always collapse it, forcing it to assume either the $|0\rangle$ or the $|1\rangle$ state: the measured outcome of a quantum operation is intrinsically classic per nature. A qubit can be embodied by any physical system that allows the existence of a two-state superposition:

the polarization state of a single photon inside a photonic quantum device, the charge state or the spin state of a gate-defined quantum dot, the state of a superconducting current in a resonant non-linear LC circuit (i.e. with a Josephson Junction) and more, can all represent the quantum information unit to manipulate. Despite the choice of platform, any physical implementation of a quantum processing device should fulfill some common-sense criteria:

- **Full qubit characterization**: the physical parameters of the qubit system and its Hamiltonian are fully known, together with probability of coupling to other levels if it's a system that hosts more than two levels, and the probability of coupling to other qubits.
- **Scalability**: the physical system can deliver the same performance when it is increased in size.
- **State initialization**: before any quantum computation operation, the string of qubit should be supplied in a known, systematically obtainable state. This can be achieved by letting the system reach the ground state or forcing the state by performing a measurement.
- **Long coherence times**: coherence encloses the dynamic of a qubit with its environment. A qubit that interacts with its surroundings loses the well-defined phase relationship between its two states transforming into a classical mixture. An example of a decohering qubit is an initialized electron spin state that, interacting with external spins (let's say nuclear ones), collapses and immediately reacquires its precession without memory of the phase relation established by the initialization process. Coherence times need to exceed by far the time scale of qubit manipulation.
- **Universal set of quantum gates**: just like NAND and NOR constitute a universal set of logic gates through which combination any logic operation can be performed, likewise, quantum devices should be working with a set of universal quantum gates to perform the set of Hamiltonians (unitary transformations) needed in a specific algorithm.

- **Specific measurement capability**: a measurement system should be able to collapse the qubit telling the state in which the qubit is in and its probability, without being influenced by the measured state itself or any other parameter of the system. Moreover, measuring a qubit should leave unaltered the state of the rest of the quantum computer.
- **Interconvert stationary and flying qubits**: the ability to transfer the same qubit state from a stationary qubit to mobile (flying) qubit, that hence, acquires the information, and vice versa.
- **Faithfully transmit flying qubits between specified locations**: flying qubit should be unperturbed by their transmission channel remaining unchanged, without decohering.

This set of requirements is extensively discussed by David Di Vincenzo in his essay "The Physical Implementation of Quantum Computation"[8].

1.2 Platforms

Up to present time, the most advanced quantum computing systems are based on superconducting qubits. D-Wave exploits flux qubits where the Josephson's Junction (JJ) part of the LCJ circuit is biased at a constant flux value, creating two potential wells at the bottom of the parabolic potential and allowing for the existence of a two-level system made of right- and left-rotating supercurrent states[9,10]; the company addresses optimization and sampling problems framing them as energy minimization tasks[9]. IBM, on the contrary, uses qubits defined from the states of a multilevel system of a *transmon,* where two JJ SQUID are in the middle of a large shunt capacitor and the charge state is acted upon through coupling with a coplanar waveguide resonator. They can avail of many qubits through which run specific quantum computation tasks, but the general-purpose quantum computation has been, till recently, restricted to a less the 100 qubits operations (plans for improved error corrected >1000 qubits are being implemented as we write and part of the short-term IBM roadmap). Superconducting

qubits benefit from the solid knowledge of microelectronic chip-making, rendering superconducting circuits highly designable and tuneable (the Hamiltonian of the system can be easily tailored changing circuit parameters), easily scalable and interconnectable[10]. Furthermore, coherence times have reached around 100us thanks to noise suppression and deign of less sensitive qubits[11].

Longer coherence times can be witnessed in colour centres in diamond. Ventures like Quantum Brilliance and Diatope supply quantum computing solutions exploiting Nitrogen Vacancies in Diamond, as they come with milliseconds scale coherence times[12] and, remarkably, with room temperature operating conditions, which allows cutting one-time costs for cryogenic equipment and recurring cost for operating them. Alternative solutions avail of trapped atoms qubits systems: a commercial gate-universal platform, made available by Atom Computing, encodes the qubit in the two nuclear spin states of the optically trapped neutral ^{87}Sr atoms achieving a coherence time of 40s[13].

A very large population of devices that allow implementations of qubit and quantum protocols are fabricated out of semiconductor materials. The low defect density of heteroepitaxial GaAs/AlGaAs layers allows for few-electron population regime of the vertically confined two-dimensional electron gas (2DEG), where addition lateral confinement obtained through top metal contracts permits to design gate-defined quantum dots (gdQDs). Charge-based qubit encoding can be realized trapping a single electron in adjacent QDs, with left and right electron localization corresponding to the two-level basis of the qubit. Similar hardware architectures can host spin-based qubit as well: the single-spin qubit exploits the Zeeman spin splitting of an unpaired electron in a gdQD, the singlet-triplet qubit is defined from the singlet state and the unpolarized triplet state of two electrons in a double gdQD. Many more exists[14], and many of them fulfil most requirements a quantum computing system should have, demonstrating the versatility and the potential of the gated QDs approach.

In this work we will concentrate our attention onto the Photonic Quantum Computing (PQC) platform, specifically addressing a particular kind of semiconductor quantum dots that could play a role as single and entangled photon sources, and potentially quantum gates. PQC aims at performing quantum (discrete/bulk) optics operations through classical integrated photonic for the obvious necessity of miniaturizing optical setups as the number of photons and gates involved gets larger. Photonic Integrated Circuits (PICs) hence offer the scalability required, being able to address high optical component density and, at the same time, providing limited transmission and coupling losses. Furthermore, photons can epitomize qubits as they are weakly interacting with the optical channel and among themselves, conferring robustness to the information they encode against decoherence mechanisms. However, despite integrated photonics leverages the wafer-scale fabrication techniques borrowed from electronics, competing functionalities ushered to a plethora of different material platforms (Silicon Photonics, III-V photonics, polymers, Lithium Niobate waveguides etc..) each excelling in addressing particular tasks, nevertheless incompatible with *monolithic* integration. Hence the need for heterogeneous integration of active components like light sources or detectors on photonic waveguide chips. This is being dealt with techniques like heteroepitaxy and transfer printing, however standardised practises have yet to be established. References 15 and 16 provide an overview of the state of the art and outline the challenges the community must overcome to bring Quantum Photonic Technologies to the market.

Several companies are advancing photonic quantum computing, using photons as the carriers of quantum information. For example, **PsiQuantum** leverages silicon photonics — integrating on-chip sources, detectors, interferometers, and switches — on CMOS-compatible processes; its design is measurement-based (using cluster states, i.e. entanglement, and fusion protocols) rather than the conventional gate model, with scalability built around semiconductor fab infrastructure. **Xanadu**, by contrast, develops continuous-variable photonic hardware based on squeezed states of light, using Gaussian boson sampling, interferometric networks, and homodyne detection; its

Borealis device offers tens to hundreds of squeezed-mode resources rather than discrete qubits, useful for sampling tasks, simulation, and variational protocols. In Europe, **Quandela** is developing deterministic single-photon sources using semiconductor quantum dots embedded in micropillar cavities, plus reconfigurable photonic circuits; its devices while enabling boson sampling, aim to develop and support universal photonic quantum computation (when fusion protocols are applied) and are accessible via cloud platforms. Photonic approaches benefit from low decoherence, compatibility with telecom infrastructure and high speed, but still face significant obstacles: between which, photon losses, achieving high success probability of entangling operations (deterministic vs probabilistic), efficient error correction, and large-scale integration of sources, switches, and detectors.

1.3 Solid-state single- and entangled- photon sources

One way of encoding a qubit with a photon is by exploiting its polarization

$$|\psi\rangle = a|H\rangle + b|\mathrm{V}\rangle, \tag{1.2}$$

where $|H\rangle$ and $|\mathrm{V}\rangle$ are the horizontal and vertical polarizations eigenstates, respectively. Manipulation of the photon qubit, however, requires operating at the single-photon level. A device like a stabilized laser is far from satisfying the single photons production requirement: its pulses are a superposition of number-states of light, each differing from the others, and hence characterised by photon numbers fluctuation despite the macroscopic amplitude reproducibility. Indeed, lasers belong to the family of coherent light sources, where photons follow a Poissonian statistic, and the standard deviation quantifying photon fluctuations is the square root of the average number of photons. Another kind of light is thermal light, which is the electromagnetic radiation emitted by a hot body. A single mode of thermal radiation has a Bose-Einstein distribution with a variance (standard deviation squared) equal to $\underline{n} + \underline{n}^2$, with $\underline{n}$ being the average number of photons. When a continuum of modes is considered, the distribution converges to a less broad one, however with a larger standard deviation than a Poissonian distribution. Such light is often referred to as super-Poissonian light. The last and, for our purposes,

most useful kind of light is the sub-Poissonian light, characterized by a standard deviation smaller than the Poissonian distribution. There is no classic equivalent to sub-Poissonian light, which we can think of as a stream of photons in between which time intervals are almost identical.

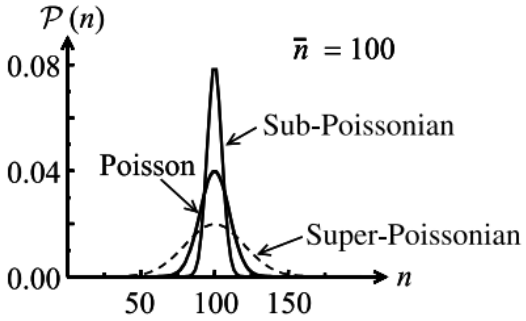

Figure 1.3-1: representation of Super-Poissonian, Poissonian and Sub-Poissonian distributions. Image taken from "Quantum Optics: An Introduction", Mark Fox

The purity of a single photon source is determined by calculating its **second-order autocorrelation function** at zero delay $g^2(0)$. The function, defined as

$$g^2(\tau) = \frac{< n_1(t) n_2(t+\tau) >}{< n_1(t) >< n_2(t+\tau) >}, \qquad (1.3)$$

is the conditional probability of measuring a photon at detector 2 after a time $t + \tau$, given that a photon at time t has already been detected at detector 1, and is measured with an Hanbury Brown–Twiss set up (reported in Figure 1.3-1Figure 1.3-2, left) consisting of a 50:50 beam splitter that redirects half of the impinging photons flux towards D1 and half towards D2. Calculating the function at zero delay means counting the number of clicks D2 has had immediately after the first click at D1. If $g^2(0) = 0$, then no photon has arrived at D2, and the source is a single photon source. This condition is referred to as *antibunching,* (see Figure 1.3-2, right).

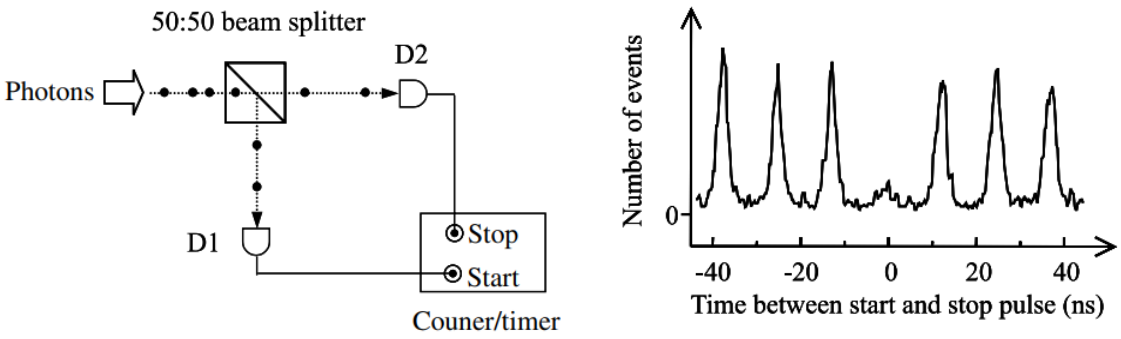

Figure 1.3-2: On the left, an Hanbury Brown-Twiss set up for single photons correlation measurements; on the right a single photon correlation curve obtained under pulsed excitation, where low coincidences are counted for τ=0. Image taken from "Quantum Optics: An Introduction", Mark Fox.

Semiconductor QDs can be exploited for production of trains of single photons and entangled photon pairs thanks to their atom-like response under excitation. QDs are clusters of atoms (10^3-10^5 atoms) of a low energy band gap surrounded by high energy band gap material. This three-dimensional confinement is what allows to trap charged carriers inside QDs on discrete energy level states. Population of these states can happen, e.g., by promoting carriers from the valence band to the conduction band in the barriers and letting those carriers minimize their energy occupying the QD's states by means of a laser with energy greater than the barriers' energy (above-band excitation), or by tuning the laser energy to the energy of the target state to promote an electron inside the QD (resonant excitation). Regardless of the population method employed, after a time that is characteristic for each complex, spontaneous emission occurs, and electron-hole (e-h) recombination produces a photon. Because of the presence of strong confinement and Coulomb interaction between excited electrons and holes inside the QD, *e-h* pairs bind forming excitonic complexes. Considering that, according to Pauli exclusion principles there can be two electrons with opposite spin for each energy level (same applies to holes), several kinds of excitonic complexes can be formed: a single e-h pair gives rise to a neutral exciton (X), two e-h couples form a biexciton complex (XX), an e-h pair and a hole (electron) make up a positively (negatively) charged trion X^+(X^-).

Furthermore, these complexes differentiate with respect to the kind of hole involved, since, for each case listed above, excitons can be formed from heavy holes or light holes, just as each charged complex can. By shining a pulsed laser with a pulse frequency such that $1/f_{pulse} > \tau_R$, where τ_R is the average recombination lifetime of an excitonic complex, the QD can be turned into an on-demand source of single photons.

The formation of an excitonic complex does not always result in the emission of a photon, since the radiative recombination depends on the spin and angular momentum configuration of the electron and hole. Electrons have a quantum angular moment, known as Spin, of S=1/2, and its projection on the z axis is S_z=±1/2. Likewise, the total angular momentum of a heavy hole is J=3/2 with a z projection J_z=±3/2. In case of the neutral exciton, the exchange interaction that couples the electron spin and the hole angular momentum gives rise to 4 energetically degenerate excitonic states with four different values of total angular momentum along the quantization axis[17]:

$$M = S_z + J_z = 1, -1, 2, -2.$$

Due to spin selection rules, complexes with M=±2 cannot recombine to the M=0 ground state losing a unit of angular moment to the vacuum photon state. A more complex picture involving mixing of heavy and light hole states would show that M=±2 excitons (often referred to as ***dark states***) can eventually emit as well[18]. On the other hand, M=±1 states, can recombine radiatively and are for this reason called ***bright states***, and are part of the mechanisms that allows entangled photons emission.

Quantum entanglement is a fundamental phenomenon of quantum mechanics according to which, when two or more particles are entangled, they become correlated such that none of the particles can be described independently of the state of any other particle involved. Mathematically, an entangled state is a non-separable superposition state that for a two-particle state can be expressed for example as:

$$|\psi\rangle = \frac{1}{\sqrt{2}}(|0\rangle_A|1\rangle_B + |1\rangle_A|0\rangle_B) \qquad (1.4)$$

where |0⟩ and |1⟩ are the state basis and A and B are the two particles. Measuring the state of one particle determines instantaneously the state of the other, regardless of the distance between the particles.

Generation of entangled photons exploiting QDs transitions was first proposed by Benson et al.[19] and can occur as a result of a recombination cascade where a first photon is emitted when the dot transitions from the biexcitonic state (XX ,M=0) to the excitonic one (X, M=+1,-1); the emitted photon acquires a left(right)-handed circular polarization upon a momentum change of +1(-1). When the dot relaxes to the M=0 ground state, the total angular momentum preservation entails an opposite momentum change with respect to the previous transition, causing the emission of a right(left)-handed circularly polarized photon (see Figure 1.3-3). By preserving the spin entanglement of the electron-hole pairs from which they are generated, the two emitted photons are polarization-entangled, and their state can be written as:

$$|\psi\rangle = \frac{1}{\sqrt{2}}(|R\rangle_{XX}|L\rangle_X + |L\rangle_{XX}|R\rangle_X) \tag{1.5}$$

or in horizontal (H) and vertical (V) polarization basis as:

$$|\psi\rangle = \frac{1}{\sqrt{2}}(|H\rangle_{XX}|H\rangle_X + |V\rangle_{XX}|V\rangle_X). \tag{1.6}$$

The states above are called maximally entangled states, or Bell states.

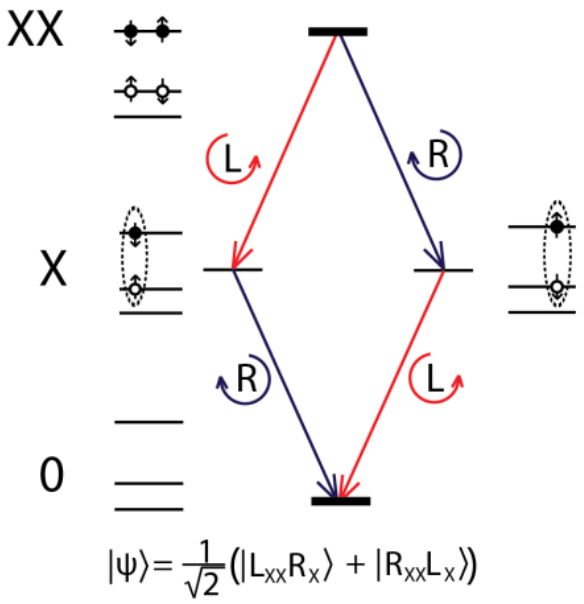

Figure 1.3-3: biexciton-exciton recombination cascade. Image taken from "Pyramidal quantum dots: single and entangled photon sources and correlation studies", UCC PhD thesis, Juska G.

However, the Coulomb interaction and, more significantly, the exchange interaction between electron-hole pairs break the confining potential symmetry of the crystal, mixing the states. This results in an energy splitting of the two bright excitonic states, known as the Fine Structure Splitting (FSS), which reduces the fidelity of the emitted photons to the ideal Bell state, thereby compromising the quality of entanglement. Indeed, upon the first recombination, the state XX state transitions to

$$|\psi\rangle = \frac{1}{\sqrt{2}}\left(|H\rangle_{XX}|X\rangle_H + e^{-i\frac{FSS}{\hbar}t}|V\rangle_{XX}|X\rangle_V\right), \tag{1.7}$$

where the photon polarization is entangled with the exciton, and an additional relative phase term between the exciton states starts to build up overt time. Emission of the second photon happens after a recombination time τ_R and the state becomes

$$|\psi\rangle = \frac{1}{\sqrt{2}}\left(|H\rangle_{XX}|H\rangle_X + e^{-i\frac{FSS}{\hbar}\tau_R}|V\rangle_{XX}|V\rangle_X\right). \tag{1.8}$$

The FSS is detrimental to entanglement because the extra phase term introduced during the intermediate recombination step disrupts the fixed complex phase relationship between the two photons. As a result, when measured in bases different from the eigenstates (D/A and R/L), the polarization is projected onto those bases with probabilities altered by the FSS-induced phase shift.

Entanglement between two states can be measured in different ways.

Concurrence C is a direct measurement of entanglement for a two-qubit system and is calculated from its density matrix ρ:

$$C = \max\left(0, \sqrt{\lambda_1} - \sqrt{\lambda_2} - \sqrt{\lambda_3} - \sqrt{\lambda_4}\right) \tag{1.9}$$

where λ_i are the eigenvalues of the operator $R = \rho\left(\sigma_y \otimes \sigma_y\right)\rho^*\left(\sigma_y \otimes \sigma_y\right)$. C=0 implies a separable state, whereas 0 < C ≤ 1indicates and entangled state (C=1 being the maximally entangled state).

Fidelity, on the other hand, doesn't measure directly the level of entanglement but determines the similarity of a prepared state to an ideal one (Bell state). It can be defined as

$$F = \left(Tr\left(\sqrt{\sqrt{\rho}\sigma\sqrt{\rho}}\right)\right)^2 \tag{1.10}$$

for mixed states, where ρ and σ are the density matrices of the prepared state and the reference one respectively. When F = 1 the state coincides with the ideal maximally entangled state, whereas with F<1, it is degraded with respect to the reference state. The entangled nature of light is revealed when F > 0.5, that is the fidelity value of a separable state.

The ***Peres Criterion*** is a necessary and sufficient test for determining whether a two-particle state is entangled or separable. It is based on the partial transposed ρ^{T_A} of the density matrix, where only components of one subsystem (A) are transposed. If the matrix is a positive semidefinite matrix (all its eigenvalues are ≥0), the state is separable.

When some or all the eigenstates are negative, ρ^{T_A} is not a positive semidefinite matrix and the state is not separable.

A biexciton-exciton cascade-generated entangled state will inevitably bear the imprint of the FFS in its density matrix:

$$\rho = |\psi\rangle\langle\psi| = \begin{pmatrix} 1 & 0 & 0 & e^{-i\Delta\phi} \\ 0 & 0 & 0 & 0 \\ 0 & 0 & 0 & 0 \\ e^{i\Delta\phi} & 0 & 0 & 1 \end{pmatrix}. \quad (1.11)$$

For such a state, as in (1.8), with an FSS-induced phase shift $\Delta\phi = \mathrm{FSS} * \tau_R$, Concurrence, Fidelity and eigenvalues for Peres Criterion would be affected by $\Delta\phi$ in the following way:

$$Concurrence: C = |\cos\Delta\phi|; \quad (1.12)$$

$$Fidelity: F = \frac{1}{2}(1 + \cos\Delta\phi); \quad (1.13)$$

$$Peres\ Criterion: \det(\rho^{T_A} - \lambda I) = 0 \rightarrow \quad (1.14)$$

$$\lambda_1 = \frac{1}{2}(1 + \cos\Delta\phi), \lambda_2 = \frac{1}{2}(1 - \cos\Delta\phi), \lambda_3 = 0, \lambda_4 = 0; \quad (1.15)$$

Lastly, a non-separable state will violate ***Bell's inequalities***, which distinguish between systems that obey local realistic theories (where results are predetermined by hidden variables) and those that follow quantum mechanics (which allows for non-local correlations). Violation of Bell inequalities indicates quantum entanglement, while obeying these inequalities suggests the system can be explained by classical, local theories. The first experiment that tested Bell's inequalities was performed in 1972 by Freedman and Clauser[20], where the polarization correlations of couples of photons emitted in cascade by a calcium atom were measured. In 1981[21], Alain Aspect, using more efficient equipment and closing the locality loophole introducing rapid-changing polarizers while photons where on flight, repeated a similar experiments violating Bell's

inequalities. This experiment provided tangible, experimentally measurable evidence to settle the debate between local realism and non-local quantum theory. About ten years later, Ekert[22] proposed using Bell's inequalities to test whether the exchange of entangled photon pairs between two parties is being intercepted by an eavesdropper. If external interference tampers with the communication channel, the violation of Bell's inequality diminishes or disappears, indicating that the entangled pairs have been disturbed.

Thanks to these pivotal advancements (and many others that followed), non-locality evolved from being conceived as unreasonable and controversial (1930s) to being experimentally measurable (1972 on) and ultimately recognized as an enabling principle for quantum technologies (1991 on)[23].

1.4 Requirements of ideal QDs

The following is a set of requirements, aligned with Di Vincenzo's criteria, that specifically focuses on QDs as sources of photon qubit states, outlining the key features these quantum emitters must have to function as ideal sources.

- **Emitted-Photons Indistinguishability**: For photons to exhibit indistinguishability, they must have the same energy and fully overlapping wavepackets. This requires identical spatial power distributions (e.g., plane wave, Gaussian beam) and identical temporal profiles (e.g., Gaussian, Lorentzian, rectangular), which represent the probability distribution of the photon's presence in time. Bosonic coalescence (Hong-Ou-Mandel effect) occurs only between fully indistinguishable photons. Any differences between the photons will degrade the bunching effect observed in two-photon correlation experiments (HOM).
- **Single- and entangled-photon emission**: Quantum operations are carried out at the single-qubit level. The emission of single photons ensures that each qubit

is treated independently, minimizing errors from mixed photon states or interference from multiple photons. On the other hand, the ability to generate entangled states is crucial for implementing quantum algorithms and protocols, such from the basic quantum teleportation to more complex algorithms such as Shor's algorithm, Grover's algorithm, and the BB84 protocol for quantum key distribution. Entanglement is the mechanism that enables conditional operations in quantum technologies. A classic example is the C-NOT gate, which flips the target qubit if and only if the control qubit is in the state $|1\rangle$.

- **Scalability**: QDs must be fabricated using techniques capable of producing them in large quantities while maintaining spectral homogeneity. As any small variation (size, symmetry, composition, defects) deteriorates uniformity, this task is one of the most challenging.
- **Integrability**: The fabrication of QDs must align with the production flow of PICs to enable on-chip quantum operations. This requires achieving platform compatibility, replacing traditional bulk optics and electronics with fully integrated solutions, and some of the necessary criteria are: **i)** ***On-chip on-demand photon generation*** requires optical or electrical pumping, which can be achieved through the integration of a compatibly grown (or transfer-printed, or wafer bonded etc.) laser, or, e.g., by embedding QDs in p-i-n junctions controlled by driving RF electronic circuits. **ii)** ***Wavelength compatibility*** with established waveguiding platforms (e.g., SiN_x waveguides)[24] and on-chip single-photon detection technologies (e.g., SNSPDs or SPADs)[25,26]. **iii)** ***Fine-tuning*** individual QDs using electrical or strain-based[27–29] control mechanisms to achieve spectral alignment for multi-qubit operations. **iv)** ***Precise control over QD positioning*** facilitates integration with other photonic components, as they can be photolithographically aligned to a common set of markers, leveraging standardized microelectronics fabrication processes. Furthermore, this approach enhances device uniformity[30], which is an essential feature for enabling scalable systems.

- **High Brightness**: A fundamental requirement for on-demand photon generation is achieving nearly unitary collection efficiency, defined as the ratio of harvested photons per second to the frequency of the electrical or optical trigger pulses—that is, ensuring that each trigger generates exactly one photon. The extraction efficiency is influenced by multiple factors, including the population and recombination mechanism, which can be degraded by surface state charging, nearby defects, spin flipping, or any other phenomenon that causes blinking[31,32]. Additionally, the high refractive index of the semiconductor matrix embedding the QDs contributes to photon losses as it increases total internal reflection. Extraction efficiency is also strongly dependent on the geometry of the semiconductor matrix, which determines how the emitted photon beam is focused and hence, whether it achieves a narrow angular power distribution suitable for efficient coupling. Exploiting a resonant cavity integrated on-chip (e.g., Circular Bragg Reflectors[33]), can reduce the average exciton lifetime through Purcell enhancement. This reduction effectively minimizes the influence of degrading phenomena that occur on comparable or longer time scales, at the same time improving the FSS-induced decoherence in entangled photons.

  A resonating cavity confines light at specific resonant wavelengths, creating discrete optical modes that strongly influence how a nearby quantum emitter (like a quantum dot) radiates. The key parameters are the quality factor (Q), which measures how long light is stored, and the mode volume (V), which describes spatial confinement; together they determine the Purcell effect, i.e. the enhancement or suppression of spontaneous emission. When the emitter's transition matches the cavity resonance, emission can be directed and amplified, and in the strong coupling regime, light and matter form hybrid states. Different cavity designs—such as Fabry–Pérot resonators, whispering gallery modes, photonic crystals, or micropillars—are used to boost light–matter interaction for applications like single-photon sources, low-threshold lasers, and

quantum networks. A more detailed discussion of resonating cavities is presented in Chapter 6.

More on Quantum Dots

Before Quantum Dots were proposed as a means of producing single photons or entangled photons through the biexciton-exciton cascade, they were employed in lasers as active region due to the potential advantages provided by their delta function-like Density of States[34]. In principle, the discrete availability of energy states improves the lasing mode's linewidth, reduces the threshold current, and enhances temperature stability by requiring carriers to overcome a higher energy gap to reach states at higher energy. The first QD laser[35] was fabricated using a top-down approach, where "quantum boxes" were defined via electron beam lithography (EBL) and wet etching on an MOVPE-grown InGaAs/InGaAsP quantum well, subsequently capped with an overgrowth layer. At T=77K, threshold current was s 7.6kA/cm^2, a value kept relatively high by the large density of surface defect states introduced during the etching process to provide 3D confinement. In the same year (1994), N. Kirstaedter et al[36] demonstrated lower threshold current lasing (120 A/cm^2, 77K to 140K temperature range) using MBE-grown InGaAs SK QDs embedded in GaAs barriers, showcasing the potential of self-assembled QDs for achieving superior performance in optoelectronic devices. This work marked a significant shift toward bottom-up approaches in QD laser development, emphasizing the advantages of defect-free, epitaxially grown structures for practical applications.

The success story of QDs is unquestionably linked to Stransky-Krastanov dots[37], being central to numerous breakthroughs in quantum optics: they were the first QDs to demonstrate entanglement[38,39] and showing tuneability of the fine structure splitting (FSS)[39–41]. SK QDs form during MBE heteroepitaxial growths, thanks to the lattice mismatch between the substrate (e.g. GaAs) and the growing layer (e.g. InAs, InGaAs, etc): monolayers of the material depositing on the substrate wet the surface, proceeding conformally layer by layer, until the thickness of the wetting layer exceeds the critical thickness for lattice-matching conditions. The excess energy stored is then minimized

through lateral relaxation[37], leading to formation of 3D islands (Figure 1.4-1). SK dots however present several limitations: the presence of the 2D epilayer from which the dot originates weakens carrier confinement, the residual strain causes anisotropic piezoelectric field potentials and increases the intermixing during growth of active and capping layers, and more[42].

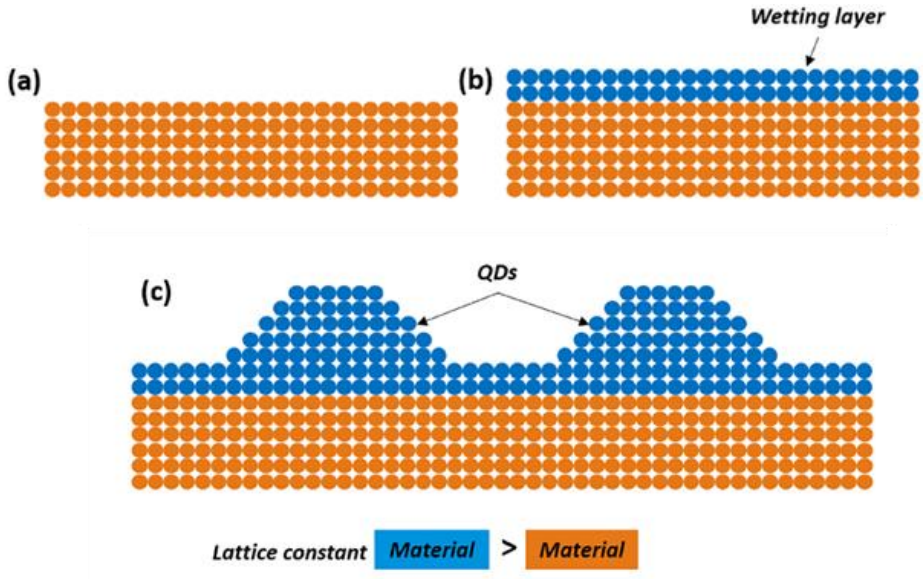

Figure 1.4-1: Stransky-Kranstanov QDs growth mode: a) buffer/substrate; b) few strained monolayers of wetting layer form on the substrate; c) strain is released and islanding takes place. Image taken from "Atomic-Scale Characterization of Droplet Epitaxy Quantum Dots. Nanomaterials", R.S.R Gajjela.

A more flexible approach in nanostructure design, that implies the possibility to produce QDs from lattice-matched materials, has emerged to be the Droplet Epitaxy (DE) method. DE QDs (typically GaAs in AlGaAs barriers) are formed via a fundamentally different mechanism: instead of relying on strain-induced self-assembly, they are fabricated by depositing droplets of group-III materials (Ga) on a metal-stabilized surface (AlGaAs). The droplets form, in a way, following the Volmer-Weber growth mode, nucleating into islands without the necessity of a wetting layer (Figure 1.4-2). Substrate temperature and metal areal density (amount of metal per unit surface) control droplets density and size[43,44]. Exposure to a group-V element flux (e.g., arsenic) crystallizes the

droplets in a non-trivial manner, influenced by factors such as substrate orientation, flux partial pressure, and temperature. On (100)-oriented substrates, this process can yield disks, domes[45], or even nano-rings[46] when Ga out diffusion dominates crystallization. In contrast, on (111)A-oriented substrates, the QDs tend to form truncated pyramids with triangular or hexagonal bases[47].

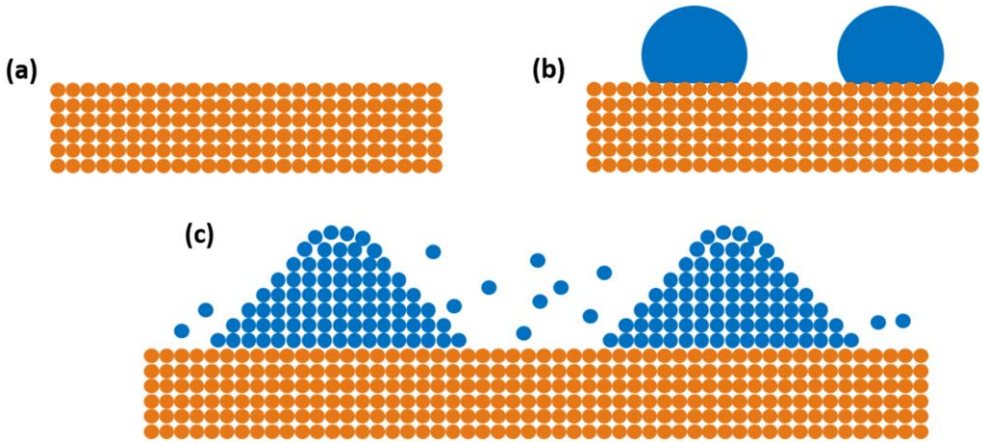

Figure 1.4-2: Formation process DE QDs: a) buffer/substrate; b) (group III) metallic droplet deposition; c) droplet crystallization in rich group V environment. Image taken from "Atomic-Scale Characterization of Droplet Epitaxy Quantum Dots. Nanomaterials", R.S.R Gajjela.

Despite the excellent results achieved by DE QDs[45], they still suffer from drawbacks like poor optical quality, probably stemming from the low crystallization temperature required on (100) substrates, as well as spectral diffusion and line broadening caused by the presence of defects in the QD environment[48]. These limitations have been addressed with the introduction of Local Droplet Etching (LDE) QDs.

The growth process of LDE QDs begins similarly to that of DE QDs, with the deposition of metal droplets on the substrate. However, in this case, the droplets serve the purpose of defining the geometric template for QD growth. Annealing at high temperatures (580°C) under a low group-V flux causes etching of the semiconductor beneath the droplet (typically AlGaAs), resulting in the formation of a circular nanohole surrounded by a crystallized ridge. Prolonged etching completes the nanohole formation and removes any trace of the original metal droplet (Figure 1.4-3). Since this etching occurs

under controlled growth conditions, the resulting template is free of defects and impurities[42]. Subsequent steps consist in filling the patterned nanohole to form the QD and capping it with a protective layer.

LDE QDs have achieved remarkable milestones, including ultra-small FSS[49] and nearly unitary fidelity and concurrence values for entangled photon emission[29].

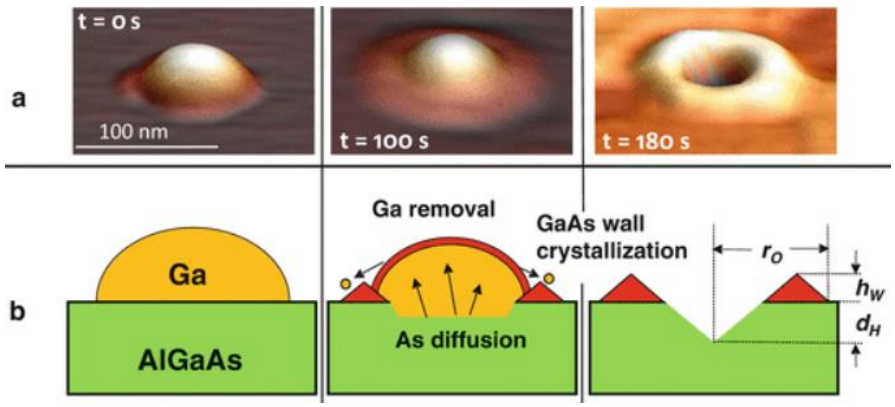

Figure 1.4-3: LDE process: a) Ga droplet formation on AlGaAs buffer followed by As out diffusion under annealing conditions. The etched nanohole template is characterized by crystallized walls; b) sketches of the tree steps listes. Image taken from "Local Droplet Etching: Self-assembled Nanoholes for Quantum Dots and Nanopillars", Heyn, C et al.

Given the brilliant results strain-driven and droplet-based QDs have accomplished, one might think that this extended family of QDs has settled the debate on which is the quantum dot technology that meets the requirements an ideal quantum source should have. Indeed, self-assembled QDs offer significant advantages not only due to their intrinsic optical properties but also because their inherently planar growth simplifies the integration of tuning and enhancement strategies, such as embedding QDs in resonant cavities or p-i-n junctions[50].

However, for technology to transition from prototype to widespread adoption, it must scale efficiently to mass production. Standardization relies on establishing processes that guarantee consistent and repeatable results across large-scale manufacturing. In

the context of quantum dot technology, this means not only ensuring uniformity in optical and electronic properties but also achieving precise spatial control over QD positioning. The random nucleation of self-assembled QDs poses a significant challenge to meet these requirements. This is where site-controlled technologies step in.

By defining nucleation sites through lithography, site-controlled systems enable on-wafer high-density of quantum sources while ensuring control over QD position. Over the years, extensive efforts have focused on eliminating random nucleation entirely. For instance, Große et al.[51] demonstrated the use of oxide apertures atop mesas embedding buried stressors, arranged in a 28×28 square array, to define nucleation sites for MOVPE-grown InGaAs QDs. More common and long-standing strategies for site-controlled QDs consist in inverted pyramids on (111) GaAs substrates[52], EBL-defined nanohole arrays[53], gold-catalysed VLS nanowires[54], and AFM-induced surface oxidation[55]. These approaches collectively address the challenges of scalability and reproducibility.

Subject of this study are QDs grown in inverted tetrahedral recesses on (111)B Gallium Arsenide substrates. PQDs have been extensively studied at EPFL, where single-photon emission was first demonstrated in this QD family[56]. Subsequently, our group accomplished high-density QDs emitting polarization-entangled photons without requiring external manipulation of excitonic states[30]. Similar outcomes were achieved some years later when we first implemented electrically pumped PQDs[57].

These results underline the spectral homogeneity provided by this site-controlled system, a feature often absent in self-assembled QDs. Moreover, PQDs are believed to preserve C3v symmetry[58], which, according to group theory, predicts the absence FSS, although it remains experimentally detectable.

Nevertheless, during experiments, we often find ourselves in need of brighter sources and straightforward tuning knobs—traits that PQDs inherently lack. Their intrinsic three-dimensional tetrahedral geometry limits processing, making it more difficult to implement strategies for efficient light extraction or to couple them reliably to photonic

structures such as cavities and waveguides. The non-planar shape also limits the applicability of post-growth tuning techniques, such as strain or electric-field modulation, which are more easily applied to planar QDs. In addition, geometry hinders heterogeneous integration, as the peculiar selective growth impedes design of transfer printable QDs coupons, further restricting their incorporation into complex photonic circuits. As a result, despite the advantages of site control and uniformity, PQDs currently require additional engineering to meet the brightness, tunability, and scalability demands of practical quantum photonic applications.

From this point onward, this manuscript will discuss the challenges encountered and the strategies employed to functionalize this family of QDs.

In chapter 2, PQDs growth is analyzed and discussed through a series of cross-sectional AFM measurements, pointing out the complexity of thickness calibration. The chapter presents the main standard processing techniques and configuration (polished, back-etched and micro/nano-pillars), alongside a novel approach, the mirrored pyramids, I introduced to simplify the application of Au contacts in view of applying an electric field. The effects of the processing are analyzed with systematic photoluminescence measurements.

In chapter 3, single-photon and entangled-photon emission under two-photon excitation (TPE), and an additional fabrication method that enhances light extraction efficiency by up to 12%, are demonstrated employing InGaAs QDs embedded in micropillars.

In chapter 4, a thorough simulation study performed using Lumerical, identifies the geometric parameters for which best transmission performances are obtained from the back-etched and pillars configurations, and validates the mirrored pyramids approach indicating a comparable, and in some cases higher-than-BE, transmission efficiency. Moreover, simulations show for the first time the possibility of transforming the pyramid

into a resonating cavity with Gaussian-like farfield power projections and Purcell factor ≈8 through the simple introduction of gold mirror at the bottom.

The influence of an external electric field on PQDs, applied by means of a standard tip-up/back etched configuration and of the new mirrored pyramids configuration, is investigated in chapter 5. The non-homogeneous three-dimensional confinement that characterizes PQDs hinders effective stark tuning, opening the question of how to increase confinement on a level higher than the one explored.

Finally, chapter 6 reports on the attempt to realize the Pyramidal Resonating Cavity. While the fabrication process appears straightforward, it is offset by several challenges, primarily the lack of control over the QD position along the vertical axis, followed by the detrimental effects of back-etching

References

(1) House, M. E. *The Physics of Computation Conference*. MIT Endicott House. https://mitendicotthouse.org/physics-computation-conference/ (accessed 2024-12-23).

(2) Manin, Y. I. Classical Computing, Quantum Computing, and Shor's Factoring Algorithm. arXiv March 2, 1999. https://doi.org/10.48550/arXiv.quant-ph/9903008.

(3) Benioff, P. The Computer as a Physical System: A Microscopic Quantum Mechanical Hamiltonian Model of Computers as Represented by Turing Machines. *J. Stat. Phys.* **1980**, *22* (5), 563–591. https://doi.org/10.1007/BF01011339.

(4) 40 Years of Quantum Computing. *Nat. Rev. Phys.* **2022**, *4* (1), 1–1. https://doi.org/10.1038/s42254-021-00410-6.

(5) Feynman, R. P. Simulating Physics with Computers. *Int. J. Theor. Phys.* **1982**, *21* (6), 467–488. https://doi.org/10.1007/BF02650179.

(6) Shor, P. W. Polynomial-Time Algorithms for Prime Factorization and Discrete Logarithms on a Quantum Computer. *SIAM J. Comput.* **1997**, *26* (5), 1484–1509. https://doi.org/10.1137/S0097539795293172.

(7) MacQuarrie, E. R.; Simon, C.; Simmons, S.; Maine, E. The Emerging Commercial Landscape of Quantum Computing. *Nat. Rev. Phys.* **2020**, *2* (11), 596–598. https://doi.org/10.1038/s42254-020-00247-5.

(8) DiVincenzo, D. P. The Physical Implementation of Quantum Computation. *Fortschritte Phys.* **2000**, *48* (9–11), 771–783. https://doi.org/10.1002/1521-3978(200009)48:9/11<771::AID-PROP771>3.0.CO;2-E.

(9) *What is Quantum Annealing? — D-Wave System Documentation documentation*. https://docs.dwavesys.com/docs/latest/c_gs_2.html#getting-started-qa (accessed 2024-12-23).

(10) *Quantum information processing with superconducting circuits: a review - IOPscience*. https://iopscience.iop.org/article/10.1088/1361-6633/aa7e1a (accessed 2024-12-23).
(11) Huang, H.-L.; Wu, D.; Fan, D.; Zhu, X. Superconducting Quantum Computing: A Review. *Sci. China Inf. Sci.* **2020**, *63* (8), 180501. https://doi.org/10.1007/s11432-020-2881-9.
(12) Pezzagna, S.; Meijer, J. Quantum Computer Based on Color Centers in Diamond. *Appl. Phys. Rev.* **2021**, *8* (1), 011308. https://doi.org/10.1063/5.0007444.
(13) Barnes, K.; Battaglino, P.; Bloom, B. J.; Cassella, K.; Coxe, R.; Crisosto, N.; King, J. P.; Kondov, S. S.; Kotru, K.; Larsen, S. C.; Lauigan, J.; Lester, B. J.; McDonald, M.; Megidish, E.; Narayanaswami, S.; Nishiguchi, C.; Notermans, R.; Peng, L. S.; Ryou, A.; Wu, T.-Y.; Yarwood, M. Assembly and Coherent Control of a Register of Nuclear Spin Qubits. *Nat. Commun.* **2022**, *13* (1), 2779. https://doi.org/10.1038/s41467-022-29977-z.
(14) Chatterjee, A.; Stevenson, P.; De Franceschi, S.; Morello, A.; De Leon, N. P.; Kuemmeth, F. Semiconductor Qubits in Practice. *Nat. Rev. Phys.* **2021**, *3* (3), 157–177. https://doi.org/10.1038/s42254-021-00283-9.
(15) Pelucchi, E.; Fagas, G.; Aharonovich, I.; Englund, D.; Figueroa, E.; Gong, Q.; Hannes, H.; Liu, J.; Lu, C.-Y.; Matsuda, N.; Pan, J.-W.; Schreck, F.; Sciarrino, F.; Silberhorn, C.; Wang, J.; Jöns, K. D. The Potential and Global Outlook of Integrated Photonics for Quantum Technologies. *Nat. Rev. Phys.* **2021**, *4* (3), 194–208. https://doi.org/10.1038/s42254-021-00398-z.
(16) Slussarenko, S.; Pryde, G. J. Photonic Quantum Information Processing: A Concise Review. *Appl. Phys. Rev.* **2019**, *6* (4), 041303. https://doi.org/10.1063/1.5115814.
(17) Bayer, M. Fine Structure of Neutral and Charged Excitons in Self-Assembled In(Ga)As/(Al)GaAs Quantum Dots. *Phys. Rev. B* **2002**, *65* (19). https://doi.org/10.1103/PhysRevB.65.195315.
(18) Sallen, G.; Urbaszek, B.; Glazov, M. M.; Ivchenko, E. L.; Kuroda, T.; Mano, T.; Kunz, S.; Abbarchi, M.; Sakoda, K.; Lagarde, D.; Balocchi, A.; Marie, X.; Amand, T. Dark-Bright Mixing of Interband Transitions in Symmetric Semiconductor Quantum Dots. *Phys. Rev. Lett.* **2011**, *107* (16), 166604. https://doi.org/10.1103/PhysRevLett.107.166604.
(19) Benson, O.; Santori, C.; Pelton, M.; Yamamoto, Y. Regulated and Entangled Photons from a Single Quantum Dot. *Phys. Rev. Lett.* **2000**, *84* (11), 2513–2516. https://doi.org/10.1103/PhysRevLett.84.2513.
(20) Freedman, S. J.; Clauser, J. F. Experimental Test of Local Hidden-Variable Theories. *Phys. Rev. Lett.* **1972**, *28* (14), 938–941. https://doi.org/10.1103/PhysRevLett.28.938.
(21) Bell, J. S. On the Einstein Podolsky Rosen Paradox. *Phys. Phys. Fiz.* **1964**, *1* (3), 195–200. https://doi.org/10.1103/PhysicsPhysiqueFizika.1.195.
(22) Ekert, A. K. Quantum Cryptography Based on Bell's Theorem. *Phys. Rev. Lett.* **1991**, *67* (6), 661–663. https://doi.org/10.1103/PhysRevLett.67.661.
(23) Georgescu, I. How the Bell Tests Changed Quantum Physics. *Nat. Rev. Phys.* **2021**, *3* (10), 674–676. https://doi.org/10.1038/s42254-021-00365-8.
(24) Mnaymneh, K.; Dalacu, D.; McKee, J.; Lapointe, J.; Haffouz, S.; Weber, J. F.; Northeast, D. B.; Poole, P. J.; Aers, G. C.; Williams, R. L. On-Chip Integration of Single Photon Sources via Evanescent Coupling of Tapered Nanowires to SiN Waveguides. *Adv. Quantum Technol.* **2020**, *3* (2), 1900021. https://doi.org/10.1002/qute.201900021.
(25) Charaev, I.; Bandurin, D. A.; Bollinger, A. T.; Phinney, I. Y.; Drozdov, I.; Colangelo, M.; Butters, B. A.; Taniguchi, T.; Watanabe, K.; He, X.; Medeiros, O.; Božović, I.; Jarillo-Herrero, P.; Berggren, K. K. Single-Photon Detection Using High-Temperature Superconductors. *Nat. Nanotechnol.* **2023**, *18* (4), 343–349. https://doi.org/10.1038/s41565-023-01325-2.
(26) Reithmaier, G.; Lichtmannecker, S.; Reichert, T.; Hasch, P.; Müller, K.; Bichler, M.; Gross, R.; Finley, J. J. On-Chip Time Resolved Detection of Quantum Dot Emission Using Integrated Superconducting Single Photon Detectors. *Sci. Rep.* **2013**, *3* (1), 1901. https://doi.org/10.1038/srep01901.
(27) Plumhof, J. D.; Trotta, R.; Rastelli, A.; Schmidt, O. G. Experimental Methods of Post-Growth Tuning of the Excitonic Fine Structure Splitting in Semiconductor Quantum Dots. *Nanoscale Res. Lett.* **2012**, *7* (1), 336. https://doi.org/10.1186/1556-276X-7-336.
(28) Ou, W.; Wang, X.; Wei, W.; Jin, T.; Zhu, Y.; Wang, T.; Zhang, J.; Ou, X.; Zhang, J. Strain Tuning Self-Assembled Quantum Dots for Energy-Tunable Entangled-Photon Sources Using a

Photolithographically Fabricated Microelectromechanical System. *ACS Photonics* **2022**, *9* (10), 3421–3428. https://doi.org/10.1021/acsphotonics.2c01033.
(29) Huber, D.; Reindl, M.; Covre Da Silva, S. F.; Schimpf, C.; Martín-Sánchez, J.; Huang, H.; Piredda, G.; Edlinger, J.; Rastelli, A.; Trotta, R. Strain-Tunable GaAs Quantum Dot: A Nearly Dephasing-Free Source of Entangled Photon Pairs on Demand. *Phys. Rev. Lett.* **2018**, *121* (3), 033902. https://doi.org/10.1103/PhysRevLett.121.033902.
(30) Juska, G.; Dimastrodonato, V.; Mereni, L. O.; Gocalinska, A.; Pelucchi, E. Towards Quantum-Dot Arrays of Entangled Photon Emitters. *Nat. Photonics* **2013**, *7* (7), 527–531. https://doi.org/10.1038/nphoton.2013.128.
(31) Efros, A. L.; Nesbitt, D. J. Origin and Control of Blinking in Quantum Dots. *Nat. Nanotechnol.* **2016**, *11* (8), 661–671. https://doi.org/10.1038/nnano.2016.140.
(32) Yuan, G.; Gómez, D. E.; Kirkwood, N.; Boldt, K.; Mulvaney, P. Two Mechanisms Determine Quantum Dot Blinking. *ACS Nano* **2018**, *12* (4), 3397–3405. https://doi.org/10.1021/acsnano.7b09052.
(33) Rota, M. B.; Krieger, T. M.; Buchinger, Q.; Beccaceci, M.; Neuwirth, J.; Huet, H.; Horová, N.; Lovicu, G.; Ronco, G.; Covre da Silva, S. F.; Pettinari, G.; Moczała-Dusanowska, M.; Kohlberger, C.; Manna, S.; Stroj, S.; Freund, J.; Yuan, X.; Schneider, C.; Ježek, M.; Höfling, S.; Basso Basset, F.; Huber-Loyola, T.; Rastelli, A.; Trotta, R. A Source of Entangled Photons Based on a Cavity-Enhanced and Strain-Tuned GaAs Quantum Dot. *eLight* **2024**, *4* (1), 13. https://doi.org/10.1186/s43593-024-00072-8.
(34) Arakawa, Y.; Sakaki, H. Multidimensional Quantum Well Laser and Temperature Dependence of Its Threshold Current. *Appl. Phys. Lett.* **1982**, *40* (11), 939–941. https://doi.org/10.1063/1.92959.
(35) Hirayama, H.; Matsunaga, K.; Asada, M.; Suematsu, Y. Lasing Action of $Ga_{0.67}$ $In_{0.33}$ As/GaInAsP/InPtensile-Strained Quantum-Box Laser. *Electron. Lett.* **1994**, *30* (2), 142–143. https://doi.org/10.1049/el:19940082.
(36) Kirstaedter, N.; Ledentsov, N. N.; Grundmann, M.; Bimberg, D.; Ustinov, V. M.; Ruvimov, S. S.; Maximov, M. V.; Kop'ev, P. S.; Alferov, Zh. I.; Richter, U.; Werner, P.; Gösele, U.; Heydenreich, J. Low Threshold, Large T_o Injectionlaser Emissionfrom (InGa)As Quantum Dots. *Electron. Lett.* **1994**, *30* (17), 1416–1417. https://doi.org/10.1049/el:19940939.
(37) Pelucchi, E. On the Multifaceted Journey for the Invention of Epitaxial Quantum Dots. *Prog. Cryst. Growth Charact. Mater.* **2023**, *69* (2–4), 100603. https://doi.org/10.1016/j.pcrysgrow.2023.100603.
(38) Akimov, I. A.; Andrews, J. T.; Henneberger, F. Stimulated Emission from the Biexciton in a Single Self-Assembled II-VI Quantum Dot. *Phys. Rev. Lett.* **2006**, *96* (6), 067401. https://doi.org/10.1103/PhysRevLett.96.067401.
(39) Stevenson, R. M.; Young, R. J.; See, P.; Gevaux, D. G.; Cooper, K.; Atkinson, P.; Farrer, I.; Ritchie, D. A.; Shields, A. J. Magnetic-Field-Induced Reduction of the Exciton Polarization Splitting in InAs Quantum Dots. *Phys. Rev. B* **2006**, *73* (3), 033306. https://doi.org/10.1103/PhysRevB.73.033306.
(40) *Control of fine-structure splitting of individual InAs quantum dots by rapid thermal annealing | Applied Physics Letters | AIP Publishing*. https://pubs.aip.org/aip/apl/article/90/1/011907/332802/Control-of-fine-structure-splitting-of-individual (accessed 2024-12-23).
(41) Bennett, A. J.; Pooley, M. A.; Stevenson, R. M.; Ward, M. B.; Patel, R. B.; de la Giroday, A. B.; Sköld, N.; Farrer, I.; Nicoll, C. A.; Ritchie, D. A.; Shields, A. J. Electric-Field-Induced Coherent Coupling of the Exciton States in a Single Quantum Dot. *Nat. Phys.* **2010**, *6* (12), 947–950. https://doi.org/10.1038/nphys1780.
(42) Gurioli, M.; Wang, Z.; Rastelli, A.; Kuroda, T.; Sanguinetti, S. Droplet Epitaxy of Semiconductor Nanostructures for Quantum Photonic Devices. *Nat. Mater.* **2019**, *18* (8), 799–810. https://doi.org/10.1038/s41563-019-0355-y.
(43) Venables, J. A. Atomic Processes in Crystal Growth. *Surf. Sci.* **1994**, *299–300*, 798–817. https://doi.org/10.1016/0039-6028(94)90698-X.
(44) Heyn, Ch.; Stemmann, A.; Schramm, A.; Welsch, H.; Hansen, W.; Nemcsics, Á. Regimes of GaAs Quantum Dot Self-Assembly by Droplet Epitaxy. *Phys. Rev. B* **2007**, *76* (7), 075317. https://doi.org/10.1103/PhysRevB.76.075317.
(45) Gajjela, R. S. R.; Koenraad, P. M. Atomic-Scale Characterization of Droplet Epitaxy Quantum Dots. *Nanomaterials* **2021**, *11* (1), 85. https://doi.org/10.3390/nano11010085.

(46) Somaschini, C.; Bietti, S.; Koguchi, N.; Sanguinetti, S. Fabrication of Multiple Concentric Nanoring Structures. *Nano Lett.* **2009**, *9* (10), 3419–3424. https://doi.org/10.1021/nl901493f.
(47) Bietti, S.; Basset, F. B.; Tuktamyshev, A.; Bonera, E.; Fedorov, A.; Sanguinetti, S. High–Temperature Droplet Epitaxy of Symmetric GaAs/AlGaAs Quantum Dots. *Sci. Rep.* **2020**, *10* (1), 6532. https://doi.org/10.1038/s41598-020-62248-9.
(48) Abbarchi, M.; Troiani, F.; Mastrandrea, C.; Goldoni, G.; Kuroda, T.; Mano, T.; Sakoda, K.; Koguchi, N.; Sanguinetti, S.; Vinattieri, A.; Gurioli, M. Spectral Diffusion and Line Broadening in Single Self-Assembled GaAs/AlGaAs Quantum Dot Photoluminescence. *Appl. Phys. Lett.* **2008**, *93* (16), 162101. https://doi.org/10.1063/1.3003578.
(49) Huo, Y. H.; Rastelli, A.; Schmidt, O. G. Ultra-Small Excitonic Fine Structure Splitting in Highly Symmetric Quantum Dots on GaAs (001) Substrate. *Appl. Phys. Lett.* **2013**, *102* (15), 152105. https://doi.org/10.1063/1.4802088.
(50) Ollivier, H.; Priya, P.; Harouri, A.; Sagnes, I.; Lemaître, A.; Krebs, O.; Lanco, L.; Lanzillotti-Kimura, N. D.; Esmann, M.; Senellart, P. Three-Dimensional Electrical Control of the Excitonic Fine Structure for a Quantum Dot in a Cavity. *Phys. Rev. Lett.* **2022**, *129* (5), 057401. https://doi.org/10.1103/PhysRevLett.129.057401.
(51) Große, J.; Von Helversen, M.; Koulas-Simos, A.; Hermann, M.; Reitzenstein, S. Development of Site-Controlled Quantum Dot Arrays Acting as Scalable Sources of Indistinguishable Photons. *APL Photonics* **2020**, *5* (9), 096107. https://doi.org/10.1063/5.0013718.
(52) *Structure and optical properties of semiconductor quantum nanostructures self-formed in inverted tetrahedral pyramids - IOPscience*. https://iopscience.iop.org/article/10.1088/0953-8984/11/31/302/meta (accessed 2024-12-23).
(53) Nakamura, Y.; Ikeda, N.; Sugimoto, Y.; Nakamura, H.; Ohkouchi, S.; Asakawa, K. Two-Dimensional Ordering of InGaAs Quantum Dots Formed on an Artificial Nano-Hole Array with 100 Nm Periodicity. *Phys. Status Solidi B* **2003**, *238* (2), 237–240. https://doi.org/10.1002/pssb.200303014.
(54) Zhang, C.; Miao, X.; Mohseni, P. K.; Choi, W.; Li, X. *Site-Controlled VLS Growth of Planar Nanowires: Yield and Mechanism*. ACS Publications. https://doi.org/10.1021/nl502525z.
(55) Kim, J. S.; Kawabe, M.; Koguchi, N. Ordering of High-Quality InAs Quantum Dots on Defect-Free Nanoholes. *Appl. Phys. Lett.* **2006**, *88* (7), 072107. https://doi.org/10.1063/1.2174097.
(56) Kapon, E.; Pelucchi, E.; Watanabe, S.; Malko, A.; Baier, M. H.; Leifer, K.; Dwir, B.; Michelini, F.; Dupertuis, M.-A. Site- and Energy-Controlled Pyramidal Quantum Dot Heterostructures. *Phys. E Low-Dimens. Syst. Nanostructures* **2004**, *25* (2–3), 288–297. https://doi.org/10.1016/j.physe.2004.06.033.
(57) Chung, T. H.; Juska, G.; Moroni, S. T.; Pescaglini, A.; Gocalinska, A.; Pelucchi, E. Selective Carrier Injection into Patterned Arrays of Pyramidal Quantum Dots for Entangled Photon Light-Emitting Diodes. *Nat. Photonics* **2016**, *10* (12), 782–787. https://doi.org/10.1038/nphoton.2016.203.
(58) Dupertuis, M. A.; Karlsson, K. F.; Oberli, D. Y.; Pelucchi, E.; Rudra, A.; Holtz, P. O.; Kapon, E. Symmetries and the Polarized Optical Spectra of Exciton Complexes in Quantum Dots. *Phys. Rev. Lett.* **2011**, *107* (12), 127403. https://doi.org/10.1103/PhysRevLett.107.127403.

Chapter 2

2 Pyramidal Quantum Dots: growth, processing and characterization

2.1 MOVPE Growth mechanism

Metalorganic chemical vapor deposition (or also known as Metalorganic vapor phase epitaxy, MOVPE) sees its birth in the late 60s in the first attempts of depositing semiconductors for optoelectronics on non-lattice-matched substrates by flowing metalorganic precursors and hydrides to supply Group III and Group V elements respectively[1,2]. A decade later[3,4], electron mobility >100 000 cm^2/Vs is measured from a GaAs heteroepitaxial layer grown with purified TMGa and AsH3.

Indeed, purification of precursors turned out to be one of the key elements to grow low density defects layers, as it soon led to the demonstration of low-threshold lasers, and consequently, to commercialization of MOVPE. However, not all materials found their easy access way to MOVPE growth: if GaAs development was relatively easy, it wasn't likewise for Indium Phosphide, which growth was hindered by a polymerization reaction that was occurring between TMIn and PH_3. It took the addition of an adduct (triethylphosphine) to overcome polymerization, together with other precautions adopted to improve TMIn purity and overcome the fact that it is a solid precursor at room temperature, to grow InP and (ternaries/quaternaries) related alloys reliably, and eventually access the 1.5 µm wavelength lasers and detectors. Nowadays, the use of dedicated lines for metalorganics and hydrides circumvents the problem of parasitic reaction in the lines, sparing the addition of adducts. MOVPE proved to be a versatile technique allowing growth of Antimonides and MCTs (Mercury Cadmium Tellurides) and recently saw its widespread diffusion with the introduction on the market of high-brightness InGaN blue LEDs[5].

Metalorganic precursors have the characteristic of being volatile and thermally stable at room temperature. Normally, the metalorganic precursor molar flow brought to the

reactor can be controlled by influencing its vapor pressure by adjusting the temperature of the bubbler that contains it (usually kept lower than ambient temperature to avoid condensation in the lines), and by adjusting the flow of carrier gas (Nitrogen in our case) streamed through the bubbler's line. Precursors are generally mixed before the reaction chamber, where they are directed onto a hot substrate, where a series of diffusion and decomposition mechanisms occur, and new crystal is deposited. In the following image, Figure 2.1-1, the main steps of MOVPE growth are schematically depicted

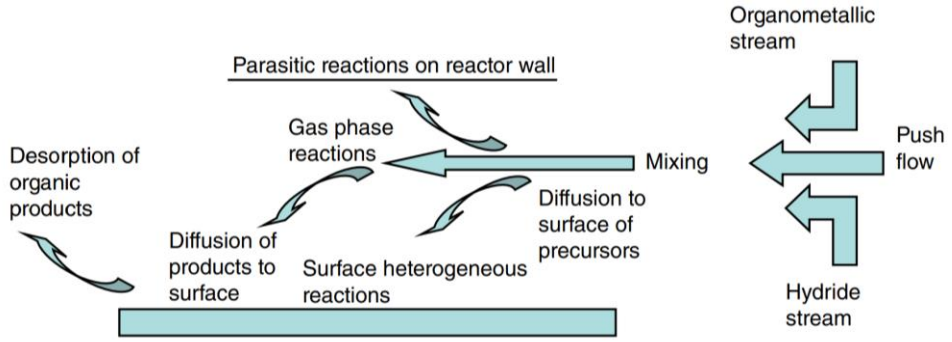

Figure 2.1-1: schematic representation of main gas transport and reaction processes during MOVPE growth. Image is taken from "Introduction to Metalorganic Vapor Phase Epitaxy", Irvine, S.J.C[6].

From a stochiometric point of view, if we take into consideration GaAs MOVPE growth, the chemical reaction that leads to formation of new GaAs can be summarized in the chemical equation $(CH_3)Ga + AsH_3 = GaAs + 3CH_4$. This representation, which suggests that CH_3 radical bond is fulfilled by H atoms supplied by cracked Arsine, is however hiding the complexity of the kinetics taking place inside a reactor[7], where thermal decomposition characteristic is likely to be different between metalorganics and hydrides, and deposition relies on the interplay that radical intermediates of different species have between them and with the substrate. Surface chemistry has been demonstrated to be as fundamental as thermally induced kinetics[8] in MOVPE growth. A schematic example of precursors decomposition is shown in Figure 2.1-2, where homolysis of TMGA (and DMGA successively) releases CH_3 radicals, that induce, together with temperature, cracking of AsH_3 and formation of stable AsH_2 during the gas

phase reaction. These radicals then diffuse to the substrate and surface reactions catalyze final decomposition and atoms adsorption.

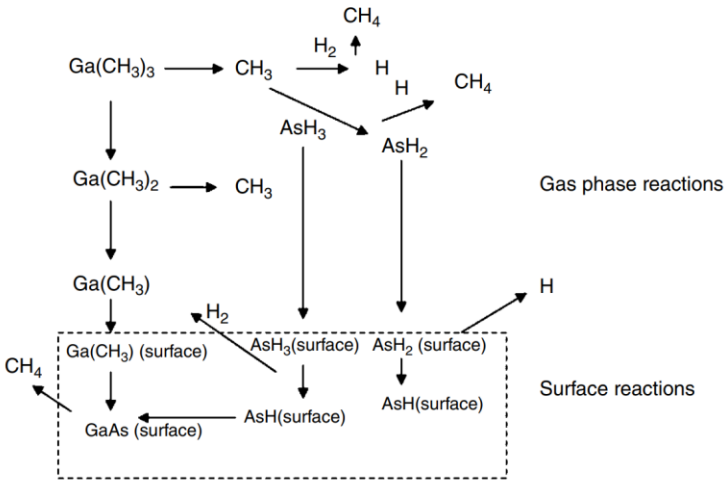

Figure 2.1-2: TMGA and AsH_3 precursor key intermediate decomposition steps during GaAs growth. Image from "Introduction to Metalorganic Vapor Phase Epitaxy", Irvine, S.J.C[6].

Hence, the two processes coexist in the environment, but temperature will determine which will be the dominating one. In general, lower temperatures translate into a more efficient surface adsorption at the expense of a slow vapor reaction rate. This regime is called Kinetic Limited regime. As temperature increases, the increase in growth rate decelerates, surface kinetics is saturated and the mechanism driving growth is the larger supply of precursor to the substrate: higher vapor decomposition right above the surface reflects into a creation of a precursors depletion region, which in turn sets a gradient towards the un-depleted precursors reservoir above. Device growths generally take place in this Transport Limited regime, as growth rate is less sensitive to small T variations. Higher temperatures cause desorption of precursors, etching of radicals and mainly evaporation of the film into the stream of gases, inducing a reduction of growth rate. These three growth regimes are represented in Figure 2.1-3 below. A more detailed outlook on MOVPE crystal growth can be found in "Introduction to Metalorganic Vapor Phase Epitaxy", by Irvine and Capper for example[6].

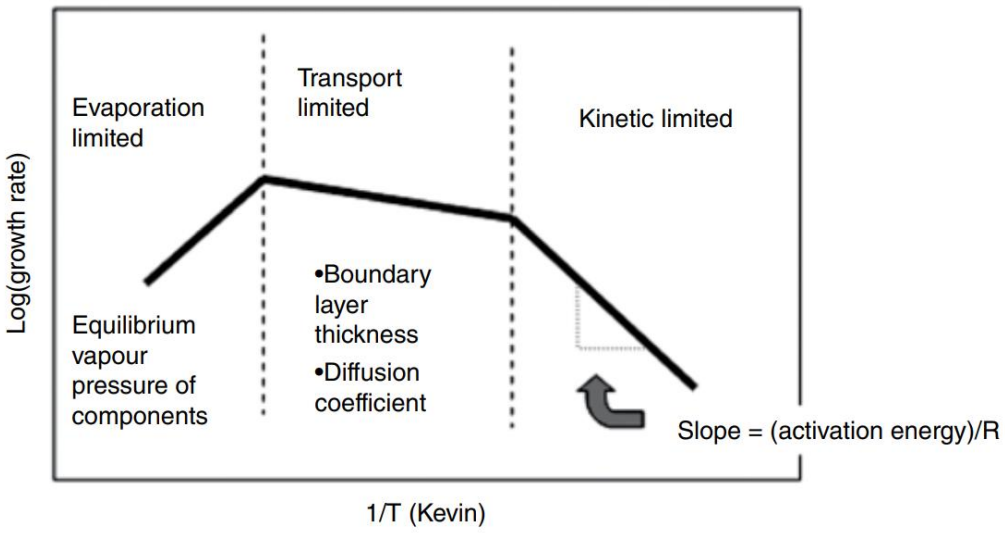

Figure 2.1-3: three different regimes depending on growth temperature. Image from "Introduction to Metalorganic Vapor Phase Epitaxy", Irvine, S.J.C[6].

Compared to Molecular-Beam Epitaxy (MBE), MOVPE has the natural advantage of being compatible with industry production volumes, and, in terms of quality of devices, over the years it has closed the gap with MBE, and in some cases, overcome it: in 2006 Pelucchi et al[9] demonstrate unmatched 15nm GaAs Quantum Well linewidth performing a systematic growth study with different substrate misorientations, and 4 years later FWHM of the same material system is improved to ≈412 μeV[10], very close to the ≈300μeV obtained by MBE. However, the precursors "mediated" growth upon which MOVPE relies, imposes restrictions regarding the orientation of the substrate. If planar growth on GaAs <100> and <111>A (Gallium terminated surface) oriented substrates is well established for T≈700 °C[11–13], mirror-like growth on <111>B (Arsenic terminated surface) seems more difficult to obtain. Dzurko et al.[14] study the growth of AlGaAs/GaAs layers on non-planar {111} GaAs substrates at high temperature (850°C), highlighting a stark difference between the thin growth on flat <111>B and the thick layer grown on slanted <100> surface. They propose that growth is characterized by the presence of a lateral diffusion mechanism established by a reactants concentration gradient due to different growth rate on the two facets, however, the absence of a thickness gradient on the

<111>B towards the <100> slanted surface, suggests that the <111>B layer is growing in a Kinetic limited regime, while the <100> layer is dominated by Transport limited regime. To the contrary, the ballistic growth mechanism of MBE is what accounts for differences on non-planar substrates, where layer thicknesses are proportional to collection areas.

MOVPE non-planar growth was extensively studied with V-grooves patterned on (100) GaAs substrates and exploited for laser fabrication making use of the self-forming single quantum wire active region[15]. This concept was later translated to (111)B GaAs wafers[16], where the patterned template permits three-dimensional confinement of the growing nanostructures.

2.2 Pyramidal Quantum Dots

We refer to our Quantum Dots as Pyramidal QDs because of the unusual template in which the growth takes place. In contrast to self-assembled QDs, where the nucleation of the dot happens randomly on the planar surface of the wafer, pyramidal quantum dots grow inside tetrahedral recesses: we cover the surface of a GaAs (111)B epi-ready wafer (allegedly with perfect orientation) with 50 nm of sputtered SiO_2; successively, an hexagonal pattern of triangles is imprinted via photolithography on a layer of photoresist (S1805) and transferred to the underlying dielectric through a wet etching step using BOE. Once the GaAs surface is exposed, an etch step with Bromine:Methanol - 1:20 solution follows. This solution, as many other GaAs etchants, is selective to crystal planes, and in particular, when put in contact with a (111)B surface, the etch of the material is bound by the (111)A planes, which are the slowest to be etched. Because of this, the result of the Br:Me etch step is a tetrahedral recess defined by the three (111)A planes intercepting the (111)B top surface (see Figure 2.2-1).

Once wafers are patterned, we put the samples inside the MOVPE reactor, where, assisted by the high temperature of the environment, decomposition of precursors occurs mostly on the (111)A planes, causing new crystal to grow only on the sidewalls

of the pyramids and leaving the flat surface on the top mostly unaffected by growth. Three-dimensional carriers' confinement is realized performing a short growth step, during which decomposing precursors crystallize in the low bandgap QD, in between two growth steps, when high band-gap barriers are grown.

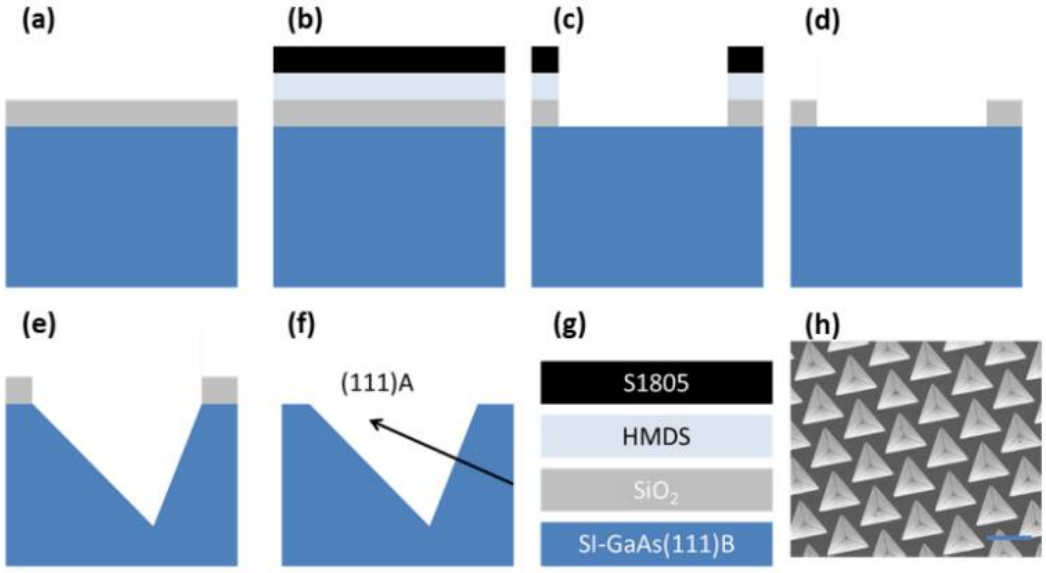

Figure 2.2-1: Patterning process stepflow. a) 50nm thick SiO_2 mask sputtering on GaAs <111>B; b) HMDS surface priming and S1805 resist spinning; c) pattern imprinting via photolithography, resist development and pattern transfer to SiO_2 mask; d) resist stripping; e) Br:Me wet etch step for definition of recesses; f) SiO_2 mask strip; g) color legend; h) SEM top view of patterned substrate. Image taken from "Pyramidal quantum dots: single and entangled photon sources and correlation studies", PhD thesis, Juska G.[17]

The reactor is brought to ≈730^{0}C with a pressure of 20mbar and precursors are streamed inside with a V/III ratio of about 700. In this conditions, (111)A surface growth takes place in a mass transport regime, making growth rate dependent only on the amount of precursors flown. High V/III ratio reduces precursor and adatoms diffusion lengths; in our case, adatoms diffusion lengths are smaller than the dimension of the (111)A bound recess (usually ~9 μm wide). As stated before, in these operating conditions, growth on (111)B top surface is negligible, if not absent, due to minimal precursors decomposition and also (but minorly) to the precursor concentration gradient established between the

flat surface and recess surface. The only (111)B surface that consents growth is the small triangular apex at the bottom of the recesses, which, in absence of the decomposition hurdle present on the top, accommodates the adatoms that diffuse down the sidewalls into the new crystal facet. This peculiar behavior leads to two competing growth mechanisms: the high growth rate on sidewalls works to shrink the already small (111)B bottom facet leading to a reduction of the top layer profile angle with respect to the bottom angle ($\theta_T < \theta_B$), while the threefold adatoms diffusion contribution, stemming from the very same (111)A sidewalls, works in the opposite way causing the small collection area to widen the profile top angle with respect to the bottom one ($\theta_T > \theta_B$). These two mechanisms are referred to in literature as Growth Rate Anisotropy (GRA) and Capillarity/Diffusion effect, respectively. After a transient, the stationary Self-Limiting Profile, where the two mechanisms compensate each other, establishes (Figure 2.2-2).

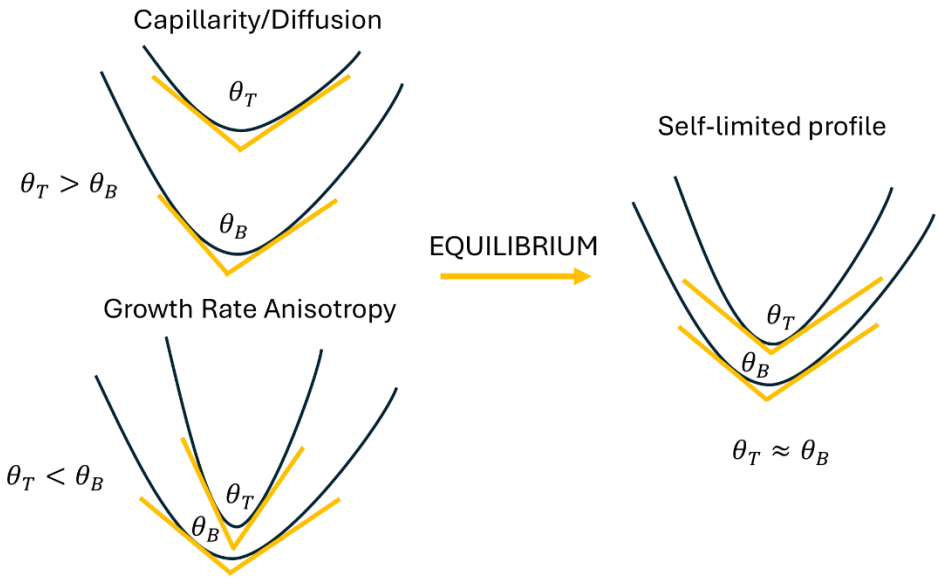

Figure 2.2-2: Diffusion/Capillarity and Growth Rate Anisotropy mechanisms coexist during growth in recesses. After a transient period, equilibrium establishes, and a self-limited profile grows

In case of a binary alloy, like GaAs for example, the growth conditions specified above make sure that at each instant of the growth there is an excess of Arsine, making growth

dependent only on the amount of Trimethyl-Gallium (TMGa) injected: the two species are complementary and Ga adatoms have no competitors. Different is the case of a ternary alloy, with the third species belonging to the III group elements. As an example, in correspondence of Trimethyl-Aluminium (TMAl) introduction, different kinetic diffusion and incorporation barriers, and hence different diffusion lengths of Ga/Al adatoms, slow down growth rate and cause the ternary alloy to be spatially non-uniform in concentration. Aluminium has a smaller mobility than Gallium, meaning it tends to diffuse less on the surfaces and to be incorporated in the crystal structure sooner than Ga, which, unlike Al, travels easily towards the bottom of the recess. The outcome of this segregation effect is a central region right on the vertical axes of the recess with a smaller band gap than the lateral regions, where the Aluminium content is higher. This creates a Vertical Quantum Wire (VQWr) structure, and overall, affects the self-limiting profile, steering it towards steeper sidewalls and smaller apexes, effectively reducing the capillarity-induced profile contribution.

Figure 2.2-3-a is an AFM cross-section scan of 7x150 nm nominally thick $Al_{65}Ga_{35}As$ layers distanced by 6 GaAs spacers with decreasing nominal thickness (from 10 to 5 nm) that shows Ga segregation on the vertical axis of the recess, together with the sidewall's angle change (right half of Figure 2.2-3-a) as the AlGaAs grows thicker. The vertical thickness of AlGaAs layers has been measured from the top of the GaAs spacer below to the bottom of the GaAs spacer above for 9 different recesses, and the average plotted against the cumulative nominal $Al_{65}Ga_{35}As$ thickness. Graph in Figure 2.2-3-c underlines the obvious change in growth rate, but also the astounding difference between nominal and actual thicknesses, as the recess fills up: the average bottom layer is ≈50% of the nominal value, whereas the average top layer reaches 90% of the nominal set value. To the contrary, graph in Figure 2.2-3-d supports the hypothesis of the suppression of the diffusion-induced profile contribution in presence of Al, as it shows that, ***in absence of Aluminium***, GaAs spacers' average vertical thickness, starting from an initial 10nm nominal value that turns into a ≈30nm thick layer, keeps increasing as the recess closes, settling to a measured thickness (53nm) about 10 times the nominal one (5nm). Most

importantly, GaAs re-establishes the self-limiting profile: the GaAs base layer grows with a wider angle than the underlying AlGaAs layers, providing the template for the subsequent AlGaAs deposition, as shown in Figure 2.2-3-a.

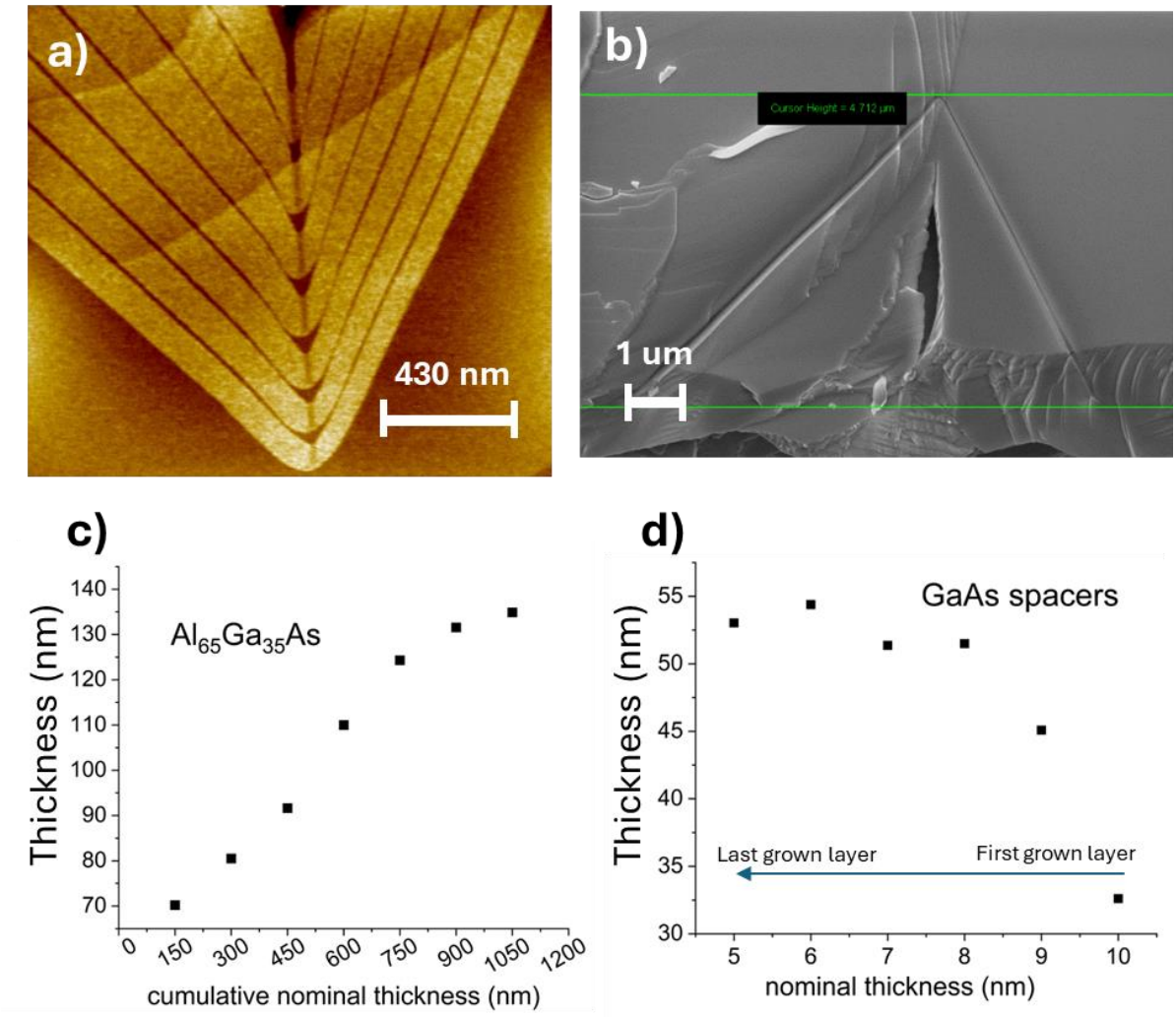

Figure 2.2-3: a) AFM recess cross-section of 7x150nm $Al_{65}Ga_{35}As$ layers spaced by thin GaAs spacers; b) SEM cross-section view of >1 µm thick $Al_{65}Ga_{35}As$: the recess closes leaving behind empty space along the vertical axis of the structure; c) the average thickness of the measured $Al_{65}Ga_{35}As$ single layers increases with the nominal cumulative thickness; d) the average thickness of the measured GaAs single spacers against their nominal thickness values (growth order is from right to left).

Besides the thickness calibration, which poses a challenge with respect to precisely positioning the dot on the vertical axis of the pyramid, the sidewall's angle change is an

obstacle to realization of nearly identical QDs. Directly linked to this issue, the unwelcome effect of high Aluminium concentration is the closure of the recess, that happens after less than 1 μm of effective vertical growth and impedes further conformal deposition when only high Al content AlGaAs is grown. Sidewalls become so steep that growth at the bottom of the recess ceases, while adatoms incorporate at the top closing the pyramidal aperture and leaving behind an empty space on the vertical axis of the recess, as shown in Figure 2.2-3-b. This behavior can be pointed out from Figure 2.2-3-a already, where GaAs (dark brown) grown on the last $Al_{65}Ga_{35}As$ layer (light brown) infills the sharpest and longest apex. To the contrary, GaAs carries out a smoothing action, widening the apexes: the GaAs spacers presence is most probably the only reason why we were able to grow such thick structure.

Infilling the recesses in a controlled and "tetrahedrally" conformal way is a task that needs to be addressed if we want to transform the pyramidal structure into a resonant cavity working on GaAs QDs embedded in a solid volume of AlGaAs alloy: AlGaAs' wider-than-GaAs band gap would ideally not absoprb GaAs QD emission, avoiding quenching the resonance (details on realization of a pyramidal cavity are explained in chapter 4). One solution is to characterize growth at lower Al concentrations and determine the average maximum thickness that can be grown; an alternative, although more radical, would be to implement the cavity with InGaAs QDs confined by GaAs, which growth mode adheres more closely to the self-limiting description given above.

Thickness calibration issue

Thickness calibration, however, is not a task that can be overlooked. Measurement of the $Al_{65}Ga_{35}As$ layers vertical thickness takes place by cleaving the as-grown sample by one of its three principal cleaving directions ([01$\bar{1}$], [10$\bar{1}$], [110]), and by placing the sample upright on the AFM stage with the cleaved edge facing the AFM probe. AlGaAs oxidizes easily when in contact with air, making it possible to detect height variations produced by the Al oxide layer sticking out of the cleaving plane. The honeycomb pattern of triangles that is imprinted during the photolithography step is such that each triangle side is perpendicular to one cleaving direction, and, to make sure that a cleaving plane

always intercepts recesses and doesn't go through the space in between them, the pattern is rotated by 0.1degree. Hence, the cleaving plane cuts through the recess in different points, and to determine the real thickness of the growth at the bottom of the recess, several AFM measurements must be performed to understand whether the plane is cutting through the middle or not. In ref 16, with a series of $Al_{40}Ga_{60}As$/GaAs alternating layers (nominal thickness is not reported), Hartmann et al.[18] show how they can unequivocally distinguish between a cut through the middle of the structure and a cut passing nearby, thanks to the presence of an additional feature that generates during growth, bisecting each (111)A facet: the most plausible explanation behind the appearance of those extra features is that the intersections of two (111)A facets constitutes a V-groove, where, similarly to what happens in the middle of the recess, there is a twofold contribution of adatoms from the sidewalls, that increases the growth rate. The resulting effect of a thicker growth at the three vertices is the gradual transition of each (111)A wall into two vicinal specular facets pivoting onto the median line of the sidewall itself. In correspondence of the median line, a groove-like conformation, easily seen in cross-sectional AFM, takes place, and its distance (labelled as *vc* in Figure 2.2-4-a) from the vertical wire is what discriminates a middle cut from a side cut.

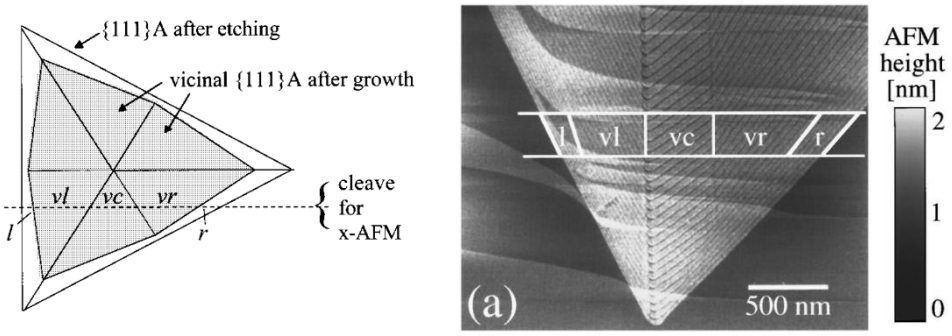

Figure 2.2-4: Left: top-view representation of faceting inside recesses; Right: cross-sectional AFM image of recess where different region is highlighted with labels. Image taken from "Sel-limiting growth of quantum dot heterostructures on non-planar {111}B substrates ", Hartmann et al[19].

While this is a remarkable finding, it must be noticed that the concentration of Aluminium they report is 40%, lower than the one we use. Figure 2.2-5-a shows an SEM

top view of the seven stacked $Al_{65}Ga_{35}As$ layers grown inside 9 μm wide recesses: the evident absence of faceting is a signature of the fact that high Aluminium content tends to suppress the capillarity mechanism coincidently with all groove-like features in the tetrahedral hole. Moreover, the initial recess dimensions might be playing a role[20]: the authors[19] performed those measurements on 1.4 μm wide recesses. To assess the facets evolution isolating the sole role of the recess dimensions, we bring as an example, shown in Figure 2.2-5-b, the top SEM view of stacked InGaAs QD confined by GaAs barriers. Despite the absence of Aluminium, hexagonal reshaping is barely initiated, which supports the hypothesis that a small recess (defined as such by photolithography or shrunk after a long growth), will be more prone to faceting: what is surely changing when in presence of small recesses is the edge size to adatoms diffusion length ratio, that is not >>1 anymore. Independent of what is the leading cause among the two mentioned, the 9 μm-wide recess AFM cross-section above doesn't show any vertical feature but the axial VQWr, demonstrating the inapplicability of the approach just discussed to our case.

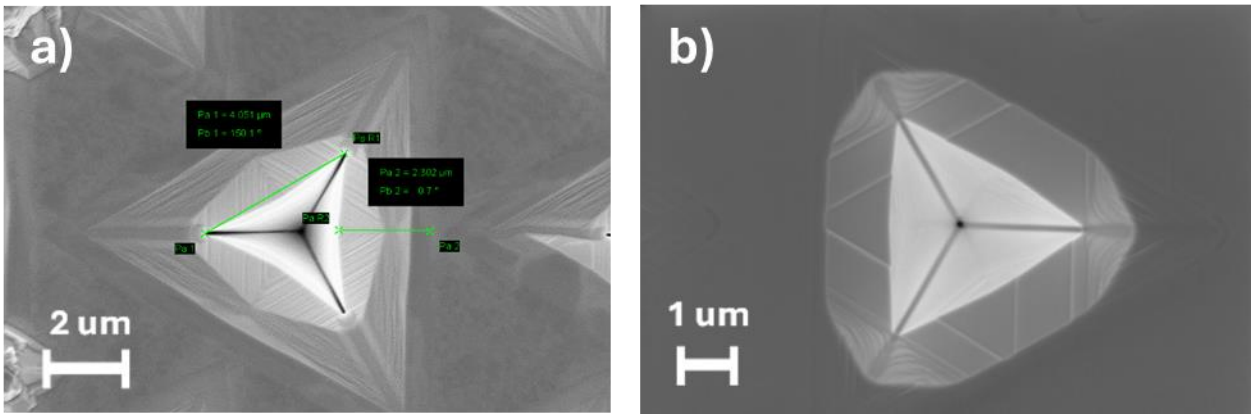

Figure 2.2-5: SEM top view of: a) 7 stacked $Al_{65}Ga_{35}As$ layer 150nm thick: b) InGaAs QD in full GaAs cladding barriers. In both cases, despite the difference in composition, the hexagonal reshaping of the 9 μm wide triangular template is barely visible.

We found it useful to acquire AFM scans every 200 μm, moving along the cleaved edge of the sample, to compare vertical thickness measurements of different cross-sections (labeled as *cs#,* where *#* is the numeric index). In Figure 2.2-6-a every layer

measurement belonging to the same recess is designated with the same symbol and plotted in succession against the cumulative nominal thickness. The crux of the finding is that, as the acquisition moves from a side cut (*cs1,* small top triangle of inset) to a middle cut (*cs9,* big bottom triangle of inset), the thickness of the AlGaAs layers decreases. Cs1 and cs9 values are taken from AFM scans reported in Figure 2.2-3-a and Figure 2.2-6-b respectively. Comparing the two pictures, is apparent that the VQWr in cs9 cuts through the middle of the structure while in cs1 the vertical line is displaced slightly aside, and that the triangular-like GaAs tips are more symmetrical in cs9 with respect to those in cs1. Furthermore, focusing on the left half of both pictures, which, as per Hartmann representation would be the region labelled as *vr*, we can see that the GaAs spacers are thicker in cs9 and thinner in cs1. All these visual considerations, complemented with what just said about the growth mode of GaAs and AlGaAs in the previous section, lead us to to the conclusion that, among the studied pyramids, cs9 is the only recess cut through the middle, while the remaining are cut on the side. In another words, as shown in the sketch Figure 2.2-6-c, cs1 measurements (p1) are a projection of the grown layers' dimensions (d1), perpendicular to the sidewalls of the tetrahedron, on the cs1 cleaving plane. As the cleaving plane moves to the center of the recess, the projection becomes smaller until it coincides with the layers' dimensions (d9≡c9), which we interpret is the case with cs9.

Here I want to stress out how complex and complicated is calibrating thickness growth inside tetrahedral recesses, as: **i)** growth rates and faceting depend on the starting dimension of the recess itself, on its real-time filling level and on the alloy that is being grown; **ii)** identifying pyramids cut through the middle requires a trained eye and systematic acquisitions of several successive cross-sectioned recesses, after which all side cuts are discarded, making it a very inefficient measurement process; **iii)** the measure becomes outrageously time consuming. Nevertheless, as we show in chapter 4, calibration is a crucial aspect because precise control of the QD position inside the recess can unlock high brightness, low angular (emitted-) power spreading and Purcell enhancement.

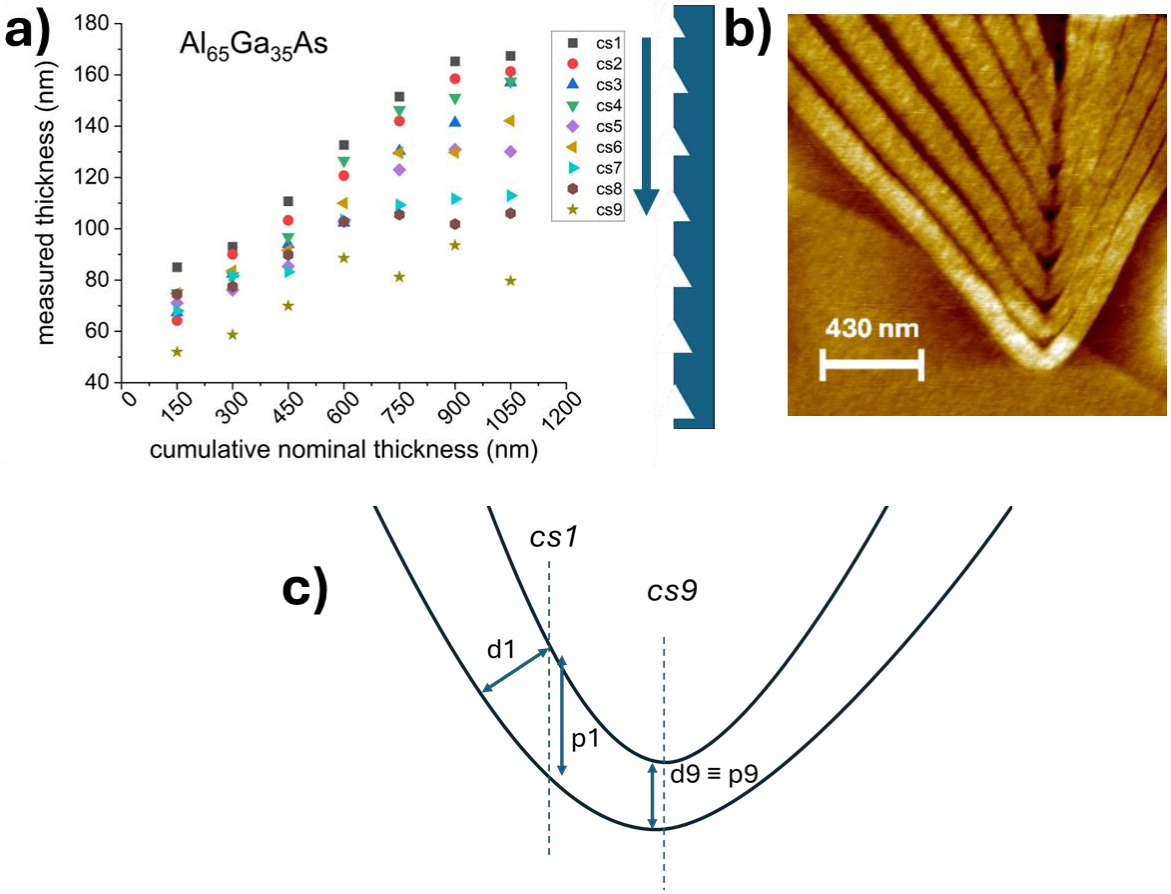

Figure 2.2-6: a) The image shows the layers' measurements for each cross-section scanned (labelled as cs1, cs2, cs3...). Moving along the cleaved edge from a small recess to a wider one, as indicated by the arrow on the right, that points towards the direction in which the half-triangles in the top view (sketch on the right of the arrow) increase in size, thickness values decrease; b) AFM cross-section #9 (cs9) where cleaving plane is closest to the middle of the recess; c) sketch that explains the difference between measurements of various cross-sections, highlighting the importance of the cleaving plane position with respect to the vertical axis.

Nanostructures inside the recess

It should be clear by now that the species in a ternary/quaternary alloy grown in a recess segregate, giving rise to a series of nanostructures. When AlGaAs barriers are grown, together with the VQWr already introduced, three additional low-Al concentration Vertical Quantum Wells (VQWs) grow in coincidence of the three lateral grooves, developing for the whole extent of AlGaAs barrier thickness. In a similar fashion, during the brief InGaAs QDs growths, Indium segregates in the grooves and causes the

formation of three Indium-rich Lateral Quantum Wires (LQWrs). GaAs Lateral Quantum Wells (LQWs) arise on the (111)A sidewalls when a GaAs QD is grown since the thin GaAs layer deposited is sandwiched between higher band gap barriers that provide 2D-carrier confinement. We don't know how these accessory entities affect QDs states, however we acknowledge the fact that the confining potential is far from being homogeneous: when choosing the Al concentration of confining barriers, we expect a lower effective confinement on the vertical axis and at the three vertices; while this accounts for reduced (energy) space in valence and conduction band, it's been exploited in the past as preferential channel to electrically pump QDs[18]. LQWrs in InGaAs QDs and LQWs/VQWrs in GaAs QDs might have evanescent tails overlapping excitonic QD states and so represent a leakage channel that tampers with QDs efficient population.

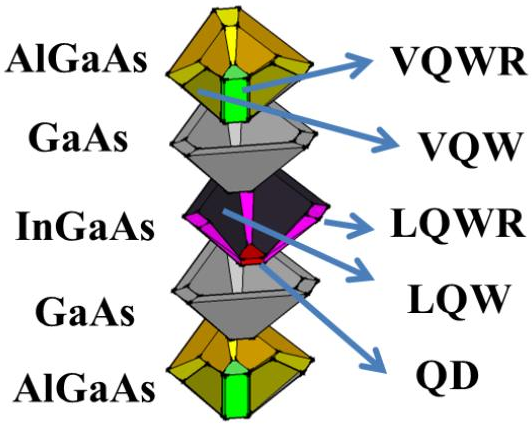

Figure 2.2-7: example of several nanostructures that form during growth in the tetrahedral template.

A mathematical description of growth inside the recesses[21] was developed in our group (with external collaborators), and is based on the following (standard) reaction-diffusion equation

$$D_i \nabla^2 n_i + F_i - \frac{n_i}{\tau_i} = 0 \qquad (2.1)$$

which takes into account the diffusion constants D_i, the effective atomic flux F_i, the effective incorporation time for each species τ_i and the adatom concentration n_i. Here, only kinetics of III precursors are considered because of the As-rich environment, and the stationary self-limited profile is evaluated. The model reproduces the experimental evidence observable through AFM characterization (segregation effect, sidewalls' angle change) and has proved to be a valuable guideline for designing epitaxial structures over the years[22,23].

2.2.1 Processing

As happens with many QD systems, as-grown QDs are most often not ready for use[24]. Instead, they require post-growth processing to acquire essential properties—most notably, enhanced brightness—without which neither basic assessments nor complex protocols can be carried out. If light extraction is poor in planar as-grown self-assembled QDs, where the main hurdle—besides the isotropic emission of the dipole common to all as grown systems—is the high refractive index of the semiconductor matrix, in pyramidal QDs the presence of a vestigial tetrahedral recess introduces an additional scattering element that hampers extraction, making post-processing unavoidable. In the following paragraphs the main processing techniques adopted in our group in Tyndall will be introduced; they consist of two easy to easy-to-perform processes, (the polishing of as-grown samples being the quickest and the back-etching the historical one) and two recently introduced self-aligning procedures, micro/nano-pillars and mirrored pyramids fabrication, that avail of dry etching steps: the former, developed few years ago, holds great potential for chip integration, whereas the latter, devised by myself during the course of this PhD research, could drastically simplify the implementation of electrically driven/tuned PQDs.

2.2.2 Polished and Back-etched configurations

As-grown polished: The polished configuration, introduced some years ago[25], is the easiest to obtain, but it allows a quick evaluation of the sample quality with low processing effort. The restored sample planarity can be exploited using Solid Immersion Lenses (SIL)[26] to boost collection without resorting to any kind of etching step.

The sample is bonded through yellow wax to a circular quartz glass-slide, and then placed facedown at the bottom of a steel jig and held in position by vacuum. The surface is lapped against a soft pad glued to a polishing plate and, a polishing slurry (Pureon - Ultra SolEX), containing Silica particles of about 80nm in diameter, is periodically poured onto the pad (Figure 2.2-8). The equipment used during this step is a PM5 Polishing machine produced by Logitech. After polishing, to dissolve any trace of organic, the sample is rinsed with Acetone and successively with IPA, and N_2 blown.

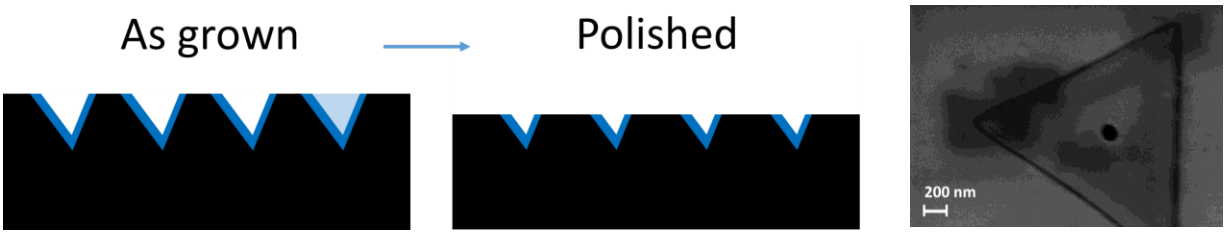

Figure 2.2-8: The as-grown grown sample is polished until the recess lateral dimension is ≈1 μm or smaller. On the right an SEM top view where the recess is almost disappearing.

Back-etched: The back-etched (BE) approach is a standard method historically applied to pyramidal QDs[27]. It is attractive due to its simplicity – typically requiring only a conventional wet etching process – and its moderately high yield of structures with good optical properties, making them suitable for a range of advanced fundamental studies.

Just like the above-mentioned process, it consists of a lapping step which, however, is performed on the back surface of the sample that is bonded with hard baked SU8 to a <100> GaAs carrier, in turn glued onto a glass slide with yellow wax. The lapping plate used consists of a glass plate and the Silica slurry is substituted with a coarser (1 μm

diameter) Aluminum Calcined Oxide powder dispersed in DI water for a faster lapping rate; we refer to this process as ***grinding***. Once the membrane reaches a thickness of about 20 μm (from the initial 360 μm), the sample is dipped into an Ammonium Hydroxide 8,28M : Hydrogen Peroxide 30% - 3:100 solution for several relatively short baths after each of which optical inspection is performed until pyramids start to appear out of the substrate (Figure 2.2-9).

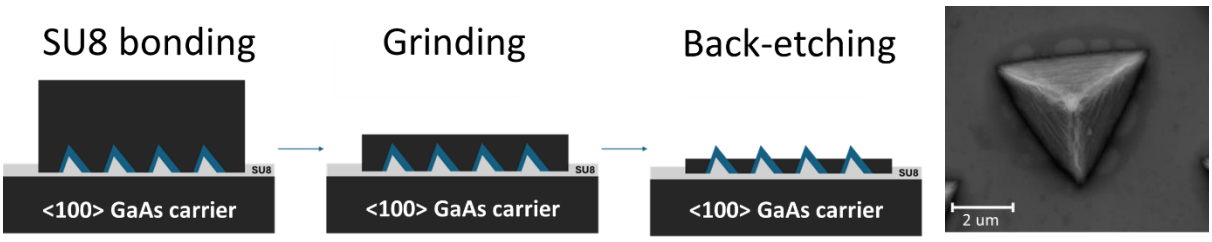

Figure 2.2-9: BE configuration fabrication: the sample is bonded through SU8 to a <100> GaAs carrier with the pyramids pointing upwards, then ground down to ≈30μm followed by a subsequently back-etch until the tips of the pyramids stick out from the GaAs substrate. On the right side is a SEM top view of a back-etched pyramid.

2.2.3 Dry etching approach: Pillars and Mirrored Pyramids configurations

Dry etching is a fabrication technology that is as vital as photolithography for the realization of microelectronic devices, yet, unlike the latter one, its understanding is more difficult to grasp because of the several complex phenomena that take place inside an etch chamber. The key ingredient that allows dry etching to occur is plasma, which, simply put, is an electrically neutral ionized gas, where the number of free electrons equals the number of typically singly charged ions. The application of a radiofrequency (usually 13.56 MHz) signal on a pair of electrodes, in between which a gas resides, causes electrons to accelerate, acquire kinetic energy and eventually collide with other atoms and molecules inside the gas. Collisions can release other electrons that in turn accelerate and collide with more molecules, giving rise to a transient avalanche effect that establishes plasma. In such a state, electrons are free to move within the plasma, conferring to it electrical properties.

The plasma exploited for dry etching purposes is a glow discharge plasma, a weakly ionized plasma characterized by the coexistence of electrons, ions and neutral species. Indeed, in such state of matter, the equivalent electron temperature T_e, related to the electron kinetic energy through the equation

$$\frac{1}{2} m_e v_e^2 = \frac{3}{2} k T_e \qquad (2.2)$$

(where m_e is the electron mass, v_e is its velocity and k is the Boltzmann's constant) can reach about 1000K as opposed to an arc discharge plasma, where 100% of species are ionized and T_e can reach 6000K.

The nature of collisions, and the following effects, depend on the energy that the electron acquires, and hence, on the acceleration/final velocity at which it collides. When a collision is elastic, there is only exchange of kinetic energy, the impinging electron is bounced back or driven askew losing some momentum that is transferred to the atom. Whereas, upon the occurrence of an inelastic collision, the electron's kinetic energy can be converted **i)** promoting the excitation of an atom's bound electron to and excited state that quickly reverts to the ground state emitting a photon, **ii)** ionizing the hit atom by expelling the outermost/weakest bound electron leaving behind a positive species, **iii)** breaking a molecule (dissociation) into its byproducts (radicals), **iv)** by electron attachment to the hit atom that becomes a negative ion (Figure 2.2-10). These steps are represented in the figure below.

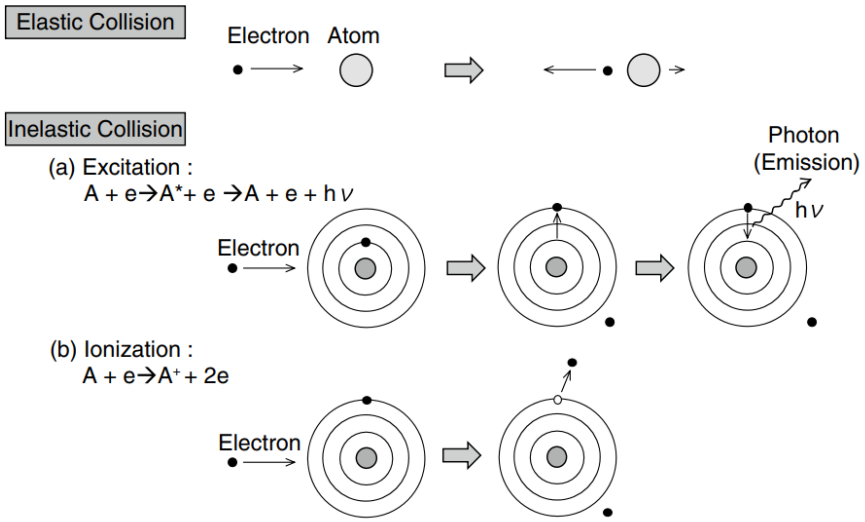

Figure 2.2-10: Collision processes in a plasma. Image taken from "Dry etching technology for semiconductors", Kazuo Noriji [28].

The ignition of plasma between the two parallel plates at which the RF signal is applied, is accompanied by the building up of a DC voltage at the electrode that is hosting the wafer to be etched. The presence of the series capacitor in the circuit allows the light electrons that are following RF electric field oscillations to leave the equipotential (V_p) plasma and accumulate at the lower electrode, gradually biasing it to a negative potential (V_{dc}). Negatively charged electrons are repelled from the platen while positive species are attracted to it and hence accelerated towards the target by the electric potential jump ($V_{plasma} + V_{dc}$) in this electron-depleted/ion-rich region, called ion sheath, immediately above the plate (Figure 2.2-11).

The ion sheath thickness (d_{is}) becomes important when compared to the mean free path ions have inside the sheath region. The mean free path λ is the average distance that a particle can travel without colliding with another particle. A tall sheath region ($d_{is}/\lambda>1$) would imply most ions being scattered because of collision with neutral species. To the contrary, a short sheath region ($d_{is}/\lambda <0.1$) would allow the majority of ions to reach the surface. Such low d_{is}/λ ratios can be obtained combining low chamber pressures, which

reflects in a λ increase, and a high-density plasma (ICP, ECR systems) that offers thin sheath regions.

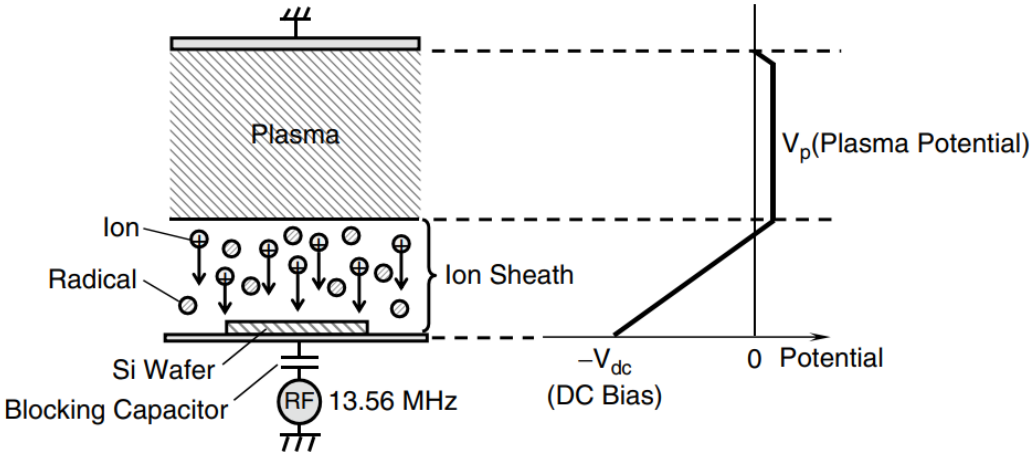

Figure 2.2-11: Ion sheath region in a plasma chamber and corresponding DC biasing voltage. Image taken from "Dry etching technology for semiconductors", Kazuo Noriji[28].

The introduction of dry etching in the process flow has given us one more degree of freedom through which to look for alternative solutions to improve light extraction efficiency and implement tuning and coupling strategies (the latter not addressed in this thesis). Below, the fabrication process of micro-pillars and mirrored pyramids is reported and discussed.

Pillars: The idea behind the fabrication of micro-pillars is to protect the dots from etching by masking the surface above them, and to subsequently perform a dry etching step that attacks the unprotected area, leaving tall posts at which top QDs dwell, precisely centered along the vertical axis[29]. In general, photolithography or e-beam lithography can be used to pattern such protective islands, however, both techniques require the spun layer of photo(e-beam)-resist, through which the pattern is impressed, to be planar and conformal. This outcome would not be the case were resists to be spun on a surface patterned with an array of tetrahedral recesses, which depths can range

from 3 μm to 6 μm, depending on the thickness of the growth. We exploited the topology of the surface and developed a process that is self-aligning.

Fabrication of micro/nano-pillars starts by depositing a conformal layer of SiO_2 ≈1 μm thick through PECVD, covering the recesses together with the ingrown (111)B flat surface. To expose the flat GaAs, a long polishing step is performed (see ***as grown polished***). Once SiO_2 is removed from everywhere but the recesses, which have shrunk to a dimension of 1 μm or less in terms of side of the triangle, the sample undergoes a dry etching step that eats into Gallium Arsenide leaving almost unaffected the protecting SiO_2 hard mask (Figure 2.2-12). Plasma is generated from a mixture of BCl_3, Cl_2, Ar and N_2 (13,13,13,5 sccm)[30] with a chamber pressure of 5mTorr, ICP power of 600W and HF power of 55W. Addition of Ar to BCl_3/Cl_2 environment stabilizes plasma and improves surface roughness sputtering away nonvolatile products[31,32], whereas the presence of N_2 enhances dissociation of BCl_3 and fosters passivation of sidewalls[30,32]. Dry etching is performed with a PlasmaPro 100 Cobra ICP RIE system. This self-aligning technique avoids the need for lithographic steps, ensuring near-perfect alignment of the QDs along the vertical symmetry axis – a significant advantage, as misalignment, as shown in other photonic devices based on pillar-type elements (wires, cylinders), can lead to far-field profile distortions, and polarization anisotropy in the emitted light[33–35].

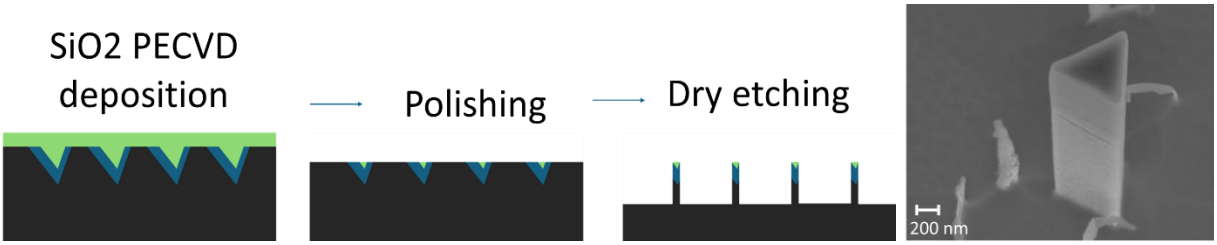

Figure 2.2-12: Pillars fabrication: a thick SiO_2 mask is deposited via PECVD on the as-grown sample, and then polished away until recesses have a lateral dimension ≈1 μm. The following dry etching step eats into the unprotected GaAs leaving unaffected the semiconductor masked under the SiO_2 inside the recesses. On the right, an SEM image of a micro-pillar.

Mirrored Pyramids: In the wake of the process just described, I developed a similar approach to create mirrored pyramidal structures with a tunable aspect ratio, discussed for the first time in our publication[36] on which Chapter 4 is based. This design retains the pyramidal shape but differs from the back-etched process in that it creates a mirrored version of the initial three-dimensional structure of the SU8 photoresist infill of the recess (i.e. the recess is still pointing down as in as-grown structures, but at the end of the process is embedded in a pyramid-like structure, see Figure 2.2-14).

The reason for introducing mirrored pyramids is found in another application investigated in this document: the supply of an electric field to specific QDs to tune their spectral properties. Electrode deposition and field application in non-planar structures is challenging, requiring a non-conventional fabrication procedure[18]. As will be shown later in the thesis, most experiments for tuning spectra have been performed using back-etched samples. However, this procedure has large disadvantages: grinding a sample from 360 μm to 20 μm in thickness can often result in a partial loss of the sample itself and sometimes in its complete destruction; grinding introduces also a tilt throughout the surface of the sample leading to a loss of parallelism: a 10 μm height difference at two points of a 0.5 cm wide sample consists in a tilt of less than one degree. Nevertheless, this causes, in the subsequent wet back-etching step, the exposure of only a fraction of the pyramids, turning into a loss of specimen yield. In case all the pyramids were to be exposed and, hence, the sample fully back etched, the etchant would have penetrated the etch stop barrier because of the longer exposure to the chemical required to uncover pyramids under a thicker GaAs layer: again, this would reflect in a low yield.

Mirroring the shape of the recess with respect to a horizontal plane parallel to the (111)B surface of the sample, aims at combining the advantages of the pillar process together with those of the back etching. A properly timed dry etching step on a sample where recesses are masked gives access to nearly all the QDs present on the surface with an extraction efficiency comparable to, or higher than, the back etching methodology. At the same time, with a view to the development of electrically tunable QDs, the typical

slanted sidewalls of the back etched pyramids reproduced in the mirroring process allow the deposition of a conformal and continuous layer of thin metal contact, ruling out the possibility of open circuit as might be the case in the pillar configuration. The latter should undergo a planarization process that we're developing.

Pyramids are inverted starting from spinning SU8-2 resist on the sample and following the standard procedure of SU8 patterning: after resist is spun on the surface, the layer is soft baked for 1 minute at 65°C and 3 minutes at 95 °C. The sample is subsequently flood exposed for about 10 seconds (the exposure dose for SU8-2 is 100mJ/cm^2, for a lamp with intensity different from 10mW/cm^2 time must be adjusted accordingly). The last step consists of post exposure baking for about 2 minutes at 65 °C followed by another 2 minutes at 95°C.

SU8 is an epoxy based negative photoresist, where each monomer is composed of eight epoxy groups as shown in Figure 2.2-13:

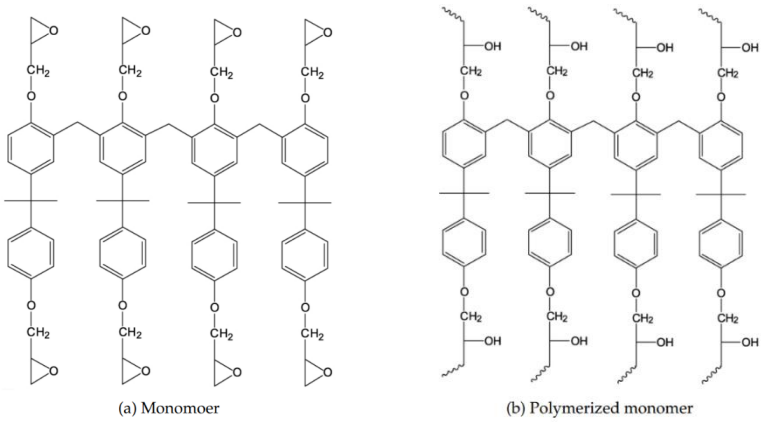

Figure 2.2-13 : SU8 molecular structure before (left) and after (right) polymerization, taken from "Immobilization of DNA and protein to polymerized SU-8 photoresist investigated with microarray assays", by Silvan Schmid, master thesis.

After light exposure, a photoacid reaction is triggered on the surface crosslinking the monomers into a polymer. This process, however, needs to be assisted by temperature for the chemical amplification to travel down through the layer, crosslinking all the

monomers and making SU8 an incredible chemically, thermally and mechanically stable material.

The polymer is polished away from the planar surface and recesses shrunk to a dimension of about 3 μm in side. Sample is then dry etched in an atmosphere of BCl_3 and N_2 at very low pressure (BCl_3:N_2 – 30:2 sccm, 2 mTorr, 180 W HF, 1000 W ICP): this allows the etching mechanism to be prevalently mechanical, fostering vertical etching over isotropic etching. The result, with a selectivity between 2:1 and 3:1 for SU8:GaAs, is a mirrored quasi-tetrahedral profile (Figure 2.2-14).

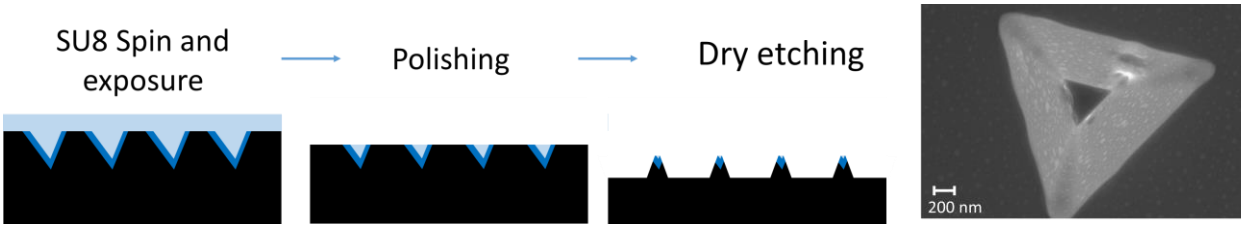

Figure 2.2-14: Mirrored pyramids fabrication: SU8 resist is spun on the as-grown sample and exposed, and then polished away until recesses have a lateral dimension ≈3 μm. The subsequent dry etching step attacks GaAs and SU8 with a selectivity between 2:1 and 3:1 mirroring the tetrahedral shape of the recess. On the right, an SEM image of a mirrored pyramid.

2.3 Optical characterization

The optical characterization of the samples is performed using a conventional micro-photoluminescence (μPL) setup. The system includes a low-vibration, closed-cycle cryostat that achieves a minimum temperature of 12K. The application of thermal paste (usually silver-based paint) is necessary to ensure proper thermal contact between the sample and the cooled copper stage.

The chamber is evacuated to a vacuum level of approximately 10^{-6} mbar while cooling down. Excitation and emission collection are performed using a single objective lens with a numerical aperture of 0.42, 50X magnification, and a working distance of 17 mm,

arranged in a confocal geometry. The QDs are excited non-resonantly by a laser diode (PicoQuant LDH-D-C-635M, λ = 635 nm), which can operate in both continuous-wave (cw) and pulsed modes. The laser beam is focused to a spot size of 1–2 μm, enabling precise excitation of individual PQDs. The typical laser excitation power on the sample ranges from 50 to 200 nW/μm^2.

Polarization resolved measurements of the FSS (Figure 2.3-1-a) are performed by placing a half-wave retardation plate and a polarizer in the optical axis of the system. By rotating the lambda/2 plate one can cycle through H and V polarization of the (bi)excitons, selected by the fixed polarizer. By tracking the spectral position of the (bi)excitonic peaks and plotting it against the rotation angle, is possible to visualize the FSS, which corresponds to the peak-to-peak value of the (fitted) sinusoidal curve, as shown in Figure 2.3-1-b. To eliminate the influence of systematic errors introduced by sometimes observed overall energy shifts and jumps due to both internal and external factors, FSS value is generally obtained subtracting the corresponding biexciton position to the excitonic one.

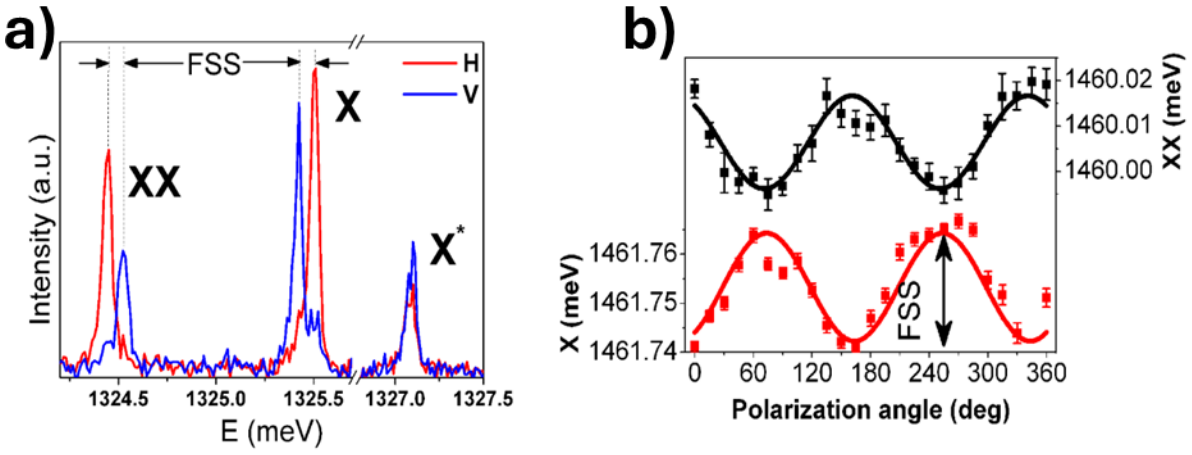

Figure 2.3-1: a) Polarization resolved spectra of an InGaAs QD. The spectral position of the $H_{X(XX)}$ and $V_{X(XX)}$ peaks is marked to underline the energetic difference; b) X and XX energetic sinusoidal dependence on the polarization angle. Images taken from "Pyramidal quantum dots: single and entangled photon sources and correlation studies", UCC PhD Thesis, Juska G[17].

Additionally time-correlated single photon counting (TCSPC) measurements were performed. This is an efficient technique to analyze photoluminescence kinetics, especially when the photon flux is low (<1000 counts/s) and picoseconds resolution is required. QDs are optically excited through pulsed excitation, and their emitted light is sent to a monochromator that operates as a narrow band-pass filter and through a slit, to select the wavelength and resolution. Light is eventually measured by a single photon avalanche photodiode. At the same time, a clock synchronized with the laser pulses is sent to a photon counting module. For each collected photon, the time elapsed between the clock pulse and the collection event is recorded, and, over time, a histogram where the x axis corresponds to time bins (time slots in between which measured elapsed times fall) and the y axis corresponds to the number of events for each time bin, is built (Figure 2.3-2). The average lifetime of a recombining complex is conventionally set as the time τ_R at which the normalized magnitude of the photoluminescence decay curve is 1/e.

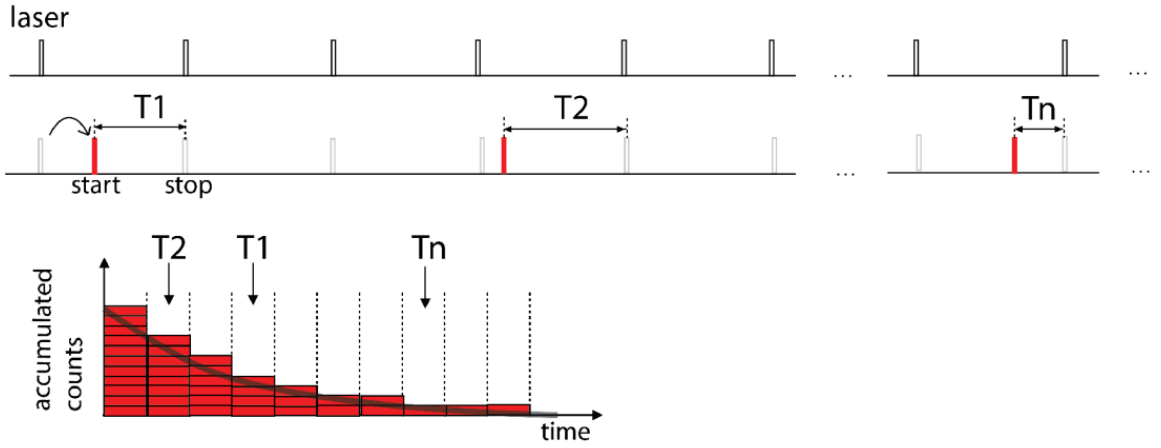

Figure 2.3-2: Time-resolved measurements: laser is shone following a clock signal and the time elapse from the pulse until the SP detection event is recorded (top). Time events are ordered into time bins, and the amplitude of the bins defines the photoluminescence decay curve of the transition (bottom). Image taken from "Pyramidal quantum dots: single and entangled photon sources and correlation studies", UCC PhD thesis, Juska G[17].

In some cases, linewidth measurements were performed to probe noise from nearby charging of the quantum dots. The standard set up exploits a 950/mm grating, that is capable of delivering a resolution of ~50 μeV. To resolve narrower lines, a finer 1800/mm grating with a resolution of 20 μeV is employed.

2.3.1 Effects of processing on the photoluminescence of QDs

To highlight the effect of the processes on the QDs' photoluminescence, we performed a systematic study using one kind of QDs. The epitaxial structure grown inside the recesses, besides the buffer and the etch stop layer, is made of two AlGaAs cladding layers (55% and 45%) that encase two superlattice (SL) AlAs/GaAs barriers, in turn sandwiching a GaAs QD. We decided to employ such a QD because the digital alloy in the barrier has been proven to confer brightness and the smallest FSS, among other kind of structures, to GaAs QDs[37]. The epitaxial structure along with thickness values are reported below in Figure 2.3-3.

Every experiment was performed using a cleaved piece of the same growth run. We ran 3 experiments:

1. **As-grown → Polished → Back-etched**
2. **Polished → Mirrored Pyramids → SEM**
3. **Polished → Pillars → SEM**

μPL measurements were consistently obtained from the same designated QDs for each set of experiments, made possible by the introduction of a patterning-mask that groups QDs under two levels of nested sub cells, allowing individual QD labelling. This innovation enables tracking the evolution of individual QDs throughout multiple processing steps.

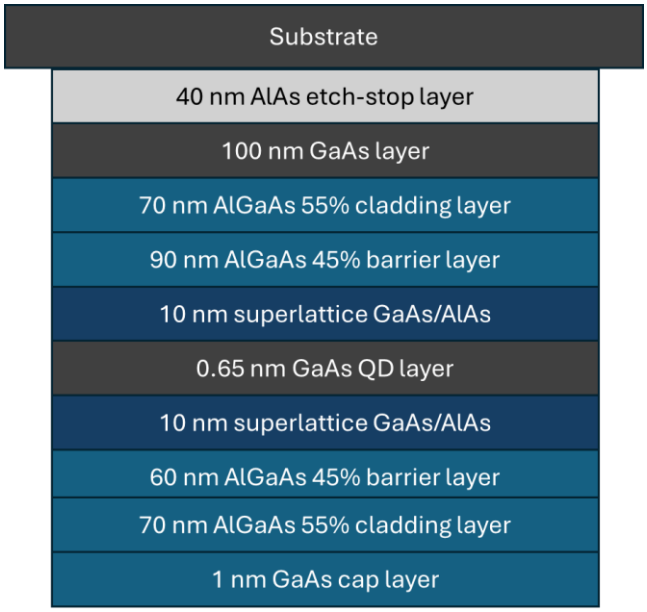

Figure 2.3-3: epitaxial structure and nominal thickness values of GaAs QD in GaAs/AlAs Superlattice barriers

As-grown → Polished → Back-etched

For the apex-down configuration, polishing the sample is essential, as the large vestigial recess prevents effective excitation and extraction. Figure 2.3-4 below shows two spectra acquired for the polished (red) and as-grown (black) configurations. In the polished configuration, excitonic transitions are clearly visible, whereas the as-grown spectra lack distinguishable QD features, with luminescence likely originating from the quantum well-like layer used to cap the AlGaAs. This demonstrates that polishing is an indispensable and effective method for evaluating QD quality in the apex-down configuration.

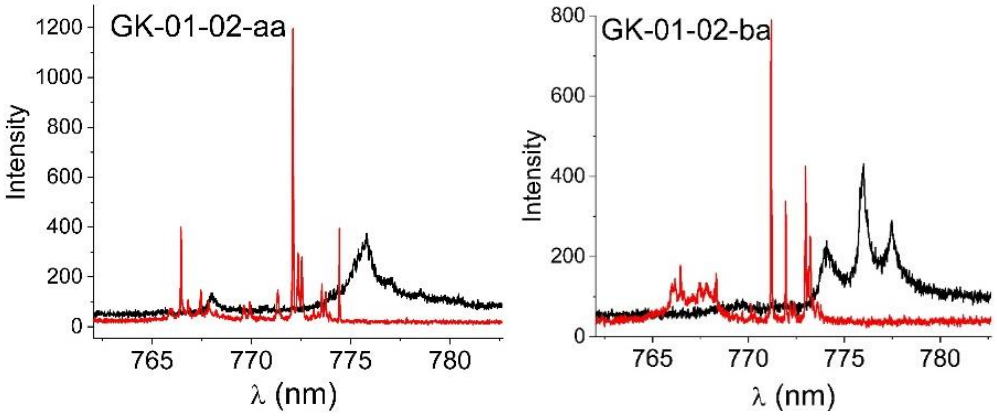

Figure 2.3-4 spectra of QDs GK-01-01 aa and ba before (black) and after polishing (red)

On the other hand, back-etching introduced significant changes in the spectra. While confirming its light extraction enhancement (peaks increased from less than 1 kcounts/s to 20 kcounts/s), it also caused a population shift towards positively charged trions (X^+) at the expense of neutral excitons (X) (Figure 2.3-5-a). Additionally, we observed a slight blue shift (+0.005eV) and an increase in the FSS from an average of 5.7 μeV in the polished configuration to 20 μeV (Figure 2.3-5-b). These effects may be related to the position of the QDs measured, which, as shown in Figure 2.3-5-c, are located near the edge of the sample. We attribute this behavior to the action of the SU8 layer used as a bonding medium, which strains the thin GaAs back-etched membrane at cryogenic temperatures. The effect appears more pronounced near the edge because the bonding process typically involves depositing a drop of resist rather than spinning it evenly across the substrate. Pressing the sample to seek parallelism between top and bottom planes causes excess SU8 to flow out from below the sample and to accumulate at the edges. This thicker resist at the perimeter likely dominates the temperature-induced strain in the GaAs, leading to spectral shifts and FSS changes. This could be the reason for some of the differences observed during a systematic study conducted earlier[37], where back-etched GaAs QD in SL samples exhibited the smallest FSS.

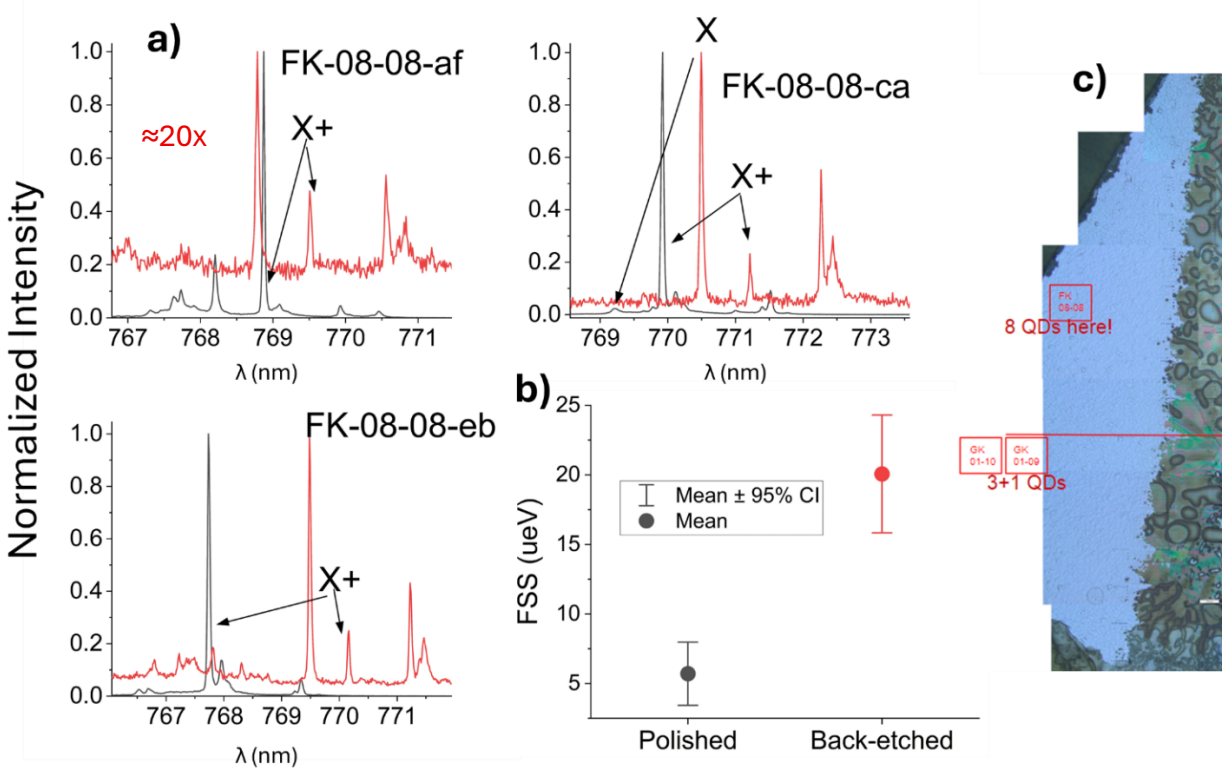

Figure 2.3-5: a) Spectra of QDs FK-08-08 af, ca, be when polished (red) and BE (black), the latter characterized by a blue-shift and a population mechanism favoring X^+s over Xs; b) FSS distribution before and after BE; c) partial image of a BE sample taken with optical microscope.

Polished → Mirrored Pyramids → SEM

For the second experiment, we had to make a compromise. As previously discussed, QD features are not visible when the polishing is shallow (recess shrunk to a lateral size of 3 to 4 μm). While these conditions are ideal for mirroring the shape of the recess, they are incompatible with the approach of this study, where we take as a reference the initial condition (polished) for all samples and compare changes induced by subsequent procedures. We reduced anyway the dimension of recesses to less than 1 μm (side), but we limited the time duration of the mirroring process to be conservative. This led to the formation of squat (100-300 nm tall) truncated mirrored pyramids (Figure 2.3-6-a), a suboptimal design since it sees the QD still buried in the substrate. Furthermore, since recesses were smaller than the optimal dimension, polishing caused in some cases the partial removal of the SU8 protective cap, leading to formation non-uniform structures;

in other cases (see QDs *si*, *sb*, *cf* of Figure 2.3-7-a)) there is no structure at all above the substrate plane.

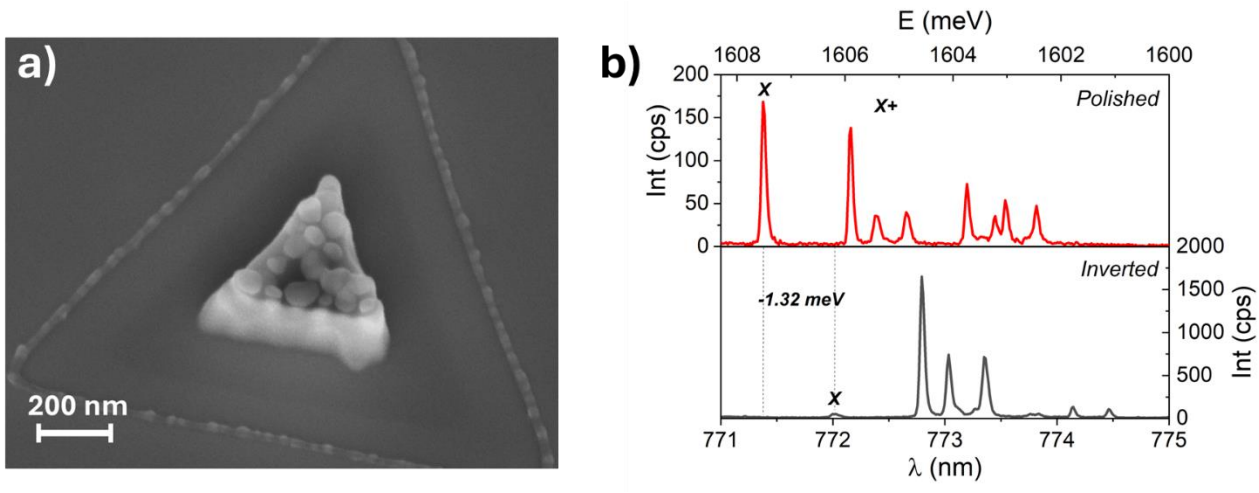

Figure 2.3-6: a) QD HK-02-02-aa SEM top view: the structure left after the short dry etching step is a squat truncated pyramid, suboptimal for light extraction enhancement. On top of the recess is possible to spot Silica particles bonded to the protective SU8 infilling the recess. The triangular curb all around the structure is the AlAs etch-stop layer (effective only for BE) that after the dry etch process oxidizes and sticks out of the substrate plane; b) spectra of dot aa before (top, red) and after (bottom, black) the mirroring process.

Figure 2.3-6-b displays the spectrum acquired before (top red curve) and after (bottom black curve) the dry etching step of QD (HK-02-02-) *aa*, where an order of magnitude gain in the count/s collected is put in evidence in the bottom graph, but also a redshift of the excitonic lines, which balance is altered in favor of the positively charged trion.

However, this appears to be an isolated case, as the remaining QDs studied in this cell show a more balanced intensity increase between X and X^+. Figure 2.3-7-b indicates that, after etching, the individual QD charging changes still favor X complexes over X^+ ones. In Figure 2.3-7-c, the mirrored intensity values are summed and normalized to those of the polished configuration according to $(X_{mirrored}+X^+_{mirrored})/(X_{polished}+X^+_{polished})$, revealing a modest brightness improvement (≤10×) in most cases. Exceptions are QDs *bb*, *sg*, and *si*, where their uniform structure may have enhanced extraction efficiency by factors of up to 40 (*bb*, *sg*) and 15 (*si*).

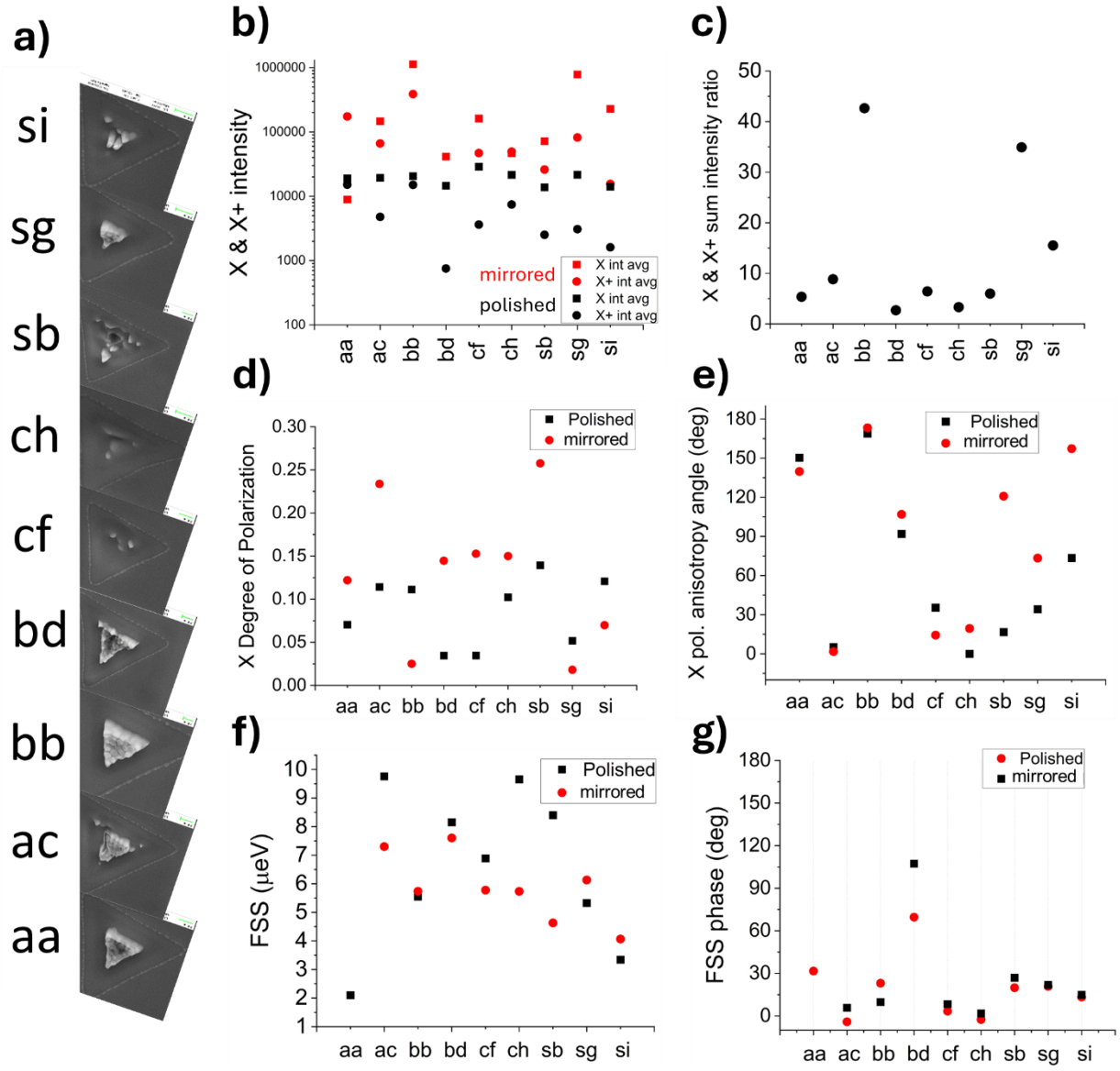

Figure 2.3-7: a) SEM top view of 9 of mirrored QDs from cell HK-02-02; b) X and X^+ intensities for polished and mirrored pyramids; c) $(X_{mirrored}+X^+_{mirrored})/(X_{polished}+X^+_{polished})$ intensities ratio; d) Linear DoP of X transitions before and after mirroring; e) polarization anisotropy of X transitions before and after mirroring; f) polished vs mirrored FSS: there is a general FSS improvement, beyond the statistical error, on the mirrored pyramids; g) polished vs mirrored FSS phase.

We also investigated the linear Degree of Polarization (DoP) of neutral excitons, calculated as $I_X^{max}(\theta) - I_X^{min}(\theta) / (I_X^{max}(\theta) + I_X^{min}(\theta))$, shown in Figure 2.3-7-d. This definition is equivalent to $(I_H-I_V)/(I_H+I_V)$, and it's extracted from the same measurements for FSS by using a set of spectra. Compared to the polished case, mirrored pyramids exhibit a

change in the polarization of emitted light in both directions. Notably, the QDs that exhibit higher brightness tend to emit less polarized light. Conversely, the angle of polarization anisotropy for X does not show a clear correlation with either geometrical features or DoP. Three out of nine QDs (*sb*, *sg*, *si*) display a distinct rotation of the polarization axis (Figure 2.3-7-e).

As for the FSS, mirroring didn't alter appreciably the energy difference between H_X and V_X in most cases, if not for three cases (QDs *ac, ch, sb*), where FSS was reduced by 2-3 μeV, beyond the statistical error (Figure 2.3-7-f). Similarly to what we said about the X polarization anisotropy, no inference can be made from the FSS phase change, which is negligible for all cases but one (QD *bd,* Figure 2.3-7-g)

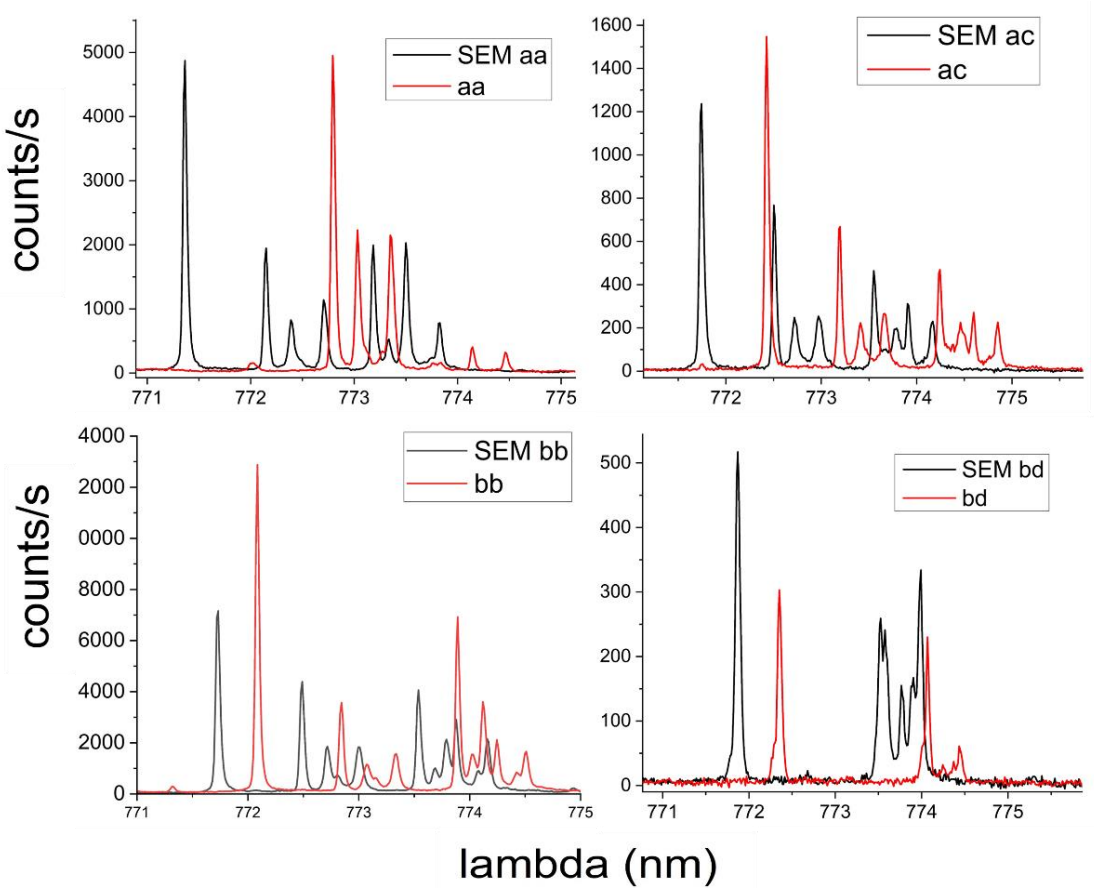

Figure 2.3-8: extract of some spectra taken before (red curve) and after SEM characterization (black curve). Spectral features are not altered if not for a blue shift.

SEM images of Figure 2.3-7-a were taken after the optical characterization of the mirrored structures; an accelerating voltage of 5KV was used. To check whether exposure to accelerated electrons during SEM made an effect, the same QDs were measured repeatedly. μPL showed a negligible change in population charging but, overall, all spectra underwent a blue shift (Figure 2.3-8).

Polished → Pillars → SEM

If a compromise was necessary to proceed with the study of mirrored pyramids, no such compromise was required for micro/nano pillars. Their fabrication process involves a thorough polishing step (compatible with the experiment design), during which intermediate measurements are often taken to assess growth quality, as already mentioned in the processing section of this chapter. Moreover, in contrast to mirrored pyramids—where recess dimensions determined by the polishing time are compromised due to the not-so-hard nature of the protective mask (which is affected by both the lapping action and the uneven impact of dry etching)—pillar fabrication preserves the dimensions at the end of the polishing step, since it makes use of an SiO_2 mask. This ensures that the edge dimensions of the pillars remain intact and allows quantum dot photoluminescence features to be reliably referenced to the pillar edge. As a result, the edge length of the pillars becomes a well-defined and easily identifiable variable.

Figure 2.3-9-a shows top views of several pillars characterized during this study, belonging to sub cells EI-01-16 and EJ-11-01, along with their edge measurements. Here it's worth noticing how broad is the size distribution of the pillar edge within a single sub cell, that spans from 600 nm to 1.6 μm. Although it may appear to hinder reproducibility, it turns out to be a convenient feature that helps excluding one degree of freedom: we can assume growth to be homogeneous enough over the restricted sub cell area, ascribing differences in PL behavior, somehow, to the size of the pillar and/or the processes associated.

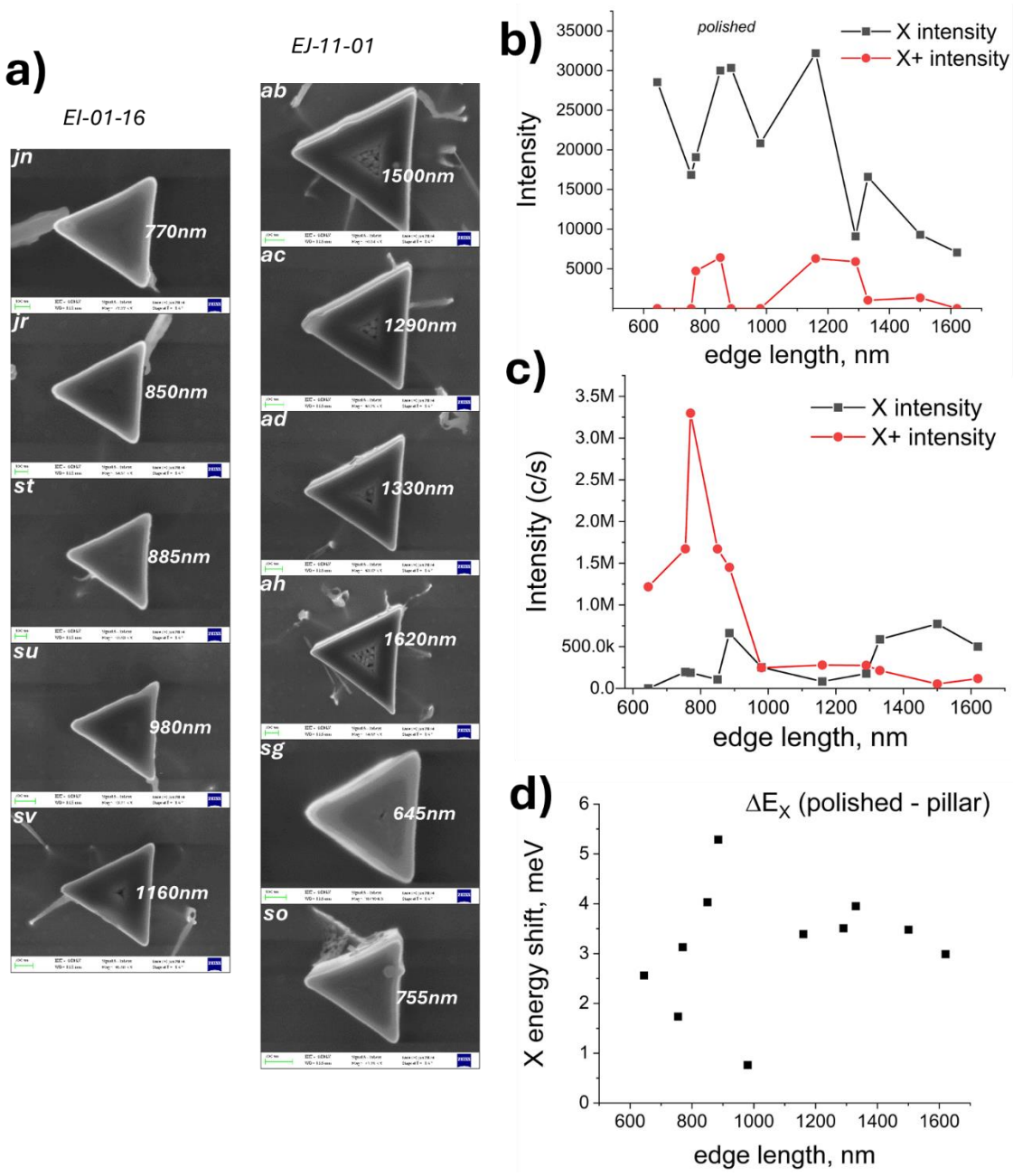

Figure 2.3-9: a) SEM top view of micro-pillars along with size measurement; b) X and X^+ intensities in polished configuration; c) X and X^+ intensities in pillars; d) X peaks energy shift from polished to pillars

The first characteristic we want to point out is the QD population distribution that we observed in the polished samples, reported in Figure 2.3-9-b: QDs are prevalently populated by neutral excitons, whose PL intensities are about 5 times higher than X^+

ones, however, when the pillar edge crosses 1.2 μm, luminescence plummets; a clear sign that the QD is deeper in the bulk. When the specimens are turned into pillars, the equilibrium just described is overruled and high total emission intensity ($X+X^+$) is obtained for small-sided pillars. The intensity curve peaks when the edge size is around 800 nm with an intensity 200 times higher than when the sample was only polished (Figure 2.3-9-c), but luminescence is prevalently dominated by X^+ recombinations that account for ≈94% of the total emitted $X+X^+$ power. For edge length greater than 1 μm, intensities drop to values about 40 times the respective polished ones.

Figure 2.3-9-c highlights the QDs population change with respect the pillar size: small pillars are dominated by charged states, most likely due to the influence of defected etched sidewall near to the QD. These defects might be the cause of a nearby electric field and trap states that change population dynamics transforming the neutral excitons to positively charged ones upon optical excitation. X^+ states cease to be efficiently populated when the pillars edge crosses 1.2 μm in length, in favor of X states, mechanism reflected in the slight increase of X and the drastic drop of X^+ intensities. This dynamic supports the hypothesis that surface states on the sidewall are interfering with the QD population mechanism, suggesting that the active region restores its charging balance when sidewalls are far apart, and defects can't exert their influence anymore.

If states population shows a correlation with pillar size, the same cannot be said for the energy shift of the X peaks from before and after pillars fabrication: in Figure 2.3-9-d ΔE_X, defined as $E_{X\_polished} - E_{X\_pillars}$, is positive for all QDs at all edge lengths. A redshift could be the sign of the presence of a surface state-induced electric field, but this hypothesis wouldn't comply with the apparent redshift magnitude independence on the length of the edge. Temperature-induced strain might play a role, but no trend is evident from the data, so a more thorough systematic study would be needed to have a deeper understanding.

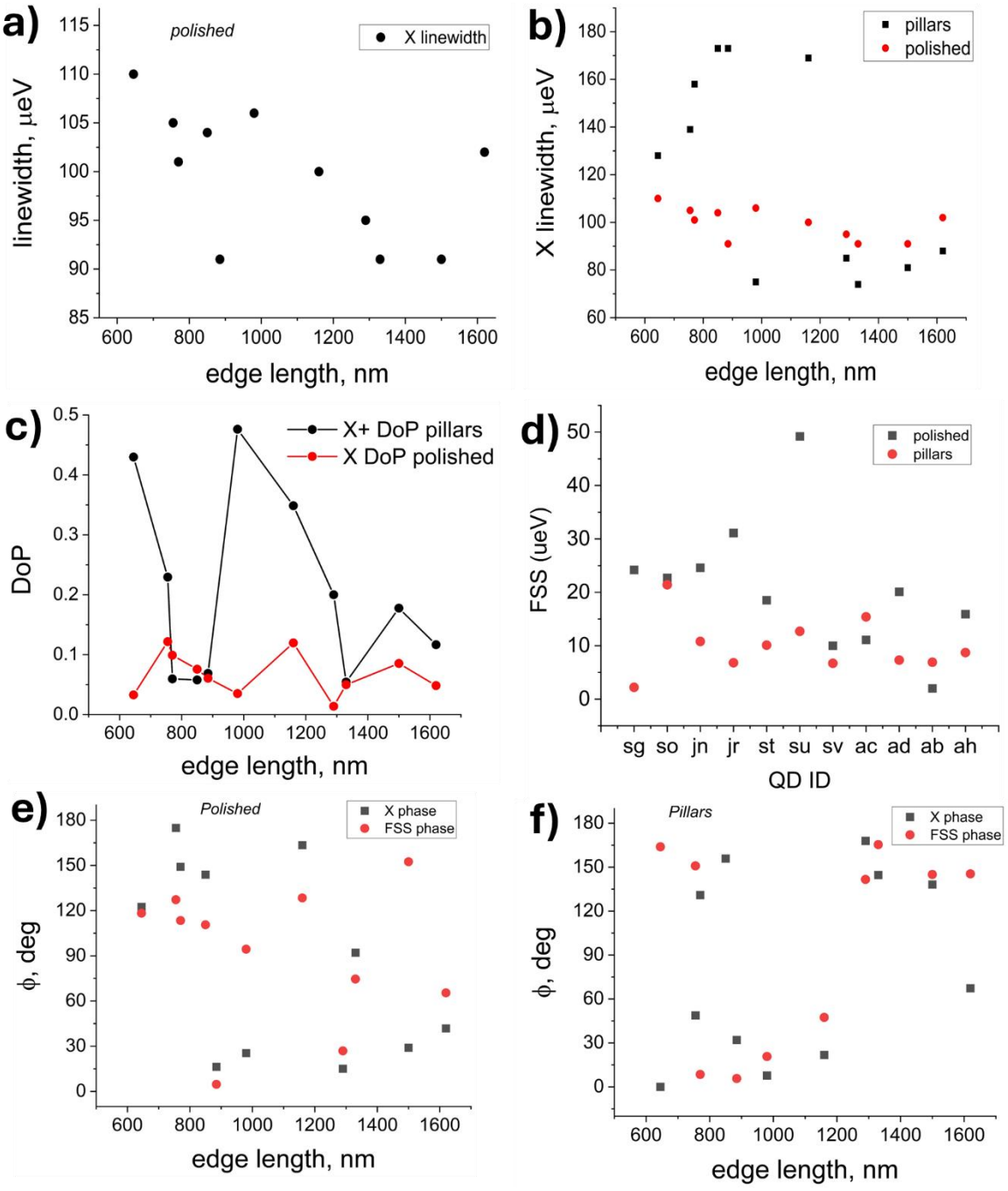

Figure 2.3-10: a) slow decaying linear trend of X linewidth in polished configuration as the size of recess edge increases; b) X linewidth polished vs pillars. For small edges, linewidth in pillars is more than twice that in polished configuration. Remarkably, the trend is not confirmed for big pillars, where linewidth narrows; c) linear DoP of polished vs pillar configuration. The DoP change in pillars, from an almost constant (low) value for the polished configuration, suggests the triangular symmetry of the pillar waveguide is affecting the polarization of the light; d) FSS values after pillar fabrication change but show no trend with respect to the dimension of the

pillar edge; e) FSS phase and X polarization anisotropy phase in polished configurations are randomly distributed; f) FSS phase and X polarization anisotropy phase in pillar cluster around 30 and 150 degrees.

Although for this analysis we have excluded one variable assuming the QD geometrical properties uniform and not crucial (for the time being at least), we haven't taken into consideration the coupling efficiency that the dipole-like emitted power has with the sustained modes of the waveguiding pillar structure. These modes vary in effective refractive index and in number depending on the width of the horizontal triangular cross-section of the pillar and on the wavelength, and coupling to them contributes to defining the emitted power farfield distribution and most probably its DoP too. Figure 2.3-10-c shows that the linear DoP of pillars with respect to their polished counterpart undergoes a general increase but displays a peculiar behavior as the curve has a quite sharp drop around 800nm, in correspondence of the maximum intensity peak. This size might be a sweet spot for obtaining bright unpolarized emitting pillars, however, comes with the drawback of an altered population mechanism that hugely favors X^+s over Xs.

When excitons linewidth is probed, the polished sample exhibits a slow linearly decreasing change as the edge length increases (Figure 2.3-10-a). This behavior can be attributed to the fact that larger recesses position the QD farther from the polished top surface, thereby reducing the influence of surface defects. When the recesses are turned to pillars, the same X transitions see their linewidths increase, doubling in magnitude in some cases (Figure 2.3-10-b). The linewidth of the transition generally reflects the environment that surrounds the QD: the random Coulomb interaction between excitons and nearby charges establishes fluctuating electric fields that are the cause of spectral diffusion and broadening[38,39]. Hence, QDs are likely affected by surface states on the sidewalls of small-sided pillars. Beyond an edge length of 1.2 μm, the influence of surface states is no longer significant, and the linewidth improves to values smaller than the corresponding polished ones.

It proves to be more challenging to find an explanation of the FSS trend for both configurations. The energy splitting of the polished QDs is overall higher than the smallest established in literature[37] for PQDs, and the biggest values are observed for small-sided recesses (Figure 2.3-10-d, red marks). FSS values obtained from pillars are lower in almost all cases, except for two pillars with edge length greater than 1.2 μm (Figure 2.3-10-d, black marks). The poorer performance of the polished configuration might be due to the SiO_2 mask straining the QDs underneath, and the subsequent FSS reduction for the pillar case would be compatible with the strain release mechanism typical of 3D nanostructures[40], although it wouldn't yet explicate the high FSS values correspondent to small polished recesses, where the SiO_2 mask volume is smaller and one would expect it to exert less stress over the bulk all around. Also, polished samples require several times higher optical power density to excite the structures, creating electrically much noisier environment of a QD possibly also contributing to the increase in FSS.

Interestingly, we found the FSS and the X polarization anisotropy phases bunching around 30 and 150 degrees (Figure 2.3-10-f) in case of the pillars, which seem anyway uncorrelated with the edge dimension. Before the dry etching, the polished recesses exhibited a more random distribution of both phases (Figure 2.3-10-e). The change from a random phase distribution to a clustered one could be the effect of the C_{3v} symmetry forced by the triangular cross-section of the pillar waveguide.

Lastly, as was done for the mirrored pyramids, SEM (5 kV e-beam) images were taken, and the effect was again probed under laser excitation. A smoothly decaying redshift curve was observed as the edge size increased ($\Delta\lambda=\lambda_{pillar+SEM}-\lambda_{pillar}$, Figure 2.3-11-b). Simultaneously, a rebalancing of QD charging was noticed: the dominant X^+ peaks in the spectra of the pillars (Figure 2.3-11-a, black curve) diminish for small edges at the expense of X transitions that become prominent (Figure 2.3-11-a, red curve). For larger pillars, the spectra remain essentially unaltered, aside from the slight redshift.

Both behaviors seem to validate the hypothesis that the surface states introduced by damaged pillars sidewalls are the source of the unbalanced population mechanism that feeds positively charged trions inside QDs: the SEM electron beam most likely populates those defects, whose charged states-induced electric field sums up to the excitons' confining potential and shifts the wavefunctions energies. Such influence is stronger for thin pillars, where the proximity of the states to the dipole causes greater energy shifts. Analogously, upon (e-beam) population of those states, the probability of inducing an additional hole inside the QD lowers, reducing the rate of X^+ transitions while increasing that of the neutral excitons. Again, big pillars seem to be unaffected as they already revealed an X/X^+ ratio greater than one.

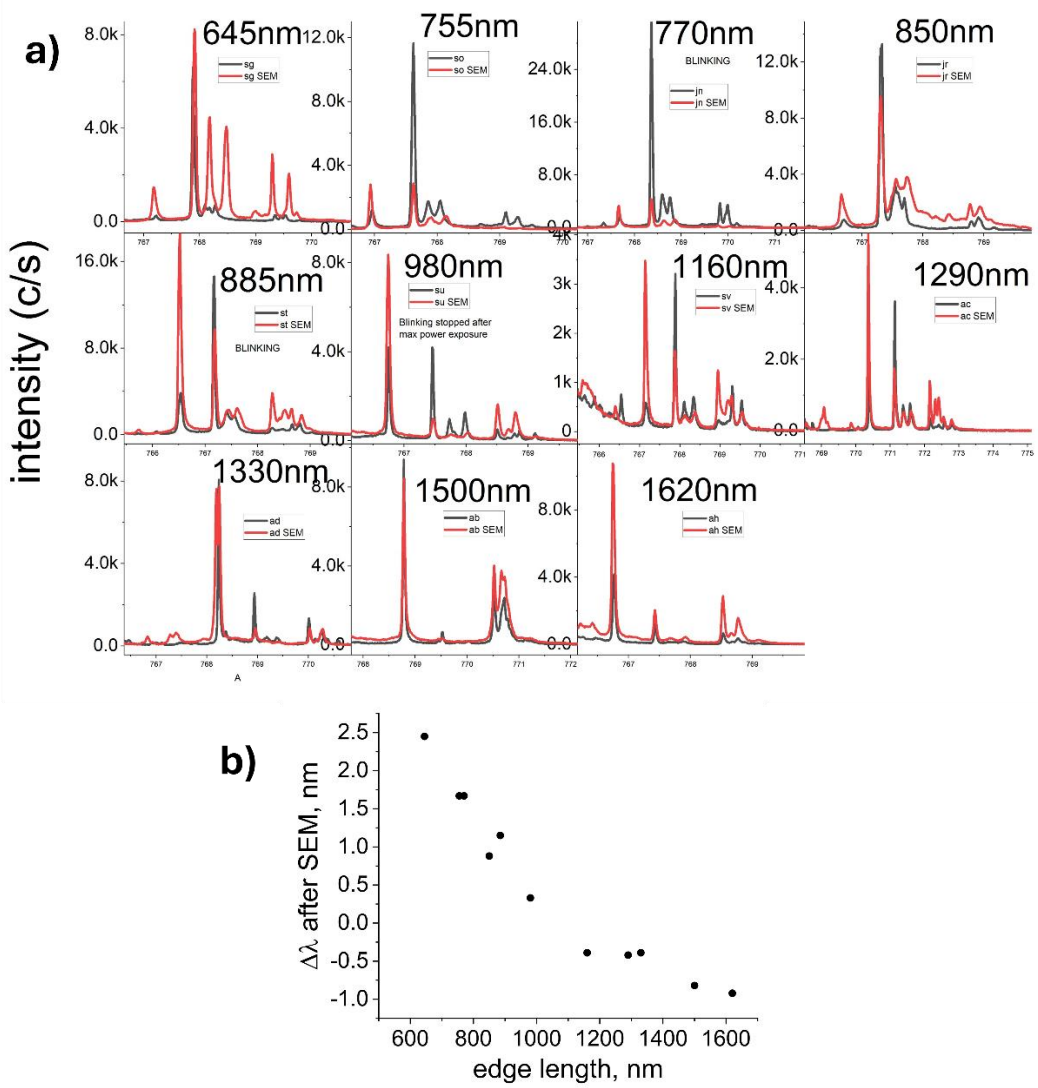

Figure 2.3-11: a) series of spectra taken from pillars of different lateral size, taken before (black lines) and after (red lines) the SEM visual characterization. The SEM effect is to balance the population mechanism suppressing X^+ states in favor of X ones. Figure b) on the bottom right show the energy shift the X peaks undertake after SEM.

2.4 Summary

In this chapter I outlined the main workflow steps that we generally perform when we decide to produce a QD sample. The introductory growth section contains an analysis that leverages AFM cross-sectional measurements to show how nontrivial it is to calibrate thickness inside tetrahedral recesses. While the thickness of the layers growing on the (111)A sidewalls is, with due care, close to the nominal thickness set during the design of the structure, growth in grooves is less foreseeable, and, despite we

have a general understanding of the principal competing mechanisms, we weren't able to predict the closure of the recess for high Al content, nor are we able to predict with high confidence the actual position of a QD on the vertical axis. I deem this ability empowering for PQDs, as in chapter 4 one of the potentialities of this system will emerge, circumventing in a straightforward way the difficulties the recess geometry puts against the realization of a resonating structure, which, as per literature, is feasible, but far from being a simple process[20]. On the fabrication side, all the configurations that we exploit have been presented. We have standardized the pillar fabrication procedure and, leveraging the same self-aligning mechanism, I was able to introduce a new configuration with the aim of simplifying the fabrication process of an electrically tuneable QD. Nonetheless, standardization doesn't only come from process repeatability, but also from understanding the effects of the process on the source, and, eventually from being able to act on the causes if needed. The systematic optical characterization study provided some insights into the QD overall behavior: BE was confirmed to be a great configuration for light extraction; however, care needs to be taken when measurements are obtained from peripheral QDs, which might be subjected to the bonding medium straining action.

The polished configuration came out as valuable in assessing QD properties despite the low number of c/s. The mirrored pyramids fabrication is a young process but demonstrated to be great in boosting brightness and preserving (in many cases improving) the FSS measured in the polished configuration. Finally, the highest intensity was observed in micro/nano-pillars, which however stood out also for the complex behavior they displayed: it is clear that the damage induced to the semiconductor during dry etching interferes with the QDs population/recombination mechanisms, and it's visible in those features that change along with the edge size (X/X^+ balance, DoP, emission energy after SEM), although a bigger statistic would be needed to unequivocally identify trends. Three parameters that behaved independently of the size of the pillars were the FSS, which underwent through a general reduction, and the FSS and X polarization anisotropy phases, that clustered around 30 and 150 degrees. This

behavior might stem from the imposition of C_{3v} symmetry on the electromagnetic modes to which the recombining dipole couples power. However, further studies are needed to explore this hypothesis.

References

(1) Manasevit, H. M. SINGLE-CRYSTAL GALLIUM ARSENIDE ON INSULATING SUBSTRATES. *Appl. Phys. Lett.* **1968**, *12* (4), 156–159. https://doi.org/10.1063/1.1651934.

(2) Manasevit, H. M.; Simpson, W. I. The Use of Metal-Organics in the Preparation of Semiconductor Materials: I . Epitaxial Gallium- V Compounds. *J. Electrochem. Soc.* **1969**, *116* (12), 1725. https://doi.org/10.1149/1.2411685.

(3) Dapkus, P. D.; Manasevit, H. M.; Hess, K. L.; Low, T. S.; Stillman, G. E. High Purity GaAs Prepared from Trimethylgallium and Arsine. *J. Cryst. Growth* **1981**, *55* (1), 10–23. https://doi.org/10.1016/0022-0248(81)90265-7.

(4) Manasevit, H. M. Recollections and Reflections of MO-CVD. *J. Cryst. Growth* **1981**, *55* (1), 1–9. https://doi.org/10.1016/0022-0248(81)90264-5.

(5) Pimputkar, S.; Speck, J. S.; DenBaars, S. P.; Nakamura, S. Prospects for LED Lighting. *Nat. Photonics* **2009**, *3* (4), 180–182. https://doi.org/10.1038/nphoton.2009.32.

(6) Irvine, S. J. C.; Capper, P. Introduction to Metalorganic Vapor Phase Epitaxy. In *Metalorganic Vapor Phase Epitaxy (MOVPE)*; Irvine, S., Capper, P., Eds.; Wiley, 2019; pp 1–18. https://doi.org/10.1002/9781119313021.ch1.

(7) Jensen, K. F.; Fotiadis, D. I.; Mountziaris, T. J. Detailed Models of the MOVPE Process. *J. Cryst. Growth* **1991**, *107* (1), 1–11. https://doi.org/10.1016/0022-0248(91)90428-8.

(8) DenBaars, S. P.; Maa, B. Y.; Dapkus, P. D.; Danner, A. D.; Lee, H. C. Homogeneous and Heterogeneous Thermal Decomposition Rates of Trimethylgallium and Arsine and Their Relevance to the Growth of GaAs by MOCVD. *J. Cryst. Growth* **1986**, *77* (1), 188–193. https://doi.org/10.1016/0022-0248(86)90300-3.

(9) Pelucchi, E.; Moret, N.; Dwir, B.; Oberli, D. Y.; Rudra, A.; Gogneau, N.; Kumar, A.; Kapon, E.; Levy, E.; Palevski, A. Sub-meV Photoluminescence Linewidth and >106cm2/Vs Electron Mobility in AlGaAs/GaAs Quantum Wells Grown by Metalorganic Vapor Phase Epitaxy on Slightly Misoriented Substrates. *J. Appl. Phys.* **2006**, *99* (9), 093515. https://doi.org/10.1063/1.2195370.

(10) Dimastrodonato, V.; Mereni, L. O.; Young, R. J.; Pelucchi, E. AlGaAs/GaAs/AlGaAs Quantum Wells as a Sensitive Tool for the MOVPE Reactor Environment. *J. Cryst. Growth* **2010**, *312* (21), 3057–3062. https://doi.org/10.1016/j.jcrysgro.2010.07.021.

(11) Rudra, A.; Pelucchi, E.; Oberli, D. Y.; Nicolas Moret; Dwir, B.; Kapon, E. Properties of GaAs/AlGaAs Quantum Wells Grown by MOVPE Using Vicinal GaAs Substrates. *J. Cryst. Growth* **2004**, *272* (1–4), 615–620. https://doi.org/10.1016/j.jcrysgro.2004.09.047.

(12) Kim, J.; Cho, S.; Sanz-Hervás, A.; Majerfeld, A.; Kim, B. W. MOVPE Growth of Highly-Strained Piezoelectric InGaAs/GaAs Quantum Wells on [111]A-Oriented Substrates. *J. Cryst. Growth* **2001**, *225* (2–4), 415–419. https://doi.org/10.1016/S0022-0248(01)00903-4.

(13) Mayo, E.; Dickey, S. A.; Majerfeld, A.; Sanz-Hervás, A.; Kim, B. W. High Quality GaAs/AlGaAs Quantum Wells Grown on (111)A Substrates by Metalorganic Vapor Phase Epitaxy. *Microelectron. J.* **1997**, *28* (8–10), 727–734. https://doi.org/10.1016/S0026-2692(96)00110-3.

(14) Dzurko, K. M.; Hummell, S. G.; Menu, E. P.; Dapkus, P. D. MOCVD Growth of AlGaAs/GaAs Structures on Nonplanar {111} Substrates: Evidence for Lateral Gas Phase Diffusion. *J. Electron. Mater.* **1990**, *19* (12), 1367–1372. https://doi.org/10.1007/BF02662826.

(15) Kapon, E.; Simhony, S.; Bhat, R.; Hwang, D. M. Single Quantum Wire Semiconductor Lasers. *Appl. Phys. Lett.* **1989**, *55* (26), 2715–2717. https://doi.org/10.1063/1.101934.

(16) Sugiyama, Y.; Sakuma, Y.; Muto, S.; Yokoyama, N. Novel InGaAs/GaAs Quantum Dot Structures Formed in Tetrahedral-shaped Recesses on (111)B GaAs Substrate Using Metalorganic Vapor Phase Epitaxy. *Appl. Phys. Lett.* **1995**, *67* (2), 256–258. https://doi.org/10.1063/1.114685.
(17) Juska, G. Pyramidal Quantum Dots: Single and Entangled Photon Sources and Correlation Studies. **2013**.
(18) Chung, T. H.; Juska, G.; Moroni, S. T.; Pescaglini, A.; Gocalinska, A.; Pelucchi, E. Selective Carrier Injection into Patterned Arrays of Pyramidal Quantum Dots for Entangled Photon Light-Emitting Diodes. *Nat. Photonics* **2016**, *10* (12), 782–787. https://doi.org/10.1038/nphoton.2016.203.
(19) Hartmann, A.; Loubies, L.; Reinhardt, F.; Kapon, E. Self-Limiting Growth of Quantum Dot Heterostructures on Nonplanar {111}B Substrates. *Appl. Phys. Lett.* **1997**, *71* (10), 1314–1316. https://doi.org/10.1063/1.119882.
(20) Gallo, P.; Felici, M.; Dwir, B.; Atlasov, K. A.; Karlsson, K. F.; Rudra, A.; Mohan, A.; Biasiol, G.; Sorba, L.; Kapon, E. Integration of Site-Controlled Pyramidal Quantum Dots and Photonic Crystal Membrane Cavities. *Appl. Phys. Lett.* **2008**, *92* (26), 263101. https://doi.org/10.1063/1.2952278.
(21) Dimastrodonato, V.; Pelucchi, E.; Vvedensky, D. D. Self-Limiting Evolution of Seeded Quantum Wires and Dots on Patterned Substrates. *Phys. Rev. Lett.* **2012**, *108* (25), 256102. https://doi.org/10.1103/PhysRevLett.108.256102.
(22) Mereni, L. O.; Dimastrodonato, V.; Young, R. J.; Pelucchi, E. A Site-Controlled Quantum Dot System Offering Both High Uniformity and Spectral Purity. *Appl. Phys. Lett.* **2009**, *94* (22), 223121. https://doi.org/10.1063/1.3147213.
(23) Dimastrodonato, V.; Mereni, L. O.; Young, R. J.; Pelucchi, E. Growth and Structural Characterization of Pyramidal Site-Controlled Quantum Dots with High Uniformity and Spectral Purity. *Phys. Status Solidi B* **2010**, *247* (8), 1862–1866. https://doi.org/10.1002/pssb.200983803.
(24) Plumhof, J. D.; Trotta, R.; Rastelli, A.; Schmidt, O. G. Experimental Methods of Post-Growth Tuning of the Excitonic Fine Structure Splitting in Semiconductor Quantum Dots. *Nanoscale Res. Lett.* **2012**, *7* (1), 336. https://doi.org/10.1186/1556-276X-7-336.
(25) Varo, S.; Li, X.; Juska, G.; Jahromi, I. R.; Gocalinska, A. M.; Falco, A. D.; Pelucchi, E. Planar Semiconductor Membranes with Brightness Enhanced Embedded Quantum Dots via Electron Beam Induced Deposition of 3D Nanostructures: Implications for Solid State Lighting. *ACS Appl. Nano Mater.* **2020**. https://doi.org/10.1021/acsanm.0c02969.
(26) Varo, S. Advanced Processing Strategies for Site-Controlled Pyramidal Quantum Dots. **2021**.
(27) Hartmann, A.; Ducommun, Y.; Leifer, K.; Kapon, E. Structure and Optical Properties of Semiconductor Quantum Nanostructures Self-Formed in Inverted Tetrahedral Pyramids. *J. Phys. Condens. Matter* **1999**, *11* (31), 5901. https://doi.org/10.1088/0953-8984/11/31/302.
(28) *Dry Etching Technology for Semiconductors | SpringerLink*. https://link.springer.com/book/10.1007/978-3-319-10295-5 (accessed 2025-01-08).
(29) Varo, S.; Juska, G.; Ranjbar, I.; Moroni, S. T.; Gocalinska, A.; Pelucchi, E. Engineering Site-Controlled Quantum Dots for Optical Quantum Information Processing. In *Low-Dimensional Materials and Devices 2019*; SPIE, 2019; Vol. 11085, p 1108507. https://doi.org/10.1117/12.2528830.
(30) Volatier, M.; Duchesne, D.; Morandotti, R.; Arès, R.; Aimez, V. Extremely High Aspect Ratio GaAs and GaAs/AlGaAs Nanowaveguides Fabricated Using Chlorine ICP Etching with N_2 -Promoted Passivation. *Nanotechnology* **2010**, *21* (13), 134014. https://doi.org/10.1088/0957-4484/21/13/134014.
(31) Wang, X.-Y.; Huang, C.-H.; Ohno, Y.; Igarashi, M.; Murayama, A.; Samukawa, S. Defect-Free Etching Process for GaAs/AlGaAs Hetero-Nanostructure Using Chlorine/Argon Mixed Neutral Beam. *J. Vac. Sci. Technol. B* **2010**, *28* (6), 1138–1142. https://doi.org/10.1116/1.3499716.
(32) Vigneron, P. B.; Joint, F.; Isac, N.; Colombelli, R.; Herth, E. Advanced and Reliable GaAs/AlGaAs ICP-DRIE Etching for Optoelectronic, Microelectronic and Microsystem Applications. *Microelectron. Eng.* **2018**, *202*, 42–50. https://doi.org/10.1016/j.mee.2018.09.001.
(33) Huber, T.; Predojević, A.; Khoshnegar, M.; Dalacu, D.; Poole, P. J.; Majedi, H.; Weihs, G. *Polarization Entangled Photons from Quantum Dots Embedded in Nanowires*. ACS Publications. https://doi.org/10.1021/nl503581d.

(34) Fons, R.; Osterkryger, A. D.; Stepanov, P.; Gautier, E.; Bleuse, J.; Gérard, J.-M.; Gregersen, N.; Claudon, J. All-Optical Mapping of the Position of Quantum Dots Embedded in a Nanowire Antenna. *Nano Lett.* **2018**, *18* (10), 6434–6440. https://doi.org/10.1021/acs.nanolett.8b02826.
(35) Peniakov, G.; Buchinger, Q.; Helal, M.; Betzold, S.; Reum, Y.; Rota, M. B.; Ronco, G.; Beccaceci, M.; Krieger, T. M.; Silva, S. F. C. da; Rastelli, A.; Trotta, R.; Pfenning, A.; Höfling, S.; Huber-Loyola, T. Polarized and Unpolarized Emission from a Single Emitter in a Bullseye Resonator. *Laser Photonics Rev.* **2024**, *18* (4), 2300835. https://doi.org/10.1002/lpor.202300835.
(36) Colavecchi, L.; Juska, G.; Pelucchi, E. Optimizing Light Extraction from Non-Planar Site-Controlled Pyramidal Quantum Dot System: Comparative Modeling of Three Fabricable Geometries. *Mater. Quantum Technol.* **2025**. https://doi.org/10.1088/2633-4356/adb6ec.
(37) Ranjbar Jahromi, I.; Juska, G.; Varo, S.; Basso Basset, F.; Salusti, F.; Trotta, R.; Gocalinska, A.; Mattana, F.; Pelucchi, E. Optical Properties and Symmetry Optimization of Spectrally (Excitonically) Uniform Site-Controlled GaAs Pyramidal Quantum Dots. *Appl. Phys. Lett.* **2021**, *118* (7), 073103. https://doi.org/10.1063/5.0030296.
(38) Kamada, H.; Kutsuwa, T. Broadening of Single Quantum Dot Exciton Luminescence Spectra Due to Interaction with Randomly Fluctuating Environmental Charges. *Phys. Rev. B* **2008**, *78* (15), 155324. https://doi.org/10.1103/PhysRevB.78.155324.
(39) Abbarchi, M.; Troiani, F.; Mastrandrea, C.; Goldoni, G.; Kuroda, T.; Mano, T.; Sakoda, K.; Koguchi, N.; Sanguinetti, S.; Vinattieri, A.; Gurioli, M. Spectral Diffusion and Line Broadening in Single Self-Assembled GaAs/AlGaAs Quantum Dot Photoluminescence. *Appl. Phys. Lett.* **2008**, *93* (16), 162101. https://doi.org/10.1063/1.3003578.
(40) Tseng, W. J.; Gonzalez, M.; Dillemans, L.; Cheng, K.; Jiang, S. J.; Vereecken, P. M.; Borghs, G.; Lieten, R. R. Strain Relaxation in GaN Nanopillars. *Appl. Phys. Lett.* **2012**, *101* (25), 253102. https://doi.org/10.1063/1.4772481.

Chapter 3

3 Non-classical light emission from InGaAs QDs embedded in micropillars

In the final section of Chapter 2, we presented a systematic study aimed at understanding how the micro/nano pillar fabrication process and resulting geometry affect the emission properties of the QDs. This is contrasted with their optical behaviour in the as-grown, polished configuration, where the most evident feature is the low transmission efficiency.

In this chapter I present the results of a work my team has produced, where I collaborated by optimizing process and epitaxial structure of InGaAs QDs in GaAs barriers, which, similarly to the GaAs QDs in GaAs/AlAs SL, have been turned to micropillars. We demonstrated their single-photon and entangled-photon emission under two-photon excitation (TPE) and introduced an additional fabrication method that allowed to demonstrate an absolupte light extraction efficiency under pulsed excitation up to 12%.

3.1 Introduction

Up to this point, we have already discussed about the advantages a site-controlled QD technology can bring in terms of integration and scalability. On a downside note, generally this kind of quantum emitters struggle to achieve high photon extraction efficiency, which is a fundamental requirement. So far, extremely high extraction efficiency (30%) has been reached by site-controlled VLS QDs embedded in nanowires[1]; these devices are grown via a bottom-up method, for which each nanowire nucleates in a symmetrically circular dielectric aperture, and the QD is grows co-axially with the photonic nanowire waveguide. The alleged absence of any misplacement/asymmetry of the QD with respect to the centre of symmetry of the waveguide enhances the coupling

and minimizes polarization anisotropies (a concept we will encounter again in the sixth chapter).

Such advantages are the same that can be sought leveraging the micropillar structure we have introduced. The fabrication of pillars with bound individual PQDs aims at boosting extraction efficiency[2,3] and offers a promising route for photonic circuits integration. The fabricated micro- and nano-pillars mainly act as waveguides, directing emission into modes that travel along the vertical optical axis, thus improving light collection efficiency. A major benefit of our fabrication method is its self-aligning feature. By utilizing the system's inherent non-planarity, this process removes the need for extra photolithographic steps, greatly easing alignment requirements. Pillar structures such as wires and cylindrical Fabry-Pérot microcavities, effectively enhance light extraction while largely preserving QD emission properties like indistinguishability and single-photon purity[4–6]. However, most approaches lack site control, relying on randomly positioned structures, QD pre-selection, or chance alignment. Even state-of-the-art top-down methods face positioning inaccuracies[7], leading to polarization anisotropy[8], weaker light-matter interaction[9], and coupling to decoherence channels[10].

In contrast, this fabrication process ensures QDs are precisely aligned along the pillar's central axis. This approach, along with future optimizations, marks a significant step forward in site-controlled QD-based nanostructures for quantum information processing.

The fabrication process is identical to the one described in Chapter 2 and will not be repeated here.

3.2 Optical measurements

The $In_{0.25}Ga_{0.75}As$ QDs confined by GaAs barriers have been already demonstrated as highly reproducible emitters of polarization entangled photon pairs[11,12]. The fabricated pillar structures demonstrated highly promising results, with light collection efficiency

improving by at least two orders of magnitude. Total efficiency ranged from 0.5% to 5% at the objective. Figure 3.2-1a presents spectra acquired under non-resonant (635 nm) continuous-wave (CW) and pulsed (80 MHz) excitation. The data show a strong correlation between light collection and the numerical aperture (NA) of the objective, confirming the broad angular emission from the pillars. Notably, collection efficiency increased several-fold when using a high-NA (0.8) objective compared to an NA of 0.42.

To assess the practical applicability and rule out catastrophic processing damage, the biexciton state was initialized via two-photon excitation (TPE), despite the known challenges in this QD system. Rabi oscillations of the biexciton (XX) and exciton (X) states (Figure 3.2-1b) confirm the coherent nature of the excitation process. The exciton state exhibits higher intensity, a characteristic of these $In_{0.25}Ga_{0.75}As$ QDs, which always feature an anti-binding biexciton state[13]. Here, the laser was tuned to the TPE resonance, positioned above the exciton state, efficiently coupling to the asymmetric acoustic phonon distribution. Due to phonon interactions, even at the moderate excitation powers required for π pulses, the phonon-assisted exciton population (X_{ph}) becomes comparable to that from the biexciton-exciton recombination cascade (Figure 3.2-1b). The extent of exciton population via the phonon-dressed state depends on several factors, including sample temperature, QD dimensions, pulse duration and shape, and optimal pumping conditions, which may vary from sample to sample.

The unwanted photons generated through the phonon-assisted excitation pathway can be effectively filtered out during second-order correlation function measurements relating biexciton and exciton. In these measurements, the correlation events occurring around the first excitation pulse (±6.25 ns) are exclusively linked to the biexciton-exciton recombination cascade. The purity of the single-photon emission, as confirmed by the second order autocorrelation functions for the exciton and biexciton (0.046±0.037 and 0.032±0.025, respectively), indicates good single-photon emission triggered by the excitation pulse (Figure 3.2-1c). These photon pairs, originating from the recombination cascade, are well known to serve as a resource for polarization entanglement. However, one of the major challenges in using these photon pairs for practical applications is the

fine structure splitting (S) of the exciton level. This splitting typically causes the precession of the non-degenerate exciton spin state after the biexciton recombination, leading to a randomization of the overall two-photon polarization states[11,15,16].

The fine structure splitting issue in the pyramidal QD system is known to be largely mitigated by the intrinsically high rotational symmetry[14]. Although other factors, such as QD or confinement barrier alloy disorder, may introduce deviations from this ideal model, several highly symmetric pyramidal QD designs, and fabrication strategies were developed[11,15]. The thin (0.9 nm) $In_{0.25}Ga_{0.75}As$ QDs presented here, with ground bound states near the confinement barrier energy, generally exhibit an average S of a few μeV (1.6±0.8 μeV for this sample). The representative QD shown in Figure 3.2-1 has S=1.3±0.4 μeV extracted from the two-photon polarization state phase oscillation observed in diagonal and circular polarization bases. By measuring the full set of linear, diagonal, and circular polarization bases for the two-photon (biexciton-exciton) intensity correlations (Figure 3.2-1d), we calculated the fidelity to the expected maximally entangled state $\sqrt{}0.5(|HH\rangle + |VV\rangle)$ to be 0.59±0.01. This value significantly exceeds the 0.5 limit for a statistical mixture of $|HH\rangle$ and $|VV\rangle$ (which corresponds to classical light), confirming polarization entanglement.

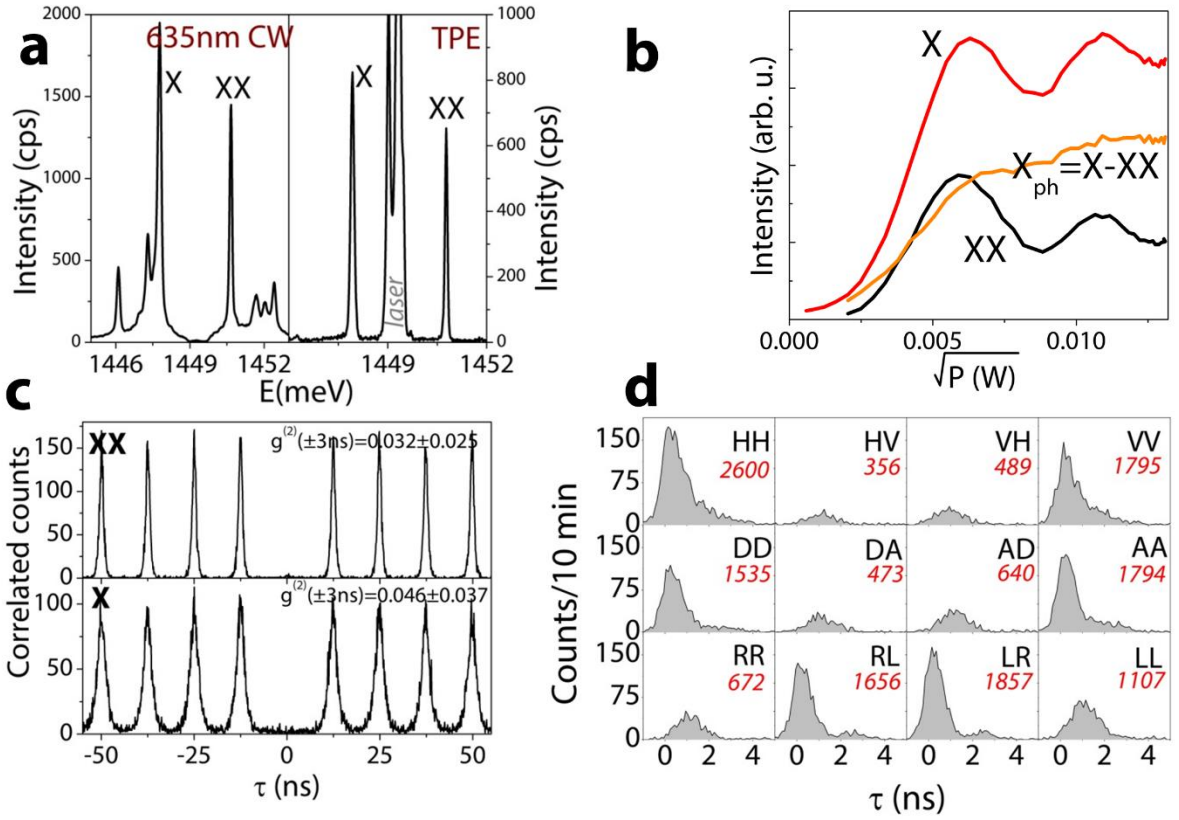

Figure 3.2-1. Non-classical light emission. (a) Comparison of the QD spectra under the non-resonant CW excitation and resonant two-photon excitation of the biexciton state. (b) The coherent nature of the biexciton state population is attested by Rabi oscillations as a function of the excitation power (laser pulse area). Xph represents the difference between the total measured intensity of exciton and biexciton transitions, corresponding to the exciton intensity component from phonon-assisted excitation. (c) Pure single photon emission of the biexciton and exciton transitions. (d) Polarization-resolved cross-correlation curves measured in linear, diagonal and circular bases sufficient to measure the fidelity to the expected maximally entangled Bell's state. The integrated counts (the two-photon projection intensity) during the 10 minutes integration time are given below the projection labels.

Several factors contribute to the degradation of entanglement. First, the two-photon $|HH\rangle$ and $|VV\rangle$ intensities deviate from the ideal source, resembling the state $\sqrt{0.59}|HH\rangle + \sqrt{0.41}|VV\rangle$ due to a partially induced polarization, observed as linear polarization anisotropy from the top view. The degree of linear polarization (D) was measured to be 0.18, where $D = (I_H - I_V)/(I_H + I_V)$, with I_H and I_V representing the biexciton transition intensities of the horizontally and vertically polarized components,

respectively. Although it might be tempting to attribute the origin of this anisotropy solely to structural asymmetries in the fabricated pillars, such a conclusion cannot be made definitively. The origin of the anisotropy is likely more complex and could result from multiple contributing factors. While D does increase statistically after fabrication (samples were measured before and after processing), it was already observed as non-zero in as-grown QDs, possibly also due to some heavy-light hole mixing or other yet unclear effects.

Figure 3.2-2 shows linear polarization analysis of the exciton (X) and biexciton (XX) transitions from multiple pillars. Non-zero degree of linear polarization (D) was common to all measured structures (Figure 3.2-2b). At this stage of the research, it was impossible to identify whether the polarization anisotropy was inherited from the as-grown QD, or was introduced during the processing. Due to lack of a systematic QD tracking/mapping system, we could not measure precisely the D change after the dry etching procedure, though an overall higher statistically observed D value suggests the contribution from the fabrication process. To understand if the polarization anisotropy is related to the threefold rotational symmetry of pillars, the distribution of linear polarization axes angles was measured (Figure 3.2-2a shows H linearly polarized component orientation angle). Lack of clear bunching around the values associated with the triangular geometry (for example, QD elongation/asymmetry along one of the three equilateral axis) suggests another reason. These could be subtle geometry asymmetries of the pillar, however, photoluminescence data from individual pillars must be related to their structural analysis by electron microscopy. As compared with this material system in a pillar configuration, the GaAs QDs in SL showed a more pronounced clustering of the exciton polarization anisotropy around two values ≈120° distant from each other.

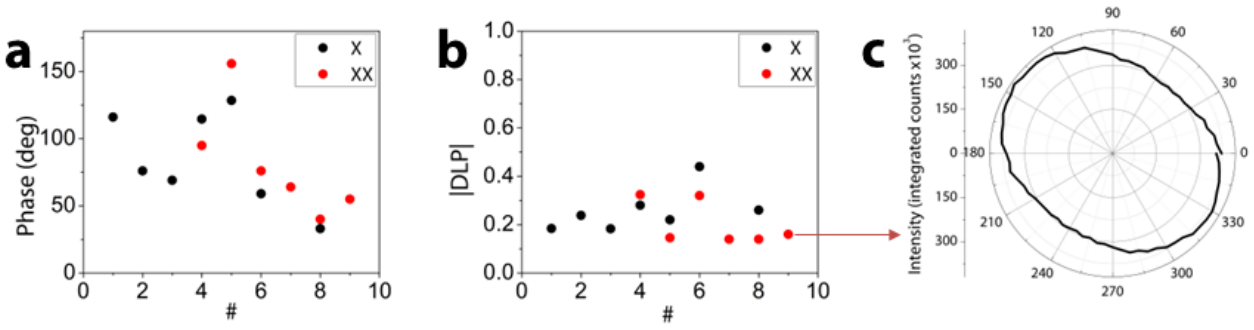

Figure 3.2-2: (a) Polarization anisotropy axis angle taken at the maximum of IH. (b) Degree of linear polarization for the exciton and biexciton transitions. (c) A representative QD with D_{XX}=0.18.

Further degradation of entanglement is obviously also related to the presence of the nonnegligible fine-structure splitting, exciton spin-scattering, and cross-dephasing events.

3.3 Brightness optimization

A potential route for brightness optimization was demonstrated by introducing additional dielectric layers covering the fabricated pillars. For example, three layers of $SiN_X/SiO_2/SiN_X$ (with approximate thickness of 50 nm, 500 nm, and 300 nm, respectively) were deposited by plasma enhanced chemical vapour deposition (PECVD) (see Figure 3.3-1a). The initial motivation for adding the dielectric layer was twofold: first, to mimic a controlled increment in the lateral dimensions of the pillar therefore modifying the optical modes supported by the pillar, and second, to create a rounded (convex) structure on the top of the pillars to induce a lensing effect for the fraction of light emitted upward. Simulations indicate that the dielectric layers alter the optimal emission geometry of the pillar, specifically in terms of the distance between the QD and the top non-planar surface. Simultaneously, the simulations show that a rounded top, modelled as depicted in the inset of Figure 3.3-2b, provides more collimated far-field emission compared to a regular pillar, particularly when the QD is positioned at the optimal distance from the top, see Figure 3.3-1d.

After the deposition of the first two dielectric layers, a significant red-shift of the average emission energy of QDs by approximately 15 meV was observed at cryogenic temperatures. This shift was likely due to the strain induced by the different thermal expansion coefficients of the materials encapsulating the pillars with respect to the GaAs one. To mitigate this effect, we chose to add a third, thick layer of SiN_X to the structure because the thermal expansion coefficient of this SiN_X is higher (3.27x10^-6/K[16]) than SiO_2 (0.3-0.5x10^-6/K[17]) and closer to that of GaAs (~6x10^-6/K[18]) . This addition resulted in a blue-shift in the average emission energy, partially restoring the QDs original emission energy. The dielectric coating significantly enhanced light extraction across the entire sample. Figure 3.3-2c shows a representative spectrum of a QD obtained by scanning the transmission wavelength of a monochromator and detecting the photoluminescence signal with an avalanche photodiode (APD) at the single-photon level. The measured single-photon emission intensities of a negatively charged trion (X^-, 450 kcps) and a neutral exciton (X, 50 kcps) correspond to a light extraction efficiency of ~9.5% after passing through the collection objective, which has a numerical aperture (NA) of 0.42. Multiple QDs with similar light extraction values were found, with a peak value of 12%. Further investigation is needed to determine the individual contributions of the modification of the guided modes of the pillar and the lensing effect to the brightness enhancement observed in the coated pillars.

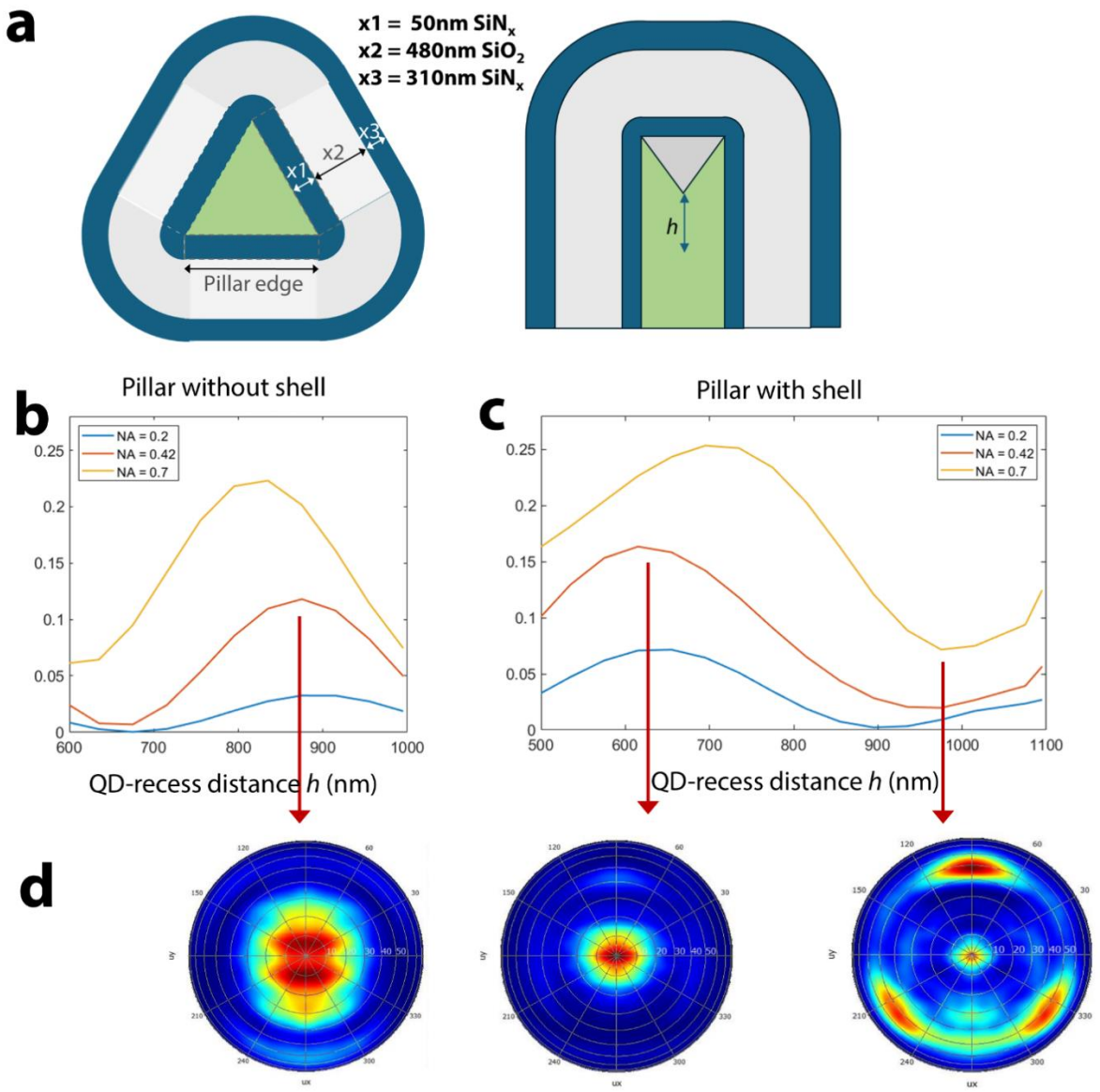

Figure 3.3-1 illustrates the effect of pillar coating with a $SiN_X/SiO_2/SiN_X$ stack, with thicknesses of 50 nm, 480 nm, and 310 nm, respectively (a). The GaAs pillar width is set to be 500nm. To investigate the impact on transmitted power, the QD vertical position h relative to the bottom of the recess was varied, and the resulting transmission was analysed for numerical apertures (NA) of 0.2, 0.45, and 0.7. Comparison of power transmission from pillars (b) without and (c) with dielectric coating as a function of the QD distance from the recess. Transmission curves are presented for three numerical aperture (NA) values: 0.2, 0.42, and 0.7. d) The corresponding far-field profiles at the indicated points are shown below.

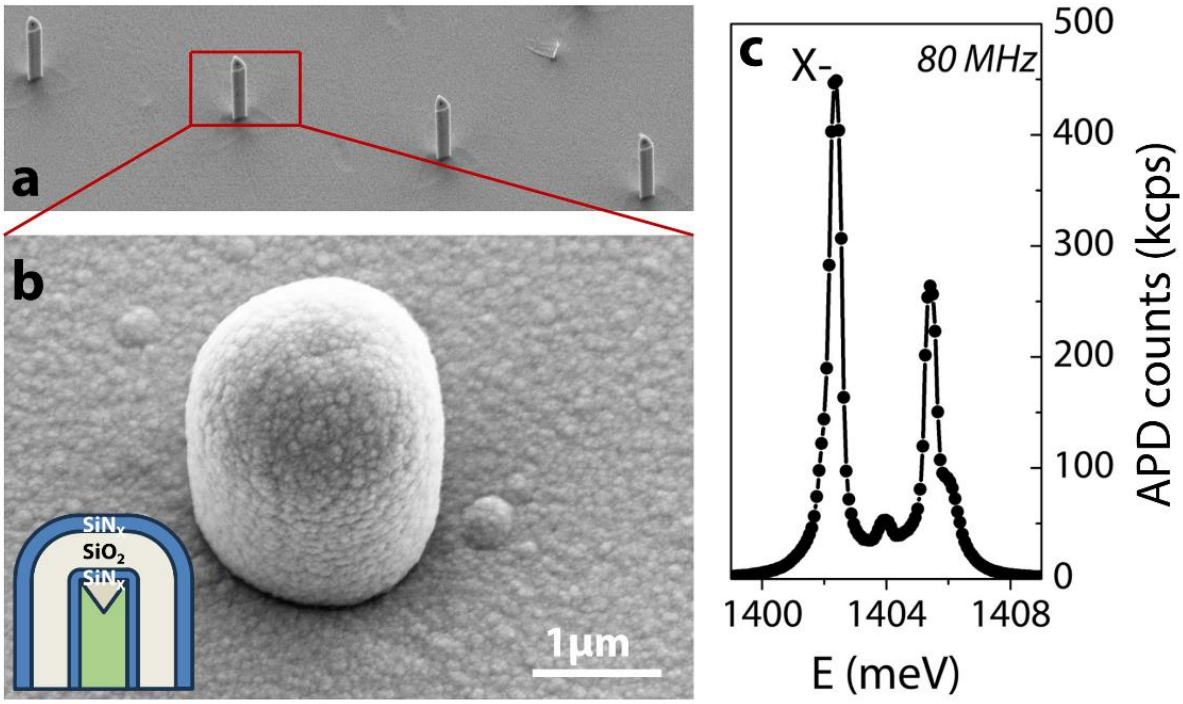

Figure 3.3-2: The SEM image of pillars before the coating by multiple dielectric layers, (b) and the formation of dome-like structures after the deposition. (c) The photoluminescence spectrum of a QD from the fabricated structures. The spectrum was obtained with a single photon detector and indicates light extraction efficiency of at least 9.5% in this representative case

3.4 Conclusions

Given their potential to dramatically enhance light extraction and simplify integration into photonic circuits, pillar-based structures warranted a dedicated chapter in this thesis. These architectures consistently outperform standard back-etched devices and may be key to unlocking the practical implementation of site-controlled quantum emitters

The key benefits of this method are: (1) deterministic control of the positions of pillars, (2) all pillars consistently containing highly accurately centred QD(s) (and potentially multiple stacked ones even if we discussed only the single QD case), and (3) achieving all of this without relying on additional lithography, registration and alignment marker steps. Moreover, both $In_xGa_{1-x}As$ QDs confined by GaAs barriers and (In)GaAs QDs

confined by $Al_xGa_{1-x}As$ barriers can be embedded to exploit the main advantages of the pyramidal QD system. These advantages include high rotational symmetry for efficient polarization-entangled photon emission and engineering flexibility to design highly reproducible single and coupled QD structures. The results presented here from $In_{0.25}Ga_{0.75}As$ QDs are first demonstrators of these capabilities and their potential.

Nevertheless, to advance towards practical applications, several optimizations and developments are necessary. The demonstrated prototype, which utilizes a dielectric coating atop the pillar to enhance the lensing effect, represents one potential optimization element part of a more overall complex picture. Another key improvement would be reducing the lateral dimensions of the pillars to limit light coupling primarily to the fundamental mode. However, this approach presents challenges due to the increased proximity of surface defect states induced by processing, making the development of effective passivation techniques critical. Several approaches are available to address this issue[19]. Additionally, the present strategy can only collect photons emitted through the pillar in the upward direction. A back reflective element would need to be engineered to increase the collection efficiency above 50%. Furthermore, the reflector could, in principle, create a micro- or nano-resonator with resonant optical modes that exhibit Purcell enhancement[9]. Even without a designed back reflector, simulations indicate the presence of an optimal QD position along the vertical axis associated with higher emission intensity, as we'll show in Chapter 4. This increase in intensity is related to constructive interference within wavefronts of optical modes supported by the pillar, reflected by the top interface. Hence, a fraction of the light is reflected back into the pillar and simulations show a moderate Purcell enhancement. The latter can be further boosted by optimizing the interface for back reflection. Due to the non-planar top surface of the pillar, we expect far-field distortions that depend on the QD position along the axis. This distortion could potentially be mitigated by developing a planarization process, possibly in combination with modified etching techniques to fabricate tapered structures. Tapered pillars could potentially be detached and flipped to ensure an adiabatic

mode transition to a near-Gaussian beam profile[20], improving both light extraction and directionality. Once optimized, a highly attractive prospect is the physical manipulation of these pillars. In Figure 3.4-1, we demonstrate a preliminary procedure for transferring a pillar onto a pre-selected surface. This opens up possibilities for positioning the pillars in alignment with waveguides, fiber cores, and similar hybrid photonic platforms.

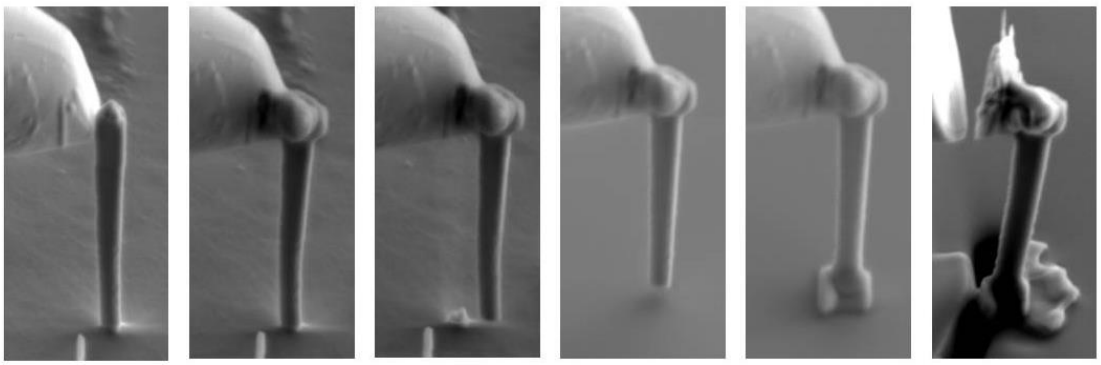

Figure 3.4-1: a Pillar transfer procedure: to probe further processing versatility, the nanopillar was transferred in a Tescan Solaris FIB-SEM. It was attached to an Omniprobe needle using e-beam deposited SiO_2. No FIB deposition was used to avoid Ga ion implantation. The nanopillar was then sheared off at the base by pushing the Omniprobe needle against the pillar. Then the base of the pillar was secured to the optical fiber by another e-beam deposited SiO_2. Finally, the tip of the Omniprobe needle was cut off using the ion beam, so the nanopillar is standing free again.

References

(1) Laferrière, P.; Yeung, E.; Miron, I.; Northeast, D. B.; Haffouz, S.; Lapointe, J.; Korkusinski, M.; Poole, P. J.; Williams, R. L.; Dalacu, D. Unity Yield of Deterministically Positioned Quantum Dot Single Photon Sources. *Sci. Rep.* **2022**, *12* (1), 6376. https://doi.org/10.1038/s41598-022-10451-1.

(2) Hartmann, A.; Ducommun, Y.; Leifer, K.; Kapon, E. Structure and Optical Properties of Semiconductor Quantum Nanostructures Self-Formed in Inverted Tetrahedral Pyramids. *J. Phys. Condens. Matter* **1999**, *11* (31), 5901–5915. https://doi.org/10.1088/0953-8984/11/31/302.

(3) Chung, T. H.; Juska, G.; Moroni, S. T.; Pescaglini, A.; Gocalinska, A.; Pelucchi, E. Selective Carrier Injection into Patterned Arrays of Pyramidal Quantum Dots for Entangled Photon Light-Emitting Diodes. *Nat. Photonics* **2016**, *10* (12), 782–787. https://doi.org/10.1038/nphoton.2016.203.

(4) Mäntynen, H.; Anttu, N.; Sun, Z.; Lipsanen, H. Single-Photon Sources with Quantum Dots in III–V Nanowires. *Nanophotonics* **2019**, *8* (5), 747–769. https://doi.org/10.1515/nanoph-2019-0007.

(5) Rodt, S.; Reitzenstein, S.; Heindel, T. Deterministically Fabricated Solid-State Quantum-Light Sources. *J. Phys. Condens. Matter* **2020**, *32* (15), 153003. https://doi.org/10.1088/1361-648X/ab5e15.

(6) Yeo, I.; De Assis, P.-L.; Gloppe, A.; Dupont-Ferrier, E.; Verlot, P.; Malik, N. S.; Dupuy, E.; Claudon, J.; Gérard, J.-M.; Auffèves, A.; Nogues, G.; Seidelin, S.; Poizat, J.-Ph.; Arcizet, O.; Richard, M. Strain-

Mediated Coupling in a Quantum Dot–Mechanical Oscillator Hybrid System. *Nat. Nanotechnol.* **2014**, *9* (2), 106–110. https://doi.org/10.1038/nnano.2013.274.

(7) Madigawa, A. A.; Donges, J. N.; Gaál, B.; Li, S.; Jacobsen, M. A.; Liu, H.; Dai, D.; Su, X.; Shang, X.; Ni, H.; Schall, J.; Rodt, S.; Niu, Z.; Gregersen, N.; Reitzenstein, S.; Munkhbat, B. Assessing the Alignment Accuracy of State-of-the-Art Deterministic Fabrication Methods for Single Quantum Dot Devices. *ACS Photonics* **2024**, *11* (3), 1012–1023. https://doi.org/10.1021/acsphotonics.3c01368.

(8) Peniakov, G.; Buchinger, Q.; Helal, M.; Betzold, S.; Reum, Y.; Rota, M. B.; Ronco, G.; Beccaceci, M.; Krieger, T. M.; Da Silva, S. F. C.; Rastelli, A.; Trotta, R.; Pfenning, A.; Höfling, S.; Huber-Loyola, T. Polarized and Unpolarized Emission from a Single Emitter in a Bullseye Resonator. *Laser Photonics Rev.* **2024**, *18* (4), 2300835. https://doi.org/10.1002/lpor.202300835.

(9) Bleuse, J.; Claudon, J.; Creasey, M.; Malik, Nitin. S.; Gérard, J.-M.; Maksymov, I.; Hugonin, J.-P.; Lalanne, P. Inhibition, Enhancement, and Control of Spontaneous Emission in Photonic Nanowires. *Phys. Rev. Lett.* **2011**, *106* (10), 103601. https://doi.org/10.1103/PhysRevLett.106.103601.

(10) Fons, R.; Osterkryger, A. D.; Stepanov, P.; Gautier, E.; Bleuse, J.; Gérard, J.-M.; Gregersen, N.; Claudon, J. All-Optical Mapping of the Position of Quantum Dots Embedded in a Nanowire Antenna. *Nano Lett.* **2018**, *18* (10), 6434–6440. https://doi.org/10.1021/acs.nanolett.8b02826.

(11) Juska, G.; Murray, E.; Dimastrodonato, V.; Chung, T. H.; Moroni, S. T.; Gocalinska, A.; Pelucchi, E. Conditions for Entangled Photon Emission from (111)B Site-Controlled Pyramidal Quantum Dots. *J. Appl. Phys.* **2015**, *117* (13), 134302. https://doi.org/10.1063/1.4916705.

(12) Juska, G.; Dimastrodonato, V.; Mereni, L. O.; Gocalinska, A.; Pelucchi, E. Towards Quantum-Dot Arrays of Entangled Photon Emitters. *Nat. Photonics* **2013**, *7* (7), 527–531. https://doi.org/10.1038/nphoton.2013.128.

(13) Juska, G.; Ranjbar Jahromi, I.; Mattana, F.; Varo, S.; Dimastrodonato, V.; Pelucchi, E. Biexciton Initialization by Two-Photon Excitation in Site-Controlled Quantum Dots: The Complexity of the Antibinding State Case. *Appl. Phys. Lett.* **2020**, *117* (13), 134001. https://doi.org/10.1063/5.0011383.

(14) Karlsson, K. F.; Oberli, D. Y.; Dupertuis, M. A.; Troncale, V.; Byszewski, M.; Pelucchi, E.; Rudra, A.; Holtz, P. O.; Kapon, E. Spectral Signatures of High-Symmetry Quantum Dots and Effects of Symmetry Breaking. *New J. Phys.* **2015**, *17* (10), 103017. https://doi.org/10.1088/1367-2630/17/10/103017.

(15) Ranjbar Jahromi, I.; Juska, G.; Varo, S.; Basso Basset, F.; Salusti, F.; Trotta, R.; Gocalinska, A.; Mattana, F.; Pelucchi, E. Optical Properties and Symmetry Optimization of Spectrally (Excitonically) Uniform Site-Controlled GaAs Pyramidal Quantum Dots. *Appl. Phys. Lett.* **2021**, *118* (7), 073103. https://doi.org/10.1063/5.0030296.

(16) Tien, C.-L.; Lin, T.-W. Thermal Expansion Coefficient and Thermomechanical Properties of SiN_x Thin Films Prepared by Plasma-Enhanced Chemical Vapor Deposition. *Appl. Opt.* **2012**, *51* (30), 7229. https://doi.org/10.1364/AO.51.007229.

(17) Wang, C.; Yang, H.; Chen, F.; Peng, L.; Gao, H.; Zhao, L. Influences of VTMS/SiO2 Ratios on the Contact Angle and Morphology of Modified Super-Hydrophobic Silicon Dioxide Material by Vinyl Trimethoxy Silane. *Results Phys.* **2018**, *10*, 891–902. https://doi.org/10.1016/j.rinp.2018.08.007.

(18) Glazov, V. M.; Pashinkin, A. S. Thermal Expansion and Heat Capacity of GaAs and InAs. *Inorg. Mater.* **2000**, *36* (3), 225–231. https://doi.org/10.1007/BF02757926.

(19) Jacob, B.; Camarneiro, F.; Borme, J.; Bondarchuk, O.; Nieder, J. B.; Romeira, B. Surface Passivation of III–V GaAs Nanopillars by Low-Frequency Plasma Deposition of Silicon Nitride for Active Nanophotonic Devices. *ACS Appl. Electron. Mater.* **2022**, *4* (7), 3399–3410. https://doi.org/10.1021/acsaelm.2c00195.

(20) Friedler, I.; Sauvan, C.; Hugonin, J. P.; Lalanne, P.; Claudon, J.; Gérard, J. M. Solid-State Single Photon Sources: The Nanowire Antenna. *Opt. Express* **2009**, *17* (4), 2095. https://doi.org/10.1364/OE.17.002095.

Chapter 4

4 Optimizing Light Extraction from Non-Planar Site-Controlled Pyramidal Quantum Dot System

This chapter is based on the published journal article "*Optimizing Light Extraction from Non-Planar Site-Controlled Pyramidal Quantum Dot System: Comparative Modeling of Three Fabricable Geometries"*[1] and explores the three different fabrication methods to improve light extraction efficiency of site-controlled pyramidal GaAs quantum dot system, presented in Chapter 2. In the theoretically analyzed structures (mimicking the as-obtained experimentally), we focus on the effects of geometry on light emission intensity, far-field profiles, and Purcell enhancement. The three methods include a back-etched approach, which exposes the pyramid's apex, a pillar fabrication process, and a "mirrored" pyramid technique. Simulation results suggest that all three techniques have the potential to improve light extraction from as grown structures, with the pillar method offering the highest extraction efficiency (43% for a numerical aperture of 0.999) and the back-etched configuration exhibiting a strong Purcell enhancement effect. The mirrored pyramid method is also of interest, as it provides a promising alternative to the back-etched approach, potentially simplifying the integration of electrical contacts for tuning quantum dot properties. Ultimately, we emphasize the importance of precise control over the fabrication process to optimize the performance of this quantum dot system for future applications in quantum information processing.

4.1 Introduction

High light extraction efficiency from III-V group semiconductor quantum dots (QDs) is essential for large-scale photonic quantum information processing platforms, where QDs serve as photonic qubit sources and spin-photon interfaces. However, the light extraction efficiency from an as-grown slab of semiconductor material with embedded QDs is typically less than one percent[2] due to broad angular emission and internal

reflections. A common strategy to enhance this efficiency is to restrict the number of QD emission optical modes in space by placing QDs in tailored nano-/micro-resonators or pillar-like structures. Also due to Purcell enhancement, QDs benefit from the decreased lifetime of excitonic complexes, and thus increased photon indistinguishability and operation speed.

The most prominent state-of-the-art sources are based on epitaxial QDs that randomly nucleate on a planar substrate: this planar geometry is convenient for integrating crucial functional layers, such as Bragg mirrors for optical cavities or sacrificial etching layers for membrane fabrication[3–5]. However, photonic circuits and devices are typically processed based on random positions of preselected QDs, which limits site-control capability, a critical factor for very large-scale systems.

Here, we concentrate on a pyramidal QD system[6,7] which is attractive due to its site-control option, and which is known for highly symmetric QDs emitting polarization-entangled photon pairs[8]. This system is named after the tetrahedral recesses with equilateral faces, which act as QD formation sites etched in a (111)B oriented GaAs substrate. The edge size of the recess is pre-defined lithographically during the substrate preparation, and, depending on the targeted application, is in the range of 5 to 10 µm in our developed samples. Structurally uniform GaAs[9] or $In_xGa_{1-x}As$ single and multiple stacked QDs[10] are fabricated at each site. While precise position control is achieved through a self-aligning QD formation process, the brightness of these as-fabricated sources is very low, ranging from a full suppression to a maximum of a few hundred counts per second on a charge-coupled device.

Unfortunately, conventional approaches to fabricating optical cavities are limited by the non-planarity of the system. Although the roadmap to fabricate 2D L_n photonic crystal membrane cavities has been demonstrated, significant improvements in source intensity and emission purity have yet to be realized[11,12].

To address this issue, we study three experimentally feasible approaches to enhance light extraction from the non-planar pyramidal QD system. In a comparative study, we

analyze light emission intensity, far-field profiles, and Purcell enhancement from three geometries: exposed apex-up pyramids, pillars, and mirrored pyramids with adjustable aspect ratios.

4.2 Simulations

In this section, we report and analyze the extraction efficiency values and far-field profiles (where relevant) for each configuration described. Simulations and optimizations were performed using the Ansys Lumerical FDTD software. The acronym FDTD stands for Finite Difference Time Domain and is a method for solving Maxwell's equation in the domain of time. The equations are numerically evaluated in time at the points of a discrete grid defined in a portion of space called simulation region. An FDTD solver is the most accurate and versatile mean in calculating electric and magnetic field propagation as it doesn't make any assumptions over the examined system. Moreover, the time dependency of the simulated result allows to carry out wide wavelength range analysis with only one run.

The simulation output – raw transmission – directly related to the extraction efficiency as described below, at each wavelength is defined as the ratio of the power collected by a monitor placed above the source to the power emitted by the source (modelled as a linear dipole) in a homogeneous medium. With this definition, the obtained raw transmitted power value can exceed the value of one as a result of the Purcell enhancement of the source[13]. As the Purcell factor is defined as the ratio of the power emitted by the source in the designed medium to that emitted in a homogeneous (bulk) medium, the obtained raw transmission data presented in the main text is normalized by the corresponding Purcell factor to get the actual power emitted by the dipole.

Under the simulation conditions employed, the square transmission monitor had dimensions ranging from 4–8 μm and was positioned 100 nm above the topmost surface of the simulated structures. In this configuration, light collection by the transmission monitor corresponds to that of an optical system with a numerical aperture (NA) of 0.999.

While such an optical system is hypothetical – typical free-space systems operate around NA = 0.8, and fiber optics around NA = 0.13 – the primary focus of this study is to investigate the influence of varying geometries on the overall emitted power and, to some extent, far-field profiles. The efficiency of light collection by specific optical systems lies beyond the main scope of this work and is only discussed for a few specific relevant cases. Therefore, unless stated otherwise, the transmission parameter presented here represents emission into a numerical aperture of 0.999. Where applicable, we report on the Purcell factor to assess any resonant behavior of the configuration.

Far-field projections are obtained via Fourier decomposition of the collected field data at the monitor into a set of plane waves propagating at different angles. This analysis helps determine how closely the QD emission resembles a Gaussian profile, which is advantageous for integrated photonics applications.

Unless otherwise specified, the simulated typical epitaxial structure, in all cases, is composed of GaAs, high Al concentration $Al_{0.65}Ga_{0.35}As$ and AlAs. Figure 4.2-1 shows the epitaxial structures for each configuration along with their thickness value along the vertical axis. GaAs QDs were selected for their strain-free nature, which promises longer spin coherence times[14], and for their experimentally observed superior optical properties compared to InGaAs QDs when used as spin-photon interfaces. Achieving multiphoton entanglement using these interfaces necessitates efficient photon extraction.

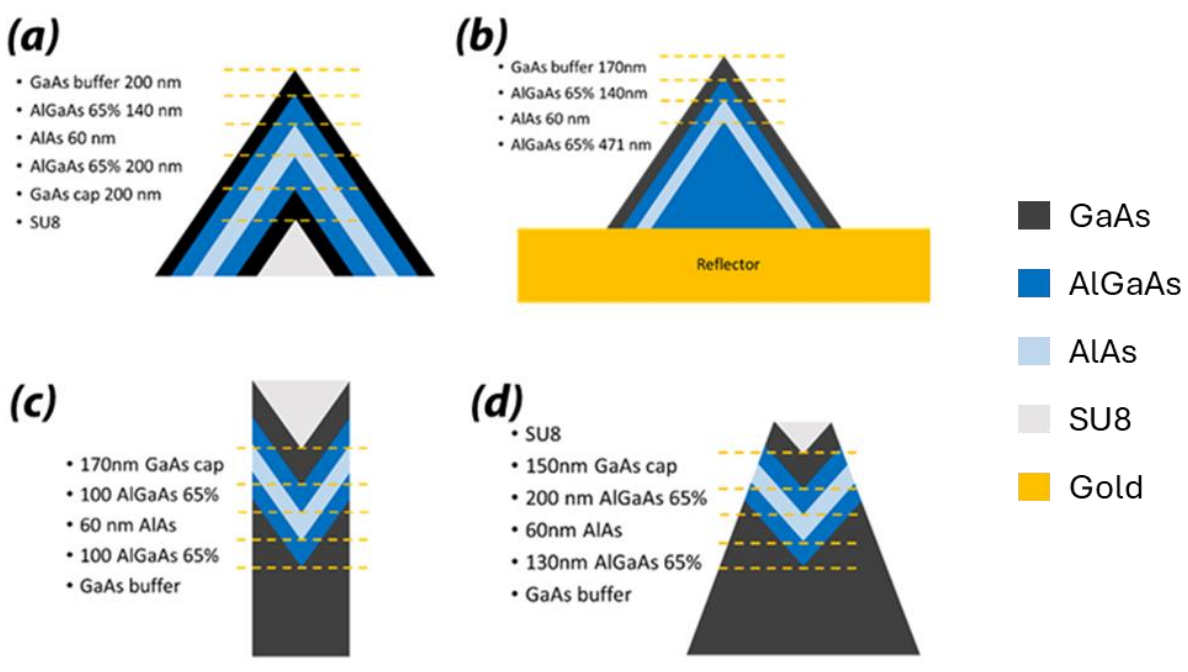

Figure 4.2-1: Epitaxial structures. a) Back-etched pyramid. b) Back-etched pyramid with a gold reflector under the base. c) Pillar (the recess is filled with SiO2). d) Mirrored pyramid

The linear dipole, simulating recombining excitons, is positioned horizontally (in-plane of the original substrate and orthogonal to the z or optical axis) in the middle of the AlAs barriers. For simplicity, a complex ensemble of nanostructures, such as the QD itself and the vertical quantum wire, formed during the actual epitaxial growth of pyramidal QDs[7] was omitted from the simulation design to avoid overcomplicating the analysis. Consequently, the segregation effects inside the structure were disregarded, and a uniform AlGaAs alloy composition was assumed. In Lumerical, material differences are represented by the refractive index, which is set at 3.6 for GaAs, 3.2 for $Al_{0.65}Ga_{0.35}As$, and 3 for AlAs[15]. SU8 and SiO_2 layers involved in the design are modelled with refractive indices of 1.6[16] and 1.4[17], respectively. Values are considered constant over the simulated wavelength range to reduce computational complexity and simplify the interpretation of the results.

In each case, a monitor placed 0.1 μm above the simulated structure collects the emitted power. This setup allows for reasonably long simulations and highly accurate

far-field decompositions due to the wide collection angle resulting from the closely positioned monitor.

Near-field effects are not considered, as the decomposition into plane waves only includes wavelengths set for the source, excluding rapidly varying components. All simulations were designed to model realistic GaAs QD structures, which typically emit in the range of 760-780 nm.

Back-etched. In this configuration, the pyramid is placed in the apex-up orientation and the source positioned 380 nm below the tip. As discussed below, while the QD position within the pyramid is a sensitive parameter influencing light extraction efficiency, the specific focus of this study is to understand the effect of the pyramid tip exposure. On the other hand, the chosen QD position is already near one of the optimal points as discussed later in the text. To simulate the varying conditions caused by the wet back-etching procedure, the surrounding GaAs substrate is initially set at the same level as the pyramid tip and then lowered in increments of 0.22 μm over 10 steps (inset in Figure 4.2-3-a). Since this is the conventional process for preparing and measuring these QDs, the simulation serves as a benchmark for comparison with other configurations in this study. The epitaxial structure of the pyramid consists of GaAs, $Al_{0.65}Ga_{0.35}As$ and AlAs layers, with the recess filled with SU8 photoresist for bonding purposes.

Light extraction from a fully covered pyramid in GaAs, equivalent to a QD in a semiconductor slab, is 1.7%, with a moderate Purcell enhancement of 1.12 induced by the interference effect at the flat surface. In good agreement, a similar value was obtained from the as-grown (apex-down) structure, as shown in Figure 4.2-2. Figure 4.2-2-a shows the refractive index cross-section of the constituent materials, providing a visual representation of the studied structure. Figure 4.2-2-b reports the measured transmission, yielding a value of 1.6–1.7%, consistent with typical values for QDs embedded in a slab.

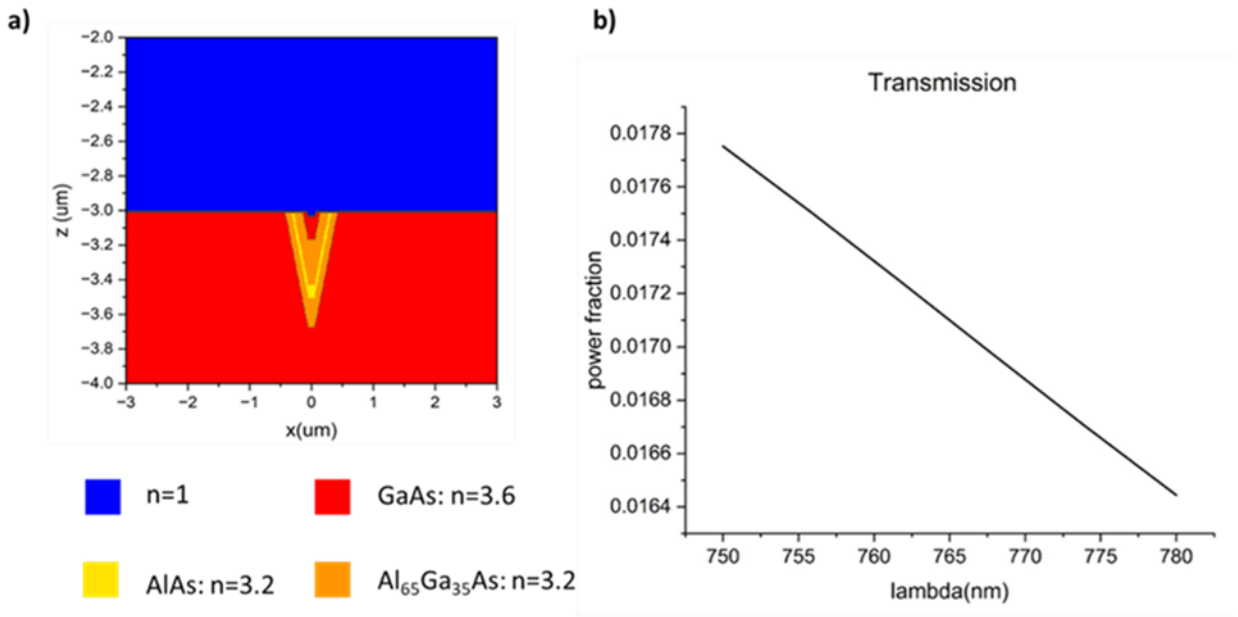

Figure 4.2-2: Results of the transmission study conducted on the as-grown sample geometry, which was polished to minimize recess. Fig.-a) displays the refractive index cross-section profile of the constituent materials, visually representing the studied geometry. Fig-*b) illustrates the measured transmission, with an obtained value of 1.6–1.7%, which is typical for QDs embedded in a slab. This configuration is valuable as it allows for an assessment of the growth quality with minimal processing effort.*

Transmission increases significantly once the tip of the pyramid starts to be exposed, even when the QD remains below the substrate. The exposed tip of the pyramid acts as a lens-like element guiding the light out of the substrate. Similar effect has been observed in previous studies on as-grown pyramidal QDs, were various dielectric and metal structures were fabricated atop of QD sites using electron beam induced deposition[18]. Once the substrate is lowered below the QD level, no further substantial changes in transmission are observed.

The maximum transmission of 8% is achieved when the substrate is lowered below the QD level (Figure 4.2-3-a and -b). The far-field profiles at 5 intermediate pyramid's exposure steps are shown to the right of Figure 4.2-3-b). These profiles are symmetric, centered, resembling a Gaussian distribution.

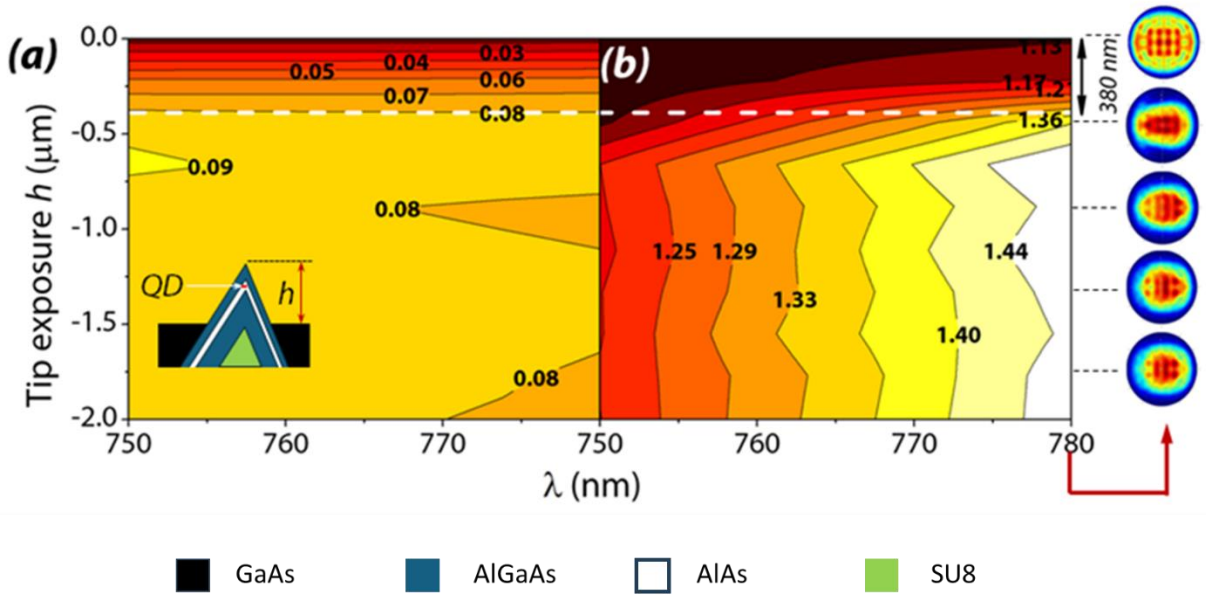

Figure 4.2-3: Study of a standard configuration of a back-etched pyramid. a) Transmission contour map: This map displays the transmission detected by a monitor positioned 100 nm above the structure, plotted as a function of wavelength (λ) and tip exposure (h), with the latter indicated in the inset. b) Purcell factor: Shown within the same parameter space as the transmission map. A white striped line highlights the tip exposure distance of 380 nm, where the QD is located relative to the tip of the pyramidal structure. The far-field profiles at 780 nm and across 5 studied h values are displayed on the right.

Since further transmission is not significantly affected when the substrate is lowered below the QD level, it indicates that the structure and composition of the underlying material do not contribute significantly to the increased light extraction efficiency. To explore whether the underlying structure could be optimized for enhanced transmission upwards, we analyzed a modified version of the system. Specifically, we removed the high-refractive-index GaAs substrate entirely, replaced the SU8-filled recess with optically transparent $Al_{0.65}Ga_{0.35}As$, and introduced a gold reflector beneath the pyramid base (see also inset Figure 4.2-4-b). Such a structure is expected to perform as a resonator supporting a unique and possibly non-trivial set of cavity modes.

To optimize the QD position along the vertical axis of the pyramid - a parameter controlled during epitaxial growth - we varied the QD position across a broad range (200 to 1200 nm from the tip) and studied the light extraction properties in the 750–810 nm

wavelength range. In the initial phase, the gold reflector was excluded, and the base was designed in the simulation to eliminate any reflection contribution from this facet (Figure 4.2-4-a).

Clear modulations of the transmission property were observed on the monitor. These modulations are directly related to the Purcell factor modulations shown in Figure 4.2-4. Since the base was not contributing to the observed phenomenon, the origin of these modulations is the result of the interference influenced by the upper structure of the tetrahedral interface. Resonances observed as Purcell enhancement occur when constructive interference conditions are met at the dipole position. For a flat surface, this is valid when a dipole is placed in the antinode of a resonant mode to fulfill the condition $2d=(m+0.5)\lambda_{eff}$ where d is the dipole's distance from the surface, λ_{eff} is the effective wavelength, m=0,1,2,3,...[19]. However, due to non-planarity of the pyramid, these resonance conditions are altered, resulting in non-monotonic change of the oscillation amplitude. The strongest resonance, with a Purcell enhancement of 1.4, was found at around 680 nm, marking the optimal vertical position for the QD.

After optimizing the QD's position relative to the upper interface of the tetrahedron, in the simulation we introduced the gold reflector under the base. Building on our initial study of tip exposure dependence, we positioned the QD within the resonance band at approximately 380 nm, where the Purcell enhancement was 1.32. The optimal position of the gold reflector was determined by sweeping its position in the simulation. The highest Purcell enhancement was identified when it was set 461nm below the dipole.

Figure 4.2-4-b shows an optical resonance band with a full width at half maximum (FWHM) of 4.8 nm and a maximum Purcell factor of 8.4 at a QD position 380 nm from the tip. The light extraction efficiency, in this case, was found to be 37% (NA=0.999). By adjusting the QD position vertically within a ±30 nm range, we were able to shift the resonance over a 10 nm wavelength range. The maximum values of each band are symmetrically distributed around 780 nm and begin to decrease when the QD is shifted

beyond the optimal range. This reduction is likely due to the QD moving out of the optimal conditions determined in the first part of the study.

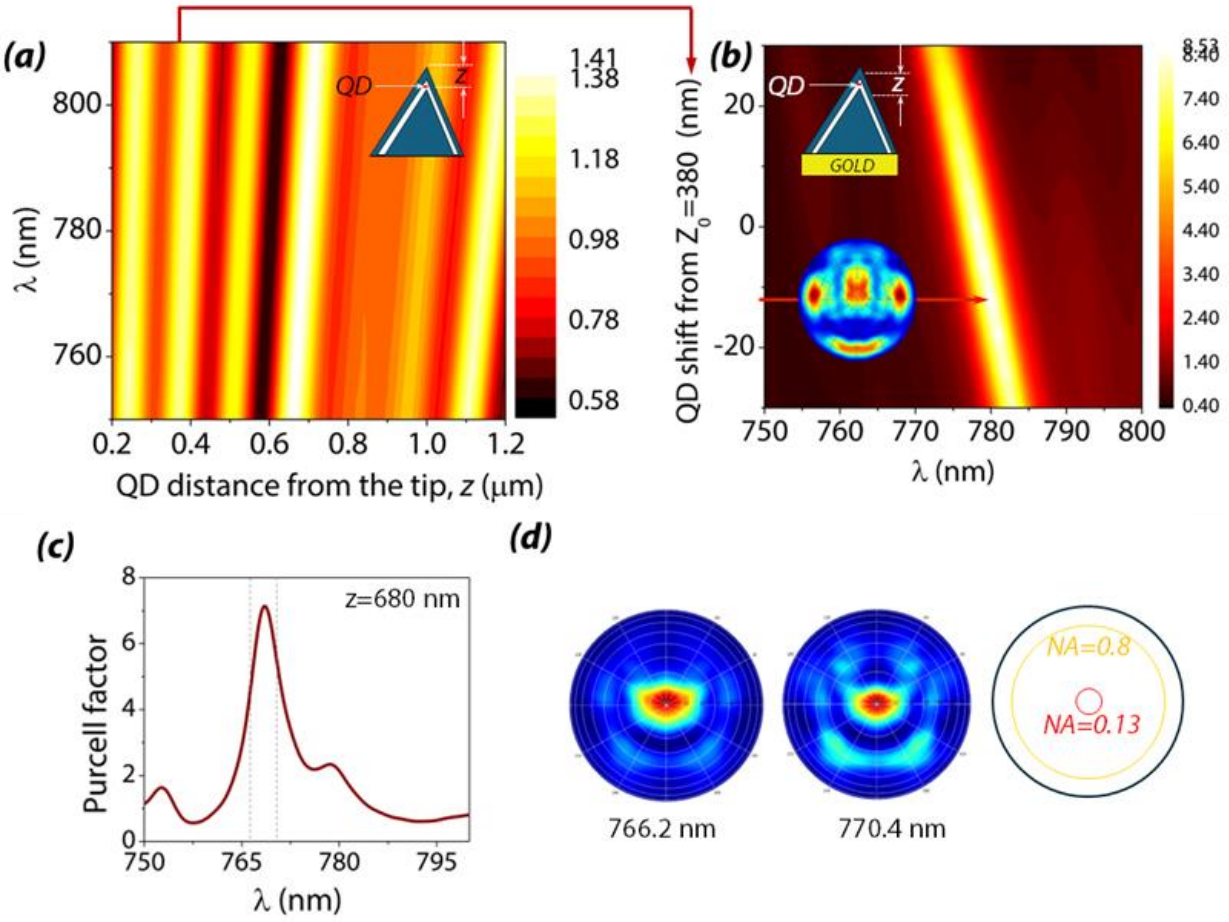

Figure 4.2-4: Study of a modified back-etched pyramid configuration as described in the text. a) Upper part optimization: The heatmap illustrates the Purcell enhancement as a function of wavelength and the QD distance (z) from the tip, as indicated in the inset. Here, reflection from the base is not considered. b) Purcell enhancement with a gold reflector: This panel shows the Purcell enhancement when the gold reflector is placed beneath the base of the pyramid. The QD is positioned at the initial distance z0=380 nm, on one of the previously found resonances. The optical resonance shift is presented as a function of the QD position (z) for fine-tuning. The far-field profile at z=-12 nm and resonant wavelength λ=780 nm is shown on the graph. c) Purcell factor curve: This curve depicts the Purcell factor when the QD is positioned at z0=680 nm. d) Far-field profiles: Two far-field profiles for the configuration at z0=680 nm, close to the optical resonance, demonstrate directional near-Gaussian emission. The far-field NA values of 0.13 and 0.8 are indicated in a separate sketch.

The far-field analysis of this configuration revealed that the profiles at the resonance maxima were not Gaussian. An example of such a profile at the QD position of -12 nm is shown as the inset of Figure 4.2-4-b; the others are shown in Figure 4.2-5 which represents a non-normalized by Purcel factor transmission map in the wavelength range of 750 to 800 nm. The source, positioned 380 nm below the tip, is swept of ±30 nm in 11 steps of 6nm each. The gold reflector is 461 nm below the QD. The far-filed power projections for each transmission peak show a complex, non-Gaussian configuration, indicating suboptimal angular spreading despite very high transmission values.

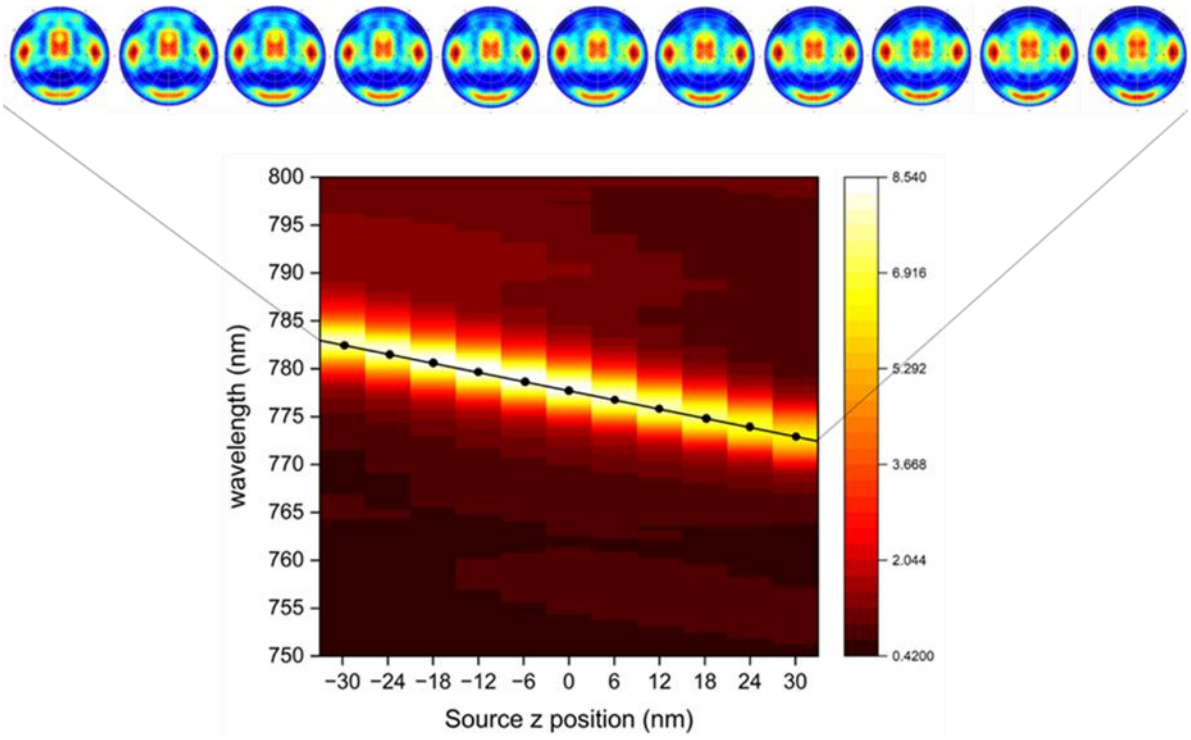

Figure 4.2-5: The resonant cavity mode shift of a back-etched pyramid as a function of the QD vertical position. Initially, the QD is positioned 380nm below the tip, and the resonator placed 461 nm below the QD

Such deviation from a Gaussian profile could negatively impact applications requiring efficient single-mode coupling. To investigate whether the trade-off between far-field quality and Purcell enhancement could be mitigated, we extended our study to optimize the reflector position. In this case, the QD was positioned 680 nm. The reflector was

initially placed at a distance from the source that satisfied the constructive interference condition $2d=2.5\lambda_{eff}$, which after further optimizations was found to be 1/3 of the pyramid height.

As shown in Figure 4.2-4-c, the optimized optical resonance achieved a Purcell factor of 7.1 at a wavelength of 768.4 nm. In this configuration, the far-field profiles (Figure 4.2-4-d) exhibited increased directionality of the emission. By shifting the substrate by 10 nm, the resonance could be tuned across a wavelength range of 25 nm while maintaining the same far-field profile (Figure 4.2-6) and the light extraction efficiency of approximately 20% (NA=0.999).

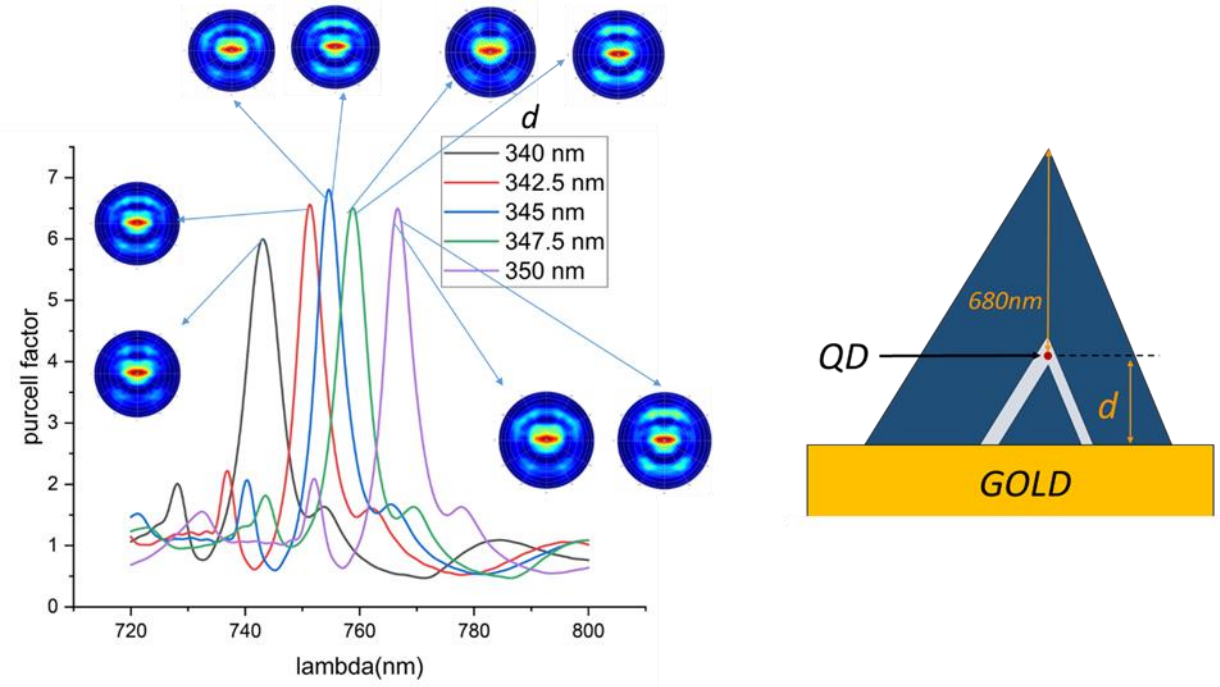

Figure 4.2-6:Cavity mode of a back-etched pyramid with a resonator placed at 1/3 of the pyramid height (left), sketch of simulated configuration (right).

To evaluate the applicability of this source, we calculated the fraction of emitted power for NA values of 0.8 and 0.13, which correspond to use cases in free-space and fiber-coupled experiments, respectively (Figure 4.2-4-d). At a wavelength of 766.2 nm, the optical power directed into NA = 0.8 and NA = 0.13 accounted for 17.2% and 1.4%,

respectively, of the total source power. Despite the improved emission directionality, this source is still less suitable for fiber-coupled applications. However, it is evident that this optimized source configuration is highly advantageous for a wide range of advanced fundamental studies and practical technological applications that rely on free-space optical configurations.

Pillars. The dependence of the emission properties on two key parameters - the lateral dimensions of the pillar and the vertical position of the QD - was investigated. The lateral dimension is defined by the triangular base (or recess) edge, denoted as *d*, while the QD distance from the base is represented as *h* (Figure 4.2-9-b). Initial conditions are set with the QD positioned 300 nm below the recess, which is fully filled with the SiO_2 mask, and with no reflection from the base of the pillar.

Since the GaAs material that composes the lower trunk of the pillar is highly absorptive, any effects resulting from reflection, such as Purcell enhancement, would be significantly damped. Although a pillar design incorporating a reflector would be meaningful for QDs emitting below the band gap of GaAs, such as $In_xGa_{1-x}As$, this falls outside the scope of the present study.

The motivation for studying the dependence on lateral dimensions stems from the fact that the ratio between the lateral dimension and the wavelength directly influences both the spontaneous emission rate (Purcell enhancement) and the types of optical modes supported by the wire. Ideally, confinement of solely a fundamental mode is preferred. In cylindrical wires, such mode is HE_{11}, and the optimal ratio between diameter and wavelength has been found to be approximately 0.23[20]. In contrast, pillars exhibit three-fold rotational symmetry and, in general, support a different set of modes that depend on their lateral dimensions[21]. However, due to absorption by GaAs below the QD position, cavity and waveguide mode analysis in this specific case is largely unphysical. Therefore, only the geometry of a transparent part atop of a QD will be considered in this study, which focuses on more practically achievable structures, with edge sizes ranging

from 345 nm to 1.5 µm. Simulations were conducted for 10 points each for the variables *h* (vertical position) and *d* (lateral dimension), resulting in 100 simulated cases.

Figure 4.2-9-a shows the source intensity map detected by the transmission monitor placed 100 nm above the pillar. The values are normalized by their corresponding Purcell factors to represent the expected source intensity under pulsed excitation, where maximum a single photon is emitted during each cycle. The raw transmission curves and the obtained Purcell factors are provided in Figure 4.2-7.

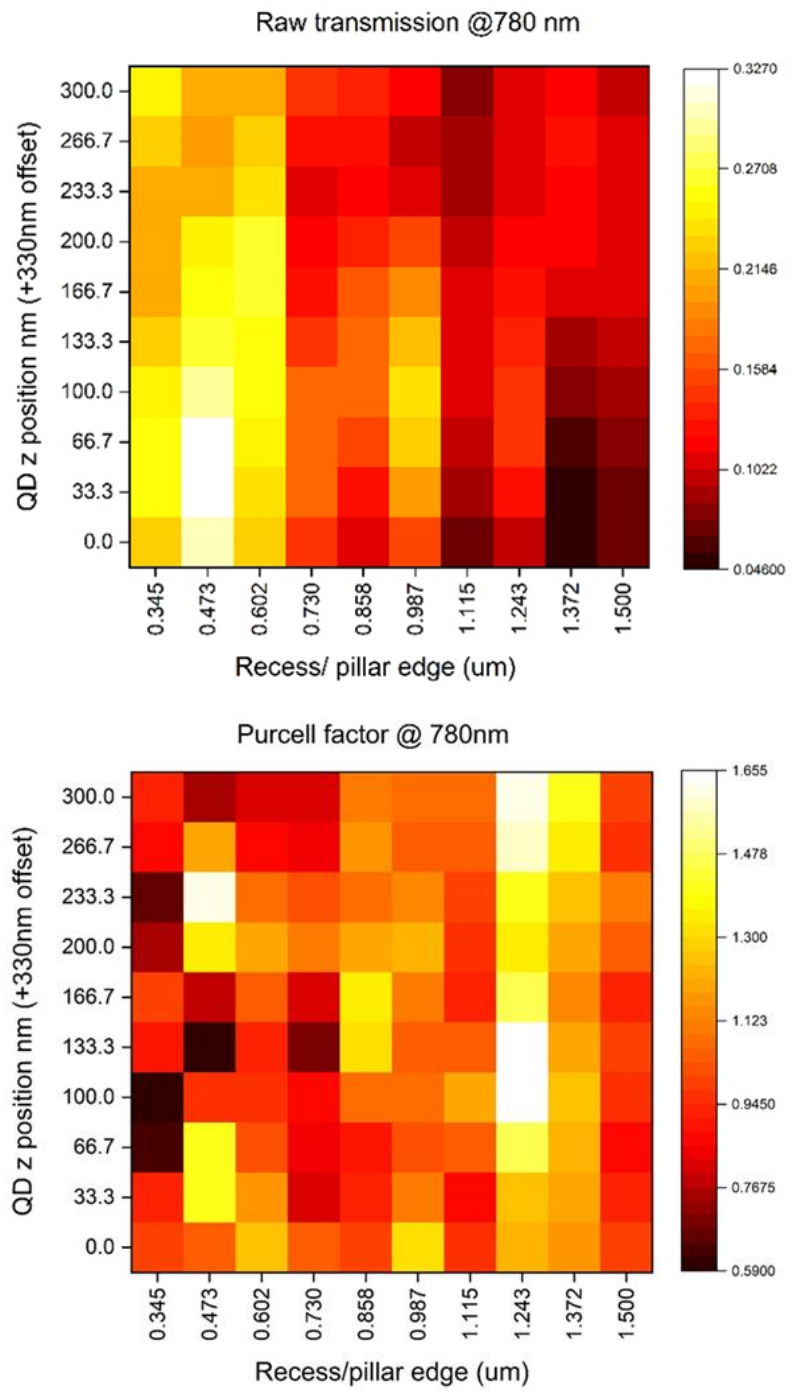

Figure 4.2-7: Raw transmission (top) and Purcell factor (bottom) heatmaps as a function of a pillar edge dimension for different dot positions

As anticipated, a significant drop in transmission (by a factor of 3-4, depending on the QD position) was observed as the edge size increased throughout the studied range. This drop is indicative of reduced coupling efficiency of the spontaneous emission to the

pillars' sustained modes along the vertical axis. After normalization, transmission values as high as 0.43 were found for a pillar with an edge size of 473 nm and a QD position of 133 nm (h), when coupling efficiency is higher.

The Purcell factor, much like in the back-etched geometry discussed earlier, exhibits oscillations related to interference at the recess interface. These oscillations are more pronounced in the laterally smallest pillars, with values ranging from 0.62 to 1.6 in structures with an edge size of 473 nm. This suggests that the QD position along the vertical axis is a highly sensitive parameter for the smallest and, as indicated by the transmission measurements, the brightest sources. The far-field study revealed a broad range of complex profiles, most of which were non-Gaussian (Figure 4.2-8).

However, two specific ranges of structures exhibited near-Gaussian profiles, as shown in Figure 4.2-9-a. The brightest pillars were found in the range with an edge size of 473 nm, making this range ideal for fabrication. Pillars with an edge size of 986 nm showed a lower transmission (~0.22) but featured directional, Gaussian-like emission. Their (typically) better optical properties due to reduced negative contributions from surface states make them an attractive option as well, particularly for free-space optical experiments. It was calculated that for the two shown cases at h=200 nm, 14.7% and 15% of the overall power is emitted into NA=0.8, while 1% and 0.7% into NA=0.13.

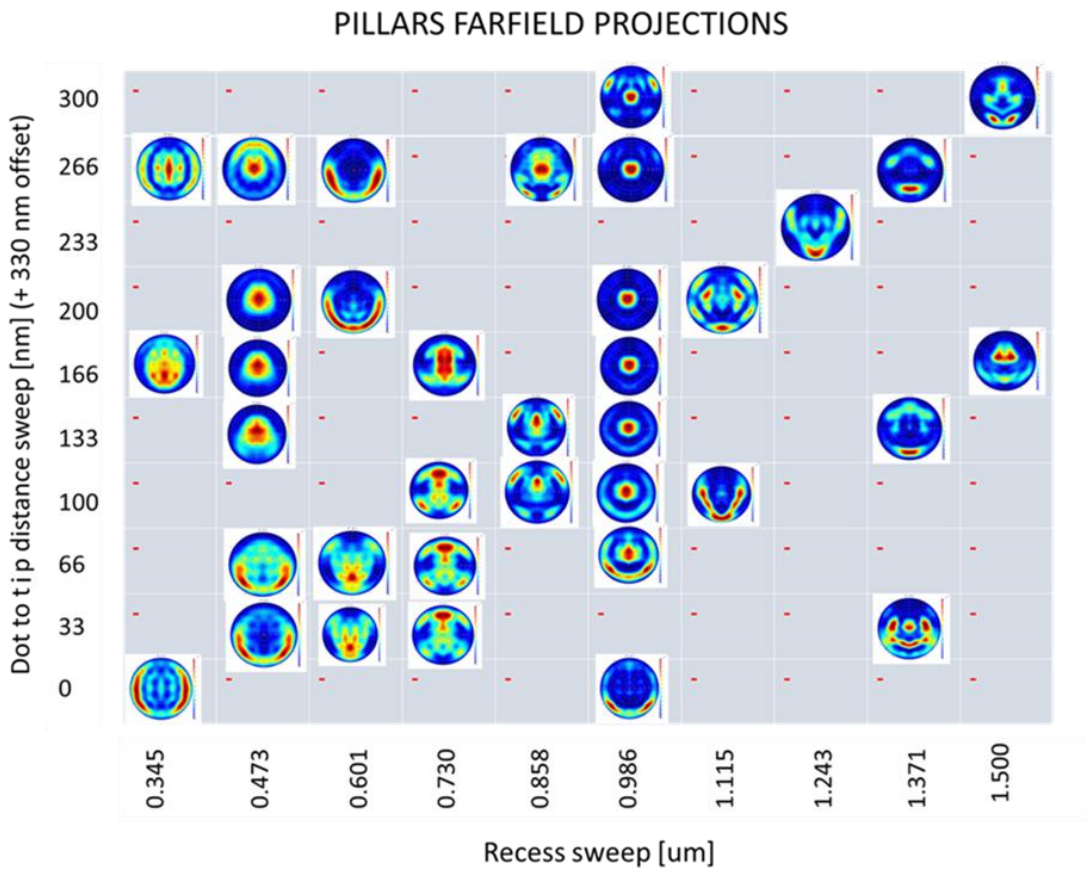

Figure 4.2-8: Far-field profiles

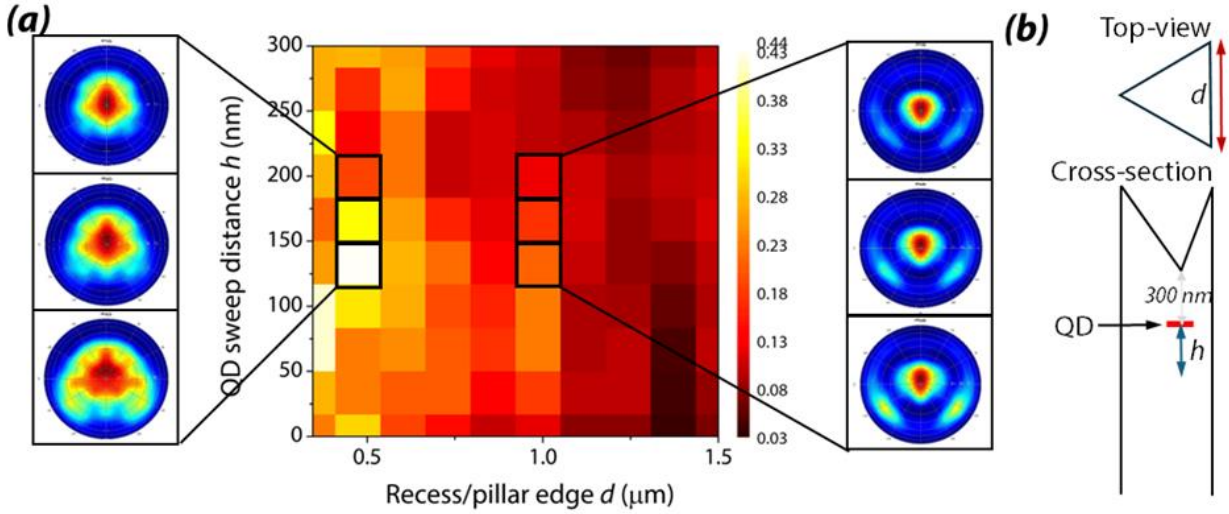

Figure 4.2-9: Study of the pillar geometry at an emission wavelength of 780 nm. a) Transmission heatmap: This map illustrates transmission as a function of the pillar edge size (d) and the QD

position (h), measured from a 300 nm offset from the bottom of the recess. The values are normalized by the corresponding Purcell factors. Two high transmission regions, characterized by Gaussian-like far-field distribution profiles, are highlighted, with corresponding profile images shown on both sides of the graph. b) Parameter illustration: This panel depicts the varied parameters during the simulations.

Mirrored pyramids. The flexibility of this method enables the fabrication of structures with a broad range of geometrical properties. The footprint of each structure is controlled by the initial recess size, which is filled with SU8 photoresist, while the height is determined by the etching time and selectivity. The angle of the lateral faces is similarly defined by the selectivity of the etching process.

Among the various possible geometries, we selected two distinct designs for the mirrored pyramids.

The first design has a smaller aspect ratio between the height and base width compared to the second, and features lateral slanted profiles with a 20° slope (Figure 4.2-10-a). The base width, denoted as *w*, corresponds to the height of the equilateral pyramidal footprint of the structure, set at *w*=2.6 µm for this configuration. The second geometry exhibits a higher aspect ratio, with a base width of *w*=1.4 µm and slanted profiles at a 10° angle. Both designs can be achieved during fabrication by tuning the selectivity of the dry etching process. A selectivity ratio of 2:1 (GaAs:SU8) is required for the first design, while a ratio of 3:1 is necessary for the second.

During simulations, we varied two key parameters: the height of the structure (*h*) and the vertical position of the QD (*z*). From a practical standpoint, different height values correspond to different etching times. The QD was initially positioned 380 nm below the recess's bottom and was shifted downward by up to 300 nm. To ensure the simulations were physically meaningful, the epitaxial structure confining the QD (AlAs and $Al_{0.65}Ga_{0.35}As$) was also adjusted accordingly. We studied six values for each variable, resulting in 36 configurations.

Figure 4.2-10-a presents the results for the first geometry. Initially, at a height of 1.1 μm, the QD is positioned 505 nm below the flat, etched surface of the substrate. As the structure's height increases to 2.1 μm, the QD rises above the substrate at intermediate values. These conditions closely resemble the first simulation of the tip's exposure from the substrate (Figure 4.2-3). Moreover, the 20° slanted profiles are nearly identical to the profile of an equilateral tetrahedron, similar to a conventional back-etched pyramid. Consequently, the transmission results are also similar. When the QD is below the substrate surface level, the transmission ranges from 1-2%. Once the QD emerges above the surface, transmission increases up to 9% for the tallest structure. Purcell enhancement in these structures is moderate (Figure 4.2-11) and will not be discussed further here. Additionally, the far-fields of this geometry are non-Gaussian (Figure 4.2-12), making these structures less suitable for applications requiring highly efficient single-mode coupling.

In the second geometry, at an initial height of 1 μm, the QD is positioned just 60 nm below the substrate level. At this transitional position, the transmission already reaches 4%. As the structure's height increases, the transmission rises to 24%, with the QD placed at z = -180 nm. This structure closely resembles previously studied pillars, resulting in similar transmission levels. The far-field pattern of these taller 2.4 μm structures is strongly dependent on the QD position (Figure 4.2-10-b). As with the majority of other structures in this study, there is a tradeoff between far-field quality and transmission. For instance, the structure with the QD at z = 0 has one of the highest Purcell factors at 1.42, with directional emission that is nearly Gaussian. However, the transmission in this case is 12%.

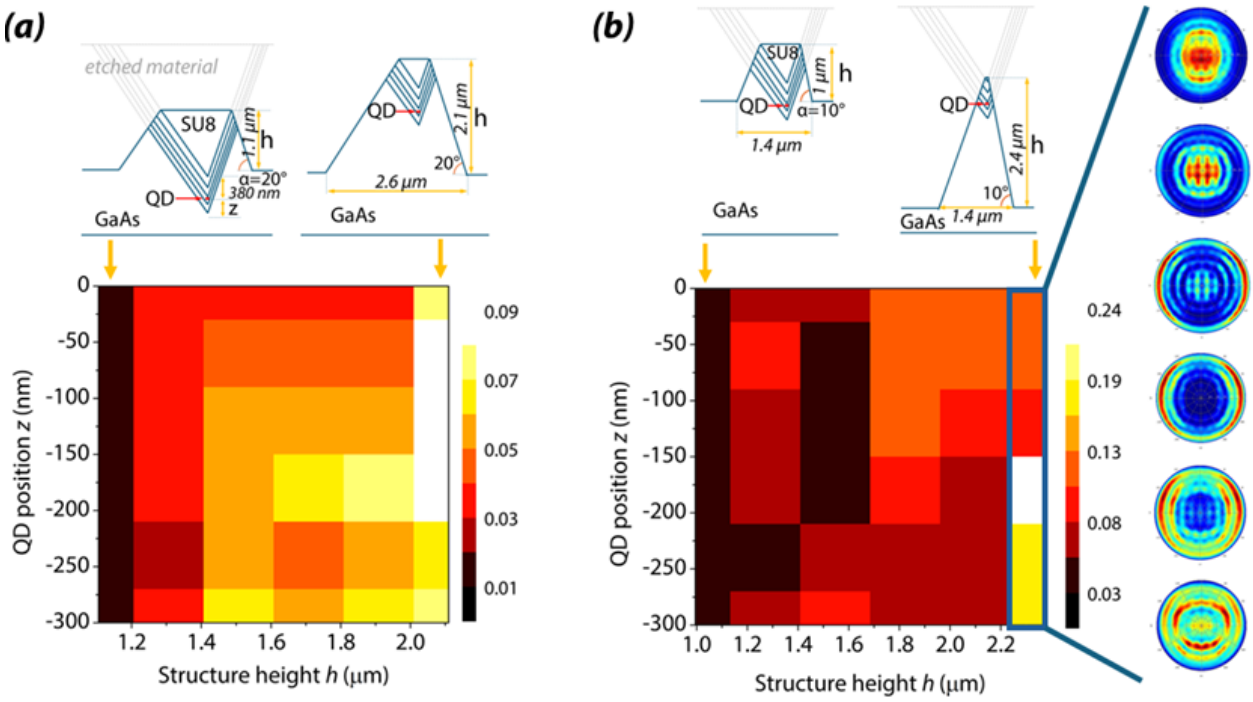

Figure 4.2-10: Study of two distinct geometries of mirrored pyramids. a) Structures obtained at a 1:2 (SU8: GaAs) etching rate: The studied structures feature a base width (height of the triangle) of 2.6 µm, with the QD positioned 380 nm below the recess, as indicated. During the simulation, both the QD position (z) and the height of the structure (h) were varied. The heatmap displays the obtained (not normalized) transmission values as a function of these parameters. b) Structures obtained at a 1:3 (SU8:GaAs) etching rate: This study is analogous to the first one except a smaller base of 1.4 µm. Far-field profiles of the brightest structures are shown on the right as a function of the QD position (z).

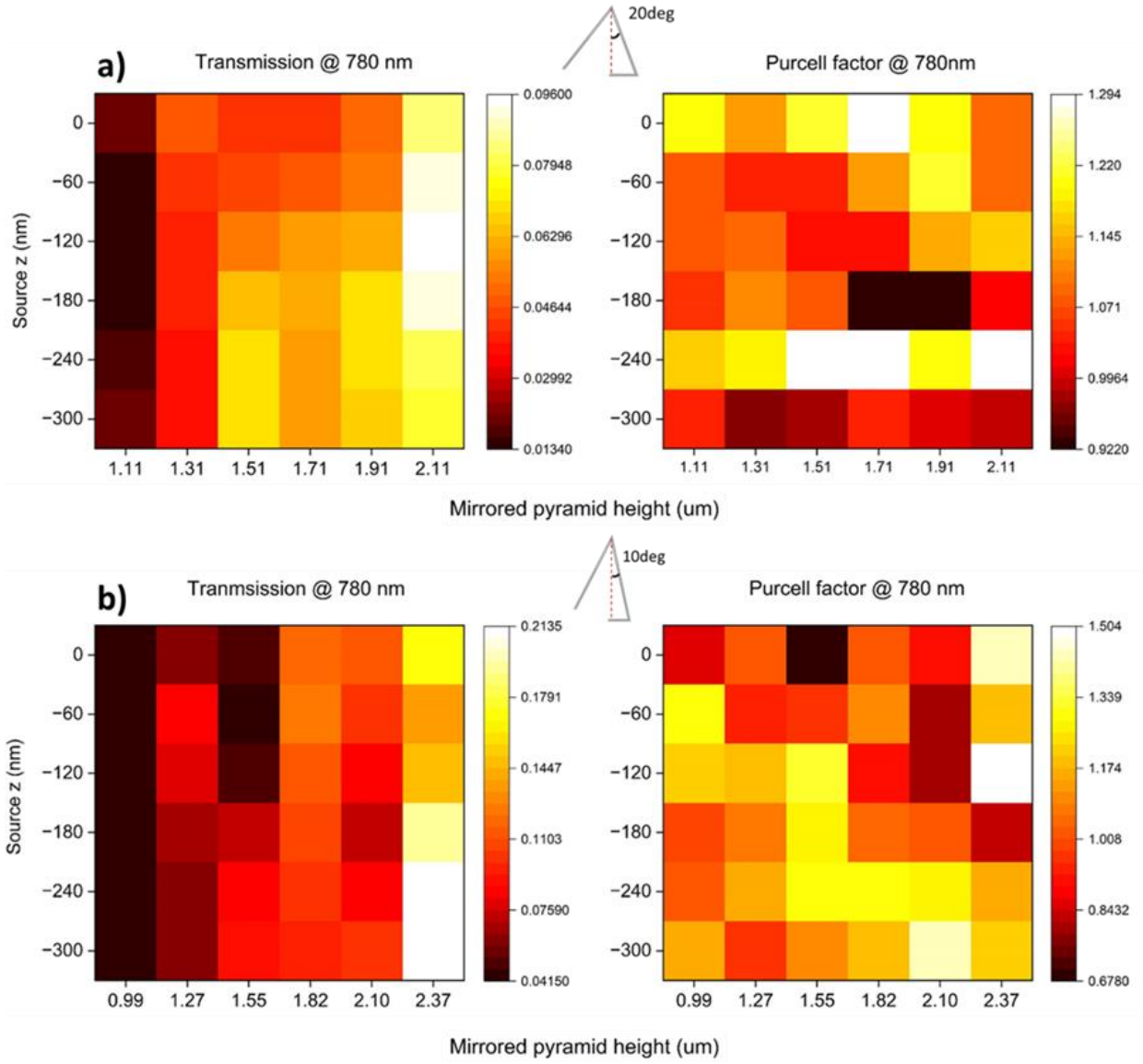

Figure 4.2-11: Transmission and Purcell factor heatmaps

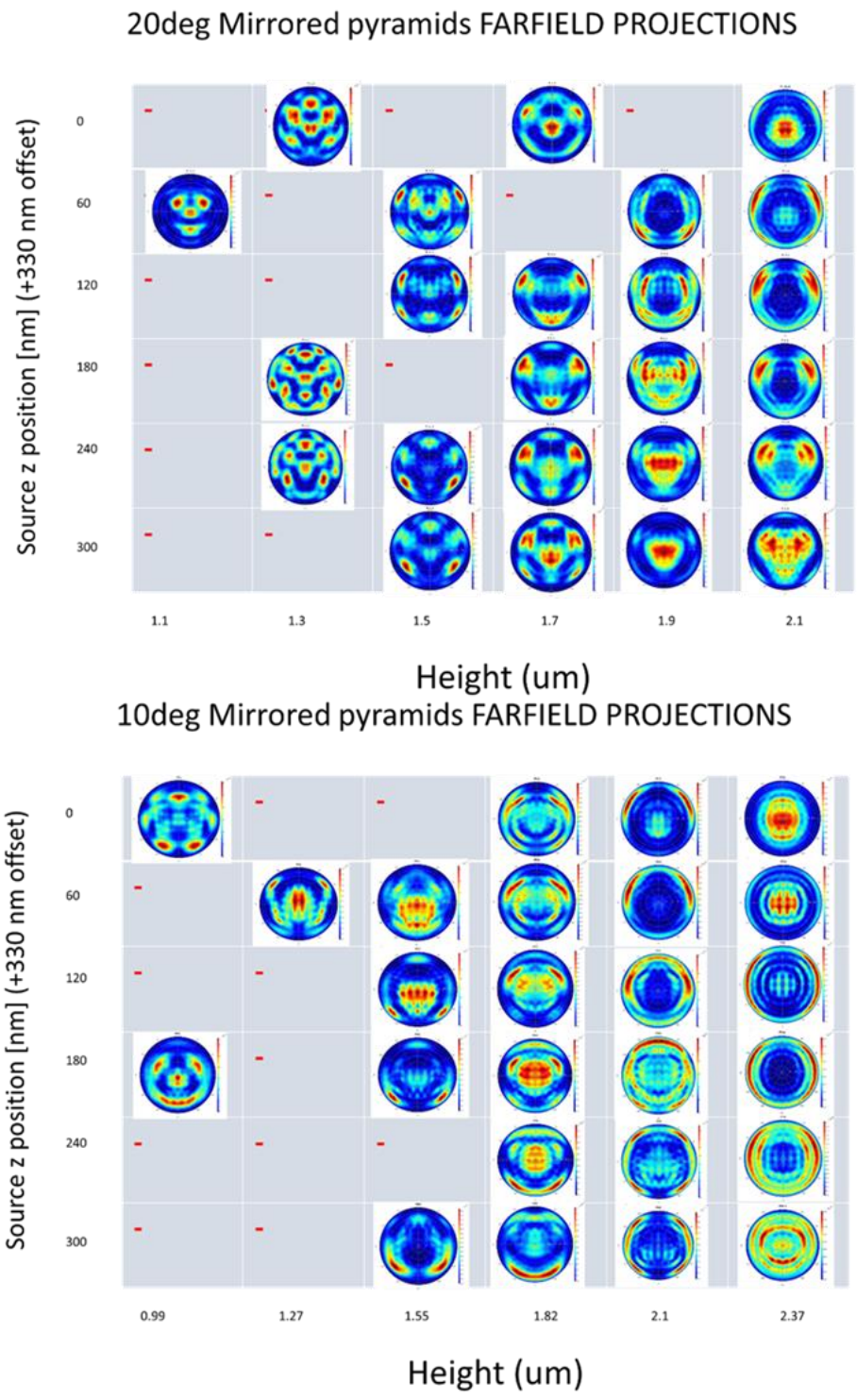

Figure 4.2-12: Far-field profiles of mirrored pyramids with a) 20 deg and b) 10 deg slanted profile angle

4.3 Discussion and conclusions

In this work, we explored three processing approaches enabled by the unconventional non-planar geometry of the site-controlled pyramidal GaAs QD platform to produce bright photon emitters. Through simulations of the discussed light extraction configurations, we gained both quantitative and qualitative insights into how the physical and geometrical parameters of micro- and nanostructures influence light extraction characteristics, including intensity, Purcell enhancement, and far-field power distribution. Table 1 summarizes the key findings.

Theoretical simulations revealed that the maximum light extraction efficiency achievable with the conventional back-etching approach, historically employed in much of our previous research, is approximately 8% within the 750-780 nm range. However, it should not be ignored that, in practice, the efficiency is reduced by at least half due to defects introduced during wet etching, QD blinking, and possibly other unidentified factors. Anyway, even in a lossy free-space optical setup, under pulsed excitation, a count rate of up to 200 kilocounts/s on a single-photon avalanche photodiode can be detected. This source intensity is more than adequate for various fundamental studies and demonstrators.

However, efforts to integrate these QDs into photonic circuits for practical applications - or demonstrators requiring high extraction efficiency and optical mode directionality, such as photonic cluster states - demand significant improvements. This work serves as an initial roadmap to identify and guide these advancements.

A modified version of the back-etched approach - integrating a gold reflector beneath the base of a fully exposed pyramid - can increase light extraction efficiency to up to 37% (NA=0.999). Although the tetrahedron shape is not optimal for confining a single optical mode, in all studied cases, an optical resonance with a Purcell enhancement of up to 8.4 and a full width at half maximum (FWHM) of 4.8 nm was observed.

Geometry	Max transmission efficiency (NA=0.999)	Tunability by geometry	Key findings
1.1 Back-etched	8%	1. Exposing the tip of the pyramid.	*Improvement in light extraction efficiency as the QD approaches the substrate surface level.
1.2 Back-etched with a reflector	37%	1. QD vertical position. 2. Reflector position.	*Significant Purcell enhancement of 8.4 under resonant conditions, along with high extraction efficiency into higher NA values. *Far-field profile is dependent on both the QD and reflector positions, but shows significantly less sensitivity compared to pillars and mirrored pyramids.
2. Pillars	43%	1. QD vertical position. 2. Lateral dimensions of the pillar.	*Higher extraction efficiency observed in more laterally confined pillars. *Strong far-field dependence on QD position and lateral dimensions. *High potential for fabricating optical cavity structures that can accommodate a single mode.
3. Mirrored	24%	1. QD vertical position. 2. Aspect ratio of the height and base.	*Increased extraction efficiency from structures with a higher aspect ratio. *Strong far-field dependence on QD position and lateral dimensions.

Table 1

This microstructure is realistic, as it can be fully fabricated from a material with a higher bandgap, such as the $Al_xGa_{1-x}As$ alloy, which does not absorb GaAs QD emission and does not suppress resonant effects.

However, the fabrication of such a structure requires high precision, with both the QD and the resonator positions needing to be engineered to within a few nanometers. The QD position can be controlled through an established calibrated epitaxial growth procedure. The distance between the QD and the reflector can be managed, for example, through a polishing process with a slight incline, along with careful SEM monitoring. While this method may not result in an entire array of optimal emitters across the sample, a significant fraction of emitters will meet the optimal design criteria.

Nearly identical precision requirements were observed for the fabrication of micro- and nanopillars. Lateral pillar dimensions can be controlled by the polishing procedure, while the QD position is managed through calibrated epitaxial growth. Due to their smaller, laterally confined volume, pillars support fewer optical modes, with most confined along the vertical axis. Specific pillar designs have demonstrated light extraction efficiencies of up to 43% (NA=0.999), with near-Gaussian far-field profiles. For the most promising cases analyzed, only about 20% of the emitted power is lost when collected within NA=0.8, which is typical for free-space experiments. In contrast, much higher losses are expected in fiber-coupled experiments (NA=0.13), where only 6–8% of the emission within NA=0.999 is captured. This finding serves as a guide for future developments aimed at fabricating pillars optimized for single-mode operation and highly directional emission.

This efficiency is achieved without the use of a back-reflector, as its introduction in the GaAs QD system is irrelevant due to absorption by the pillar material. However, $In_xGa_{1-x}As$ QDs could benefit from this modification, potentially bringing light extraction close to unity. Alternatively, GaAs QDs could be embedded in pillars fabricated from an AlGaAs alloy membrane grown on a (111)B-oriented GaAs substrate. AlGaAs is highly prone to oxidation, and the pillar sidewalls are aligned along the (211) family of planes[22],

which unfortunately exhibits a low activation energy against oxidation compared to other orientations. Therefore, treatments for passivating the lateral sidewalls would be necessary. Nevertheless, the primary challenge remains the fabrication of small, highly efficient pillars, for which sidewall passivation would be indispensable to mitigate the effects of surface defect states

It should also be noted that the studied geometry is not the only option. Truncated pillars can also be fabricated, and when combined with a reflector, could potentially improve mode guiding and offer reduced variability in far-field profiles[23].

Simulations of the mirrored pyramid approach validated its effectiveness, with transmission results comparable to, and in some cases surpassing, those of back-etched structures. Rather than being a competing technique, the mirroring process, which may enable electric field tuning of excitonic lines, simplifies the application of a metal contact to one of the doped layers, such as the back of an n+ doped substrate, in p-i-n junctions embedding the QDs. Additionally, the self-aligning technique borrowed from pillar fabrication eliminates the need for grinding and back-etching, two inherently destructive processes, especially when performed sequentially. Grinding introduces the risk of unwanted chipping, which can lead to sample loss and often compromises parallelism. This issue becomes particularly problematic during the back-etching step, where only a small fraction of the pyramids may be exposed, resulting in a lower yield. Fully exposing all pyramids would require extended etching time, increasing the risk of the etchant breaching the etch-stop barrier and further reducing yield.

Concluding, the results presented here expand our current understanding of site-controlled pyramidal QDs and underscore the potential of further enhancing extraction performance. These advancements suggest that this class of quantum emitters holds significant promise as candidates for quantum information platforms.

References

(1) Colavecchi, L.; Juska, G.; Pelucchi, E. Optimizing Light Extraction from Non-Planar Site-Controlled Pyramidal Quantum Dot System: Comparative Modeling of Three Fabricable Geometries. *Mater. Quantum Technol.* **2025**. https://doi.org/10.1088/2633-4356/adb6ec.

(2) Barnes, W. L.; Björk, G.; Gérard, J. M.; Jonsson, P.; Wasey, J. A. E.; Worthing, P. T.; Zwiller, V. Solid-State Single Photon Sources: Light Collection Strategies. *Eur. Phys. J. - At. Mol. Opt. Plasma Phys.* **2002**, *18* (2), 197–210. https://doi.org/10.1140/epjd/e20020024.

(3) Nowak, A. K.; Portalupi, S. L.; Giesz, V.; Gazzano, O.; Dal Savio, C.; Braun, P.-F.; Karrai, K.; Arnold, C.; Lanco, L.; Sagnes, I.; Lemaître, A.; Senellart, P. Deterministic and Electrically Tunable Bright Single-Photon Source. *Nat. Commun.* **2014**, *5* (1), 3240. https://doi.org/10.1038/ncomms4240.

(4) Tomm, N.; Javadi, A.; Antoniadis, N. O.; Najer, D.; Löbl, M. C.; Korsch, A. R.; Schott, R.; Valentin, S. R.; Wieck, A. D.; Ludwig, A.; Warburton, R. J. A Bright and Fast Source of Coherent Single Photons. *Nat. Nanotechnol.* **2021**, *16* (4), 399–403. https://doi.org/10.1038/s41565-020-00831-x.

(5) Uppu, R.; Pedersen, F. T.; Wang, Y.; Olesen, C. T.; Papon, C.; Zhou, X.; Midolo, L.; Scholz, S.; Wieck, A. D.; Ludwig, A.; Lodahl, P. Scalable Integrated Single-Photon Source. *Sci. Adv.* **2020**. https://doi.org/10.1126/sciadv.abc8268.

(6) Kapon, E.; Pelucchi, E.; Watanabe, S.; Malko, A.; Baier, M. H.; Leifer, K.; Dwir, B.; Michelini, F.; Dupertuis, M.-A. Site- and Energy-Controlled Pyramidal Quantum Dot Heterostructures. *Phys. E Low-Dimens. Syst. Nanostructures* **2004**, *25* (2–3), 288–297. https://doi.org/10.1016/j.physe.2004.06.033.

(7) Dimastrodonato, V.; Pelucchi, E.; Vvedensky, D. D. Self-Limiting Evolution of Seeded Quantum Wires and Dots on Patterned Substrates. *Phys. Rev. Lett.* **2012**, *108* (25), 256102. https://doi.org/10.1103/PhysRevLett.108.256102.

(8) Juska, G.; Dimastrodonato, V.; Mereni, L. O.; Gocalinska, A.; Pelucchi, E. Towards Quantum-Dot Arrays of Entangled Photon Emitters. *Nat. Photonics* **2013**, *7* (7), 527–531. https://doi.org/10.1038/nphoton.2013.128.

(9) Ranjbar Jahromi, I.; Juska, G.; Varo, S.; Basso Basset, F.; Salusti, F.; Trotta, R.; Gocalinska, A.; Mattana, F.; Pelucchi, E. Optical Properties and Symmetry Optimization of Spectrally (Excitonically) Uniform Site-Controlled GaAs Pyramidal Quantum Dots. *Appl. Phys. Lett.* **2021**, *118* (7), 073103. https://doi.org/10.1063/5.0030296.

(10) Moroni, S. T.; Chung, T. H.; Juska, G.; Gocalinska, A.; Pelucchi, E. Statistical Study of Stacked/Coupled Site-Controlled Pyramidal Quantum Dots and Their Excitonic Properties. *Appl. Phys. Lett.* **2017**, *111* (8), 083103. https://doi.org/10.1063/1.4985259.

(11) Huang, J.; Liu, W.; Cheng, X.; Miranda, A.; Dwir, B.; Rudra, A.; Kapon, E.; Wong, C. W. Single Site-Controlled Inverted Pyramidal InGaAs QD–Nanocavity Operating at the Onset of the Strong Coupling Regime. *J. Appl. Phys.* **2023**, *134* (22), 223103. https://doi.org/10.1063/5.0175055.

(12) Rigal, B.; Joanesarson, K.; Lyasota, A.; Jarlov, C.; Dwir, B.; Rudra, A.; Kulkova, I.; Kapon, E. Propagation Losses in Photonic Crystal Waveguides: Effects of Band Tail Absorption and Waveguide Dispersion. *Opt. Express* **2017**, *25* (23), 28908–28913. https://doi.org/10.1364/OE.25.028908.

(13) *Transmission Results Greater Than One – Ansys Optics*. https://optics.ansys.com/hc/en-us/articles/12614264530323-Transmission-Results-Greater-Than-One (accessed 2024-12-24).

(14) Sallen, G.; Kunz, S.; Amand, T.; Bouet, L.; Kuroda, T.; Mano, T.; Paget, D.; Krebs, O.; Marie, X.; Sakoda, K.; Urbaszek, B. Nuclear Magnetization in Gallium Arsenide Quantum Dots at Zero Magnetic Field. *Nat. Commun.* **2014**, *5* (1), 3268. https://doi.org/10.1038/ncomms4268.

(15) *Handbook of Optical Constants of Solids*; 1985.

(16) Medina-Rangel, S. A.; Maraviglia, N.; O'Hara, J.; Vorobev, A. S.; Iadanza, S.; Pelucchi, E.; O'Faolain, L. Cryogenic Thermo-Optical Coefficient of SU-8 Measured Using a Racetrack Resonator at 850 Nm. *Photonics* **2024**, *11* (9), 800. https://doi.org/10.3390/photonics11090800.

(17) Tan, C. Z.; Arndt, J. Temperature Dependence of Refractive Index of Glassy SiO2 in the Infrared Wavelength Range. *J. Phys. Chem. Solids* **2000**, *61* (8), 1315–1320. https://doi.org/10.1016/S0022-3697(99)00411-4.

(18) Varo, S.; Li, X.; Juska, G.; Jahromi, I. R.; Gocalinska, A. M.; Falco, A. D.; Pelucchi, E. Planar Semiconductor Membranes with Brightness Enhanced Embedded Quantum Dots via Electron Beam Induced Deposition of 3D Nanostructures: Implications for Solid State Lighting. *ACS Appl. Nano Mater.* **2020**. https://doi.org/10.1021/acsanm.0c02969.
(19) MORAWITZ, H. Self-Coupling of a Two-Level System by a Mirror. *Phys. Rev.* **1969**, *187* (5), 1792–1796. https://doi.org/10.1103/PhysRev.187.1792.
(20) Bleuse, J. Inhibition, Enhancement, and Control of Spontaneous Emission in Photonic Nanowires. *Phys. Rev. Lett.* **2011**, *106* (10). https://doi.org/10.1103/PhysRevLett.106.103601.
(21) Milton, K. A.; Schwinger, J. Rectangular and Triangular Waveguides. In *Electromagnetic Radiation: Variational Methods, Waveguides and Accelerators*; Milton, K. A., Schwinger, J., Eds.; Springer: Berlin, Heidelberg, 2006; pp 133–152. https://doi.org/10.1007/3-540-29306-X_7.
(22) Vaccaro, P. O.; Koizumi, K.; Fujita, K.; Ohachi, T. AlAs Oxidation Process in GaAs/AlGaAs/AlAs Heterostructures Grown by Molecular Beam Epitaxy on GaAs (N11)A Substrates. *Microelectron. J.* **1999**, *30* (4–5), 387–391. https://doi.org/10.1016/S0026-2692(98)00140-2.
(23) Friedler, I.; Sauvan, C.; Hugonin, J. P.; Lalanne, P.; Claudon, J.; Gérard, J. M. Solid-State Single Photon Sources: The Nanowire Antenna. *Opt. Express* **2009**, *17* (4), 2095–2110. https://doi.org/10.1364/OE.17.002095.

Chapter 5

5 Investigating Electric Field Influence on PQDs

As previously discussed, the availability of indistinguishable entangled photons is a crucial resource for implementing quantum gated photonic logic circuits, which rely on quantum interference. However, alternative architectures — such as Measurement-Based Quantum Computing (MBQC) — may relax this requirement. One way the QD community is trying to harness entanglement for quantum operations is by exploiting the biexciton-exciton recombination cascade that QDs provide within their population mechanism when they are excited. For entangled photons to be indistinguishable, energies and flying wave-packets need to coincide, but this is seldomly the case: low symmetry of the crystal-confining potential, together with the Coulomb and the exchange interaction between electrons and holes, cause the energy splitting of the intermediate neutral exciton states X (M=±1), rendering H_{XX} distinguishable from V_{XX} and H_X distinguishable from V_X[1] (see Fig. 1-3, Introduction). Of course, photons emitted with identical FSS can still interfere; however, the random temporal relaxation of the exciton state to the vacuum level leads to reduced indistinguishability, for example, between photons emitted by two quantum emitters initialized simultaneously.

Pre-processed QDs rarely have the requirement for such entangled photons production, that is why post-processing techniques are required to tailor the QDs emission. One approach to modify the excitonic states and reduce the FSS (others include the application of an external strain field[2] for example, or AC Stark tuning[3]) which comes with its own challenges, is the application of a static external electric field to induce Quantum-Confined Stark Effect (QCSE). To this regard, the electric field can be applied laterally, where it is perpendicular to the growth direction, or vertically, where it is parallel to the growth direction. In the second case, the most common strategy is to

embed the dot in a p-i-n structure driven in reverse and let the electric field across the intrinsic region interact with the holes and electrons wave functions[4].

The Quantum-Confined Stark Effect

The QCSE terminology was first introduced in the scientific literature in 1985 by Miller and colleagues[5], who discussed changes in the optical absorption of a ≈10 nm thick quantum well (QW) under an applied electric field. This phenomenon, known as the Franz–Keldysh effect, was already studied and exploited in bulk materials (and before in atoms, where the Stark effect nomenclature originates). Yet, the manuscript highlighted a distinct response of the excitonic resonance in thinner QWs compared to bulkier ones. In thicker QWs, the Franz–Keldysh effect typically involves a redshift of the excitonic resonance due to the tilting of the energy band gap, along with broadening of the band-edge absorption. As the electric field strength increases, the excitonic lifetime decreases drastically because of reduced wavefunction overlapping. Beyond a critical field strength—few times the ionization value—the electric field overcomes the force of the electron-hole Coulomb interaction, and the state is not confined anymore. Overall, an energy shift (or band-edge absorption broadening) of approximately 10% of the exciton binding energy can be achieved[6]. The binding energy here refers to the energy difference between an uncorrelated free electron-hole complex and an interacting electron-hole pair[7].

When an electric field perpendicular to the growth plane was applied to the ≈10 nm QW, they observed that the energy shift far exceeded the exciton binding energy, and the resonance remained well-resolved even at electric fields up to 50 times the ionization value. They explained this behavior as consequence of the tight confinement in the QW: the electric field bends the energy band gap, separating the electron and hole wavefunctions and causing a pronounced redshift in absorption; however, the QW's walls prevent carrier tunneling, preserving the exciton. With such a small well width, even a strong electric field cannot fully overcome the electron-hole Coulomb interaction, allowing the excitonic resonance to remain well-defined.

The study of the quantum-confined Stark effect (QCSE) extended to QDs, where carrier confinement is even tighter.

In the following paragraphs, I will briefly outline some of the efforts researchers have made over the years to understand and harness the response of quantum dots to applied electric fields. We'll see how the community found a convenient way of treating the electric field-induced energy shift of the excitonic peaks by encasing this behavior in a second order approximating equation of the form

$$E(F) = E_0 - \rho F + \beta F^2 \qquad (5.1)$$

where E_0 is the energy of the state under zero field, ρ is the permanent electric dipole moment (the component parallel to the applied electric field F) defined as the expectation value of the dipole operator $q\boldsymbol{r}$ (where q is the particle's charge and $\boldsymbol{r}$ is its position) using the corresponding excitonic wavefunction ($\rho = \langle\phi_{exc}|q\boldsymbol{r}|\phi_{exc}\rangle$), and β is the polarizability, that is generally defined as the ratio between the induced dipole moment and the applied electric field ($\beta = |\rho|/|F|$). β is a second rank tensor (3x3 matrix) and describes the possibility that an external electric field has of inducing a charge distribution imbalance in an atom/molecule/exciton, considering contributions that stem from the three spatial components of $\boldsymbol{F}$. The simplification of the complex interaction of a Coulomb potential ($-\frac{q^2}{\epsilon|\boldsymbol{r_e}-\boldsymbol{r_h}|}$)) in an electric field ($-q\boldsymbol{F}\boldsymbol{r}$) with the parabolic energy approximation allows to attribute the response of the dot to the electric field to the presence of a permanent charge distribution imbalance (permanent dipole moment) and to the tightness of confinement (polarizability), as I report below.

The results that follow are mainly obtained on In(Ga)As SK dots and the conclusions drawn do not translate directly on the PQDs platform, but they were useful to analyze the response we observed in our structures and to further plan experiments.

5.1 Literature review

Carrier injection

In 1994[8] Imamoglu and Yamamoto advanced the first proposal for exploiting a p-i-n heterojunction. They proposed using a mesoscopic p-i-n AlGaAs/GaAs structure driven by an AC bias voltage smaller than the built-in potential of the junction to deterministically elicit resonant tunneling of electrons and holes into the GaAs active region, where they radiatively recombine. This deterministic injection of a single electron-hole pair at a rate determined by the AC driving signal frequency would transform the junction into a high-precision single-photon source. In 2000, with the similar goal of achieving on-demand single and entangled photon generation through electrical injection, Benson et al[9]. proposed the integration of an InAs QD within a GaAs p-i-n matrix. The QD was isolated and incorporated into a mesa structure surrounded by top and bottom Bragg mirrors. The authors noticed that upon application of a critical voltage V_e, two electrons would tunnel into the conduction band ground state. Further tunneling was prevented by the Pauli Exclusion Principle and the lack of resonance in the first excited state. Subsequent application of a critical voltage for holes V_h, would result in two holes populating the valence band ground state, enabling radiative recombination and the production of single or entangled photons.

Since then, various research groups have successfully demonstrated the p-i-n structure as a promising configuration for electrically triggered single-photon sources[10–12] and entangled-photon sources. These efforts predominantly involved self-assembled QDs grown via MBE, but electroluminescence was achieved also with site-controlled PQDs[13,14].

Tuning the FSS: lateral and vertical field

The first studies involving the application of a lateral electric field aimed at tuning the excitonic optical properties of QDs[15] and characterizing the population mechanisms of ground and excited states[16]. Gotoh et al.[15] conduced a theoretical study of the optical degree of anisotropy induced by a lateral electric field on electron and hole

wavefunctions in GaAs QDs fabricated on a GaAs (311)B-oriented substrate via MOVPE. By supposing to apply a lateral E field on the *x* direction (parallel to the substrate plane) on a QD, they observed an increase of the hole wavefunction intensity, but, while on the yz plane the wave function remained symmetric with respect to the centre of the QD, on the xz plane the wavefunctions became asymmetric. Thus, the polarization showed dependency on the spatial symmetry of the wave functions. Furthermore, the induced anisotropy was enhanced in larger dot because of the weaker Coulomb interaction that acts in the opposite direction of the electric field. The theoretical work was supported by experimental results showing two different QDs, one larger than the other, emitting under the application of a lateral electric filed. In both cases rotation by 90° of the polarization was achieved, however, while a potential difference of only 4V at the metallic electrodes sufficed to get the perpendicular polarization on the larger dot, a 10V potential difference was necessary to obtain the same result on the smaller dot.

W. Heller et al[16]. also applied a lateral electric field to excited states confined in a QD defined by monolayer fluctuations in a narrow GaAs/AlGaAs quantum well. They observed a decrease in luminescence intensity with increasing field due to the induced spatial overlap reduction of the wavefunctions. A quadratic dependence of the ground state energy on the applied electric field, shifting toward smaller energies, was observed. This behavior aligned with the mechanism of effective bandgap reduction caused by the tilting of the band structure. The Stark shift was found to be larger in the excited states, albeit at the expense of luminescence intensity, as peak emission decayed more rapidly. Additionally, induced lateral tunneling effects became evident with increasing voltage, reducing the exciton lifetime and causing exponential broadening of the linewidth.

Kowalik at al[17]. analyzed the response of self-assembled InAs in GaAs quantum dots grow by MBE with the aim of compensating the FSS (in the paper referred to as Anisotropic Exchange Splitting) of the two non-degenerate bright excitonic states. They argued that the asymmetry of the wave functions of the single particles stems from the natural elongation of the dot along the [110] direction, and that it could be compensated

applying an electric field along the major axis of the dot changing the effective symmetry of the dot. An Ohmic contact and a Schottky junction are defined such that the field is parallel to the elongation axis of the dot [110]. Upon application of electric field, a red shift of the spectral lines was obtained, together with a partial reduction of the energy splitting between the horizontally [110] and vertically [1-10] polarised transitions.

In 2007 Gerardot et al[18]. investigated the effect of a lateral electric field applied to a single MBE grown InGaAs QD. The electric field was applied to the dot through the definition of two metallic contacts forming two Schottky junctions, separated by a channel 15 μm wide containing the dot. They reported an induced Stark shift of the neutral exciton up to 1.5 meV, a decreased photoluminescence intensity due to the electric field-induced separation of the electron and hole wave functions, and, most importantly, the reduction of the FSS to zero. By assuming an in-plane rotationally symmetric parabolic confinement, they set the in-plane permanent dipole moment to zero, ascribing the parabolic energy shift to polarizability and estimating a field F= 15 kV/cm to obtain a Stark shift of 1 meV. Despite achieving zero FSS, they concluded that using lateral contact for applying an electric field was not optimal due to the decrease in photoluminescence intensity with increasing field and the inability to precisely determine the field direction due to surface roughness.

Applying a vertical electric field proved to be a more elegant and less problematic solution for controlling the FSS.

In 2010 Marcet et al[19]. investigated the effects of a vertical field on the FSS of excitonic state of an MBE GaAs QD in $Al_{30}Ga_{70}As$ barriers grown on n-doped GaAs substrate. Contacts were placed on the back of the substrate and on the 50nm thick GaAs cap making a top Schottky junction, demonstrating, upon application of a voltage, the ability to tune the FSS from 15 to 30 μeV together with a Stark shift of the excitonic line of 40 meV. In the same year Bennet et al[20]. demonstrated entangled-photon generation by applying a vertical field to a dot that showed an FSS of 50 μeV at 0 field. The InAs QDs were grown in 10 nm thick GaAs surrounded by $Al_{75}Ga_{25}As$ intrinsic region. They

determined a linear dependence of the FSS on the applied field (F) given by ΔFSS = ($\rho 1$ − $\rho 2$)F, where $\rho 1$ and $\rho 2$ are the dipole moments of the two bright excitons.

From the experiments reported in literature, it can be deduced that the application of the lateral electric field is effective in changing the FSS. Neutral transitions undergo a Stark shift which is typically quadratic, an outcome that suggests that the X states don't have a permanent electric dipole moment in the x-y plane. Conversely, permanent dielectric dipole moment is not negligible in the z direction, and is the main responsible for a linear FSS change; authors in [16] argue that polarizability is affected by the size of the dot and the height of the confinement barrier, such that upon application of F, the contribution in energy shift of Xs (M=±1) are equal and cancel out when calculating the FSS. The presence of a dielectric moment on *z* can be attributed to the segregation of Indium at the top of the dot[21], and, since SK dots tend to be asymmetric, confinement along [110] is different from [1-10], leading to the existence of two different values of ρ. The clear advantage of vertical over lateral field tuning is the preservation of the PL intensity, which is drastically reduced in lateral field tuning for high field values because of the low overlap of the wavefunctions and the induced tunnelling through the barriers.

The picture is slightly different with non-SK dots: in 2021 Huang et al[22]. conducted an experimental and theoretical study of QCSE in GaAs/$Al_{0.4}Ga_{0.6}As$ quantum dot fabricated by LDE (Local Droplet Etching, see Chapter 1) epitaxy. The dot was embedded in the intrinsic region of a p-i-n junction undergoing the effect of a vertical electric field. The study focused on the permanent electric dipole moment and polarizability of the neutral exciton and the positive trion. Upon application of electric field, a 24 meV Stark shift was obtained, during which the emission line of the positive trion crossed with the one of the neutral exciton, transforming the state from binding to anti-binding. Simulation of the energy Stark shift using cones with a basal diameter of 40 nm and different heights to model the Nano Holes revealed what resembles a parabolic dependence of E on F with a maximum energy that corresponds to an F value greater than 0. However, fitting the simulation results with the quadratic approximation produced inconsistent values of ρ. The quantity ρ/e was then calculated through the Configuration Interaction (CI) method,

leading to minuscule values of electric dipole moment for X_{10} and X^{+}_{20}, which made it reasonable to neglect the linear term during the quadratic fitting. The absence of any segregation effect inside the dot due to the binary composition of the alloy is what might be granting GaAs QDs negligible charge distribution imbalances. On the other hand, calculated polarizability values seemed to have better agreement with fitted values obtained from experimental data. Furthermore, β demonstrated a clear dependence on the dot size: larger quantum dots (smaller energies) exhibited higher polarizability. This finding aligns with the intuitive mechanism that larger dots provide more spatial freedom for wavefunction displacement, facilitating the separation of charges, and is a behavior that is common to other QD systems, as mentioned above.

The relevance of this study lies in the fact that LDE QDs, due to their higher symmetry compared to SK dots[23], and their typical composition (GaAs matrix in AlGaAs barriers), are more directly comparable to GaAs PQDs.

To conclude, the application of a vertical electric field to a QD, embedding it into the intrinsic region of reverse biased p-i-n structure, is without any doubt a very promising technique for controlling excitonic states, and, for example, the realization of an entangled-photon source. However, It has to be mentioned that in a paper[24] published in 2019, a quadrupole configuration where the applied field is again perpendicular to the growth direction has been proposed and theoretically demonstrated to effectively tune the FSS of the exciton in a QD to 0, while maintaining the overlap of the electron-hole wave functions equal to 99% over the entire range of field values, leaving the brightness unaffected.

In the next section the process for fabricating electrically functionalized PQDs is introduced.

5.2 Fabrication Process and its Optimization

The main obstacle that PQDs pose to the application of an electric field is their intrinsic three-dimensionality that does not allow for an easy deposition of contacts, be they for horizontal or vertical E-field. In 2016, our group published a manuscript[13] where for the first time electroluminescence of entangled-photons was being demonstrated in PQDs. Selective carrier injection was achieved by making use of the low-resistivity, low-bandgap nanowire that segregates during $Al_xGa_{1-x}As$ growth along the vertical axis of the recess. However, the process that led to contacting both the p- and n- grown layers, which exploits BE, required careful and ad-hoc solutions to be adopted, and in the original design inverse bias did not have significant effects on the excitonic states.

In this circumstance, I replicated the process, optimizing some steps that I believe to be the cause of the original open circuits and high resistance paths, and developed an alternative method that shortens the procedure while increasing the specimen yield as it simplifies the deposition of metal contacts.

GaAs QDs in AlAs

First, we decided to opt for a different epitaxial stack, moving from an $In_{25}Ga_{75}As$ QD in GaAs (Figure 5.2-2-a) barriers to GaAs QD in AlAs barriers (Figure 5.2-2-b) (concentrations values are nominal). Although in the above-cited work (ref 13) electrical injection was successful, upon reverse-biasing the sample, no photoluminescence from any state of the QD was visible from those samples, probably meaning that the charges promoted from the valence to the conduction band by the excitation laser were either swept out of the QDs due to the low confinement potential of GaAs, or were unable to efficiently reach and populate the dot. At T=10K, the flat band model gives a confining energy that is about 400 meV (Figure 5.2-2-a, bottom left), however, considering that the holes are confined less as the difference in bandgap splits as 40/60 % ratio between valence and conduction band[25,26] respectively, the effective confining energy was not preventing the electric field to make charges tunnel out of the dot.

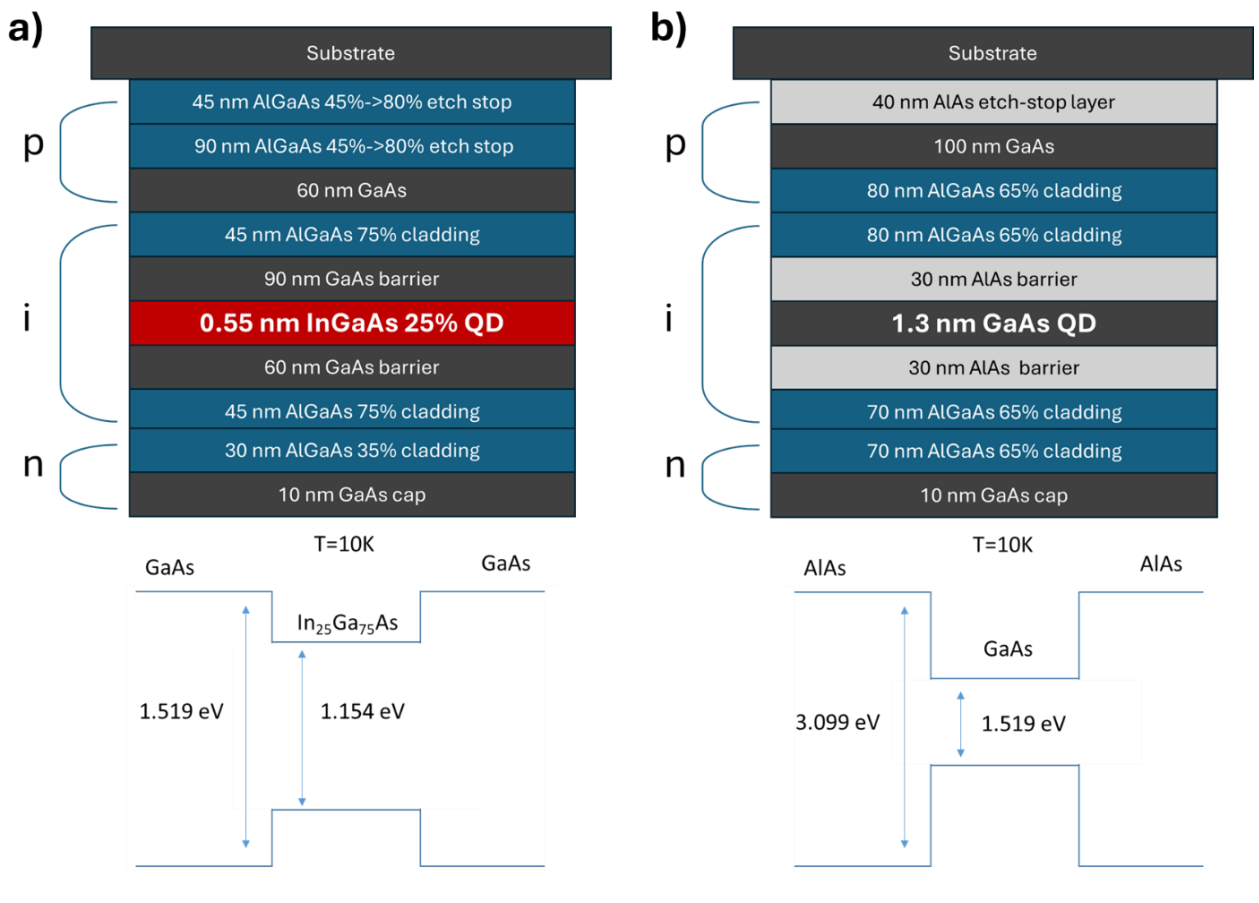

Figure 5.2-1

*Figure 5.2-2 Epitaxial structure (top) and **direct** energy band gap profile for a) $In_{25}Ga_{75}As$ QD in GaAs barriers used in ref. 11 and b) GaAs QD in AlAs barriers used in this thesis work. Thicknesses are all nominal*

The strategy here was to simply increase the difference in energy bandgaps, for this reason we moved to a GaAs dot surrounded by an intrinsic AlAs matrix. Nevertheless, it must be mentioned that the indirect nature of the AlAs bandgap is likely to influence the effective confinement of excitonic complexes: while the ***direct*** confining barrier (**k**=0) for GaAs in AlAs is of

$$\mathrm{E}_{\mathrm{gap}_{\mathrm{AlAs}}}(\Gamma) - \mathrm{E}_{\mathrm{gap}_{\mathrm{GaAs}}}(\Gamma) \approx \mathbf{1.5}\ \text{eV}$$ (at T=10K, Figure 5.2-2-b, bottom right),

the AlAs conduction band minima are the X valleys along the six (100) directions with an indirect energy band gap of $\Delta\mathrm{E}_{\mathrm{X}_{\mathrm{AlAs}}} = \mathrm{E}_{\mathrm{X}}^{\mathrm{c}} - \mathrm{E}_{\Gamma}^{\mathrm{v}} \approx 2.16$ eV, and relative minima are also

found on the L valleys along the (111) crystallographic directions, where the indirect energy band gap is $\Delta E_{L_{AlAs}} = E_L^c - E_\Gamma^v \approx 2.4$ eV[27,28]. Hence, the chosen configuration grants higher confinement than in the InGaAs/GaAs configuration, but likely introduces complex population mechanisms that involve, especially for above-band excitation, phonon-assisted relaxations and tunneling from the X (and probably even L) conduction band valley to the **k**=0 Γ conduction-band minimum of the GaAs QD. Such a picture needs to be kept in mind, as, the application of an electric field could promote carriers' jumps from the QD Γ minimum to local potential valleys (X, L).

Two other important reasons for choosing GaAs QDs confined by AlAs barriers, instead of thick $Al_xGa_{1-x}As$ barriers, were: **i)** to decouple the QD from VQWrs states, which would have otherwise introduced an additional leakage channel and reduced confinement along the [111] growth direction due to the Ga-rich VQWr, and **ii)** to eliminate the possibility of inefficient biexciton-exciton cascade population under a resonant two-photon excitation (TPE) scheme, where the laser energy is tuned to be the average between those of the X and XX. In 2020[29], our group discussed the presence of an acoustic phonon-assisted population of the intermediate exciton state in InGaAs PQDs (Figure 5.2-3). This phenomenon is caused by the peculiar anti-binding biexcitonic state (XX), whose energy lies above that of the exciton (X). The competing phonon-dressed state (strictly speaking, a virtual state) populates the neutral exciton as efficiently as the biexciton-exciton cascade process, thereby compromising deterministic photon emission.

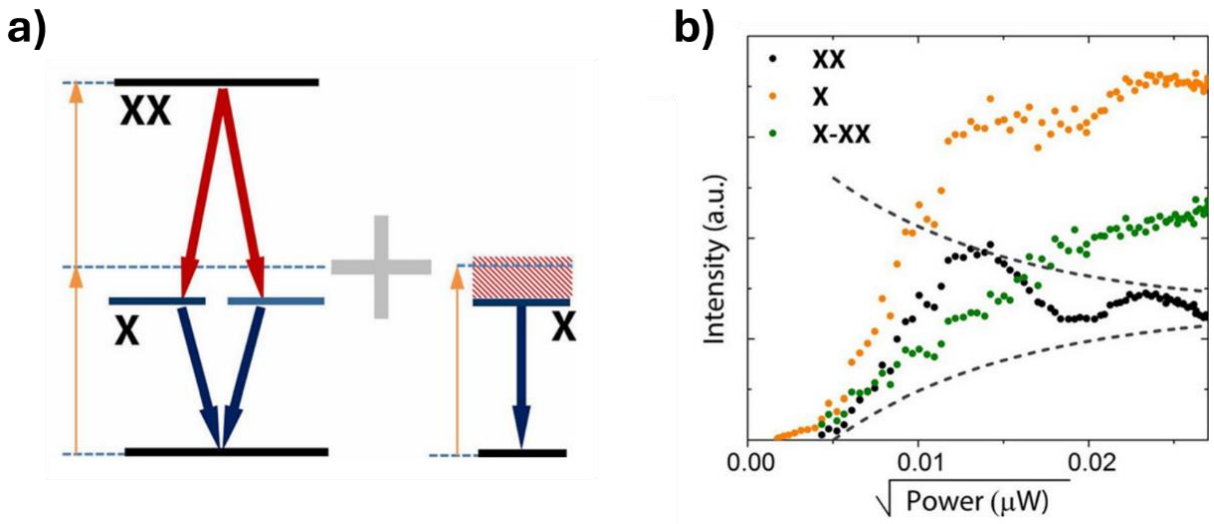

Figure 5.2-3: a) Phonon assisted population of X under TPE resonant excitation when XX is anti-binding and b) Rabi oscillations of X and XX transition and (in green) the X-XX intensity difference demonstrating population of the X state out of the biexciton-exciton cascade mechanism (ref. 27).

As for the composition of the cladding layer grown before and after the AlAs barriers, we chose to systematically employ $Al_{65}Ga_{35}As$ since it combines emission from the VQWr spectrally distant from the QD and a uniformly smooth surface of the last grown layer (Figure 5.2-4-a left and right, respectively). Lower Al concentrations (45%, Figure 5.2-4-b) caused the VQWr emission to almost overlap with the QD one, whereas higher concentrations (85%,Figure 5.2-4-c), although would push the wire emission at even higher energies, led the last grown layer to have irregular and bumpy surface, which we deemed non-optimal for the conformal deposition of a gold contact. We noticed that the AlAs confinement allows for the existence of multiple electronic excited state shells other than the first one involved in the formation of the complexes mentioned throughout the text so far. Such peculiarity, although not investigated during my work, might be the way to implement a lambda system, a three-level quantum system where two lower states are coupled to a common excited state, here envisioned as being shared between two coupled QDs.[30,31]

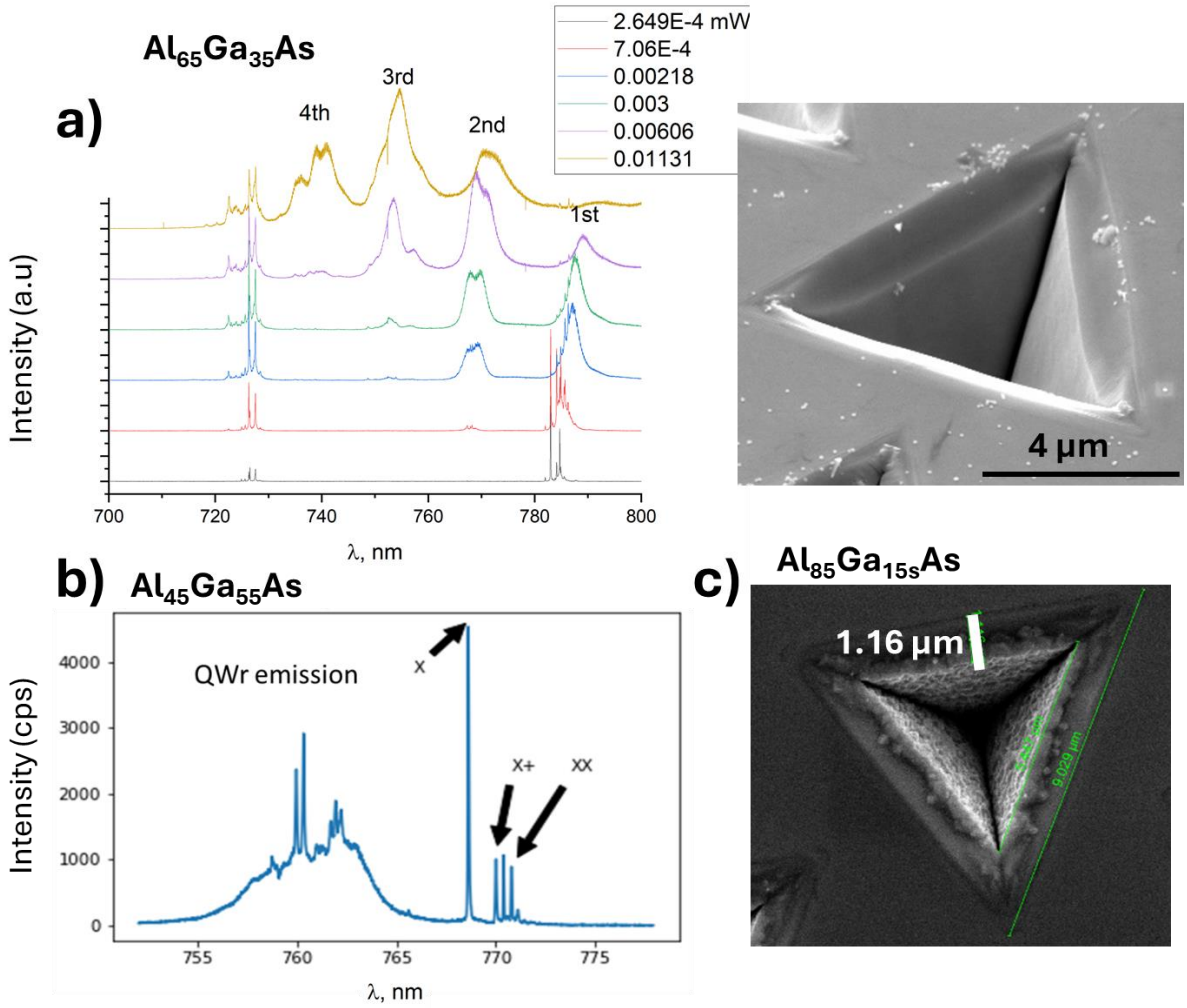

Figure 5.2-4: a) Power dependent spectra of GaAs QD in AlAs, showing the appearance of bound excited electronic states other than the first involved. In this case, the cladding is composed of $Al_{65}Ga_{35}As$ and the VQWr emission takes place between 720 and 730nm, far from the QD transitions, while maintaining a smooth surface of the last grown layer (top right). b) Typical VQWr emission from $Al_{45}Ga_{65}As$ cladding that almost overlaps with the QD states. c) SEM top view of a last grown $Al_{85}Ga_{15}As$ layer, which we decided to avoid in our structures.

Yet, in the Experimental Results section, as well as the outcomes of the GaAs in AlAs configuration, we present results of vertical electric field applied to GaAs QDs with slight adjustments in the confining barrier, as the findings from the GaAs/AlAs configuration gave us reasons to investigate so.

5.2.1 Process steps

Once the quantum dot (QD) is grown and embedded in a p-i-n structure, the next steps focus on contacting the two epitaxial layers. Due to the non-planar nature of the structure and to the triangular concentric geometry, it's impossible to create two separate apertures on the surface to individually contact the p and n layers, as would be the case of an edge emitting laser. Additionally, depositing a metal layer on the top surface would result in a short circuit, as both epitaxial contacts share the same top surface (Figure 5.2-5).

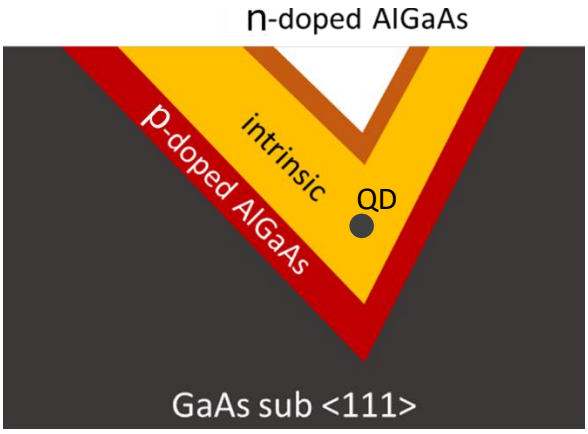

Figure 5.2-5: Cross-section view of a p-i-n structure grown inside tetrahedral recess, highlighting the impossibility to flood evaporate a "back" metal contact since the p-doped(red) and the n-doped(light brown) layers share the same surface .

The strategy for establishing back contact leverages the non-planarity of the structure, allowing for anisotropic deposition of subsequent layers. A 200 nm thick layer of Silicon Nitride (SiN_x) is deposited through PECVD, homogeneously covering the top surface, including the sidewalls of the recesses. Once the dielectric is in place, three subsequent gold evaporations are performed to mask the SiN_x layer everywhere except the bottom of the recesses. Samples are placed upside-down on a copper holder tilted at 55° with respect to the horizontal. This orientation ensures that the vertical evaporated beam of gold cannot deposit on the bottom of the recess, which is shadowed by the sidewall. This step is repeated three times, each time rotating the sample by 120° on the 55°

inclined plane of the copper holder. As a result, only a spot of SiN_x at the bottom of the pyramidal recess remains unprotected. We refer to this process as “triple tilted evaporation” (Figure 5.2-6).

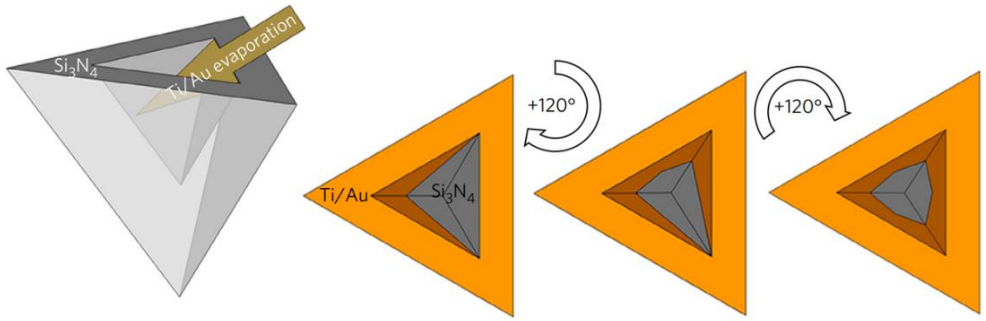

Figure 5.2-6: Triple tilted evaporation, image taken from ref. 11.

A CF4 dry etching step inside a plasma asher is then performed to remove the SiN_x window on the bottom and allow the subsequent gold evaporation, this time with the sample placed perpendicularly to the evaporated gold beam, to exclusively reach the n-epitaxial layer.

After reaching this point, we proceed to process the other side of the wafer. Over the years, it has been proven that exciting through a pyramid with a laser in a tip-up configuration results in significantly higher counts compared to when the excitation reaches the dots from the recesses in the as-grown geometry (see Chapter 4). Additionally, in the case of a p-i-n tetrahedral structure, the only way to contact the first-grown epitaxial layer is from the opposite side. To achieve this, once the n-layer is contacted, we bond the sample in a tip-up configuration to a GaAs (100) carrier, on top of which a layer of SU8 is spun. Bringing SU8 to its reflow temperature (≈250°C) ensures strong adhesion of the sample to the carrier and resistance to any subsequent solvent cleaning steps.

BE procedure described in Chapter 2 is then performed.

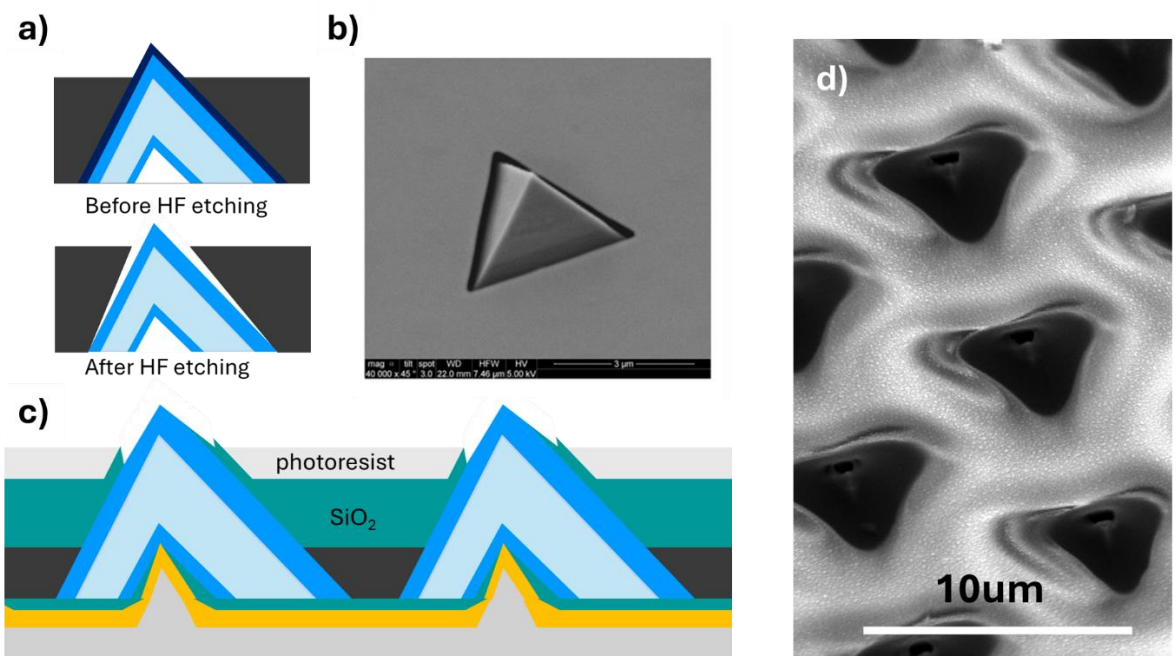

Figure 5.2-7: a) BOE (HF) etching of the AlAs etch stop barrier and subsequent formation of trenches all around the pyramids; b) SEM tilted view of a pyramid that underwent the BOE etching; c) Trenches are then filled with SiO_2 that however has to be removed from the pyramids' tips. SiO_2 on top is removed by masking the surface with photoresist and partially etching it away, a process that exposes the pyramids' tips first; d) SEM tilted view of a sample after partial removal of photoresist and followed by BOE etching.

As a final step before applying the top contact, the Aluminum Oxide formed upon exposure of AlAs etch stop layer to H_2O_2: NH_4OH during BE, must be removed. The sample is dipped in BOE for two minutes, but this step etches the AlAs, leaving trenches about 60 nm wide around the pyramids (Figure 5.2-7-a and -b). To prevent these trenches from interrupting the continuity of the final top contact, Silicon Dioxide is deposited via PECVD on top of the sample. The dielectric layer fills in the trenches and at the same time covers the n-epitaxial contact. Like the process for the n contact, where a small area is targeted, we must selectively remove the SiO_2 from the tips of the exposed pyramids. To do so, S1813 positive photoresist is spun onto the sample and then etched back through oxygen plasma ashing in consecutive steps, with SEM inspection after each step to determine the level of tip exposure. Once the tips are partially exposed, a brief dip in BOE etches away the unprotected SiO_2 (Figure 5.2-7-c and -d). The sample is

then ready for the final evaporation, where a semitransparent Ti/Au (3/20 nm) contact is deposited.

Finally, gold is evaporated to contact the p-epitaxial contact. The structure looks like this:

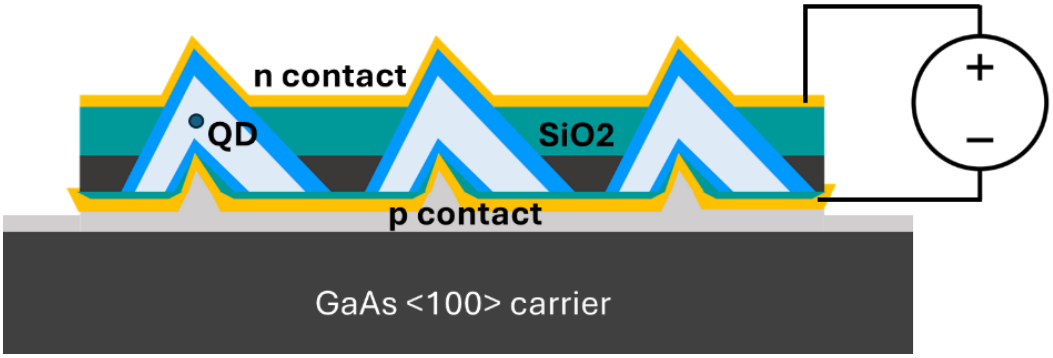

Figure 5.2-8: Schematic representation of a pyramidal p-i-n junction after is electrically functionalized.

5.2.2 Optimizations

Altogether, the process is complex, comprising many steps, some of which are intrinsically destructive (e.g., wet etching, grinding). This complexity results in a low throughput of completely processed and ready-to-measure samples.

In the following paragraphs, some of the major setbacks discovered during the analysis of the process are listed, together with the strategy to circumvent them:

Triple tilted evaporation and window etching

For the triple tilted gold evaporation, for each evaporation we used to deposit 5/20 nm of Ti/Au, and after etching the sample with CF_4 in the plasma asher at 70 W. Taking a closer look with the SEM, we discovered that the ashing step was etching away not only the bottom window, but also the SiN_x deposited at the intersections of the sloped sidewalls of the recess, causing the gold mask to lift off, and potentially removing the mask on the planar surface. The first solution adopted was to lower the CF_4 plasma power and increase the duration of the etching, however SEM inspection revealed a

swollen residual dielectric layer (Figure 5.2-9-b) that would have surely impeded the bottom contact to touch the doped layer. In these circumstances, we couldn't reduce the ashing power. We figured out that, during the triple evaporation, the superposition of the "shadow" of each sidewall projected onto the other two walls is such that the central regions of the sidewalls were covered by gold twice (Figure 5.2-9-a, layers labelled with "2"), whereas the areas corresponding to the intersections were being covered only once (Figure 5.2-9-a, layers labelled with "1"). The 25 nm Ti/Au layer was evidently too thin (and porous) to prevent plasma reaching the SiN_x layer. We then tweaked the process by increasing the thickness of each deposition by 40 nm, for a total of 65 nm per evaporation. Furthermore, to avoid any complication from the CF_4 plasma ashing, which although being effective with SiN_x, is also aggressive towards GaAs and interacts non-trivially with AlGaAs, we decided to perform the removal of the bottom dielectric mask using BOE, whose employment revealed to be exceptionally good in accomplishing the task. Such wet etching is even more effective than CF_4 ashing against SiN_x (etching time shrinks from several tens of minutes to ≈1 minute), and since we haven't noticed any gold mask detachment due to lateral under-etching, we decided to adopt it consistently. Successive experiments proved SiO_2 to work as well as SiN_x as protective mask, further reducing the etching time (Figure 5.2-9-c).

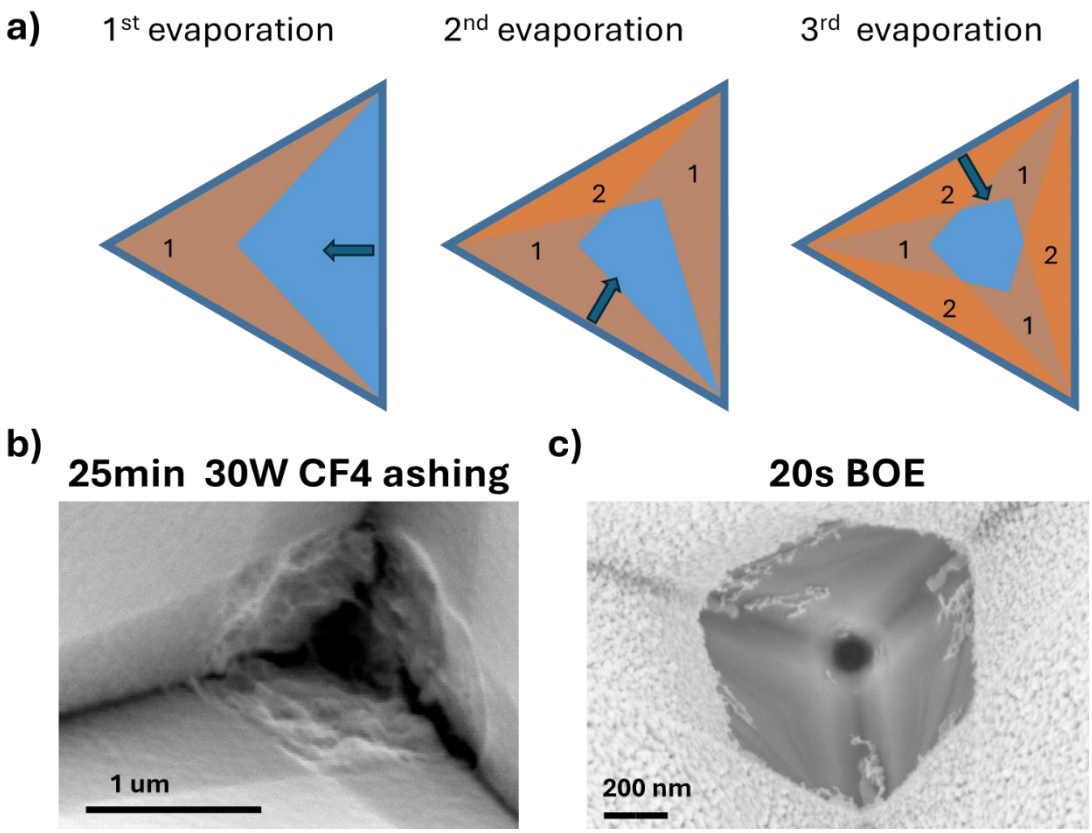

Figure 5.2-9: a) At the end of the triple tilted evaporation, regions on the sidewalls (labelled with 2) are covered with twice the amount of gold of that is deposited in correspondence of the grooves regions (labelled as 1). For a thin evaporation, regions 1 don't prevent etching the dielectric mask underneath, introducing the risk of lifting off. The arrows indicate the direction of impinging evaporated metal; b) Bottom of a recess partially protected by gold, where the low power CF_4 plasma ashing results ineffective in removing the dielectric mask; c) Bottom of a recess partially protected by gold where wet etching of the dielectric (SiO_2 in this case) using BOE deliver fast etching rates and effective removal of the material.

To be noted, a true game-changing improvement would be the deposition of the dielectric mask through e-beam evaporation, as it would allow defining the aperture with the triple tilted evaporation sparing the subsequent etching step. Also, in this way, the costly Ti/Au evaporation would be spared as well and employed only for the actual deposition of the contact.

Parallelism

An ideal sample would be a sample where, after the back etching process with H_2O_2:NH_4OH, the pyramids were all homogeneously exposed, meaning that across the

whole back-etched area, an inspection with the optical microscope would reveal triangles roughly all the same dimensions. However, the bonding steps performed to first glue the sample to a carrier and then the sample/carrier to a glass slide, introduce a tilt between the surfaces that come into contact. In case of a sample where an apparent tilt is measurable with a simple profiler, the grinding step would enhance the tilt, even till the point of breaking the sample itself. Moreover, an additional non-uniformity is introduced during grinding because of debris of sample acting as grinding elements, wearing off of the grinding plate and a slight non-orthogonality of the piston of the jig to the plate.

After the grinding, the sample goes through a chemical etching, which takes away GaAs with a rate that is roughly the same in each point of the surface undergoing the process, causing the sample thickness to shrink but maintaining the tilt of the plane. The result is a back etched surface where the pyramids at the thinnest side are exposed way before the pyramids at the thickest side: the more a pyramid is exposed to the etchant, the more likely it is that the etching will spoil the QD states introducing surface states which could badly affect the dots.

There is no way of getting rid of issues introduced by the polishing machine other than resorting to a better planarizing system. The commercially available way of minimizing the impact of grinding on the samples are bonding jigs (Figure 5.2-10-a), which, thanks to the spring system they are endowed with, can exert a downwards force on the top of the sample, meanwhile bonding to its carrier or glass slide. The idea is that the more parallel the top surface of the sample is to the top surface of the carrier to which is bonded, and, to the top surface of the glass slide to which the carrier is glued, the less likely the sample is to be broken or come out of the grinder with huge height difference between two points. However, such solutions, although effective with 2- or 3-inches wafers, are dangerous with small pieces and can lead to even more pronounced tilts. So far, the best way of achieving parallelism has been to manually push down the sample/carrier onto the glass slide during the cooldown of the wax using tweezers. Usually, a homogeneous spreading of the wax, like to one shown in Figure 5.2-10-b,

leads to a height difference between two extremes of the sample within the 10-µm sensitivity of the height gauge.

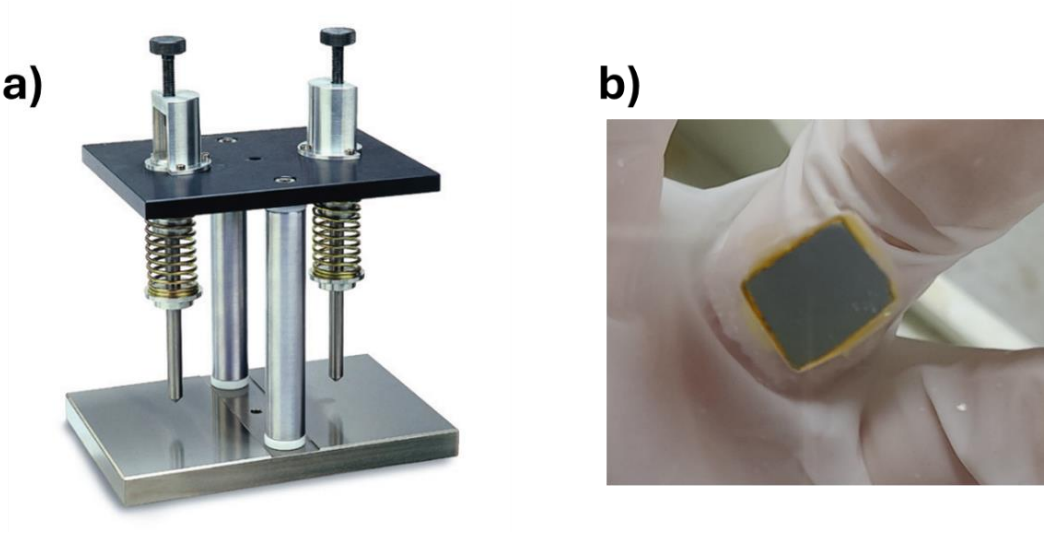

Figure 5.2-10: a) Commercially available mounting jig; b) picture of the back side of a sample bonded to a glass slide through wax. Visual inspection to ensure even spreading of the wax underneath the sample has been revealed to be crucial for minimizing sample tilt during grinding, which helps achieve uniform material removal and consistent thickness.

Back etching

One of the undesired effects of the back etching is the resulting bumpiness of the surface surrounding the pyramids: using NH_4OH:H_2O_2 - 3:100 where NH_4OH is 8.28M, leaves 60-100 µm wide, 1-2 µm deep irregular pits on the surface, which could introduce a potential discontinuity in the thin top gold contact. Even if the occurrence of this eventuality is reduced by the deposition of a layer of SiO_2 (as mentioned before), the layer would anyway follow the profile of the surface having a very light smoothing action, taking into consideration also the fact that there would be a thin layer (200 nm or less). At the optical microscope a surface etched with the BE solution looks like in Figure 5.2-11-a.

The molarity of the ammonium hydroxide was reduced to 4M, 2M, and 0.828M, and the etching, maintaining the same NH_4OH:H_2O_2 - 3:100 ratio, was performed on the back of dummy (111) substrate. Using NH_4OH 4M shrinks the pits to a width of 40/60 µm (Figure

5.2-11-b). In contrast, the 2M solution makes the pits disappear but leaves a rough surface, complicating the spotting of pyramids in the optical setup as the surface doesn't reflect as well as with the other two concentrations (Figure 5.2-11-c)). Lastly, the 0.828M solution stands out among the others: as shown in Figure 5.2-11-d), the BE region doesn't show any pits of the kind observed so far. Instead, the etching action is so smooth that the morphology of the original pits of the (111)A surface is preserved. Under the SEM, the back-etched surface with NH_4OH {0.828M}:H_2O_2 - 3:100 appears as shown in Figure 5.2-12-a and -b.

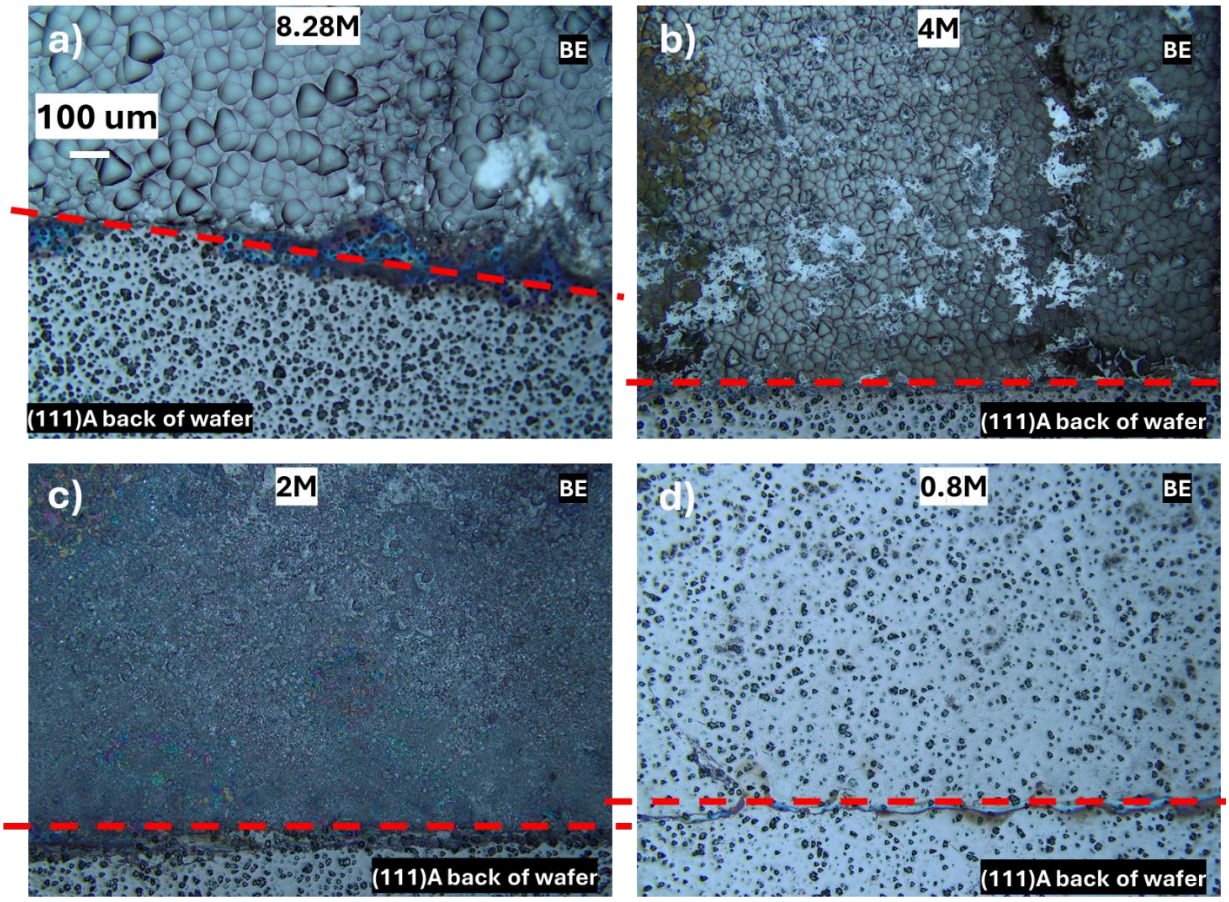

Figure 5.2-11: Back-etching of the (111)A surface using NH_4OH:H_2O_2 (3:100) with NH_4OH molar concentrations of a) 8.28M (as purchased), b) 4M, c) 2M, and d) 0.828M. In each image, the etched region is located above the red dotted line, while the area below was masked with Kapton tape to prevent etching

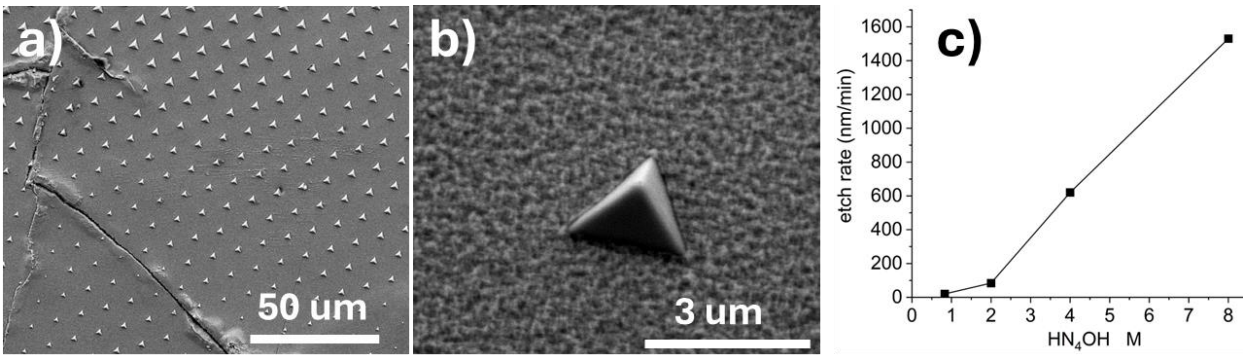

Figure 5.2-12: SEM a) top view and b) close up on single pyramid of 0.828M NH_4OH:H_2O_2 (3:100) back-etched PQD sample. c) Dependence of etching rate on NH_4OH molarity (M)

Obviously, such an improved surface comes with a trade-off in etching speed, which reduces from approximately 1.5 µm/min at 8.28M to about 15 nm/min at 0.8 (Figure 5.2-12-c).

Tip exposure and top contact evaporation

The final step of exposing the tips of the pyramids by etching the dielectric coating, which involves the partial etch-back of a photoresist, is a functional step of the process and does not introduce problems per se. However, the tilt of the plane and the non-homogeneous exposure of the pyramids across the sample lower the specimen yield: although the dry O_2 ashing acts homogeneously, some tips will be unavoidably exposed more than others, and some will not be exposed at all. This is a major issue as the barely exposed pyramids usually have a clear spectrum due to the reduced interaction time with the BE solution and high brightness due to geometrical considerations (see Chapter 3). To increase the number of good pyramids to contact, we first investigated the effect of different deposition methods. By substituting PECVD SiO_2 with PECVD SiN_x, we obtained a non-conformal deposition (Figure 5.2-13-a), which is not optimal for the subsequent thin contact evaporation. However, it is notable that SiN_x deposited only in the spaces between the pyramids, leaving the tips uncovered. This outcome could have simplified the process by allowing us to skip photoresist (PR) deposition, PR etch-back, BOE etch of SiN_x, and PR stripping. Unfortunately, PL measurements showed no

emission from the QDs, so we decided to abandon this method. Pursuing the same objective, we tried depositing the dielectric mask by sputtering SiO_2 on the sample. It is well known that sputtering is generally more directional than PECVD[32], which, on the other hand, more easily adheres to the sample topology. The sputtered layer (Figure 5.2-13-b) accomplishes the task of filling the trenches left from the AlAs wet etching, while uniformly depositing on the planar surface between the pyramids and poorly adhering to their sidewalls. A quick wet etch step in BOE removes the clusters of SiO_2 that stick to the sidewalls without completely etching away the flat layer deposited. We adopted this procedure as standard since samples processed this way consistently showed PL.

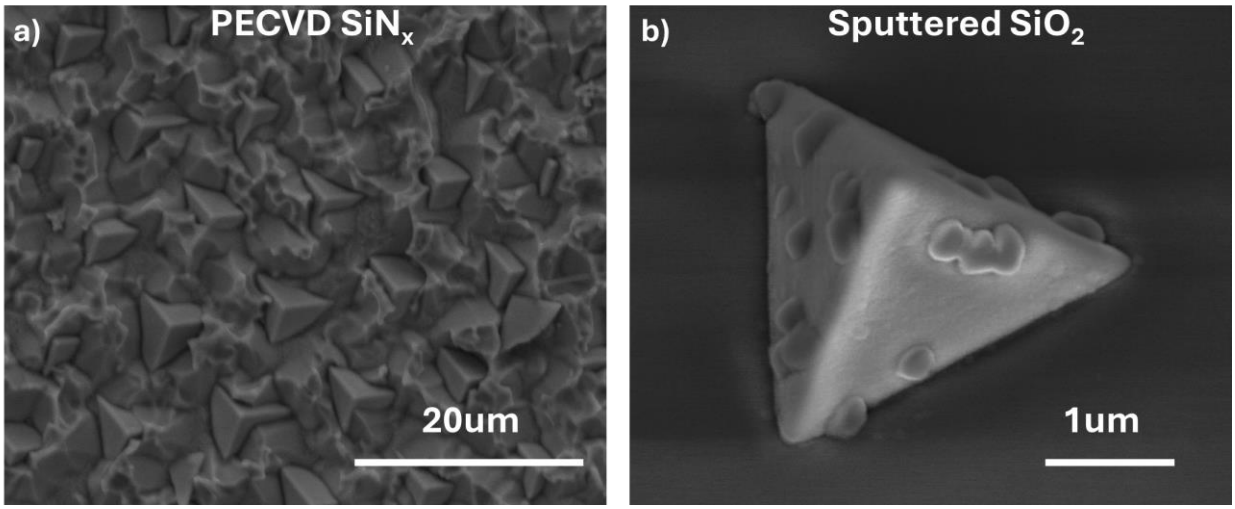

Figure 5.2-13: Back-etched surface covered with a) PECVD SiN_x and b) Sputtered SiO_2. Although the first case seems optimal as the dielectric doesn't deposit on the sidewalls of the pyramids, PL was never observed from such configuration. On the contrary, sputtering SiO_2 allowed for process simplification without altering the photoluminescence.

This last point is crucial because a reliable process ensures that any issues detected during PL measurements can be attributed to the fundamental interactions of the electric field with the QDs, rather than to any of the steps involved in functionalizing the tetrahedral p-i-n junction.

Once the dielectric is put down, the top metal contact is evaporated. The layer that supplies voltage to the pyramids must be thin enough to act as semi-transparent contact. This requirement contrasts with the need for a thick metal pad to establish good electric contact with the probe. To circumvent this issue, two sets of copper masks/stencils with a partially overlapping pattern were employed. First, the 3:15 nm Ti/Au contact is evaporated through a copper stencil with a fine square grid. Then, a thicker 5:150 nm Ti/Au metal pad is deposited through a coarse square grid copper mask (Figure 5.2-14).

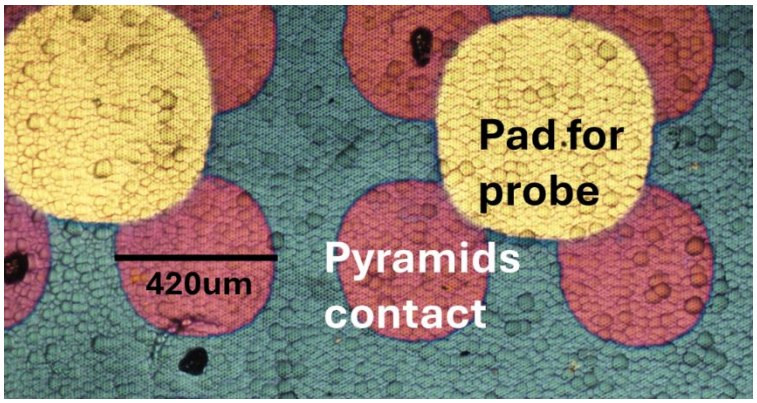

Figure 5.2-14: Top view of fully processed sample where bigger Ti/Au contacts for the probe partially overlap smaller and thinner top contact that supply the voltage to the p-i-n structures. The difference in colors is due the thickness of the Ti/Au contact: the thin semitransparent "Pyramids contact" appears in a shade of red on top of the GaAs, whereas the thick "Pad for probe" takes the well-known yellowish shade of Gold.

5.2.3 Mirrored n-i-p Pyramids

In Chapter 2, the advantages of the mirrored pyramid structure have already been mentioned. This process eliminates the need for grinding and back etching, and it simplifies the evaporation for one of the two contacts. QDs designed to interact with electric fields in the mirror configuration are grown on an n-doped substrate. During growth, the doping is swapped: first, the n epitaxial contact is grown on the n substrate, followed by the intrinsic layer, and finally, the p epitaxial contact. The effectiveness of

this process resides in its simplicity, the higher specimen yield (optically accessible pyramids/total number of pyramids), and its brevity.

After the recesses are turned into mirrored pyramids (see Chapter 2), the first step involves evaporating a Ti/Au 10:100 nm metal contact on the backside of the n-doped substrate. The top metal contact, which is deposited through the same copper masks mentioned earlier, must not touch the dry-etched surface indiscriminately. This situation is similar to the one faced with the triple tilted evaporation: although the p and n epitaxial contacts no longer lie on the same plane, they belong to the same continuous surface, hence a non-selective "flood" evaporation would cause a short circuit. To selectively evaporate gold on the p-type tips of the mirrored pyramids, we used the same process that was however eliminated in the tip-up p-i-n configuration. First, the top of the sample is covered with 100-200 nm of PECVD SiO_2, and S1805 positive PR is spun on the surface. A short O_2 dry etching step in an ICP chamber removes the thinner PR layer on the tips, exposing the SiO_2 protective layer.

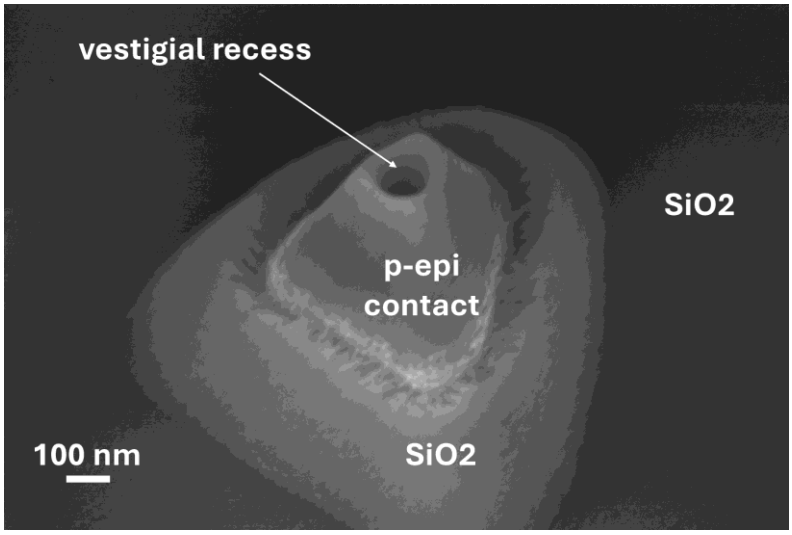

Figure 5.2-15: Tilted SEM view of a mirrored n-i-p structure, prepared for the evaporation of the top contact. The SiO_2 PECVD layer uniformly covers the substrate surface, effectively preventing any short circuit between the n-doped substrate and the p-doped epitaxial layer. Care must be taken when partially removing the dielectric to expose the tips, as BOE is highly aggressive towards SiO_2.

A quick BOE bath (5 to 10 seconds) etches away the mask, leaving the surface uncovered (Figure 5.2-15, *p-epi contact*). Finally, the PR is stripped away with acetone, and the double set of metal contacts is evaporated.

5.3 Experimental results

5.3.1 Back-Etched samples

GaAs QDs in AlAs barriers

Analysis of the PL spectra of GaAs PQDs in AlAs barriers under the application of a potential difference shows a negligible Stark redshift of some excitonic lines (X_{10}, X^{+}_{20}, X^{-}_{10}) when the junction is forward biased from 3V to 5V, and current is being injected (Figure 5.3-1-a). This Stark shift cannot be attributed to the influence of the electric field, since, in forward bias, the electric field of a p-i-n junction tends to decrease due to energy band flattening. Most likely, the current passing through the junction leads to power dissipation and local temperature increases, decreasing the magnitude of the band gap, even if this is not easily testable with just our data. Under such conditions, we were able to clearly identify the negative trions (labelled as X^{-}_{10} and X^{-}_{01} in Figure 5.3-1-b), whose intensity significantly increases under current injection. Simultaneously, the heavy-hole neutral exciton X_{10} remains well-defined, whereas the light-hole neutral exciton X_{01} becomes poorly confined, resulting in a decreased detector count. Reducing the forward bias causes the intensities of X^{-}_{10} and X^{-}_{01} to drop. Over a wide voltage range, the spectrum is almost unaffected by the increasing electric field until around 0V, when transitions from positive hot trions—formed by an electron in the conduction band and two holes, one in the heavy-hole band and the other in the light-hole band (X^{+}_{11} and X^{+}_{11}, bottom of Figure 5.3-1-b)—become bright. At the same time, neutral excitons X_{10} and X_{01}, along with the biexciton $2X_{20}$, cease to be populated.

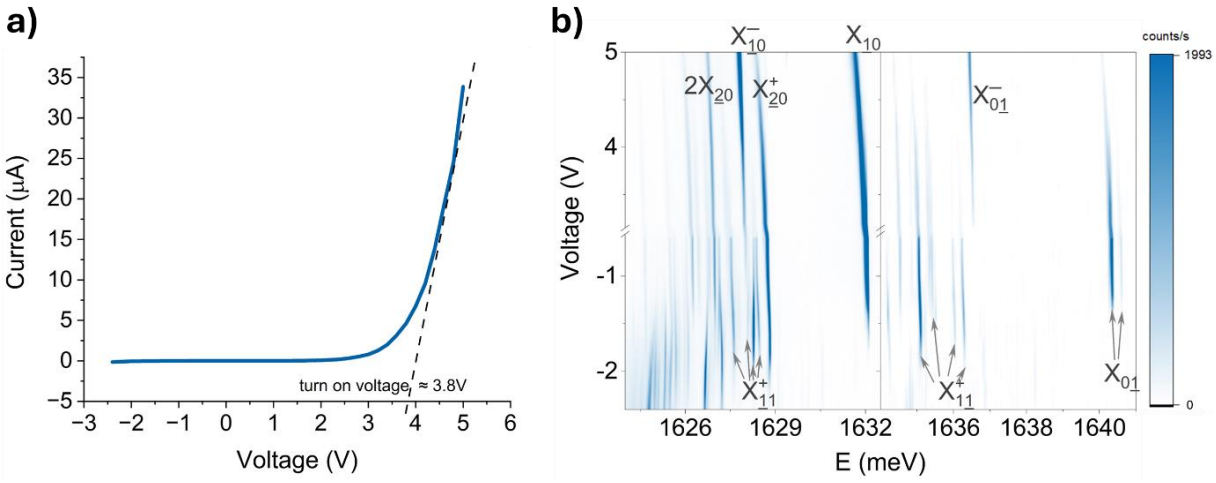

Figure 5.3-1: a) I-V curve of pyramidal p-i-n junction; b) GaAs QD in AlAs barriers PL dependence on applied voltage. We observe a possible feeble Stark shift of excitonic lines, but the passage from positive to negative bias clearly evidences a charge tuning mechanism, for which negative and neutral states cease to be populated when the reverse bias deepens, in favor of positively charged complexes.

The inability to tune the energy of the transitions over such a wide range of applied voltages is not easily attributable to a specific mechanism. However, we can speculate under certain assumptions: presuming, as suggested by Huang et al.[22], the absence of a permanent dipole moment due to the inherently homogeneous composition of the dot and its high symmetry[33], we could argue that very low polarizability is responsible for this outcome. As discussed above, polarizability depends on the size of the dot as well as the height of the confining barrier. A larger (in this case, taller) QD allows the wave-functions to be pulled apart. Similarly, the same effect can be achieved by modulating the barrier height: the ideal finite square well potential problem[34] predicts that the wavefunctions penetrate the barriers with an exponentially decaying probability, where the decay constant ($\alpha = \sqrt{2m(V_0 - E_i)}/\hbar$) is proportional to the difference between the energy height of the barrier V_0 and the energy of the eigenstate E_i associated with the wavefunction under consideration. The AlAs barrier, being the tallest we can grow, might be preventing the wavefunctions from penetrating, thereby inhibiting the establishment of an induced dipole moment.

To further investigate this hypothesis, the confining barriers were deliberately lowered.

GaAs QDs in $Al_{65}Ga_{35}As$/AlAs barriers

The epitaxial structure was adjusted by reducing the thickness of the AlAs barriers that sandwich the dot by 10 nm. Additionally, a 10 nm confining $Al_{65}Ga_{35}As$ barrier was interposed between the AlAs and the QD layer on each side (Figure 5.3-2). As we mentioned previously in Chapter 2, Ga-rich VQWrs form along the vertical axis of the recess when AlGaAs is grown, introducing an even more complex confining profile. It's been shown[35] that careful epitaxial engineering of alternating AlGaAs layers of different concentrations grown in pyramidal recesses allows control of optical polarization of the emission, switching from QD-like to VQWr structures by only adjusting the thickness of the active AlGaAs layer. Nevertheless, we exploited such configuration to reduce the height of the barriers around the GaAs QD and test the Stark effect on a dot with a supposedly greater polarizability.

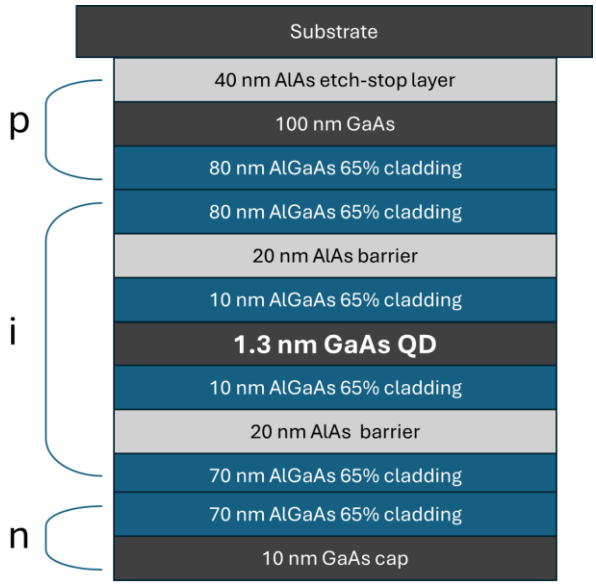

Figure 5.3-2: Epitaxial stack of a p-i-n GaAs dot in $Al_{65}Ga_{35}As$/AlAs. The overall structure remains largely unchanged compared to the GaAs dot in AlAs, with Ga introduced only in the 10 nm layers before and after the dot.

The results did not confirm our hypothesis: not only did we observe no monotonic and consistent redshift upon applying a reverse bias, but for the transitions to be clearly

defined, and thus for the states to be populated under optical excitation, we had to forward bias the diode and inject current. Figure 5.3-3-b shows how the X_{10} and X^{+}_{20} transitions start to be well defined around 3.5 V, when current is passing through the structure (Figure 5.3-3-a, blue curve)($2X_{20}$ is fainter). PL spectrum is initially very strongly positively charged, shifting towards neutral over the end of voltage range. The linewidth dependence on voltage is nonmonotonic – there is no significant reduction. For the analysis, the X_{10} single peak is used: one can see an increase from ≈70 to ≈100 μeV and then drop to ≈75 μeV (Figure 5.3-3-a, orange curve). During the broadening phase (3.5-4.7 V), the emission energy gradually redshifts by ≈15 μeV, likely due to a minor Stark effect and possible distant buildup of charges; from 4.7 V it blueshifts by ≈25 μeV. In this last phase intensity saturates.

Giving the flat band condition we induced in the junction, the effect of a residual electric field of the intrinsic region can most probably be set aside. We speculate that the transitions underwent a complex evolution because of the presence of localization centers states near the QD. In 2012, Houel et al.[36] investigated the influence of local fluctuations of hole charges on the spectral stability and linewidth broadening of excitonic transitions. In their study, holes population was generated by illuminating the sample with an off-resonant laser, while the QD was excited resonantly. The QD PL showed a clear threshold-like dependence on the off-resonant power, exhibiting discrete red-shifting jumps and a broadening of the transition's FWHM. The authors showed that individual holes accumulate at the interface between the 30 nm-thick GaAs cap layer and the AlAs/GaAs superlattice blocking layer. The discrete nature of the trapped holes population reflects discrete fluctuations in the exerted electric field. When the interface was placed 150 nm away from the QD, the spectral fluctuations disappeared and the linewidth narrowed significantly, indicating a reduction in the hole-induced electric field at the QD location.

Translating this scenario to the case of GaAs QDs embedded in $Al_{65}Ga_{35}As$/AlAs, it is important to note that the cap/blocking layer interface ($Al_{65}Ga_{35}As$/AlAs) lies only ≈10 nm or less from the QD. In this context, spectra were obtained under above-band excitation,

which not only populates the QD states but also causes holes accumulation at the interface. The fluctuating electric field induced by the hole distribution might be steadily reduced by the increasing current passing through the junction as the forward bias is raised, since it would translate to an increasing hole recombination rate as opposed to a constant holes promotion rate into the valence band, by means of the CW off-resonant laser. In support of these views, first, we notice that, simultaneously with the X_{10} peak redshift, the line broadens (Figure 5.3-3-c), reflecting an increase in the holes' electric field strength[36]. From 4.7 V onwards, a trend reversal is witnessed, where, in correspondence of the peak blueshift, the linewidth narrows.

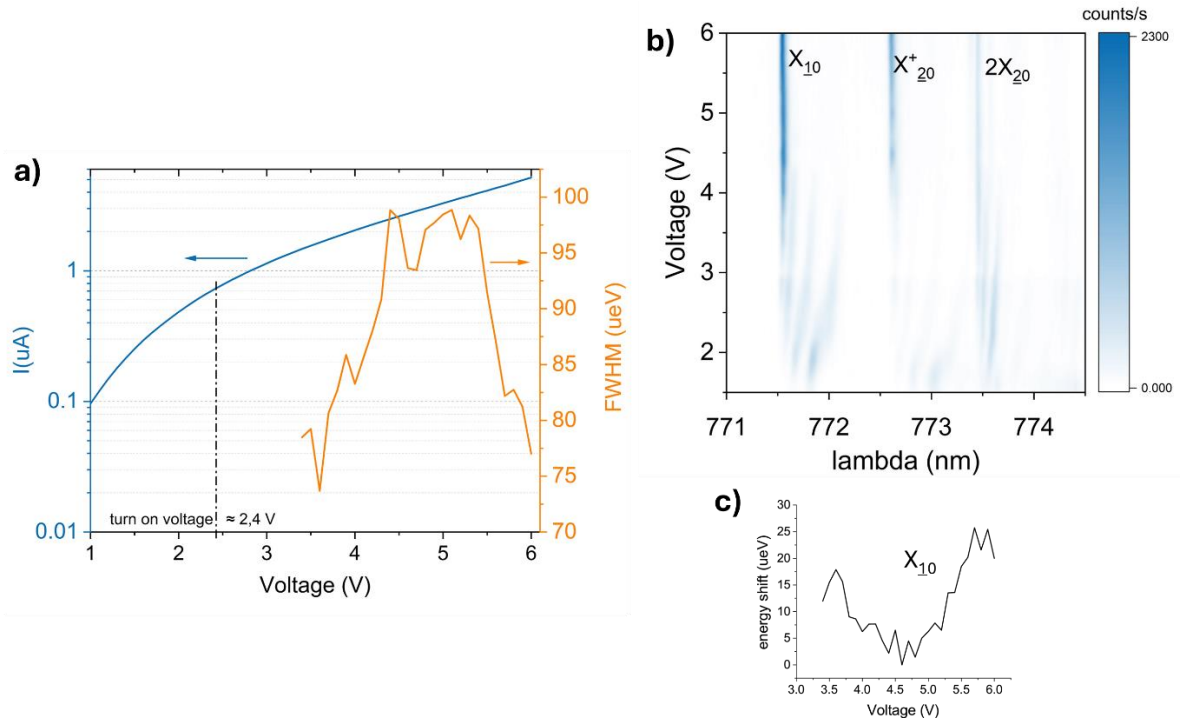

Figure 5.3-3: a) I-V (semilogarithmic) characteristic of the p-i-n GaAs dot in $Al_{65}Ga_{35}As$/AlAs structure (light blue) and X_{10} FWHM dependence of on Voltage (light orange). b) PL dependence on applied voltage: compared to the GaAs QD in AlAs, fewer confined *states are present (X_{10} and X^{+}_{20}), and they appear clearly defined only under forward bias. c) The linewidth increases in correspondence of a mild red shift of the emission, until 4,7 V, when inverts the trend simultaneously with a blueshift of the peak energy.*

The nonmonotonic behavior may arise from a complex interplay between: (i) the electric field in the junction, which must be very low to allow the population of complexes; (ii)

the current, which can both screen the fluctuating electric field of the holes and contribute to their annihilation; and (iii) the hole generation rate, which depends on the off-resonant laser power.

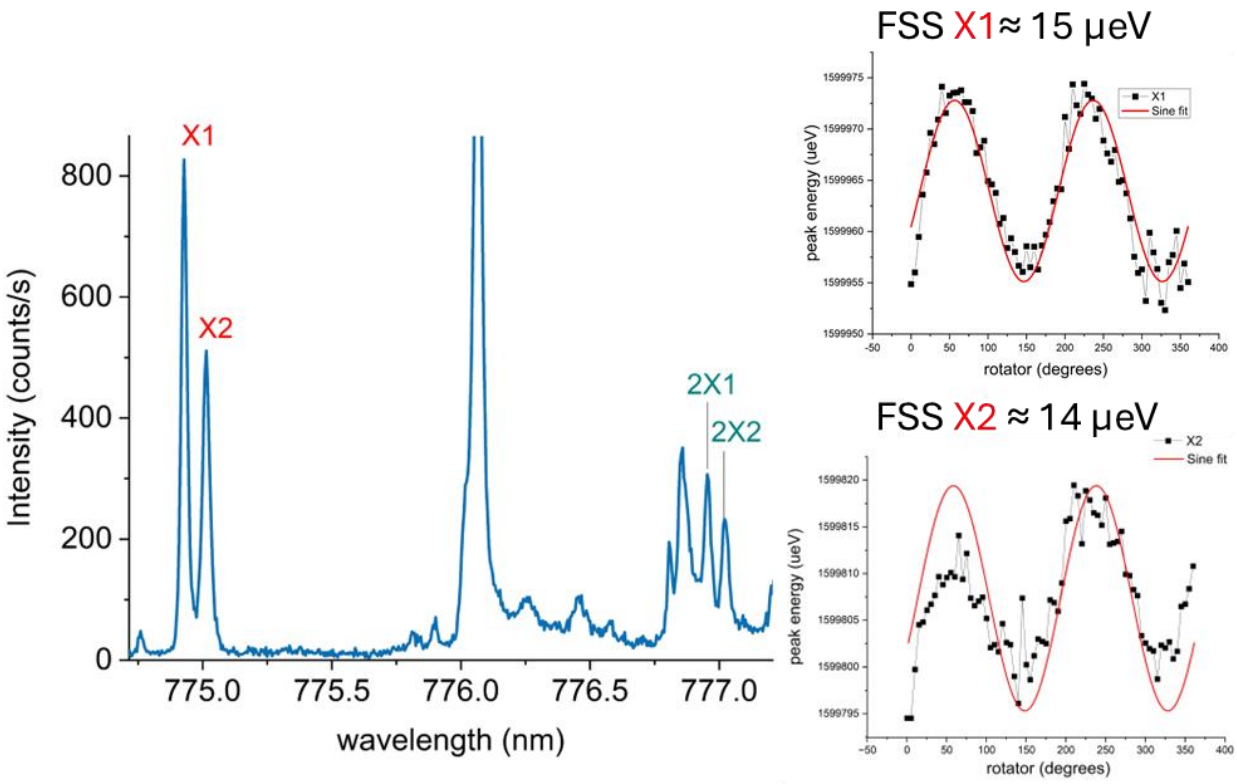

Figure 5.3-4:PL spectrum for V=2.4V. X_{10} redshifted replicas labelled X1 and X2, and $2X_{20}$ replicas labelled as 2X1 and 2X2 are confirmed as such by FSS measurement. Top and bottom insets show the FSS of X1 and X2 respectively.

This framework may also explain the presence, and the subsequent disappearance upon forward biasing the junction, of the double set of three and two transitions on the right side of the X_{10} and $2X_{20}$ lines, respectively, seen in Figure 5.3-3-b. Under the influence of the hole-induced electric field, the emission energy fluctuates widely, resulting in redshifted replicas of the transitions. The hypothesis of discrete jumps of transitions is supported by FSS measurement. Figure 5.3-4 shows the PL spectrum of a QD obtained at fixed biasing voltage of 2,4 V, where two sets of measured doublets are highlighted: X1 and X2 are identified as the same exciton as they both show FSS of 14-

15ueV (insets of Figure 5.3-4). Probing the biexcitonic replicas, 2X1 and 2X2, revealed similar FSS values. They appear in such a way that the peaks at the lowest energies are populated first, consistent with the scenario of high hole concentration at low voltage/low injection current. It is likely that the low-energy replicas are associated with a higher and discrete number of localized charges. As current injection increases, hole recombination becomes more efficient, suppressing the recombination events responsible for the redshifted replicas.

A compelling example of charge tuning—occurring during carrier injection—is provided by Figure 5.3-5-b, which reveals clear, discrete transitions between excitonic complexes differing by a single charge carrier ($X^{+3}_{22} \rightarrow X^{+2}_{21} \rightarrow X^{+1}_{11}$). While discrete spectral jumps we just attributed to changes in the local charge environment likely due to fluctuations in nearby localization centers affecting the quantum dot, are still observed, they appear mainly for X_{10} and X^{+1}_{20} transitions. Importantly, the fine control over the charging state has enabled the unambiguous identification of two rarely observed excitonic species: the doubly (X^{+2}_{21}) and triply (X^{+3}_{22}) positively charged trions (bottom right of Figure 5.3-5-b). The doubly charged positive trion had been previously proposed, and it is here definitively confirmed. Its fine structure, characterized by two linearly polarized doublets and an unpolarized high-energy transition, is in excellent agreement with previous reports[37]. The triply charged positive trion is reported here for the first time; as both lowest-energy valence states are filled with holes, its recombination results in a single, circularly polarized transition—analogous to the well-known ground-state single positive trion (X^{+}_{20}). Highlighted in figure Figure 5.3-5-b is also the hot trion X^{+1}_{11}, of which 4 transitions, very clearly visible in the GaAs dot in AlAs barriers, only three are identified here. Hot trions, along with the full spectrum of excitonic complexes that populate GaAs quantum dots, are extensively characterized in *Advanced Micro-Photoluminescence Spectroscopy of Pyramidal Site-Controlled Quantum Dots as Spin-Photon Interfaces*, a PhD thesis by my former colleague Francesco Mattana (UCC). This manuscript remains unpublished at the time of writing.

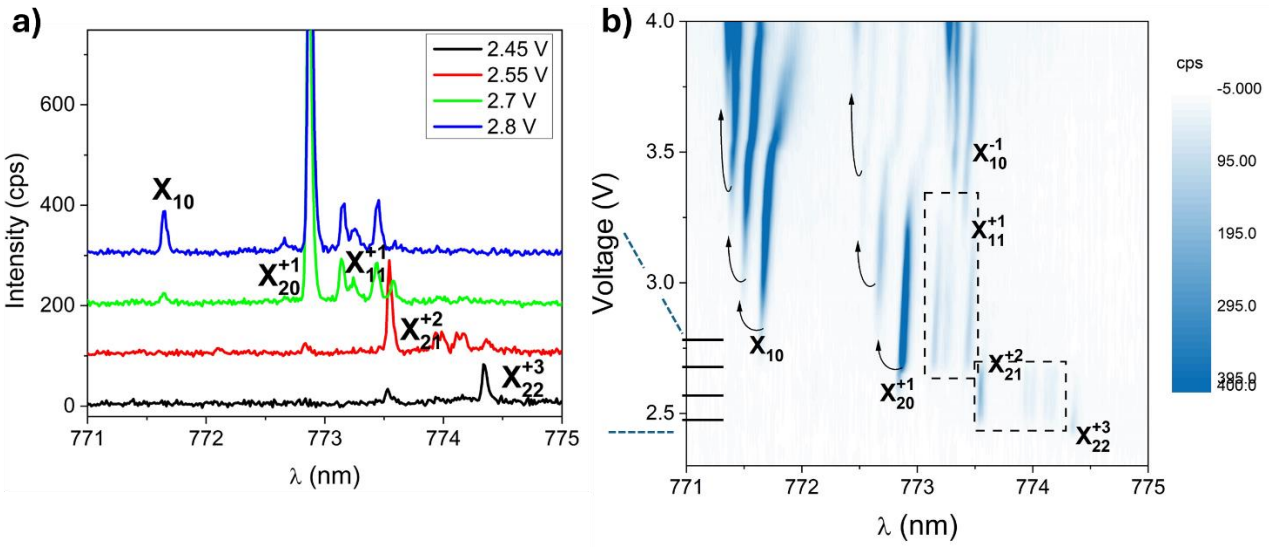

Figure 5.3-5: a) Single line spectra of at 4 different voltage values highlighting charge tuning; b) Full spectrum dependence on applied voltage. For X_{10} and $X^{+1}{}_{20}$ discrete jumps of the transitions are highlighted with arrows. Charge tuning is also observed for longer wavelengths as the $X^{+3}{}_{22}$ turns into $X^{+2}{}_{21}$, which eventually becomes $X^{+1}{}_{11}$ as current injection increases.

When TPE (two photon excitation) is performed, the picture changes slightly: excitons and biexcitons get populated at lower biasing voltages, with the most interesting feature being the possibility of exploiting the forward bias to go in and out of the resonance (Figure 5.3-6-a). The feeble Stark shift observed might be the result of a cleaner environment with respect to the above-band excitation scheme, where free charges promoted into the conduction band (and the holes accumulation layer discussed above) could be screening the QDs from the electric field in the intrinsic region of the junction. When approaching the out-of-resonance condition and due to increased negative charging of a QD, the $2X_{20}/X_{10}$ cascade becomes less efficient and a negative trion $X^{-}{}_{10}$ is populated through phonon-assisted excitation.

Moreover, although we were interested in tuning the transitions' energy and the energy splitting of the two X_{10} states, we weren't expecting to be able to witness electroluminescence from the QDs as we were retaining the 20 nm nominally thick AlAs barriers too tall to populate the QD in forward bias. Be it by tunnelling through the

barriers or through some phonon-assisted relaxation, it should be underlined that this is the first time electroluminescence (EL) is obtained from GaAs PQDs (Figure 5.3-6-b).

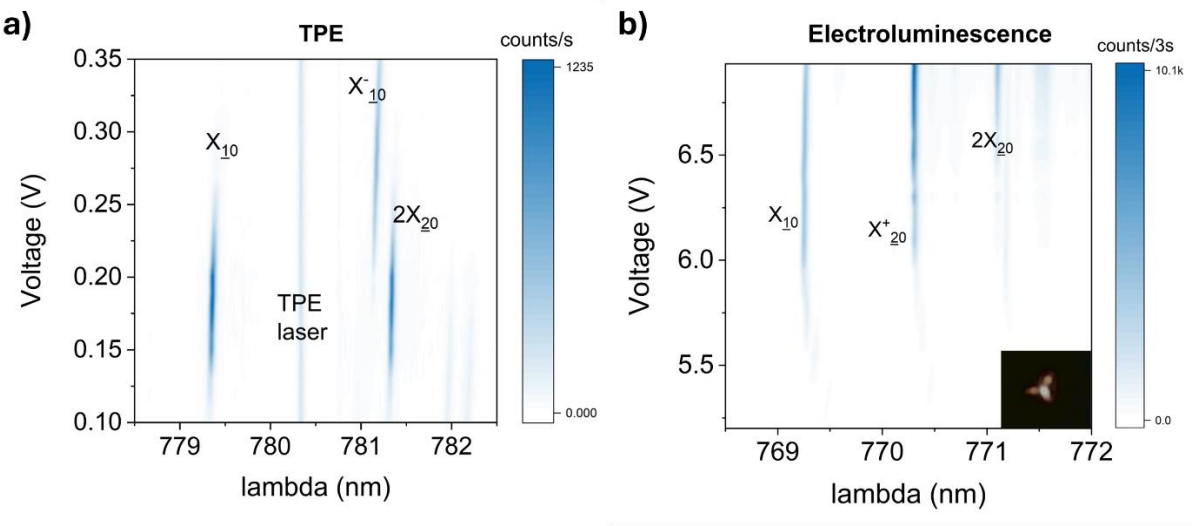

Figure 5.3-6: a) TPE PL spectrum dependence on Voltage. Compered to above-band excitation, the cleaner environment induced by the TPE process likely doesn't shield the excitons from the electric field in the intrinsic region, allowing to shift the transitions in and out of resonance. b) For the first time, EL is observed from a GaAs PQD. The graph illustrates the depth of forward bias required for carriers to tunnel into the dot. The bottom inset shows a CCD-captured image of a PQD, revealing that most recombination occurs within the Lateral and Vertical QWrs.

5.3.2 Mirrored sample

GaAs QDs on GaAs/AlAs Superlattice barrier

The epitaxial structure of the QDs that were turned into mirrored pyramids was again changed, where the only difference with the previous ones were the 10 nm thick barriers that enclose the dot, this time grown as a superlattice (0.2 nm GaAs + 0.2 nm AlAs)x25 on each side of the dot, similar to the sample used in the systematic study of Chapter 2. The intrinsic region is shown below in Figure 5.3-7-a, whereas all the other layers are kept unchanged. The motivation for using a superlattice barrier was to decouple the QD states from the VQWr of the AlGaAs barrier while maintaining a confinement potential lower than that of AlAs. However, unlike the previous configuration, we observed that the QD did not respond to an applied potential difference, neither in forward nor reverse bias. Although current could still flow through the junction, achieving a flat-band

condition did not result in sharp transitions. Instead, the photoluminescence (PL) spectrum was broad in some cases (Figure 5.3-7-b), and in others there was no emission whatsoever sweeping the voltage. We take this also as an indication that more work is necessary to improve on this front and clarify the role of the change in the processing geometry vs the superlattice structure, and be able to exclude processing imperfections.

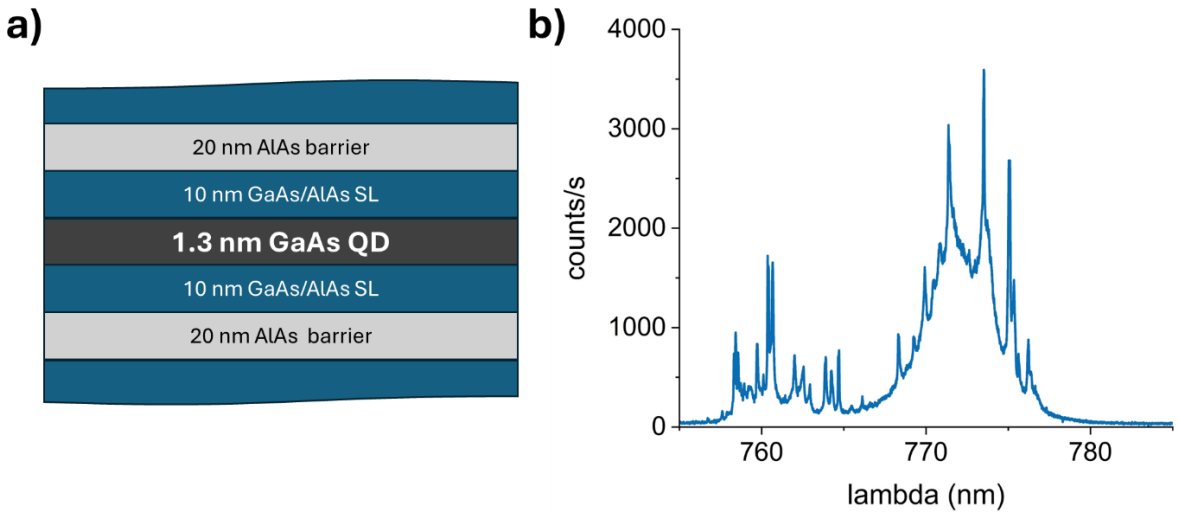

Figure 5.3-7: a) Close up of epitaxial stack of a p-i-n GaAs dot in SL/AlAs. The overall structure remains largely unchanged compared to the GaAs dot in AlAs, with SL introduced only in the 10 nm layers before and after the dot. b) PL spectrum obtained from a few GaAs QDs in SL/AlAs barriers. In emitting QDs, no clear excitonic transitions are observed, resulting in broad luminescence between 760 and 780 nm. However, in most QDs, confined state population is not possible, and only the SL states are visible.

5.4 Conclusions

The hypothesis that low polarizability prevents the energy shift of transitions under the presence of an electric field was impossible to investigate due to the response of our QDs. However, we learned that the confinement we obtain with the tetrahedral template, although being good to achieve low FSS[38], repeatable high fidelity[39] and carrier injection[13], is not complete enough to withstand an electric field. To summarize, **i)** GaAs QDs in AlAs were the only ones to support excitonic complexes under both forward and

reverse bias; **ii)** excitons were clearly defined for GaAs QDs in $Al_{65}Ga_{35}As$ only under forward biasing; **iii)** we couldn't see any clear excitonic transitions from GaAs QDs in SL under any biasing conditions.

Examining the structures individually, starting with the AlAs case, we note that while the epitaxial stack provides the strongest confinement, it allows for only a single escape channel for excitonic states to tunnel into—the GaAs LQWs connected to the GaAs QDs grown between the barriers on the sidewalls. This confinement enabled effective charge tuning, with the QD states population shifting from a neutral/negatively charged environment under forward bias to a more positively charged environment under reverse bias.

In the second case, introducing Ga in the barriers further complicated the confinement profile. Along the (111)B direction, carriers in the QD become confined by the energy band gap of the Ga-rich segregated VQWs, which, like QDs, can host carriers on discrete energy levels. Segregation also occurs along the three grooves, giving rise to three LQWrs. Compared to the AlAs configuration, these modifications introduce two additional leakage channels (VQWs, LQWrs), resulting in a lower number of states that can be excited and that are also less effectively confined. As a consequence, these states become populated only under forward bias. Nevertheless, the presence of the $Al_{65}Ga_{35}As$/AlAs interface at a very short distance from the QDs introduced discrete hopping of the transitions caused by the presence of a holes-population density at said interface. In conjunction with it, clear charge tuning was possible to observe, demonstrating the existence of the $X^{+2}{}_{21}$ which spectum agrees with the foreseen fine structure hypothesized in literature, and allowing the observation of $X^{+3}{}_{22}$ complex for the first time.

Finally, the SL barriers reduce confinement, eliminate VQWs, and maintain a compositionally uniform barrier, in principle making this configuration more comparable to the AlAs case, especially in terms of FSS magnitude and its distribution, where they outperform all other PQDs[38]. However, the SL itself gives rise to quantum-

confined states, distributed over the multiple square-well potential created by the AlAs/GaAs alternation. These states typically emit around 760–770 nm (for a 10 nm thick stack) under above-band excitation. The absence of sharp transitions suggests that this configuration provides the weakest confinement among the three investigated.

In conclusion, we found that optimizing the process for contacting the doped layers is not the only challenge in PQDs. Confinement plays a crucial role in enabling the Stark shift, and to achieve effective electric field tuning, it may be necessary to reduce or eliminate leakage channels where carriers can tunnel. Among the barriers we investigated, only binary alloys such as AlAs or GaAs/AlAs SLs are free from Lateral and Vertical QWrs. However, while GaAs/AlAs SLs eliminate these unwanted structures, they probably introduce SL states that become detrimental in the presence of an electric field. Ternary alloys would be useful for studying confined states at lower barrier heights, but their effectiveness is limited by segregation effects, as the Al concentration achieves its nominal value only along the sidewalls, excluding the possibility of studying lower uniform confinements. An alternative approach to enhancing confinement would be to replace the GaAs QD with a thin layer of low-Al-concentration AlGaAs, leveraging its segregation effects to create a QD-like structure from a short VQWr[35], sandwiched between AlAs barriers. In this configuration, the Al-poor central region, although structurally disordered compared to a uniform GaAs QD, would have only three LQWrs as potential leakage channels—formed naturally during growth. The QWs on the sidewalls, in contrast, would contain a higher Al concentration, resulting in higher barriers that would further restrict carrier escape.

Lastly, the intentional use of a hole-blocking interface positioned at a calibrated distance from the quantum dot could enable a discrete and controlled redshift of the transitions under current injection. Similarly, such structure could be leveraged to investigate rarer excitonic complexes.

References

(1) Hepp, S.; Jetter, M.; Portalupi, S. L.; Michler, P. Semiconductor Quantum Dots for Integrated Quantum Photonics. *Adv. Quantum Technol.* **2019**, *2* (9), 1900020. https://doi.org/10.1002/qute.201900020.

(2) Rota, M. B.; Krieger, T. M.; Buchinger, Q.; Beccaceci, M.; Neuwirth, J.; Huet, H.; Horová, N.; Lovicu, G.; Ronco, G.; Covre da Silva, S. F.; Pettinari, G.; Moczała-Dusanowska, M.; Kohlberger, C.; Manna, S.; Stroj, S.; Freund, J.; Yuan, X.; Schneider, C.; Ježek, M.; Höfling, S.; Basso Basset, F.; Huber-Loyola, T.; Rastelli, A.; Trotta, R. A Source of Entangled Photons Based on a Cavity-Enhanced and Strain-Tuned GaAs Quantum Dot. *eLight* **2024**, *4* (1), 13. https://doi.org/10.1186/s43593-024-00072-8.

(3) Chen, C.; Yan, J.-Y.; Babin, H.-G.; Wang, J.; Xu, X.; Lin, X.; Yu, Q.; Fang, W.; Liu, R.-Z.; Huo, Y.-H.; Cai, H.; Sha, W. E. I.; Zhang, J.; Heyn, C.; Wieck, A. D.; Ludwig, A.; Wang, D.-W.; Jin, C.-Y.; Liu, F. Wavelength-Tunable High-Fidelity Entangled Photon Sources Enabled by Dual Stark Effects. *Nat. Commun.* **2024**, *15* (1), 5792. https://doi.org/10.1038/s41467-024-50062-0.

(4) Plumhof, J. D.; Trotta, R.; Rastelli, A.; Schmidt, O. G. Experimental Methods of Post-Growth Tuning of the Excitonic Fine Structure Splitting in Semiconductor Quantum Dots. *Nanoscale Res. Lett.* **2012**, *7* (1), 336. https://doi.org/10.1186/1556-276X-7-336.

(5) Miller, D. A. B.; Chemla, D. S.; Damen, T. C.; Gossard, A. C.; Wiegmann, W.; Wood, T. H.; Burrus, C. A. Band-Edge Electroabsorption in Quantum Well Structures: The Quantum-Confined Stark Effect. *Phys. Rev. Lett.* **1984**, *53* (22), 2173–2176. https://doi.org/10.1103/PhysRevLett.53.2173.

(6) Dow, J. D.; Redfield, D. Toward a Unified Theory of Urbach's Rule and Exponential Absorption Edges. *Phys. Rev. B* **1972**, *5* (2), 594–610. https://doi.org/10.1103/PhysRevB.5.594.

(7) Lelong, Ph.; Bastard, G. Binding Energies of Excitons and Charged Excitons in Quantum Dots. *Solid State Commun.* **1996**, *98* (9), 819–823. https://doi.org/10.1016/0038-1098(96)00024-5.

(8) Imamog¯lu, A.; Yamamoto, Y. Turnstile Device for Heralded Single Photons: Coulomb Blockade of Electron and Hole Tunneling in Quantum Confined p-i-n Heterojunctions. *Phys. Rev. Lett.* **1994**, *72* (2), 210–213. https://doi.org/10.1103/PhysRevLett.72.210.

(9) Benson, O.; Santori, C.; Pelton, M.; Yamamoto, Y. Regulated and Entangled Photons from a Single Quantum Dot. *Phys. Rev. Lett.* **2000**, *84* (11), 2513–2516. https://doi.org/10.1103/PhysRevLett.84.2513.

(10) Yuan, Z.; Kardynal, B. E.; Stevenson, R. M.; Shields, A. J.; Lobo, C. J.; Cooper, K.; Beattie, N. S.; Ritchie, D. A.; Pepper, M. Electrically Driven Single-Photon Source. *Science* **2002**, *295* (5552), 102–105. https://doi.org/10.1126/science.1066790.

(11) Ward, M. B.; Farrow, T.; See, P.; Yuan, Z. L.; Karimov, O. Z.; Bennett, A. J.; Shields, A. J.; Atkinson, P.; Cooper, K.; Ritchie, D. A. Electrically Driven Telecommunication Wavelength Single-Photon Source. *Appl. Phys. Lett.* **2007**, *90* (6), 063512. https://doi.org/10.1063/1.2472172.

(12) Ellis, D. J. P.; Bennett, A. J.; Shields, A. J.; Atkinson, P.; Ritchie, D. A. Oxide-Apertured Microcavity Single-Photon Emitting Diode. *Appl. Phys. Lett.* **2007**, *90* (23), 233514. https://doi.org/10.1063/1.2747200.

(13) Chung, T. H.; Juska, G.; Moroni, S. T.; Pescaglini, A.; Gocalinska, A.; Pelucchi, E. Selective Carrier Injection into Patterned Arrays of Pyramidal Quantum Dots for Entangled Photon Light-Emitting Diodes. *Nat. Photonics* **2016**, *10* (12), 782–787. https://doi.org/10.1038/nphoton.2016.203.

(14) Baier, M. H.; Constantin, C.; Pelucchi, E.; Kapon, E. Electroluminescence from a Single Pyramidal Quantum Dot in a Light-Emitting Diode. *Appl. Phys. Lett.* **2004**, *84* (11), 1967–1969. https://doi.org/10.1063/1.1687453.

(15) Gotoh, H.; Kamada, H.; Saitoh, T.; Ando, H.; Temmyo, J. Electric-Field-Induced Anisotropy of Excitonic Optical Properties in Semiconductor Quantum Dots. *J. Appl. Phys.* **2003**, *94* (1), 342–347. https://doi.org/10.1063/1.1578524.

(16) Heller, W.; Bockelmann, U.; Abstreiter, G. Electric-Field Effects on Excitons in Quantum Dots. *Phys. Rev. B* **1998**, *57* (11), 6270–6273. https://doi.org/10.1103/PhysRevB.57.6270.

(17) Kowalik, K.; Krebs, O.; Lemaître, A.; Laurent, S.; Senellart, P.; Voisin, P.; Gaj, J. A. Influence of an In-Plane Electric Field on Exciton Fine Structure in InAs-GaAs Self-Assembled Quantum Dots. *Appl. Phys. Lett.* **2005**, *86* (4), 041907. https://doi.org/10.1063/1.1855409.
(18) Gerardot, B. D.; Seidl, S.; Dalgarno, P. A.; Warburton, R. J.; Granados, D.; Garcia, J. M.; Kowalik, K.; Krebs, O.; Karrai, K.; Badolato, A.; Petroff, P. M. Manipulating Exciton Fine Structure in Quantum Dots with a Lateral Electric Field. *Appl. Phys. Lett.* **2007**, *90* (4), 041101. https://doi.org/10.1063/1.2431758.
(19) *Vertical electric field tuning of the exciton fine structure splitting and photon correlation measurements of GaAs quantum dot | Applied Physics Letters | AIP Publishing*. https://pubs.aip.org/aip/apl/article/96/10/101117/150535/Vertical-electric-field-tuning-of-the-exciton-fine (accessed 2025-01-20).
(20) Bennett, A. J.; Pooley, M. A.; Stevenson, R. M.; Ward, M. B.; Patel, R. B.; de la Giroday, A. B.; Sköld, N.; Farrer, I.; Nicoll, C. A.; Ritchie, D. A.; Shields, A. J. Electric-Field-Induced Coherent Coupling of the Exciton States in a Single Quantum Dot. *Nat. Phys.* **2010**, *6* (12), 947–950. https://doi.org/10.1038/nphys1780.
(21) Walther, T.; Cullis, A. G.; Norris, D. J.; Hopkinson, M. Nature of the Stranski-Krastanow Transition during Epitaxy of InGaAs on GaAs. *Phys. Rev. Lett.* **2001**, *86* (11), 2381–2384. https://doi.org/10.1103/PhysRevLett.86.2381.
(22) Huang, H.; Csontosová, D.; Manna, S.; Huo, Y.; Trotta, R.; Rastelli, A.; Klenovský, P. Electric Field Induced Tuning of Electronic Correlation in Weakly Confining Quantum Dots. *Phys. Rev. B* **2021**, *104* (16), 165401. https://doi.org/10.1103/PhysRevB.104.165401.
(23) Huber, D.; Reindl, M.; Huo, Y.; Huang, H.; Wildmann, J. S.; Schmidt, O. G.; Rastelli, A.; Trotta, R. Highly Indistinguishable and Strongly Entangled Photons from Symmetric GaAs Quantum Dots. *Nat. Commun.* **2017**, *8* (1), 15506. https://doi.org/10.1038/ncomms15506.
(24) Zeeshan, M.; Sherlekar, N.; Ahmadi, A.; Williams, R. L.; Reimer, M. E. Proposed Scheme to Generate Bright Entangled Photon Pairs by Application of a Quadrupole Field to a Single Quantum Dot. *Phys. Rev. Lett.* **2019**, *122* (22), 227401. https://doi.org/10.1103/PhysRevLett.122.227401.
(25) Miller, D. A. B. Electric Field Dependence of Optical Properties of Quantum Well Structures. In *Electro-optic and Photorefractive Materials*; Günter, P., Ed.; Springer: Berlin, Heidelberg, 1987; pp 35–49. https://doi.org/10.1007/978-3-642-71907-3_3.
(26) Miller, R. C.; Kleinman, D. A.; Gossard, A. C. Energy-Gap Discontinuities and Effective Masses for $\mathrm{G}\mathrm{a}\mathrm{A}\mathrm{s}\ensuremath{-}{\mathrm{Al}}_{x}{\mathrm{Ga}}_{1\ensuremath{-}x}\mathrm{As}$ Quantum Wells. *Phys. Rev. B* **1984**, *29* (12), 7085–7087. https://doi.org/10.1103/PhysRevB.29.7085.
(27) Adachi, S. Aluminum Arsenide (AlAs). In *Optical Constants of Crystalline and Amorphous Semiconductors: Numerical Data and Graphical Information*; Adachi, S., Ed.; Springer US: Boston, MA, 1999; pp 156–165. https://doi.org/10.1007/978-1-4615-5247-5_17.
(28) Neumann, H. S. Adachi (Ed.). Properties of Aluminium Gallium Arsenide. (EMIS Datareviews Series No. 7). INSPEC; The Institution of Electrical Engineers, London 1993. 325 S., 58 Abb., 93 Tab. ISBN 0 85296 558 3, L 95. *Cryst. Res. Technol.* **1993**, *28* (6), 866–866. https://doi.org/10.1002/crat.2170280617.
(29) Juska, G.; Ranjbar Jahromi, I.; Mattana, F.; Varo, S.; Dimastrodonato, V.; Pelucchi, E. Biexciton Initialization by Two-Photon Excitation in Site-Controlled Quantum Dots: The Complexity of the Antibinding State Case. *Appl. Phys. Lett.* **2020**, *117* (13), 134001. https://doi.org/10.1063/5.0011383.
(30) Javanainen, J. Effect of State Superpositions Created by Spontaneous Emission on Laser-Driven Transitions. *Europhys. Lett.* **1992**, *17* (5), 407. https://doi.org/10.1209/0295-5075/17/5/005.
(31) Economou, S. E.; Liu, R.-B.; Sham, L. J.; Steel, D. G. Unified Theory of Consequences of Spontaneous Emission in a $\ensuremath{\Lambda}$ System. *Phys. Rev. B* **2005**, *71* (19), 195327. https://doi.org/10.1103/PhysRevB.71.195327.
(32) Schlote, J.; Hinrich, S.; Kuck, B.; Schröder, K.-W. Topological Effects Regarding Trench Structures Covered with LPCVD and PECVD Thin Films. *Surf. Coat. Technol.* **1993**, *59* (1–3), 316–320. https://doi.org/10.1016/0257-8972(93)90104-V.

(33) Karlsson, K. F.; Oberli, D. Y.; Dupertuis, M. A.; Troncale, V.; Byszewski, M.; Pelucchi, E.; Rudra, A.; Holtz, P. O.; Kapon, E. Spectral Signatures of High-Symmetry Quantum Dots and Effects of Symmetry Breaking. *New J. Phys.* **2015**, *17* (10), 103017. https://doi.org/10.1088/1367-2630/17/10/103017.

(34) Griffiths, D. J.; Schroeter, D. F. *Introduction to Quantum Mechanics*. Higher Education from Cambridge University Press. https://doi.org/10.1017/9781316995433.

(35) Zhu, Q.; Karlsson, K. F.; Pelucchi, E.; Kapon, E. Transition from Two-Dimensional to Three-Dimensional Quantum Confinement in Semiconductor Quantum Wires/Quantum Dots. *Nano Lett.* **2007**, *7* (8), 2227–2233. https://doi.org/10.1021/nl0706650.

(36) Houel, J.; Kuhlmann, A. V.; Greuter, L.; Xue, F.; Poggio, M.; Gerardot, B. D.; Dalgarno, P. A.; Badolato, A.; Petroff, P. M.; Ludwig, A.; Reuter, D.; Wieck, A. D.; Warburton, R. J. Probing Single-Charge Fluctuations at a $\mathrm{GaAs}/\mathrm{AlAs}$ Interface Using Laser Spectroscopy on a Nearby InGaAs Quantum Dot. *Phys. Rev. Lett.* **2012**, *108* (10), 107401. https://doi.org/10.1103/PhysRevLett.108.107401.

(37) *Fine Structure of Negatively and Positively Charged Excitons in Semiconductor Quantum Dots: Electron-Hole Asymmetry | Phys. Rev. Lett.* https://journals.aps.org/prl/abstract/10.1103/PhysRevLett.98.036808 (accessed 2025-06-16).

(38) Ranjbar Jahromi, I.; Juska, G.; Varo, S.; Basso Basset, F.; Salusti, F.; Trotta, R.; Gocalinska, A.; Mattana, F.; Pelucchi, E. Optical Properties and Symmetry Optimization of Spectrally (Excitonically) Uniform Site-Controlled GaAs Pyramidal Quantum Dots. *Appl. Phys. Lett.* **2021**, *118* (7), 073103. https://doi.org/10.1063/5.0030296.

(39) Juska, G.; Dimastrodonato, V.; Mereni, L. O.; Gocalinska, A.; Pelucchi, E. Towards Quantum-Dot Arrays of Entangled Photon Emitters. *Nat. Photonics* **2013**, *7* (7), 527–531. https://doi.org/10.1038/nphoton.2013.128.

Chapter 6

6 Towards Pyramidal Resonating Cavities

In Chapter 4, we introduced for the first time the possibility of implementing a resonant cavity using a pyramidal structure in a tip-up configuration. Simulations demonstrated an enhancement in the Purcell factor and an improved far-field power distribution, validating the potential of the Pyramidal Resonant Cavity. The results suggest performance that is ideally comparable to what has been experimentally achieved in other optical micro-resonators.

The work presented in this chapter focuses on the fabrication of the resonator using InGaAs QDs embedded in a GaAs matrix, and represents only an ***initial step*** in the development of this research. Many challenges remain open, requiring further studies and optimizations. This chapter aims to provide a solid foundation for future investigations and advancements in the project

6.1 Quantum Dots in optical resonating cavities

An optical resonating cavity is a structure designed to confine and control light. In a classical picture description, the correct choice of refractive index and cavity dimensions allow a particular wavelength to constructively/destructively interfere, producing resonances[1]. In this way, propagation (or leakage) of the electromagnetic wave in a particular direction can be suppressed, and device can acquire very directional emission patterns. An example can be found in lasers, where the characteristic reflectance of the two mirrors at the extremities of the Fabry-Perot cavity are asymmetric, to grant (ideally) unitary reflection on one side and allow leakage on the other. Hence, these cavities can be engineered to enhance the interaction between light and matter, enabling lasing via stimulated emission, but also playing a crucial role in quantum optics and cavity quantum electrodynamics (cQED).

In a quantum picture description, the classical concept of resonance of the electromagnetic wave translates into the modification of the photonic local density of states (LDOS). The LDOS in free space is given by the formula

$$\rho(\omega) = \frac{\omega^2}{\pi^2 c^3} \tag{6.1}$$

where ω is the angular frequency of light and c is the speed of light in vacuum.

When a cavity is introduced, its interfaces modify the properties of the surrounding space, typically creating sharp spatial variations in the refractive index. For example, consider a Distributed Bragg Reflector (DBR) grown via MBE or MOVPE on a flat surface. In the direction perpendicular to the structure, an electromagnetic wave with a wavelength equal to λ_{Bragg} propagating towards the DBR encounters a region with suppressed availability of states at that energy. As a result, the probability of waves propagating through DBR is very low. Intuitively, the DBR spatially redistributes (strictly speaking in the k-space) the photon states density at that specific energy in the opposite direction, effectively reflecting the wave.

One of the most significant consequences of placing an emitter, such as a QD, inside a resonating cavity is the modification of its spontaneous emission rate, that is governed by Fermi's Golden Rule, which states[2]:

$$\Gamma = \frac{2\pi}{\hbar} |\langle f|H_{int}|i\rangle|^2 \rho(\omega) \tag{6.2}$$

where Γ is the emission rate, H_{int} is the interaction Hamiltonian, $|f\rangle$ and $|i\rangle$ are the final and initial states respectively, and $\rho(\omega)$ is the LDOS at the emission frequency. The formula is the product of the transition probability from $|i\rangle$ to $|f\rangle$, which depends only on the interaction terms of the Hamiltonian, and the availability of photon states at the transition energy. Inside a cavity, the pronounced $\rho(\omega)$ peaks at the cavity's resonant frequencies increase the number of recombinations per second. This behaviour is well-known as Purcell effect, and the enhancement factor, known as the Purcell Factor (which we already discussed earlier in this thesis) is given by[3]:

$$F_P = \frac{3}{4\pi^2}\left(\frac{\lambda_{free}}{n}\right)^3 \frac{Q}{V} \tag{6.3}$$

where λ_{free} is the emission wavelength, n is the refractive index, Q is the quality factor of the cavity, and V is the effective mode volume. A high-Q, low-volume cavity can significantly enhance the emission of a quantum dot, making it a valuable platform for single photon applications.

This picture is what in literature is referred to as weak coupling regime, where the interaction between the emitter and the cavity is strong enough to modify the emission rate but not to reach the level of coherent energy exchange between the two systems. In contrast, the strong coupling regime occurs when the coupling strength exceeds the loss rates of both the emitter and the cavity, leading to the formation of new hybridized states known as polaritons. Understanding the interplay between quantum dots and optical cavities is crucial for optimizing photon sources and enhancing light-matter interaction, with potential applications in quantum communication, single-photon sources, and integrated photonics[3].

Several technologies have been developed to implement QDs integrated into resonant cavities, each offering specific advantages in terms of quality factor Q and mode volume V. The main approaches include: **Bragg Mirrors (DBRs) and Fabry-Pérot Microcavities**, commonly used in micropillars[4,5] and microdisk[6] structures, where vertical confinement is achieved through DBR mirrors, while lateral confinement is ensured by waveguiding effects or total internal reflection; **Photonic Crystals**, which exploit a periodic modulation of the refractive index to create photonic band gaps and high-Q cavities in localized defect regions of the structure[7–9]; **Plasmonic Nanocavities**, which, despite having lower quality factors, allow for extreme light confinement beyond the diffraction limit, significantly enhancing the spontaneous emission rate[10,11]; **Circular Bragg Reflectors (CBR or Bull's Eye Cavities)**, which consist of concentric rings of alternating refractive index materials. These structures enable efficient in-plane light confinement

and strong emission directionality, making them particularly useful for single-photon sources and quantum optics applications[12–14].

For all the aforementioned cavity designs, a critical requirement must be met: the emitting dipole must be perfectly aligned with the cavity mode to achieve optimal resonant behavior. With some exceptions in the case of plasmonic nanocavities, which do not always require top-down fabrication when Purcell enhancement is sought via surface plasmons of metal nanoparticles deposited[15] or grown[16] on top of quantum dot samples, most of the other solutions rely on Electron Beam Lithography (EBL). An accurate nanoscale optical positioning approach that is gaining traction[17], relies on the deposition of arrays of metal alignment marks via standard lift-off, followed by sample interrogation. Once the emitter is probed through PL, the positions of both the markers and the quantum dots are extracted from the PL image using orthogonal scan lines and subsequent fitting. The QD position is then referenced to the markers with very low standard deviation uncertainties (<30 nm). Next, the cavity is tailored to the QD's optical properties and designed with respect to the alignment markers to ensure precise positioning. Finally, EBL patterning and etching are performed.

Despite the impressive alignment capability, even such small uncertainties can lead to deviations from the ideally sought behavior. In 2022, Lyasota et al[18], studying a rectangular photonic crystal cavity, observed that the asymmetry in the polarization-resolved emission spectra strongly depended on the quantum dot displacement with respect to the center of the photonic crystal. In a more recent study, Peniakov et al[19]. reported strongly polarized and unpolarized emission from two different material systems in which (InGaAs and GaAs) QDs were embedded in a Circular Bragg Reflector (CBR). They attributed the polarization effects to the spatial position of the QDs within the cavity. Their simulations supported experimental evidence, showing that highly polarized emission (DOP = 0.99) and minimal mode splitting (0.9 nm) can arise when the dipole emission couples preferentially to one of the orthogonal eigenmodes sustained by the cavity due to a slight displacement from the center.

These findings underscore the crucial role of precise emitter positioning in achieving the desired optical response. Even with state-of-the-art nanoscale alignment techniques, residual uncertainties can introduce significant variations in polarization and mode coupling.

6.2 The PQDs alternative

While integration of PQDs into photonic crystal cavities has been demonstrated[20], the process remains far from straightforward. Nevertheless, precise alignment of QDs within the cavity remains a critical challenge in achieving optimal optical performance. As demonstrated in Chapter 4, PQDs offer a natural solution, as, forming exactly at the vertical axis of the inverted tetrahedral template, they ensure inherent spatial alignment precision. We've shown that shifting the dipole along this vertical axis leads to different resonant conditions, altering the far-field emission patterns accordingly[21]. The resonant behaviour is achieved in the 750–780 nm wavelength range by placing a reflecting Au mirror, assuming the dipole is a GaAs QD embedded in an AlGaAs matrix. This material system is necessary to prevent (emitted) light absorption by the surrounding matrix, which would otherwise dampen the resonance. However, as discussed at the beginning of Chapter 2, growing a thick layer of AlGaAs inside the recess leads to premature closure of the recess and spurious growth on the planar surface (Figure 1.2 3-b, Chapter 2). Determining the optimal Aluminium composition and layer thickness to prevent recess closure is an issue that requires further investigation. Since the cavity design is scalable in wavelength, we opted instead for an InGaAs QD embedded in a GaAs matrix. GaAs exhibits a more conformal growth within the recess, naturally widening the profile and mitigating the issues encountered with AlGaAs (see Chapter 2). This approach allows us to focus primarily on the post-growth fabrication challenges, ensuring that once the process is refined, it can be transferred to the GaAs/AlGaAs material system given the closure of the recess is worked out.

Simulations were performed considering the pyramid as fully made of GaAs only. Figure 6.2-1-a displays the Purcell map obtained sweeping the vertical position of the dipole

from 0.2 to 1.2 um from the tip of the pyramid, considering no reflection from the base (the bottom interface is one side of the FDTD region, set as absorbing layer), for the 800-900 nm wavelength range. Under these circumstances, the physical height of the pyramid in the simulation design, from tip to bottom base, exceeds ≈4 times the z range covered by the sweeping dipole. As already explained in Chapter 2, with the bottom interface set as absorbing layer, the Purcell fringes are only dependent on the position of the dipole with respect to the three slanted sidewalls. The resonances induced by the three top sidewalls appear in fringes like the ones simulated for shorter wavelengths (**Error! Reference source not found.**, Chapter 4). The increase in radiation length and i n refractive index of the matrix (from 3.2 AlGaAs matrix to 3.6 for GaAs matrix) compensate each other, suggesting similar pyramids volumes.

By placing a gold mirror at the bottom of the pyramid, with tip-to-dipole distance in the 0.64-0.66 μm range, setting the dipole in the fringe where resonance look more intense, and a dipole-to-mirror distance about 1/3 of the total pyramid height (≈1 μm), we are able to achieve the same resonating conditions (Gaussian-like farfield and Purcell factor ≈ 8, Figure 6.2-1-b) obtained in Chapter 4 for the 750-780nm wavelength range. It must be noted that, as in the study in Chapter 4, the actual dielectric permittivity of GaAs was neglected, and the refractive index was fixed at a constant value of 3.6. This simplification allowed the observation of resonances in the 800–830 nm range. However, such resonances would not be physically attainable, as GaAs's band-edge absorption at 10 K occurs near 818 nm, which would dampen any resonant behavior in this spectral region.

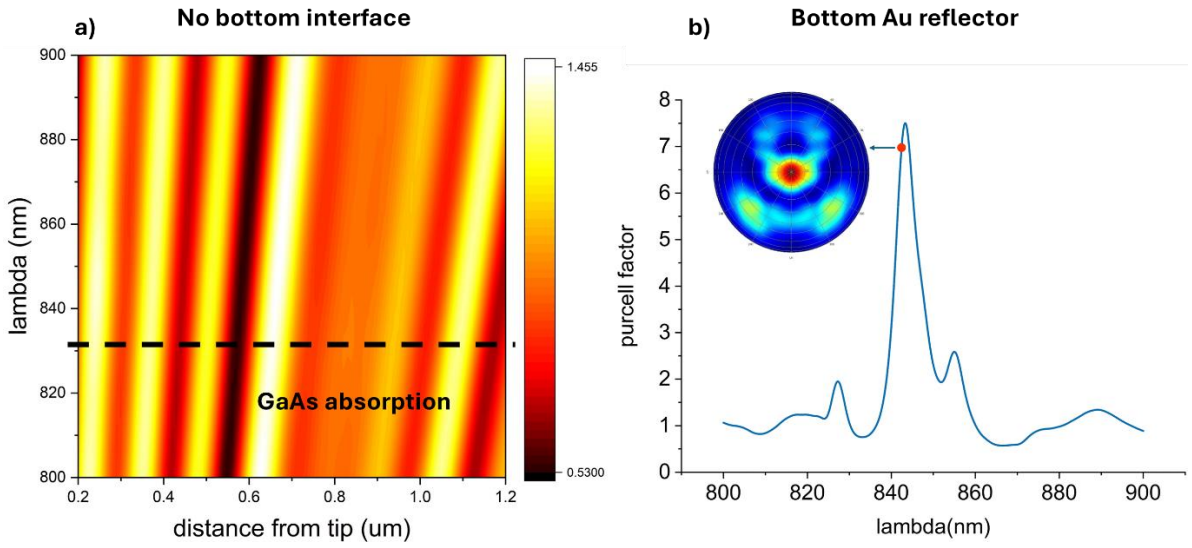

Figure 6.2-1: a) The heatmap illustrates the Purcell enhancement as a function of wavelength and the QD distance from the tip. Reflection from the base is not considered. Fringes in the spectral region below the black dashed line are not physically attainable because of the GaAs absorption. b) Purcell factor of ≈8 is obtained when the source is placed withing the strongest fringe distance range and a back reflector is placed at 1/3 of the pyramid height. The inset show the very directional farfield at a wavelength close to the resonance,

This proves the portability of the method within different material systems, theoretically functioning for a very wide range of wavelength when the pyramid volume is changed accordingly. So, we had a first go to it as discussed in the following.

6.2.1 Fabrication process

Although misalignment in the XY plane relative to the central axis is not a concern as the QD nucleates on the vertical axis of the recess, precisely positioning the QD along the vertical axis relative to the pyramid's tip, remains a challenge we have yet to fully overcome (see Chapter 2, 'Thickness Calibration Issue'). As we observed, in the pyramid structure, there are multiple resonance fringes (Figure 6.2-1-a and b) that depend on the position of the dipole. Yet, due to the inability to precisely calibrate growth thickness and deterministically control the vertical position of the QD, we cannot guarantee coupling between a single dot and a resonant mode. To increase the probability of coupling at least one quantum dot to a resonant mode, I have grown samples with 7x$In_{25}Ga_{75}As$

stacked QDs, separated by 20 nm layers of GaAs along the vertical axis, preceded and followed by thick GaAs outer barriers. Thickness of QDs was nominally varied from 0.45 nm (first grown dot) to 1.05 nm (last grown dot) in steps of 0.1 nm. In principle, the increase in growth rate as the pyramid fills is sufficient to produce QDs emitting at slightly different energies, even for nominally identical dots. In this case, the nominal size was also increased to enhance the likelihood that multiple QDs would fall within the resonant fringes.

Once growth is finished (Figure 6.2-3-a), the sample topside is polished until the recesses are completely removed (Figure 6.2-3-b). After a cleaning step in acetone/IPA to eliminate organic residues and a brief (<5 s) dip in BOE to remove traces of the silica polishing slurry, 10 nm of SiO_2 are sputtered on the surface (Figure 6.2-3-c). Two layers of LOR 3A, followed by S1805 resist, are spun onto the sample to ensure that the gold evaporation (200–300 nm) does not conformally coat the resist topology, which would hinder the final stripping (Figure 6.2-3-c). LOR is soft baked at 150°C for 2 minutes after each spinning, while S1805 is baked at 115°C for the same duration. The positive resist is exposed for 6 seconds with a dose of 100 mJ/cm^2, imprinting the same triangular pattern used to create the tetrahedral template, aligned to the polished pyramids via markers. Development is carried out by immersing the sample in MF319 for approximately 50 seconds (Figure 6.2-3-d). Successively, a 200 nm thick gold is evaporated and finally resist is stripped away immersing the sample in 1165 remover for about two hours, followed by a short ultrasonic agitation (Figure 6.2-3-e).

The primary reason for using a metallic mirror is that post-growth deposition of a DBR at the bottom of our pyramidal structures is not feasible by MOVPE. It has been shown that metallic mirrors incorporating a thin dielectric layer[22] can achieve reflectance exceeding 90%. While the cited study specifically examines how the HE_{11} fundamental mode of cylindrical nanopillars is optimally reflected by a properly designed metallic/dielectric mirror—as opposed to the lower performance of $\lambda/4$ DBRs— it might be crucial for eliciting resonances in the pyramidal structure. By analysing the complex farfield patterns of the pyramids as a function of the dipole position (Chapter 4), it becomes

evident that the resonant modes' k-vectors are not limited to those perpendicular to the bottom reflecting surface. This differs from nanopillars, where waveguiding constrains propagation direction. The presence of three slanted top sidewalls further complicates the phenomenon. Consequently, even though a high-reflectance DBR at the bottom of the pyramids maintains substantial reflectivity for incidences up to about ±20° from normal, it still primarily reflects a narrow set of k-vectors, and would not generate the resonance observed in Figure 6.2-1-b. It is highly likely that the observed directional far-field power distribution (inset of Figure 6.2-1-b) arises from a non-trivial resonance pattern. In support of this interpretation, the reflectivity spectra at normal incidence and at 45° (Figure 6.2-2) confirm the high reflectivity of the metallic/dielectric compound mirror even for very high incidence angles.

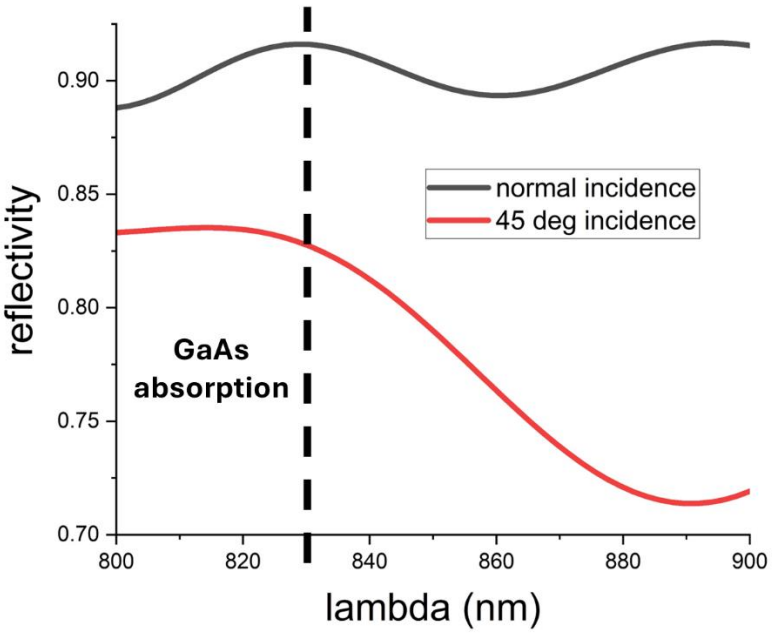

Figure 6.2-2: Simulated reflectivity spectra of the compound Au/SiO_2 mirror for a plane wave incident from the GaAs matrix side, shown for normal incidence and for 45° incidence. While very high reflectivity is maintained at normal incidence, reflectivity values greater than 70% are still obtained at 45° incidence.

Lastly, we found it necessary to use photolithography for selectively depositing the gold layer instead of flood-evaporating on the sample. While the latter eliminates alignment

constraints and avoids developing/stripping losses, it results in very poor adhesion to the GaAs carrier, where pyramids are typically transferred to (see back-etching, Chapter 2). The mask used to define the micromirrors is the same one employed to pattern the hexagonal array of triangles onto the GaAs substrate. As a result, the micromirrors are triangular, with a side length of 9 µm.

After evaporation and stripping the photoresists stack (Figure 6.2-3-e), 200 nm of SiO_2 is deposited by IC-PECVD onto the sputtered SiO_2 areas not covered by the triangular micromirrors. Finally, the sample is bonded to a <100> GaAs carrier using SU8, followed by standard back-etching (Figure 6.2-3-f).

Figure 6.2-3 shows the step flow described above.

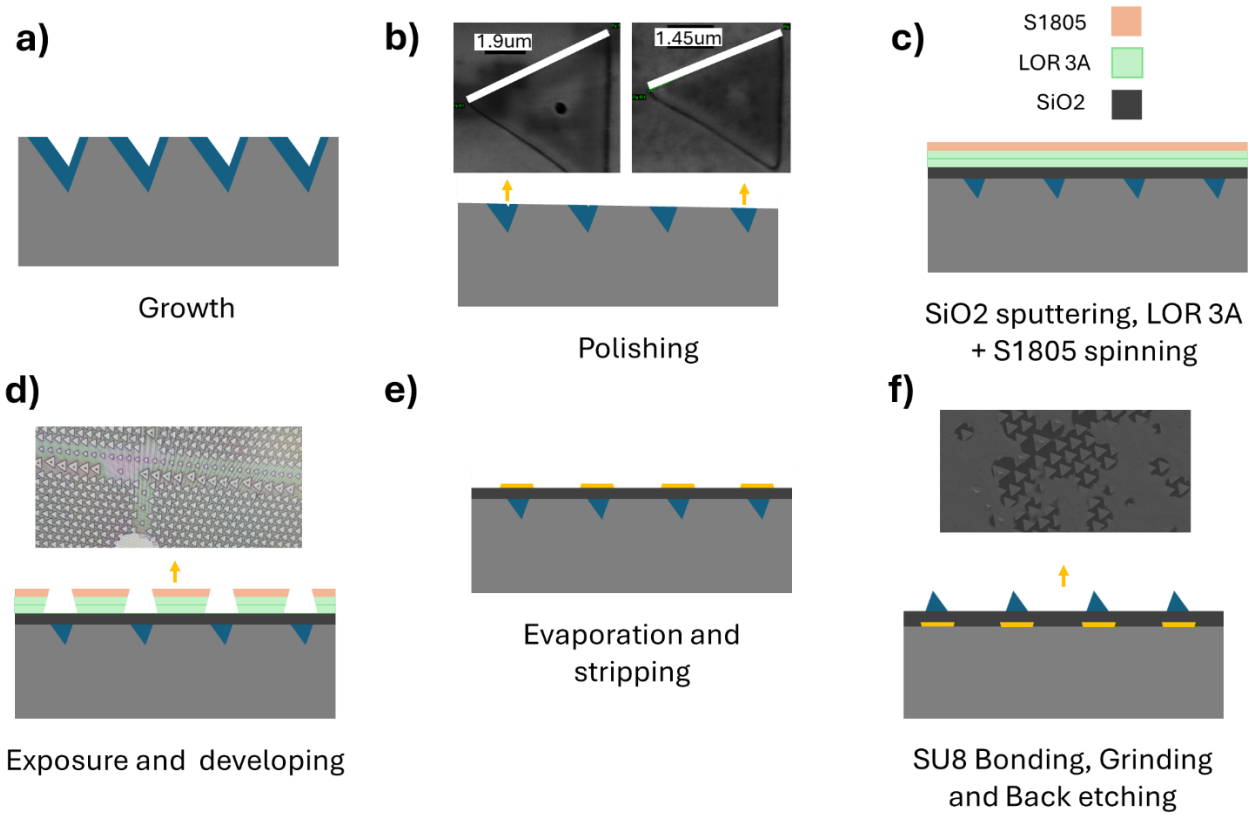

Figure 6.2-3: a) as-grown sample; b) sample is polished until recesses disappear: c) 10nm of SiO_2 are sputtered, followed by 2xLOR 3A resist and S1805 spinning: d) exposure and development allows to imprint the lift-off pattern for the deposition of triangular micromirrors; e) Au evaporation and resist stripping; f) sample follows the standard back etching procedure.

6.2.2 Experimental results

Above-band excitation was performed to investigate possible resonant behaviour within the pyramids. Indications that a QD is coupled to a resonant mode would be increased intensity on the CCD, shorter lifetimes and hence broader linewidths (if transform limited). Regrettably, none of the above was observed during the measurements. Figure 6.2-4-a presents spectra from nine QDs, where noticeable is the relatively low count rate. To this regard, the stacked QDs underperformed compared to a standard back-etched sample. This outcome is compatible with the prolonged exposure to the etchant, which was intentionally carried out to fully expose the pyramids and replicate the conditions assumed in the simulations. Spectra 4, 5, and 6 exhibit the clearest and narrowest transitions among the ones measured, as the corresponding pyramids were among the last to be fully uncovered. Consequently, they experienced a shorter etching time compared to the pyramids associated with spectra 2 and 3, where all transitions appear broadened. Systematic linewidth and lifetime studies were not conducted, as none of the spectra exhibited features out of the ordinary.

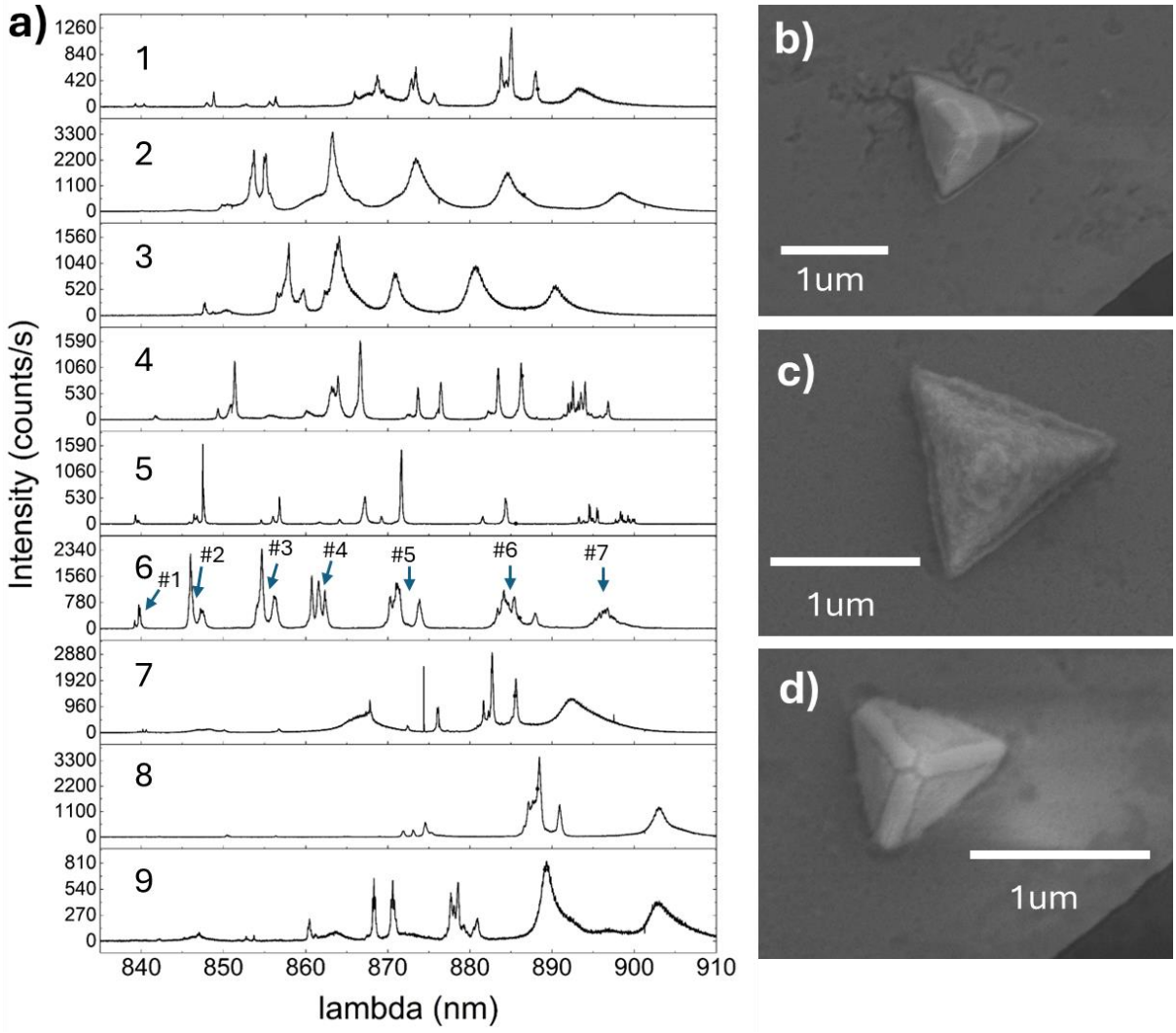

Figure 6.2-4: a) Spectra from 9 different pyramids of 7 stacked InGaAs dots. Overexposed pyramids (2,3) show broader lines than pyramids exposed for less time to the etchant (4,5,6). SEM images of fully exposed pyramids are reported on the right for b) a pyramid (over-)exposed for relatively short time and c) and d) for pyramids excessively (over-)exposed.

The detrimental effects of back-etching go beyond the introduction of surface states. In Figure 6.2-4-c, SEM inspection reveals an extremely roughened sidewall surface. In Figure 6.2-4-d, the AlAs etch-stop layer appears to be completely removed, while the three stripes running along the intersections of the sidewalls indicate the preferential etching of Ga-rich segregated lateral QWrs of the AlGaAs layer grown after the AlAs etch-

stop layer. A fully uncovered pyramid that was slightly overexposed to the etchant resembles the one shown in Figure 6.2-4-b.

6.3 Discussions and Conclusions

Attempting on realizing the Pyramidal Resonating Cavity turned out to be an extremely insightful processes, regardless of outcome. We delineated the steps to transform an as-grown sample into a functionalized one, and identified the major challenges: **i)** the absence of any resonant behaviour, even in the spectra of slightly overexposed pyramids, tells us that the QDs were most likely placed on the vertical axis out of the resonating conditions; **ii)** the long-known detrimental effects of back-etching—such as the introduction of surface states and the breaching of the etch-stop barrier, which damages the structures—are further compounded by its significant roughening of the top surfaces. This roughening may introduce additional scattering elements that contribute to the existing losses within the cavity.

As already pointed out many times throughout the text, we don't yet avail of a model to predict the vertical thickness of layers grown inside the recess. However, a possible, albeit laborious, workaround would be to define a target structure with actual dots, and then grow a similar stack, replacing the active layers (InGaAs dot in GaAs matrix or GaAs in AlGaAs dots) with slightly thicker AlAs layers. In both material systems this approach should provide good "dummy QD"-to-matrix contrast when scanning the cross-section of the modified structure under AFM, and deliver faithful position measurement of the dots inside the matrix. Furthermore, being AlAs a binary alloy, the layer will conformally grow inside the recess without significantly altering the profile.

Back-etching, on the other hand, has no workarounds: it is an unavoidable process and must therefore be improved. Solutions for passivating III-V surfaces, particularly from the electronics field, are well-established and tested. However, passivation can only help reduce surface states; it cannot prevent barrier breaching or surface roughening. What is needed is an etching solution with exceptionally high selectivity or an AlAs-passivating chemical that can be added to our Ammonium Hydroxide:Hydrogen

Peroxide solution. It is evident that the aluminum oxide compounds formed on the AlAs surface upon reaction with H_2O_2 do not sufficiently inhibit the etching action of Ammonium Hydroxide molecules. An alternative approach could be to carry out etching in an oxygen-poor (or ideally oxygen-free) environment, as in a dry etching chamber. The use of SF_6[23,24] appears crucial for achieving selectivity between GaAs and $Al_xGa_{1-x}As$, as non-volatile AlF_x byproducts form at the interface[25]. Following reference *23*, we developed a dry etching recipe consisting of a mixture of HBr/He/SF_6 (100/100/10 sccm), at a chamber pressure of 30 mTorr, ICP power at 1000 W and RF power at 150 W. This process successfully exposed the pyramids, which though did not exhibit good photoluminescence. As shown in Figure 6.3-1-a, prolonged overexposure to the etchants led to the removal of the AlAs etch-stop barrier at the tip, allowing reactive radicals to etch through the AlGaAs VQWr. On the other hand, short overexposure did not cause visible structural damage (Figure 6.3-1-b). Nevertheless, photoluminescence from the QDs was barely observed. This suggests that, beyond physical damage to the specimens, an unidentified surface-related issue is hindering population. Yet, dry back-etching could be a game changer in the fabrication of Pyramidal Resonating Cavities.

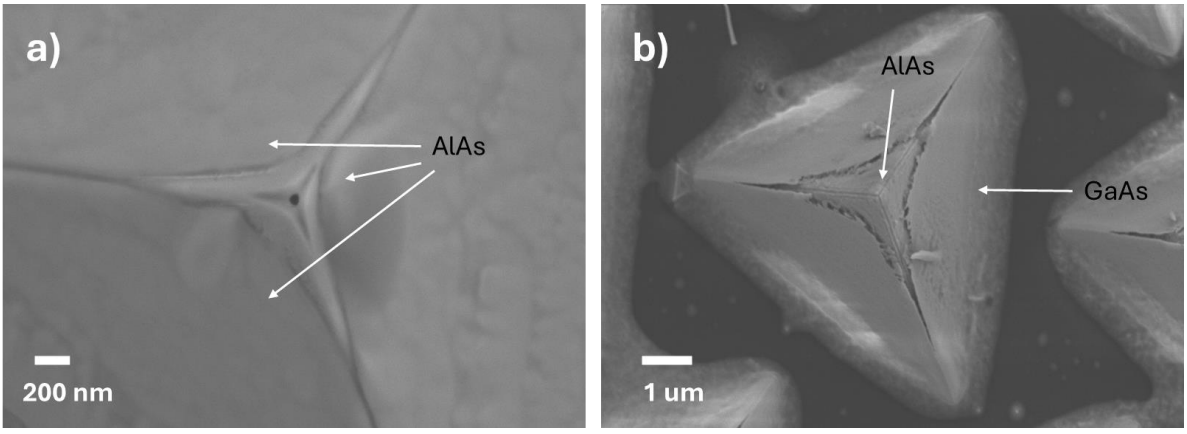

Figure 6.3-1: SEM of dry back-etched pyramids after a) prolonged and b) reduced overexposure to HBr/He/SF_6 environment.

References

(1) Vahala, K. J. Optical Microcavities. *Nature* **2003**, *424* (6950), 839–846. https://doi.org/10.1038/nature01939.
(2) Loudon, R. Quantum Mechanics of the Atom-Radiation Interaction. In *The Quantum Theory of Light*; Loudon, R., Ed.; Oxford University Press, 2000; p 0. https://doi.org/10.1093/oso/9780198501770.003.0003.
(3) Reitzenstein, S. Semiconductor Quantum Dot–Microcavities for Quantum Optics in Solid State. *IEEE J. Sel. Top. Quantum Electron.* **2012**, *18* (6), 1733–1746. https://doi.org/10.1109/JSTQE.2012.2195159.
(4) Gérard, J. M.; Barrier, D.; Marzin, J. Y.; Kuszelewicz, R.; Manin, L.; Costard, E.; Thierry-Mieg, V.; Rivera, T. Quantum Boxes as Active Probes for Photonic Microstructures: The Pillar Microcavity Case. *Appl. Phys. Lett.* **1996**, *69* (4), 449–451. https://doi.org/10.1063/1.118135.
(5) Ollivier, H.; Priya, P.; Harouri, A.; Sagnes, I.; Lemaître, A.; Krebs, O.; Lanco, L.; Lanzillotti-Kimura, N. D.; Esmann, M.; Senellart, P. Three-Dimensional Electrical Control of the Excitonic Fine Structure for a Quantum Dot in a Cavity. *Phys. Rev. Lett.* **2022**, *129* (5), 057401. https://doi.org/10.1103/PhysRevLett.129.057401.
(6) Armani, D. K.; Kippenberg, T. J.; Spillane, S. M.; Vahala, K. J. Ultra-High-Q Toroid Microcavity on a Chip. *Nature* **2003**, *421* (6926), 925–928. https://doi.org/10.1038/nature01371.
(7) Yoshie, T.; Scherer, A.; Hendrickson, J.; Khitrova, G.; Gibbs, H. M.; Rupper, G.; Ell, C.; Shchekin, O. B.; Deppe, D. G. Vacuum Rabi Splitting with a Single Quantum Dot in a Photonic Crystal Nanocavity. *Nature* **2004**, *432* (7014), 200–203. https://doi.org/10.1038/nature03119.
(8) Lodahl, P.; Floris van Driel, A.; Nikolaev, I. S.; Irman, A.; Overgaag, K.; Vanmaekelbergh, D.; Vos, W. L. Controlling the Dynamics of Spontaneous Emission from Quantum Dots by Photonic Crystals. *Nature* **2004**, *430* (7000), 654–657. https://doi.org/10.1038/nature02772.
(9) Phillips, C. L.; Brash, A. J.; Godsland, M.; Martin, N. J.; Foster, A.; Tomlinson, A.; Dost, R.; Babazadeh, N.; Sala, E. M.; Wilson, L.; Heffernan, J.; Skolnick, M. S.; Fox, A. M. Purcell-Enhanced Single Photons at Telecom Wavelengths from a Quantum Dot in a Photonic Crystal Cavity. *Sci. Rep.* **2024**, *14* (1), 4450. https://doi.org/10.1038/s41598-024-55024-6.
(10) Rakovich, A.; Albella, P.; Maier, S. A. Plasmonic Control of Radiative Properties of Semiconductor Quantum Dots Coupled to Plasmonic Ring Cavities. *ACS Nano* **2015**, *9* (3), 2648–2658. https://doi.org/10.1021/nn506433e.
(11) Tamada, A.; Ota, Y.; Kuruma, K.; Watanabe, K.; Iwamoto, S.; Arakawa, Y. Single Plasmon Generation in an InAs/GaAs Quantum Dot in a Transfer-Printed Plasmonic Microring Resonator. *ACS Photonics* **2019**, *6* (5), 1106–1110. https://doi.org/10.1021/acsphotonics.8b01749.
(12) Ates, S.; Sapienza, L.; Davanco, M.; Badolato, A.; Srinivasan, K. Bright Single-Photon Emission From a Quantum Dot in a Circular Bragg Grating Microcavity. *IEEE J. Sel. Top. Quantum Electron.* **2012**, *18* (6), 1711–1721. https://doi.org/10.1109/JSTQE.2012.2193877.
(13) Moczała-Dusanowska, M.; Dusanowski, Ł.; Iff, O.; Huber, T.; Kuhn, S.; Czyszanowski, T.; Schneider, C.; Höfling, S. Strain-Tunable Single-Photon Source Based on a Circular Bragg Grating Cavity with Embedded Quantum Dots. *ACS Photonics* **2020**, *7* (12), 3474–3480. https://doi.org/10.1021/acsphotonics.0c01465.
(14) Wijitpatima, S.; Auler, N.; Mudi, P.; Funk, T.; Barua, A.; Shrestha, B.; Schall, J.; Limame, I.; Rodt, S.; Reuter, D.; Reitzenstein, S. Bright Electrically Contacted Circular Bragg Grating Resonators with Deterministically Integrated Quantum Dots. *ACS Nano* **2024**, *18* (46), 31834–31845. https://doi.org/10.1021/acsnano.4c07820.
(15) Wu, J.; Lee, S.; Reddy, V. R.; Manasreh, M. O.; Weaver, B. D.; Yakes, M. K.; Furrow, C. S.; Kunets, Vas. P.; Benamara, M.; Salamo, G. J. Photoluminescence Plasmonic Enhancement in InAs Quantum Dots Coupled to Gold Nanoparticles. *Mater. Lett.* **2011**, *65* (23), 3605–3608. https://doi.org/10.1016/j.matlet.2011.08.019.
(16) Zhang, Y.; Eyink, K.; Urwin, B.; Mahalingam, K.; Hill, M. A Self-Assembling Method to Align Metal Nanoparticles to Quantum Dots. *J. Cryst. Growth* **2023**, *605*, 127072. https://doi.org/10.1016/j.jcrysgro.2022.127072.

(17) Sapienza, L.; Davanço, M.; Badolato, A.; Srinivasan, K. Nanoscale Optical Positioning of Single Quantum Dots for Bright and Pure Single-Photon Emission. *Nat. Commun.* **2015**, *6* (1), 7833. https://doi.org/10.1038/ncomms8833.

(18) Lyasota, A.; Jarlov, C.; Nyman, M.; Miranda, A.; Calic, M.; Dwir, B.; Rudra, A.; Shevchenko, A.; Kapon, E. Mode Interference Effect in Optical Emission of Quantum Dots in Photonic Crystal Cavities. *Phys. Rev. X* **2022**, *12* (2), 021042. https://doi.org/10.1103/PhysRevX.12.021042.

(19) Peniakov, G.; Buchinger, Q.; Helal, M.; Betzold, S.; Reum, Y.; Rota, M. B.; Ronco, G.; Beccaceci, M.; Krieger, T. M.; Da Silva, S. F. C.; Rastelli, A.; Trotta, R.; Pfenning, A.; Höfling, S.; Huber-Loyola, T. Polarized and Unpolarized Emission from a Single Emitter in a Bullseye Resonator. *Laser Photonics Rev.* **2024**, *18* (4), 2300835. https://doi.org/10.1002/lpor.202300835.

(20) Rigal, B.; Joanesarson, K.; Lyasota, A.; Jarlov, C.; Dwir, B.; Rudra, A.; Kulkova, I.; Kapon, E. Propagation Losses in Photonic Crystal Waveguides: Effects of Band Tail Absorption and Waveguide Dispersion. *Opt. Express* **2017**, *25* (23), 28908. https://doi.org/10.1364/OE.25.028908.

(21) Colavecchi, L.; Juska, G.; Pelucchi, E. Optimizing Light Extraction from Non-Planar Site-Controlled Pyramidal Quantum Dot System: Comparative Modeling of Three Fabricable Geometries. *Mater. Quantum Technol.* **2025**. https://doi.org/10.1088/2633-4356/adb6ec.

(22) Friedler, I.; Lalanne, P.; Hugonin, J. P.; Claudon, J.; Gérard, J. M.; Beveratos, A.; Robert-Philip, I. Efficient Photonic Mirrors for Semiconductor Nanowires. *Opt. Lett.* **2008**, *33* (22), 2635–2637. https://doi.org/10.1364/OL.33.002635.

(23) Barrow, M.; Wright, S.; Puzycki, S.; Shah, P.; Bedford, R.; Zhang, Y.; Phillips, J. Highly Selective GaAs/AlGaAs Dry Etching Using HBr/SF6/He. *J. Vac. Sci. Technol. B* **2021**, *39* (5), 052202. https://doi.org/10.1116/6.0001181.

(24) Lee, J. W.; Devre, M. W.; Reelfs, B. H.; Johnson, D.; Sasserath, J. N.; Clayton, F.; Hays, D.; Pearton, S. J. Advanced Selective Dry Etching of GaAs/AlGaAs in High Density Inductively Coupled Plasmas. *J. Vac. Sci. Technol. A* **2000**, *18* (4), 1220–1224. https://doi.org/10.1116/1.582329.

(25) Seaward, K. L.; Moll, N. J.; Stickle, W. F. The Role of Aluminum in Selective Reactive Ion Etching of GaAs on AlGaAs. *J. Vac. Sci. Technol. B Microelectron. Process. Phenom.* **1988**, *6* (6), 1645–1649. https://doi.org/10.1116/1.584423.

7 Conclusions

This thesis addresses the engineering challenges associated with the integration of Pyramidal Quantum Dots into photonic structures and non, by characterizing existing configurations and developing and validating novel processing methods. The work investigates how these methods, and the relative geometries, affect the optical properties of the emitters, and explores their application across multiple device configurations — from micropillars for deterministic single- and entangled-photon emission to a novel resonant cavity design based on the tetrahedral geometry. Through a combination of experimental characterization and FDTD simulations, the research aims to optimize light extraction efficiency and explore practical routes toward scalable nanophotonic device fabrication.

A recurrent theme throughout the text is the need for a calibration model closely adherent to the experimental observations found through the systematic AFM cross section investigation. Thickness calibration inside the recess would allow precise positioning of the dot with respect to the first/last grown layers unlocking control of Purcell enhancement, fundamental for the novel resonant cavity design introduced in Chapter 4 and explored in Chapter 6, but potentially pivotal for micropillar design, where simulations suggest the presence of faint constructive interference mechanisms, exploitable just as in the same way as I have done for the back-etched configuration.

The Mirrored Pyramids fabrication technique I developed to simplify the application of an electric field, enormously shortens the process for the application of the metal contacts and increases the specimen yield with respect to the back-etched configuration, representing a step forward towards scalability. The peculiar response of PQDs to an electric field is for the first time assessed and clearly needs to be better understood and harnessed. My understanding is that barrier's heights of different entities cause population of different excitonic states in presence of an electric field, but the tetrahedral geometry favours tunnelling of the confined states towards the

LQW/LQWrs/VQWr leaking paths when the junction is reverse biased in a common fashion for all kinds of confinement, impeding Stark-shifting and FSS-tuning the transitions.

Although the outcomes of this work may not represent a breakthrough in the field, they contribute to a deeper understanding of the practical challenges and possibilities involved in functionalizing PDQs. The most significant contribution of this PhD work, besides the introduction of the Mirrored Pyramids and of the Pyramidal Resonating Cavity configurations, of which I'm proud, is the systematic approach towards the fabrication process I employed, that made surface overlooked problems and delineated strategies to address them.

Building on the knowledge accumulated in these 4 years of PhD, I believe future works should adopt practical approaches to rule out all the impediments that are mentioned in the chapters.

Above all stands the ***back-etching process***, which should be systematically performed both in dry and wet environment, in the strive for the highest selectivity attainable. This would immensely benefit the Pyramidal Resonating Cavity fabrication, which exploration has just begun (and I hope will continue) and possibly reinstate the back-etched p-i-n junction configuration as still advantageous over the Mirrored Pyramid configuration.

FSS tuning is still missing within our capabilities despite the attempts reported here. Yet, the use of an electric filed doesn't have to be put aside: employing very low concentration AlGaAs QD-like structures, or InGaAs QDs, in *AlAs* barriers might result in an improved spatial confinement and reduce overlap with leakage channels. Alternatively, *piezoelectric actuators* would surely do the job, however the planarity requirement for strain transfer is not compatible with the 3D topologies which we show to be cardinal for high extraction efficiency in PQDs. To walk such a way, PQDs would have to be grown on a thin GaAs/DBR membrane bonded to a carrier/PMN-PT stack and polished down until recesses disappear. That would in principle open the door to

fabricating Circular Bragg Mirrors, at the expense of giving up the advantageous self-aligning peculiarity of micropillars/Pyramidal Resonating Cavities.

Micropillars have turned out to be our best configuration so far, however the triangular symmetry imposed on the electromagnetic modes to which dipoles couple, might be the cause of polarized emission. Effort could be put on devising solutions to reshape the pillars after the etch, or dry etching staring from a circular mask; both are non-trivial. At the same time, transfer procedure to couple pillars to waveguides should be explored. The FIB procedure shown in Chapter 3 is a viable option but with an extremely low yield. The use of polymers that can be peeled off represents a better alternative for higher specimen yield.

Additionally, micropillars could play a role in enhancing the Purcell factor, provided that a strategy is developed to incorporate a reflector at one extremity. However, this approach may prove more technically challenging than the method proposed for the pyramidal resonating cavity, and only time will determine which configuration will ultimately prevail.

Acknowledgements

During my four years at the Tyndall National Institute, I had the opportunity to collaborate with a diverse range of researchers, each with unique perspectives and approaches to research. Their different views helped me to adapt to my challenges, rethink my assumptions, and ultimately grow—both academically and personally. It is thanks to the fruitful discussions I had with them that this thesis bears some results.

I extend my gratitude to my supervisor, Dr. Emanuele Pelucchi, for his role in overseeing this thesis work, and to my Co-supervisor, Dr. Gediminas Juska, who, over these years, has taken care of the spectroscopic characterization of most of my samples, and has encouraged me to persist when results fell short of expectations.

My gratitude goes to all members of the group, past and present: to former members like Agnieska, who initiated me into the intricacies of epitaxial growth; Simone, whose expertise in fabrication taught me the value of precision and pragmatism; and then Iman, Francesco and Nicola.

To the current members—Kevin, Camille, Ayse, Swati, John, and Armando—I extend my thanks. To Armando, who is almost halfway into his PhD, I wish perseverance and success as you embark on your PhD journey.

Finally, to my dearest friend, mi hermano, Salvador: your clever, dynamic mind and unwavering optimism transformed challenges into opportunities. Thank you for keeping the lab alive with ideas—and laughter.

Thank you to all the friends I made on this demanding journey.